Solar Neutrino Physics

Solar Neutrino Physics

The Interplay between Particle Physics and Astronomy

Lothar Oberauer
Aldo Ianni
Aldo Serenelli

WILEY-VCH

Authors

Professor Lothar Oberauer
TU München
Physik Department
E15
James-Franck-Straße 1
85748 Garching
Germany

Dr. Aldo Ianni
I.N.F.N. Laboratori Nazionali del Gran Sasso
Via Giovanni Acitelli 22
67100 Assergi (AQ)
Italy

Dr. Aldo Serenelli
Institute of Space Sciences
Carrer de Can Magrans, s/n
08193 Bellaterra
Spain

Library of Congress Card No.:
applied for

British Library Cataloguing-in-Publication Data
A catalogue record for this book is available from the British Library.

Bibliographic information published by the Deutsche Nationalbibliothek
The Deutsche Nationalbibliothek lists this publication in the Deutsche Nationalbibliografie; detailed bibliographic data are available on the Internet at <http://dnb.d-nb.de>.

Print ISBN: 978-3-527-41274-7
ePDF ISBN: 978-3-527-41276-1
ePub ISBN: 978-3-527-41273-0
oBook ISBN: 978-3-527-41272-3

Cover Design Grafik-Design Schulz
Typesetting SPi Global, Chennai, India
Printing and Binding

Printed on acid-free paper

10 9 8 7 6 5 4 3 2 1

The Sun is the source of energy for life on Earth. Solar neutrinos are the gift given to guide us in unlocking its most hidden secrets.

Contents

1 Introduction *1*

2 Solar Structure and Evolution *3*
2.1 Equations of Stellar Structure and Evolution *3*
2.1.1 Mechanical Structure *3*
2.1.2 Energy Conservation and Transport *5*
2.1.2.1 Energy Transport by Radiation and Conduction *5*
2.1.2.2 Criterion for Dynamical Instability *7*
2.1.2.3 Energy Transport: Convection *9*
2.1.3 Changes in Chemical Composition *11*
2.1.3.1 Convective Mixing *11*
2.1.3.2 Changes in Chemical Composition: Atomic Diffusion *12*
2.1.3.3 Changes in Chemical Composition: Nuclear Reactions *15*
2.1.3.4 Changes in Chemical Composition: Putting Everything Together *16*
2.1.4 Full Set of Equations and Boundary Conditions *17*
2.2 Constitutive Physics *18*
2.2.1 Equation of State *18*
2.2.2 Radiative Opacities *21*
2.2.3 Nuclear Reaction Rates *25*
2.3 Calibrating Standard Solar Models *31*
2.3.1 Observational Constraints *31*
2.3.1.1 Age, Mass, Radius, and Luminosity *31*
2.3.1.2 Surface Composition *32*
2.3.2 Adjusting the Free Parameters *35*
2.4 Standard Solar Models *36*
2.4.1 Previous and Future Evolution *36*
2.4.2 The Sun Today: An Overview *39*
2.5 Solar Neutrinos *42*
2.6 Helioseismology *48*
2.6.1 Overview *48*
2.6.2 Global Structure Inversions *51*
2.6.3 Other Constraints *53*
2.7 Solar Abundance Problem *54*
2.8 Uncertainties in SSMs *58*
2.8.1 Uncertainties in SSM Inputs *58*

2.8.1.1 Nuclear Reaction Rates *58*
2.8.1.2 Microscopic Diffusion *59*
2.8.1.3 Radiative Opacities *59*
2.8.1.4 Solar Radius, Luminosity, and Age *59*
2.8.1.5 Solar Composition *59*
2.8.1.6 Equation of State *60*
2.8.2 Global Uncertainties in SSMs *60*
2.8.2.1 Nuclear Reaction Rates *61*
2.8.2.2 Constitutive Physics *61*
2.8.2.3 Element Abundances *62*
2.9 Solar Models Beyond the SSM *62*
2.9.1 Nonstandard Solar Physics *63*
2.9.2 Nonstandard Particle Physics *65*

3 Neutrino Physics *69*
3.1 Neutrinos in the Standard Model *69*
3.2 Neutrino Oscillations *75*
3.3 Matter Effects *80*
3.4 Neutrino Oscillation Experiments *84*
3.4.1 Atmospheric Neutrinos *84*
3.4.2 Long Baseline Accelerator Neutrinos *92*
3.4.2.1 Long Baseline Experiments and θ_{13} *97*
3.4.3 Reactor Neutrinos *100*
3.5 Conclusions and Open Questions *109*
3.5.1 What Is the Absolute Neutrino Mass Scale? *111*
3.5.2 Are Neutrinos Majorana or Dirac Particles? *120*
3.5.3 What Is the Neutrino Mass Ordering and How Large Is CP-δ? *127*
3.5.4 Are There Sterile Neutrinos? *135*

4 Solar Neutrino Experiments *139*
4.1 Introduction *139*
4.2 The ^{37}Cl Experiment *141*
4.3 Kamiokande-II/III *145*
4.4 The ^{71}Ga Experiments *153*
4.5 Super-Kamiokande *162*
4.6 SNO *169*
4.7 Borexino *178*
4.8 Summary and Open Questions *191*

5 Future Solar Neutrino Experiments *195*
5.1 SNO+ *196*
5.2 JUNO and LENA *199*
5.3 Hyper-Kamiokande *204*
5.4 DUNE *206*

References *209*

Index *221*

1

Introduction

In 2015 Arthur B. McDonald and Takaaki Kajita were awarded with the Nobel Prize in Physics for their discovery of neutrino oscillations and the inevitable consequence that neutrinos have a mass. The perception of non-vanishing neutrino masses implies that the standard model of particle physics has to be extended. This great discovery has been achieved by measuring solar and atmospheric neutrinos. The former are emitted as a product of thermonuclear fusion reactions inside the Sun; the latter are produced in weak decays of mesons, which are generated by the reactions of cosmic particles in the top layers of the Earth's atmosphere. Indeed, the origin of the idea of neutrino oscillations can be found in the pioneering Homestake solar neutrino experiment in the early 1970s (Nobel Prize 2002). Homestake was the first experiment able to detect solar neutrinos. In addition, it proved the basic assumption of thermonuclear fusion processes in the Sun and, at the same time, it recorded a deficit in the measured solar neutrino flux, when one compares it with theoretical predictions. Yet, it took almost 30 years and several experiments until the existence of neutrino oscillations could really be proven.

Solar neutrino experiments have a second aspect, in addition to particle physics. The production of neutrinos in the Sun is sensitive to the physical conditions in the solar interior. Therefore, solar neutrino measurements can be used to determine the physical properties of the solar core.

In this book we present and discuss the actual status of solar physics with its strong link to neutrino physics. Chapter 2 deals with the physics and basic equations that are relevant to understand the stellar structure and evolution. We show how solar models can be calibrated by confronting them to the observational constraints of the age, mass, radius, and luminosity of the Sun. We present general evolutionary properties of the Sun as a star, past and future. For the present-day Sun, a detailed presentation of its internal structure is given. This is required for then discussing the solar neutrino production via the pp chains and CNO cycle, including the important role of the chemical composition of the Sun. A very important source of information about the solar interior is offered by helioseismology, the study of solar oscillations. The topic is introduced briefly, and then the most relevant results are given, again placing some emphasis on the differences arising from the assumptions made about the solar composition. The solar abundance (or solar modeling?) problem, a now more than 15 year old

Solar Neutrino Physics: The Interplay between Particle Physics and Astronomy,
First Edition. Lothar Oberauer, Aldo Ianni, and Aldo Serenelli.

problem is discussed to some extent, both in the context of helioseismology and, very importantly, solar neutrinos. Chapter 2 closes with a description of model uncertainties and an overview about solar models beyond the standard case.

The neutrino physics is introduced in Chapter 3. First we describe neutrinos in the standard model of particle physics. Then, we introduce the concept of neutrino mass eigenstates and neutrino mixing leading to the phenomenon of neutrino oscillations. The basic equations in the case of two- and three-neutrino oscillations will be derived. As solar neutrinos are influenced by matter effects inside the Sun and at least partially also by Earth matter effects, we describe the basic impact of matter on the behavior of neutrino oscillations. In Chapter 3, we give an overview about results of neutrino oscillation experiments, which are not using solar neutrinos as source. The chapter closes with a discussion about open questions in neutrino physics. We review the concept of Dirac and Majorana neutrinos, mass ordering, and CP violation in the framework of neutrino physics. We discuss the idea of sterile neutrinos.

Solar neutrino experiments are discussed in Chapter 4. Here, we follow a historical line beginning with radiochemical experiments, where the so-called solar neutrino puzzle has been established. We continue with the description of real-time experiments, namely, Kamiokande, Super-Kamiokande, and Sudbury Neutrino Observatory (SNO). We underline the impact of these experiments on our current understanding of the solar neutrino puzzle in terms of neutrino oscillations. Finally, the performance and recent results of the Borexino experiment are reported and discussed. The chapter closes with a summary of the achievements after 50 years of solar neutrino physics and a discussion about open questions.

Chapter 5 reports a review of upcoming experiments and their capabilities to contribute to a better understanding of neutrino and solar physics. In particular, we briefly review SNO+, Jiangmen Underground Neutrino Observatory (JUNO), Low Energy Neutrino Astrophysics (LENA), Hyper-Kamiokande, and Deep Underground Neutrino Experiment (DUNE).

2

Solar Structure and Evolution

This chapter introduces the equations of stellar structure and evolution and the most important physical processes that determine the evolution of the Sun. We then present the important concept of standard solar model (SSM) and place it in the broader context of evolution of low mass stars, of which the Sun is a typical representative, by discussing the main characteristics of its evolution, from its formation to advanced evolutionary phases. The present-day properties of SSM are then discussed in detail, including theoretical predictions for solar neutrinos and helioseismic probes of the solar interior and the current theoretical uncertainties in solar models. We close the chapter with a generic discussion of nonstandard solar models (non-SSMs), i.e. in which physical processes considered nonstandard have been included in the models.

2.1 Equations of Stellar Structure and Evolution

The fundamental equations that determine the structure and evolution of stars reflect the conservation laws of mass, energy, and momentum and the physical processes that take place in stellar interiors. The resulting equations form a set of partial differential equations and the problem requires both initial and boundary conditions. Here, we derive the full set of equations and boundary conditions that underlie studies of solar models.

2.1.1 Mechanical Structure

The mechanical structure of stars, the Sun among them, is determined by the conservation laws of mass and momentum. In spherical symmetry, the equation of mass conservation can be established in a convenient form by considering the total variation of the mass $m(r, t)$ inside a sphere of radius r:

$$\mathrm{d}m(r,t) = 4\pi r^2 \rho \, \mathrm{d}r - 4\pi r^2 \rho v \, \mathrm{d}t \tag{2.1}$$

Here, the first term on the right is the mass contained in a shell of thickness $\mathrm{d}r$ and the second term is the mass flow with radial velocity v at the surface of the sphere in the time interval $\mathrm{d}t$. In this description, r is the independent coordinate.

Solar Neutrino Physics: The Interplay between Particle Physics and Astronomy,
First Edition. Lothar Oberauer, Aldo Ianni, and Aldo Serenelli.

However, in spherical symmetry it is more convenient to use the Lagrangian description in which m is the independent coordinate, i.e. to express r and other quantities as functions of m and t. The transformation between the two descriptions is obtained by considering the partial derivative:

$$\frac{\partial}{\partial m} = \frac{\partial}{\partial r}\frac{\partial r}{\partial m} = \frac{1}{4\pi r^2 \rho}\frac{\partial}{\partial r}$$

Applying this transformation to m, one readily obtains the equation of mass conservation in the Lagrangian description:

$$\frac{\partial r}{\partial m} = \frac{1}{4\pi r^2 \rho} \tag{2.2}$$

By comparing this expression with Eq. (2.1), it becomes clear that using the Lagrangian formulation equations can be written more simply.

The conservation of momentum in spherical symmetry is expressed as

$$\frac{\mathrm{d}^2 r}{\mathrm{d}t^2} = -\frac{Gm}{r^2} - \frac{1}{\rho}\frac{\partial P}{\partial r} \tag{2.3}$$

where the net acceleration is the result of the gravitational acceleration and the force per unit mass exerted by the pressure gradient.

The secular evolution of stars driven by stable nuclear burning leads to very slow changes in stellar size, leading to a negligible net acceleration. This is especially true for the Sun, a low mass main sequence star that evolves appreciably only over timescales of $\sim 10^9$ years. Estimates of the acceleration based on the evolution of detailed solar models lead to maximum values of the order of a few times 10^{-24} cm/s^2 at the solar surface. This can be compared with the gravitational acceleration that, in the solar surface, is 2.74×10^4 cm/s^2, i.e. about 28 orders of magnitude larger. Under these conditions, the conservation of momentum reduces to the equation of hydrostatic equilibrium:

$$\frac{\partial P}{\partial r} = -\frac{Gm}{r^2}\rho \tag{2.4}$$

The response timescale to departures from hydrostatic equilibrium is very short. This can be estimated by considering Eq. (2.3). If, for example, a very large increase in the pressure gradient were to occur such that the second term on the right-hand side dominates, then the response time would be of the order $\tau_{\mathrm{P}} \approx R_\odot/\overline{c}_s \approx 3500$ seconds. Here, $\overline{c}_s \propto (\overline{P}/\overline{\rho})^{1/2}$ is an average value of the sound speed in the solar interior, of the order of 10^7 cm/s. On the other hand, if the pressure gradient were to become negligible, the response time would be that of free fall: $\tau_{\mathrm{ff}} \approx (G\overline{\rho})^{-1/2} \approx 3200$ seconds, where $\overline{\rho} = 1.4$ g/cm^3 is the solar mean density. Any large-scale dynamical instability would relax in timescales extremely short compared to the evolutionary timescales of the Sun, justifying again the assumption of hydrostatic equilibrium in solar evolution models. Finally, transforming Eq. (2.4) to the Lagrangian formulation leads to

$$\frac{\partial P}{\partial m} = -\frac{Gm}{4\pi r^4} \tag{2.5}$$

Equations (2.2) and (2.5) determine the mechanical structure of the Sun.

2.1.2 Energy Conservation and Transport

The next step in deriving the full set of stellar evolution equations is to consider the energetics of stars. The first law of thermodynamics states:

$$\mathrm{d}q = \mathrm{d}u - \frac{P}{\rho^2}\,\mathrm{d}\rho$$

where q and u are respectively the heat and internal energy per unit mass for an element of specific volume $1/\rho$. Here, the first term represents a change in the internal energy and the second term the work, by expansion or contraction, done on the element. Also, if ε represents a local rate of energy production per unit mass and F is the radial component of the energy flux, the rate of change of heat in the volume element is

$$\frac{\mathrm{d}q}{\mathrm{d}t} = \varepsilon - \frac{1}{\rho r^2}\frac{\partial(r^2F)}{\partial r}$$

where the second term is the divergence of the energy flux per unit mass. This can be expressed as

$$\frac{\mathrm{d}q}{\mathrm{d}t} = \varepsilon - \frac{1}{4\pi\rho r^2}\frac{\partial l}{\partial r}.$$

Here $l = 4\pi r^2 F$ is the energy flux across a sphere of radius r, i.e. the luminosity. Using the Lagrangian transformation,

$$\frac{\mathrm{d}q}{\mathrm{d}t} = \varepsilon - \frac{\partial l}{\partial m}$$

defining

$$\varepsilon_{\mathrm{gr}} = -\frac{\mathrm{d}u}{\mathrm{d}t} + \frac{P}{\rho^2}\frac{\mathrm{d}\rho}{\mathrm{d}t}$$

and combining with the first law of thermodynamics:

$$\frac{\partial l}{\partial m} = \varepsilon + \varepsilon_{\mathrm{gr}}$$

In standard stellar evolution ε represents nuclear energy sources and neutrino energy losses, i.e. $\varepsilon = \varepsilon_{\mathrm{nuc}} - \varepsilon_{\nu}$. The second term, $\varepsilon_{\mathrm{gr}}$, usually referred to as gravothermal energy, accounts for changes in internal energy and work. The final form of the equation of energy conservation is then:

$$\frac{\partial l}{\partial m} = \varepsilon_{\mathrm{nuc}} - \varepsilon_{\nu} + \varepsilon_{\mathrm{gr}} \tag{2.6}$$

2.1.2.1 Energy Transport by Radiation and Conduction

In standard stellar models, there are three mechanisms for transporting energy that occur because of the temperature gradient that exists between the inner and outer stellar regions: radiation, (electron) conduction, and convection. From a strict point of view, the first two are always present because they directly depend on the existence of a temperature gradient. Convection, on the other hand, occurs in stars when a region becomes dynamically unstable and macroscopic convective motions set in. The actual temperature gradient in the stellar interior will be determined by the combined action of these transport mechanisms.

Radiation transport in stellar interiors can be treated under the so-called diffusion approximation, i.e. by consideration of Fick's law applied to radiation energy. This is justified because the mean free path of photons in stellar interiors is much smaller than the characteristic length scales over which physical conditions change significantly.[1] The opaqueness of matter to radiation is conveniently represented in stellar interiors by the opacity, an absorption coefficient expressed in units of cross section per unit mass. The mean free path of photons is then given by

$$\ell_{\rm ph} = \frac{1}{\kappa_r \rho} \tag{2.7}$$

where κ_r is an appropriate average, to be discussed below, of the opacity taken over the whole spectrum of photons. Typical values of $\ell_{\rm ph}$ determined from detailed solar models range between 10^{-2} and 1 cm in the solar interior. The small values of $\ell_{\rm ph}$ also mean that the variation of temperature that a photon experiences over $\ell_{\rm ph}$ is very small and local thermodynamic equilibrium (LTE) is very well satisfied in solar interiors.

Fick's law applied to radiation energy density is

$$F = -\frac{1}{3} c\, \ell_{\rm ph} \frac{\partial u}{\partial r}$$

with c as the speed of light, a the radiation density constant, and $u = aT^4$ the energy density of radiation. Expressing now the radiation flux F in terms of the luminosity, replacing the energy density gradient by its corresponding temperature gradient, and $\ell_{\rm ph}$ with Eq. (2.7):

$$\frac{\partial T}{\partial r} = -\frac{3}{16\pi\, a\, c} \frac{\kappa_r \rho l}{r^2 T^3}$$

Applying the Lagrangian transformation, the equation of radiative transport is

$$\frac{\partial T}{\partial m} = -\frac{3}{64\pi^2\, a\, c} \frac{\kappa_r l}{r^4 T^3} \tag{2.8}$$

Conduction can also be treated as a diffusive process, characterized by a conductive opacity $\kappa_{\rm cond}$. It is accounted for in the transport of energy by replacing the radiative opacity κ_r by

$$\frac{1}{\kappa} = \frac{1}{\kappa_r} + \frac{1}{\kappa_{\rm cond}}$$

In the Sun, conduction is a very inefficient transport mechanism. In an ideal gas under non-degenerate conditions, electrons have an extremely short mean free path in comparison to photons. In the solar center, where the density of free electrons is highest, the conductive opacity is $\kappa_{\rm cond} \sim 10^3$ cm^2/g, in comparison to a typical value $\sim$1 cm^2/g for the radiative opacity κ_r, i.e. $1/\kappa \approx 1/\kappa_r$. The mean free path of electrons is then shorter by the same factor, rendering conduction a negligible energy transport mechanism in the solar interior.

1 This approximation breaks down at the solar atmosphere, where the mean free path of photons becomes comparable to the size of the atmosphere.

The equation for radiative and conductive transport is then

$$\frac{\partial T}{\partial m} = -\frac{3}{64\pi^2\, a\, c}\frac{\kappa l}{r^4 T^3} \tag{2.9}$$

It is useful to express the temperature gradient in a dimensionless form:

$$\left(\frac{\partial \log T}{\partial \log P}\right)_{\text{rad}} = \nabla_{\text{rad}} \tag{2.10}$$

where the radiative gradient ∇_{rad} is defined as

$$\nabla_{\text{rad}} = \frac{3}{16\pi\, a\, c\, G}\frac{\kappa l P}{m T^4} \tag{2.11}$$

so that Eq. (2.9) reads:

$$\frac{\partial T}{\partial m} = -\frac{GmT}{4\pi r^4 P}\nabla_{\text{rad}} \tag{2.12}$$

Before, it was mentioned that κ_r is an appropriate average over the whole spectrum of photon energies. In fact, the relation $u = aT^4$ used above implicitly assumes LTE and that the radiation field is that of a black body, i.e. described by a Planck distribution. Under these conditions, it can be shown that κ_r is the Rosseland mean opacity, given by

$$\frac{1}{\kappa_r} = \frac{\pi}{a\, c\, T^3}\int_0^\infty \frac{1}{\kappa_\nu}\frac{\partial B_\nu}{\partial T}\mathrm{d}\nu \tag{2.13}$$

where ν is the radiation frequency, κ_ν the monochromatic opacity, and

$$B_\nu(T) = \frac{8\pi h}{c^3}\frac{\nu^3}{\mathrm{e}^{h\nu/kT} - 1}$$

is the Planck function for radiation intensity. The Rosseland mean opacity entering the equation of radiative transport is then the harmonic mean of the monochromatic opacity weighted by $\partial B_\nu/\partial T$.

2.1.2.2 Criterion for Dynamical Instability

Radiative transport is inefficient when ∇_{rad} is sufficiently large and the temperature gradient required to transport energy is too steep. This typically occurs under two circumstances, when κ is large as it happens in regions where dominant chemical elements are partially ionized, and when the production of nuclear energy is concentrated in small volumes such that the ratio l/m is large. The increase in ∇_{rad} inside a star can lead to the development of a dynamical instability in which macroscopic motions of the gas set in, a process known as convection.

At any given depth r, there are always small fluctuations in the thermodynamic properties of the gas. The question of dynamical instability is whether or not these fluctuations grow and develop into large-scale motions. Consider a region in the star where the actual temperature gradient is radiative, and consider a small parcel of material that experiences a small fluctuation, e.g. an increase, in its temperature:

$$\Delta T(r) = T_p(r) - T_s(r) > 0$$

where T_p and T_s are the temperatures of the small parcel of gas and the stellar surroundings at depth r, respectively. There are pressure and density fluctuations associated with ΔT. Hydrostatic equilibrium between the surrounding medium and the parcel of matter quickly restores pressure balance, i.e. $\Delta P = 0$. Under this condition, and for an ideal equation of state (EoS), the density fluctuation will be

$$\Delta\rho(r) = \rho_p(r) - \rho_s(r) < 0$$

so the parcel is less dense than the medium and experiences a net buoyancy force. Which is the situation after the parcel of material has risen an infinitesimal distance δr? In other words, is $\Delta\rho(r + \delta r)$ positive (stability) or negative (instability)? The change in $\Delta\rho$ is

$$\frac{\mathrm{d}(\Delta\rho)}{\mathrm{d}r}\delta r = \left[\left(\frac{\mathrm{d}\rho}{\mathrm{d}r}\right)_p - \left(\frac{\mathrm{d}\rho}{\mathrm{d}r}\right)_s\right]\delta r$$

Under almost every situation inside stars, and certainly in solar interiors, density gradients are negative, so that the stability condition is

$$\left[\left(\frac{\mathrm{d}\ \log\rho}{\mathrm{d}r}\right)_p - \left(\frac{\mathrm{d}\log\rho}{\mathrm{d}r}\right)_s\right] > 0 \tag{2.14}$$

The EoS $\rho = \rho(P, T, \mu)$, where μ is the mean molecular weight, relates changes among thermodynamic quantities such that

$$\begin{aligned}\frac{\mathrm{d}\rho}{\rho} &= \left(\frac{\partial\log\rho}{\partial\log P}\right)_{T,\mu}\frac{\mathrm{d}P}{P} + \left(\frac{\partial\log\rho}{\partial\log T}\right)_{P,\mu}\frac{\mathrm{d}T}{T} + \left(\frac{\partial\log\rho}{\partial\log\mu}\right)_{P,T}\frac{\mathrm{d}\mu}{\mu}\\ &= \alpha\frac{\mathrm{d}P}{P} - \delta\frac{\mathrm{d}T}{T} + \phi\frac{\mathrm{d}\mu}{\mu}\end{aligned}$$

Replacing this expression in Eq. (2.14), and using DP = 0 and that there are no changes in the chemical composition of the parcel, the stability condition is now

$$-\delta\left(\frac{\mathrm{d}\ \log T}{\mathrm{d}r}\right)_p + \delta\left(\frac{\mathrm{d}\ \log T}{\mathrm{d}r}\right)_s - \phi\left(\frac{\mathrm{d}\ \log\mu}{\mathrm{d}r}\right)_s > 0$$

By multiplying this relation by $\mathrm{d}r/\mathrm{d}\log P$, which is a negative quantity, and extending the definition of the dimensionless temperature gradient, the stability condition is now expressed more simply as

$$\nabla_s < \nabla_p + \frac{\phi}{\delta}\nabla_{\mu,s} \tag{2.15}$$

For simplicity, the subindex s can be dropped. Then, under the condition of stability, $\nabla = \nabla_{\mathrm{rad}}$. Moreover, the limiting case is established when the there is no heat exchange between the moving parcel and the surrounding medium, i.e. $\nabla_p = \nabla_{\mathrm{ad}}$, where

$$\nabla_{\mathrm{ad}} = \left(\frac{\partial\log T}{\partial\log P}\right)_{\mathrm{ad}}$$

is the adiabatic dimensionless temperature gradient that is determined solely by the EoS. Taking all this into account, the stability criterion known as the Ledoux criterion reads

$$\nabla_{\rm rad} < \nabla_{\rm ad} + \frac{\phi}{\delta}\nabla_{\mu} \tag{2.16}$$

When the layers of the star have homogeneous composition, i.e. $\nabla_{\mu} = 0$, this reduces to the Schwarzschild criterion:

$$\nabla_{\rm rad} < \nabla_{\rm ad} \tag{2.17}$$

The stability condition has been presented here in some detail because it is fundamental in the determination of the properties of the convective envelope of the Sun, particularly the location of its lower boundary that can be determined precisely using helioseismic techniques (Section 2.6).

2.1.2.3 Energy Transport: Convection

Consider a situation in which the composition is homogeneous ($\nabla_{\mu} = 0$) and in which the stability condition Eq. (2.17) is not fulfilled. Convection sets in such that hot bubbles rise and release their excess heat at outer regions. Simultaneously, cooler material is drafted downwards, also contributing to an outward transport of energy. There is always a temperature gradient present in the star, and some fraction of energy is always transported by radiation. But the presence of convection implies $\nabla < \nabla_{\rm rad}$. Also, although the motion of the parcels, or bubbles, closely follows adiabaticity, there is always some heat exchange with the surroundings so that the gradient in the moving parcel is larger than the adiabatic one, i.e. $\nabla_{\rm ad} < \nabla_{p}$. Combining these ideas with the stability condition in Eq. (2.15), the following inequality can be established in convective regions:

$$\nabla_{\rm ad} < \nabla_{p} < \nabla < \nabla_{\rm rad} \tag{2.18}$$

Here ∇ is the actual dimensionless temperature gradient in the star:

$$\nabla = \frac{\partial \log T}{\partial \log P}$$

Combining this with the equation of hydrostatic equilibrium in its Lagrangian form (Eq. (2.5)):

$$\frac{\partial T}{\partial m} = -\frac{GmT}{4\pi r^4 P}\nabla \tag{2.19}$$

This equation has the same structure as the equation of radiative energy transport (Eq. (2.12)) with the difference that $\nabla_{\rm rad}$ has been replaced by ∇. In practice, ∇ has to be determined from a theory of convection across all convective regions in a star.

In stellar interiors, convection is turbulent and there is no first principles solution of the hydrodynamics equations from which to determine the properties of convective flows such as convective velocities, size of convective eddies,

and temperature gradient. In stellar models, the most widely used theory of convection is the mixing length theory (MLT) [1]. Despite its simplicity, MLT has been used with great success in stellar interior and atmosphere models that show very good agreement with observations. We present here a basic outline of MLT, following closely that in Ref. [2].

In a convective region the total energy flux, $F = l/4\pi r^2$, can be expressed as the sum of the radiative and the convective fluxes, F_R and F_C respectively:

$$F = F_R + F_C = \frac{4acG}{3}\frac{mT^4}{\kappa r^2 P}\nabla_{\text{rad}} \tag{2.20}$$

and F_R is determined by the, yet unknown, actual gradient ∇:

$$F_R = \frac{4acG}{3}\frac{mT^4}{\kappa r^2 P}\nabla$$

MLT provides an expression for F_C based only on local quantities. If a rising bubble has an excess temperature ΔT with respect to the medium, then F_C is

$$F_C = \rho v_c c_P \Delta T$$

where c_P, the specific heat per mass unit at constant pressure, is used because the pressure in the bubble and the medium are assumed equal: i.e. heat exchange takes place under the condition $\Delta P = 0$. v_c is the velocity of the convective motions. In MLT, it is assumed all moving elements at a given radius travel at the same velocity and the same distance Λ, the mixing length, before dissolving and releasing their excess heat into the surroundings. On average, then, at a given location in the star, it is assumed that the crossing elements have traveled $\Lambda/2$. With these assumptions, the convective flux can be expressed as

$$F_C = \frac{1}{2}\rho v_c c_P \frac{\Lambda}{H_P}(\nabla - \nabla_p)$$

where the pressure scale height, $H_P = -(\mathrm{d}\log P/\mathrm{d}r)^{-1} = P/g\rho$, has been used to relate ΔT to the dimensionless temperature gradients. Λ can be related to H_P introducing the so-called mixing length parameter α_{mlt} such that

$$\Lambda = \alpha_{\text{mlt}} H_P \tag{2.21}$$

Note that α_{mlt} is a free parameter in the theory that needs to be calibrated using observational constraints. This is discussed further in Section 2.3.2.

In the expressions above, v_c, ∇, and ∇_p are unknown but related by Eq. (2.20). Additional considerations are required to establish a closed system of equations. The first one is the balance between the kinetic energy acquired by the work done by the rising element and the energy deposited in the surroundings. The second one is related to the temperature changes taking place inside the bubble that are related both to adiabatic cooling due to expansion and to radiative heat transfer with the surroundings. The final set of expressions that allow the calculation of ∇, given here without demonstration, are [2]

$$\xi = \sqrt{\nabla - \nabla_{\text{ad}} + U^2}$$
$$W = \nabla_{\text{rad}} - \nabla_{\text{ad}}$$

$$U = \frac{3acT^3}{c_P \rho^2 \kappa \alpha_{\rm mlt}^2 H_P^2} \sqrt{\frac{8H_P}{g\delta}}$$

Then, ∇ is determined by solving for ξ in the cubic equation:

$$(\xi - U)^3 + \frac{8U}{9}(\xi^2 - U^2 - W) = 0 \tag{2.22}$$

which has only one real solution. Note that all quantities entering the calculation of W and U are local. The gradient ∇ determined from MLT is therefore local as well.

The difference $\nabla - \nabla_{\rm ad}$ is sometimes referred to as overadiabaticity. There are two limiting solutions for a given value of W which correspond to cases where $U \to 0$ or $U \to \infty$. Convection is nearly adiabatic and a small overadiabaticity of the order 10^{-6}–10^{-8} suffices to transport all the energy. This is typical of conditions in stellar interiors, and it is also the case at the base of the solar convective envelope. Physically, it occurs when the thermal radiation timescale is long compared to the convective timescale so heat exchange between the moving bubbles and the surroundings is negligible. In this limit, where convection is almost completely adiabatic, there is no need for a full solution of Eq. (2.22) as $\nabla_{\rm ad}$ is determined from the EoS. The second case leads to $\nabla - \nabla_{\rm ad} \to \nabla_{\rm rad} - \nabla_{\rm ad}$, i.e. $\nabla \to \nabla_{\rm rad}$. Here, convection is very inefficient and heat exchange through radiation dominates. This is typical of very low density environments, for which the mean free path of photons is long. The intermediate case requires determining the actual solution of Eq. (2.22). In the Sun, this is needed in the outermost layers, at $R \approx 0.99\ R_\odot$. This is discussed further in some detail in Section 2.4.2.

A more general and thorough discussion of the solutions of Eq. (2.22) can be found, for example, in [2, 3].

2.1.3 Changes in Chemical Composition

2.1.3.1 Convective Mixing

An order of magnitude estimate of the typical velocity of convective flows can be done without recurring to theories of convection. Assume convective transport is efficient, such that the convective flux is $F_C \simeq l/(4\pi r^2)$. The flow of heat and kinetic energy density are comparable. The latter is proportional to $\rho v^2 v$, so at a given radius r:

$$\frac{l}{4\pi r^2} \sim \frac{1}{2}\rho v_c^3$$

Typical values in the convective envelope of the Sun are $\rho = 0.05$ g/cm^3, $r = 6 \times 10^{10}$ cm, and $l = L_\odot = 3.8418 \times 10^{33}$ erg/s. From the relation above, the estimation of the convective velocity is $v_c \sim 1.5 \times 10^4$ cm/s. The extension of the solar convective envelope is $\sim 2 \times 10^{10}$ cm. After neglecting factors of order unity, this yields an estimate of the global timescale for convection $\tau_c \sim 10^6$ seconds. Convection is a fast process in comparison with the secular timescales linked to solar evolution. Convective mixing will be comparably fast in maintaining chemical homogeneity in the convective regions. As a result, the solar convective envelope can be considered at all times to be chemically homogeneous.

Under certain circumstances, it is useful to use a more general approach in which convective mixing is treated as a time-dependent process. This simplifies the inclusion of other types of mixing processes that might not be as fast as convection, or special situations in which nuclear burning and convective mixing occur on comparable timescales. A widely used approach is to consider convective mixing as a diffusive process. A convection theory, e.g. MLT, is used to determine the average velocity of the flow at a given location in the star and the characteristic length over which convective elements travel. From Section 2.1.2.3, these quantities are v_c and $\Lambda = \alpha_{\rm mlt} H_P$. The diffusive coefficient for convective mixing is therefore $D_c = v_c \Lambda/3$. Convection is a macroscopic process and D_c is the same for all chemical species present in the convective regions. In radiatively stable zones, formally $D_c = 0$ because $v_c = 0$ and no convective mixing occurs.

If $X_i = \rho_i/\rho$ is the mass fraction of nuclear species i then, in spherical symmetry, the diffusion equation is [4, 5]

$$\rho\left(\frac{\partial X_i}{\partial t}\right)_c = \frac{1}{r^2}\frac{\partial}{\partial r}\left(r^2 D_c \rho \frac{\partial X_i}{\partial r}\right) \tag{2.23}$$

and, in Lagrangian form,

$$\left(\frac{\partial X_i}{\partial t}\right)_c = \frac{\partial}{\partial m}\left((4\pi r^2 \rho)^2 D_c \frac{\partial X_i}{\partial m}\right) \tag{2.24}$$

An improved estimate of the convective mixing timescale in the solar envelope can now be obtained, where typical values are $H_P \sim 10^9$ cm and v_c was estimated above. The convective diffusion coefficient is then $D_c \sim 10^{13}$ cm^2/s so the diffusive timescale across the convective envelope is $\tau_{c,\rm mix} \approx R_{\rm CZ}^2/D_c \sim 10^7$ seconds, with factors of order unity neglected again.

2.1.3.2 Changes in Chemical Composition: Atomic Diffusion

In the Sun, there is strong evidence from helioseismology that the helium fractional mass abundance in the solar convective envelope is lower by 10–12% than in the stably stratified radiative interior below it and lower than the helium abundance with which the Sun formed [6–8]. Accordingly, the hydrogen fractional mass abundance in the solar envelope is higher that the initial solar abundance. This cannot be accounted for by any sort of macroscopic mixing and it leads to consideration of several other mixing processes, generically grouped under the name of microscopic mixing, that induce a separation of elements by acting differentially on individual chemical species.

Following [9], a simple understanding of microscopic mixing can be obtained by considering a simple situation in which the chemical composition is given by a dominant component (protons) and a trace element t. The partial pressure of each component must satisfy the equation of hydrostatic equilibrium. The gravitational force must be taken into account together with other forces such as the electric force due to the presence of an electric field E. Assuming an ideal EoS, and that ρ_i and A_i are the mass density and atomic mass of species i, the partial pressure of component i is given by $P_i = \rho_i kT/A_i m_u$. Then, the hydrostatic

equilibrium equations for all the gas components are

$$\frac{\partial \log P_e}{\partial r} = -\frac{m_e g}{kT} - \frac{eE}{kT} + f_e \tag{2.25}$$

$$\frac{\partial \log P_p}{\partial r} = -\frac{A_p m_u g}{kT} + \frac{eE}{kT} + f_p \tag{2.26}$$

$$\frac{\partial \log P_t}{\partial r} = -\frac{A_t m_u g}{kT} + \frac{Z_t eE}{kT} + f_t \tag{2.27}$$

where the last term in each equation represents additional forces, for example, exerted by a magnetic field, acting on nuclei and electrons. For simplicity, the discussion is restricted only to the gravitational and electric forces so that the last term in each of the above equations is neglected. The assumption that t is a trace element implies $P_t \ll P_p$ which, together with the requirement of charge neutrality on macroscopic scales, leads to the condition:

$$-m_e g - eE = -m_p g + eE$$

where $m_p = A_p m_u$, so that

$$eE = \frac{1}{2}(m_p - m_e)g \approx \frac{1}{2} m_p g \tag{2.28}$$

The electric and gravitational forces acting on particles are comparable to each other.[2]

By comparing Eqs. (2.26) and (2.27), it can be seen that the characteristic length scale over which the partial pressures vary, $(\mathrm{d}\ \log\ P_i/\mathrm{d}r)^{-1}$, will be generally different from that of the partial pressure of protons, i.e. the equilibrium configuration is not a homogeneous mixture. The mass fraction of species t is $X_t = \rho_t/\rho$ but, considering that $m_e \ll m_p$ and that t is a trace element, can be approximated as $X_t \approx \rho_t/\rho_p$. Then, the equilibrium value $X_{t,\mathrm{eq}}$ can be obtained by combining Eqs. (2.26) and (2.27) as

$$\frac{\partial \log X_{t,\mathrm{eq}}}{\partial r} = -\frac{m_u g}{kT}(A_t - A_p) + \frac{eE}{kT}(Z_t - 1) \tag{2.29}$$

Assuming that diffusion is a first order process, then the diffusion velocity is proportional to the difference between the actual and the equilibrium X_t distributions:

$$v_t = -D_t \left[\frac{\partial \log X_t}{\mathrm{d}r} - \frac{\partial \log X_{t,\mathrm{eq}}}{\mathrm{d}r} \right] \tag{2.30}$$

Using Eq. (2.29), v_t can be expressed as

$$v_t = -D_t \left[\frac{\partial \log X_t}{\mathrm{d}r} + \frac{m_u g}{kT}(A_t - A_p) - \frac{eE}{kT}(Z_t - 1) \right] \tag{2.31}$$

2 The electric force has been neglected when considering hydrostatic equilibrium (Eq. (2.3)) because charge separation is in fact very small and electrical neutrality leads to the cancellation of electric forces in a volume element when hydrostatic equilibrium is considered for the gas as a whole.

and using the previous estimate of eE:

$$v_t \approx -D_t \left[\frac{\partial \log X_t}{\mathrm{d}r} + \frac{m_u g}{2kT}[2(A_t - A_p) - (Z_t - 1)] \right] \tag{2.32}$$

This expression allows understanding two main effects. The first term on the right-hand side accounts for diffusion corresponding to a fractional abundance gradient and would lead to a homogeneous equilibrium configuration. This is modified when the second term is considered. For any atomic species t other than hydrogen, the factor $2(A_t - A_p) - (Z_t - 1)$ is positive. This implies that the equilibrium configuration, $v_t = 0$, can only be reached with a negative gradient of X_t, i.e. the trace element, heavier than hydrogen, tends to sink due to the action of the pressure gradient. This effect is known as gravitational settling, or sedimentation, and it is mainly responsible for the helium depletion in the solar convective envelope that has been inferred from helioseismology. It must be kept in mind, however, that helium is not a trace element in the solar envelope, which makes the derivation of v_t carried out here applicable only qualitatively. All metals, on the other hand, can be considered trace elements against a mixture of hydrogen and helium.

A full treatment of the microscopic diffusion does not rely in the assumption of trace elements and includes the presence of the temperature gradient that has not been considered above. A full treatment appropriate for solar conditions, based on the treatment of flows in multicomponent plasmas by Burgers [10], shows that the diffusion velocity v_i of a species i is given by [11]:

$$v_i = \frac{T^{5/2}}{\rho} \left(\sum_{j \neq \mathrm{He}} B_j(i) \frac{\partial \log C_j}{\partial r} + B_p(i) \frac{\partial \log P_i}{\partial r} + B_T(i) \frac{\partial \log T}{\partial r} \right) \tag{2.33}$$

where the factor $T^{5/2}$ is simply a convenient scaling for the diffusion velocity. The first sum is the diffusion due to concentration gradients, defined here with respect to the electron number density ($C_j = n_j/N_e$), and has to be carried out over all nuclear species used in the calculations except for one taken here as helium, because the total mass is normalized to one. In solar models, the term due to hydrogen is strongly dominant in comparison to other chemical species because hydrogen is much more abundant. The second and third terms are contributions to diffusion due to the pressure and thermal gradients. The generalized diffusion coefficients B_j, B_p, and B_T and depend on the binary collision cross sections between pairs of species. Detailed calculations are presented in several places [11–13]. The final equation for the rate of change of the mass fraction X_i is

$$\rho \left(\frac{\partial X_i}{\partial t} \right)_{\mathrm{mic}} = \frac{1}{r^2} \frac{\partial}{\partial r} [r^2 \rho X_i v_i(r)] \tag{2.34}$$

and, after the Lagrangian transformation,

$$\left(\frac{\partial X_i}{\partial t} \right)_{\mathrm{mic}} = \frac{\partial}{\partial m} [(4\pi r^2 \rho)^2 X_i v_i(m)] \tag{2.35}$$

where it should be noted that gradients involved in the calculation of v_i are now computed with respect to the mass coordinate m.

Microscopic diffusion is a slow process. For the Sun, the global timescale associated with it is of the order of 10^{13} year, much larger than the age of the Sun and even of the Universe. However, the changes it produces in solar models need to be taken into account and are, in fact, detectable with precise studies of the solar interior by means of helioseismology. One important effect, already mentioned in the beginning of the section is the apparent depletion of helium in the solar envelope compared to its primordial abundance. Other effects will be discussed later in Section 2.6.

2.1.3.3 Changes in Chemical Composition: Nuclear Reactions

The evolution of stars is driven during most of their lives by the chemical composition changes produced by nuclear reactions that create and destroy nuclei, releasing energy in the process. Any process that involves the transformation of a nuclear species into a different one is considered here, i.e. not only reactions such as proton captures involving two or more reacting nuclei but β^-, β^+ decays and electron captures as well.

In general, the rate of change of the number density n_i of a nuclear species i will be the combined result of reactions that can create or destroy it. Let $r_{i\alpha}$ represent the rate per unit volume at which species i is destroyed by reaction α and $r_{\beta i}$ represent the rate per unit volume at which i is created by reaction β. Then,

$$\left(\frac{\partial n_i}{\partial t}\right)_{\text{nuc}} = -\sum_{\alpha} K_{i,\alpha} r_{i\alpha} + \sum_{\beta} K_{\beta,i} r_{\beta i} \tag{2.36}$$

Here, Greek and Latin indices are reserved for labeling nuclear reactions and atomic species, respectively. The factors $K_{i\alpha}$ and $K_{\beta i}$ are the number of nuclei of species i destroyed or created by each reaction respectively. For example, the rate of the reaction ^{3}He(^{3}He, 2p)^{4}He has a factor 2 when accounting for ^{3} He destruction and proton creation, and a factor 1 when accounting for ^{4}He creation. Note that nuclear reactions do not destroy or create baryons, so the total baryon number density has to be preserved, i.e.

$$\sum_i \left(\tilde{A}_i \frac{\partial n_i}{\partial t}\right)_{\text{nuc}} = 0 \tag{2.37}$$

where $\tilde{A}_i$ is the baryon number (protons plus neutrons) in species i.

Consider, for example, the destruction of species i by reaction with a species j. The rate at which such reaction occurs is

$$r_{ij} = \frac{n_i n_j}{1 + \delta_{ij}} \lambda_{ij} \tag{2.38}$$

The product $n_i n_j$ is the number of possible interacting pairs of nuclei. The factor $(1 + \delta_{ij})$ avoids double counting pairs when the two interacting particles are identical, such as in the proton–proton reaction. The effective rate per pair of particles is

$$\lambda_{ij} = \langle \sigma_{ij} v \rangle f_{ij}^e \tag{2.39}$$

the product of the integrated cross reaction rate per pair of particles and the electron screening factor. Both are discussed in Section 2.2.3.

The relation between n_i and the mass fraction X_i for a given element is $n_i = X_i \rho / m_u A_i$. For simplicity, assume all reactions are binary reactions. Then, Eq. (2.36), in combination with the general expression for r_{ij} given in Eq. (2.38), leads to

$$\left(\frac{\partial(X_i/A_i)}{\partial t}\right)_{\rm nuc} = -\sum_j \frac{K_{i,j}}{1+\delta_{ij}} \frac{X_i X_j}{A_j A_i} \frac{\rho}{m_u} \lambda_{ij} + \sum_{jk} \frac{K_{jk,i}}{1+\delta_{jk}} \frac{X_j X_k}{A_j A_k} \frac{\rho}{m_u} \lambda_{jk} \quad (2.40)$$

where the second sum extends over all pairs jk of species that create species i.

In Eq. (2.40) it has been assumed that $(\partial\rho/\partial t)_{\rm nuc} = 0$. Without this assumption, there should be an additional term in the right-hand side, $-X_i(\partial\rho/\partial t)_{\rm nuc}$. This term accounts for the change in the mass fraction X_i of an element due to the transformation of mass into energy and it is typically neglected in calculations because density variations due to the evolution of the star are dominant. However, this term is necessary to guarantee that $\sum_i X_i = 1$ is satisfied at all times. A workaround usually employed in stellar evolution codes is to use the $\tilde{A}_i$ of species i instead of A_i on the left-hand side of the equation. Although this is not formally correct, it preserves the total baryon number and leads to very small errors in the calculations because $|1 - \tilde{A}_i/A_i| \ll 1$.

Eq. (2.40) can be easily generalized to other classes of nuclear reactions, such as β decays, for which the total rate is

$$r_i = n_i \lambda_c \quad (2.41)$$

with λ_c the decay rate of species i through a specific channel c.

2.1.3.4 Changes in Chemical Composition: Putting Everything Together

The total rate of change in mass fraction of species i is given by the combined addition of macroscopic and microscopic mixing processes and nuclear reactions. This is written as

$$\frac{\partial X_i}{\partial t} = \left.\frac{\partial X_i}{\partial t}\right|_{\rm conv} + \left.\frac{\partial X_i}{\partial t}\right|_{\rm mic} + \left.\frac{\partial X_i}{\partial t}\right|_{\rm nuc}, \quad i = 1, \ldots, N \quad (2.42)$$

where the three terms on the right-hand side are given by Eqs. (2.24), (2.35), and (2.40). Here, N is the total number of atomic species included in the calculation of a solar model. Note that nuclear reactions, and also microscopic diffusion, couple the N partial differential equations. The N nuclear species and the reactions that link their evolution are generically known as a nuclear reactions network. For solar models, a nuclear network that includes light elements involved in hydrogen burning through the proton-proton (pp) chains and carbon-nitrogen-oxygen (CNO) bicycle is necessary.

In stellar regions that are stably stratified, i.e. where there is no convection, $D_c = 0$ so the first term on the right-hand side vanishes. The general form of the equations of chemical evolution given above can be formally used in any layer of the star regardless of its dynamical stability.

2.1.4 Full Set of Equations and Boundary Conditions

The complete set of standard equations describing the evolution of stars, and in particular of the Sun, is given by Eqs. (2.2), (2.5), (2.6), (2.10), (2.19) and the set of N Eqs. (2.42). Together, they form the system of $4 + N$ partial differential equations:

$$\frac{\partial r}{\partial m} = \frac{1}{4\pi r^2 \rho} \tag{2.43a}$$

$$\frac{\partial P}{\partial m} = -\frac{Gm}{4\pi r^4} \tag{2.43b}$$

$$\frac{\partial l}{\partial m} = \varepsilon_{\mathrm{nuc}} - \varepsilon_{\nu} + \varepsilon_{\mathrm{gr}} \tag{2.43c}$$

$$\frac{\partial T}{\partial m} = -\frac{GmT}{4\pi r^4 P} \begin{cases} \nabla_{\mathrm{rad}} & \text{radiative regions} \\ \nabla & \text{convective regions} \end{cases} \tag{2.43d}$$

$$\frac{\partial X_i}{\partial t} = \left.\frac{\partial X_i}{\partial t}\right|_{\mathrm{conv}} + \left.\frac{\partial X_i}{\partial t}\right|_{\mathrm{mic}} + \left.\frac{\partial X_i}{\partial t}\right|_{\mathrm{nuc}} \tag{2.43e}$$

The integration of this system requires boundary conditions. For the chemical composition, these conditions are that there is no flux of matter at the center and at the surface of the Sun. For the structure equations, four boundary conditions are necessary. The first two are given at the center:

$$r_{m=0} = 0$$
$$l_{m=0} = 0$$

For pressure and temperature, the boundary conditions are obtained from the integration of a stellar atmosphere model. This is necessary because close to the stellar surface the mean free path of photons increases largely and the diffusion approximation leading to Eq. (2.43d) breaks down. This region defines the photosphere, at which photons start to escape from the star. Above the photosphere, stellar atmosphere equations need to be considered.

The simplest way to treat the atmosphere is to consider a gray atmosphere, i.e. one constructed using an opacity that has been averaged over the whole electromagnetic spectrum, such as the Rosseland mean opacity. The optical depth τ is then related to opacity as

$$\mathrm{d}\tau = -\rho\kappa \, \mathrm{d}r \tag{2.44}$$

with $\tau = 0$ at infinity. Combined with hydrostatic equilibrium (Eq. (2.4)), this leads to

$$\frac{\mathrm{d}P}{\mathrm{d}\tau} = \frac{g}{\kappa} \tag{2.45}$$

This equation needs to be complemented with a relation between temperature and optical depth, generically known as T–τ relations, of which the most widely

used defines the Eddington atmosphere [14] and is given by

$$T^4(\tau) = \frac{3}{4} T_{\rm eff}^4 (\tau + 2/3) \tag{2.46}$$

The effective temperature $T_{\rm eff}$ is the blackbody temperature at the radius R of the star and is defined through the relation:

$$L = 4\pi\sigma R^2 T_{\rm eff}^4 \tag{2.47}$$

where σ is the Stefan–Boltzmann constant and L is the luminosity of the star. In the T–τ relation above, $T_{\rm eff}$ corresponds to $\tau_{\rm eff} = 2/3$. The Eddington relation is obtained from the theory of radiation transport [14], but other T–τ relations have been determined semiempirically by reconstructing the thermal profile of the solar atmosphere through the observation of spectral lines formed at different depths, i.e. at different τ [15, 16]. Recently, sophisticated three dimensional simulations of the solar atmosphere have been developed that account for radiation transport in great detail as well as hydrodynamic modeling of near-surface convection [17–19]. A theoretical T–τ relation can be obtained from this class of models and used to construct the outer boundary conditions for stellar model calculations [20].

In practice, Eq. (2.45) is integrated from $\tau = 0$ together with the chosen T–τ relation inwards, up to $\tau_{\rm eff}$ and, at that depth, physical quantities determined from this integration ($T_{\rm eff}$ and $P_{\rm eff}$) act as outer boundary conditions for the equations of stellar structure and evolution. The apparent freedom related to the choice of T–τ relation is compensated in the calibration of solar models, discussed later in Section 2.3, through changes in the mixing length parameter $\alpha_{\rm mlt}$. Results from solar model calculations, particularly in the solar interior, are not very sensitive to the specific choice of the T–τ relation.

2.2 Constitutive Physics

2.2.1 Equation of State

The EoS relates P, T, ρ and the detailed chemical composition of stellar matter. The pressure P results from the added contributions of gas and radiation pressure. In the Sun the gas pressure is very close to that of an ideal classical (nonrelativistic) gas, i.e. a gas where interaction among its constituents are negligible. Under this assumption, the pressure P is given by

$$P = P_{\rm gas} + P_{\rm rad} = nkT + \frac{a}{3} T^4 \tag{2.48}$$

The gas pressure is the first term, where n represents the number density of particles. The second term is the radiation pressure. In the Sun, gas pressure is always dominant such that

$$\beta = P_{\rm gas}/P \approx 1$$

It is often convenient to express n as a function of density and composition:

$$n = \rho/(\mu m_u) \tag{2.49}$$

where μ is the mean molecular weight of the gas. In the limit where all atoms are neutral at low temperature and density, μ can be approximated as

$$\mu_0 \approx \frac{1}{X + Y/4 + Z/16} \tag{2.50}$$

Here $X + Y + Z = 1$ and each represent, respectively, the mass fractions of hydrogen, helium, and metals (understood here as all elements heavier than helium). In this expression, it has been assumed that on average metals present in the Sun have an atomic weight equal to 16 corresponding to oxygen, the most abundant metal. Typical values for the solar composition in the surface are $X = 0.74$, $Y = 0.245$, $Z = 0.015$, from which $\mu_0 = 1.246$.

In the opposite limit of complete ionization (CI), μ is given by

$$\mu_{\rm CI} = \frac{1}{2X + 3Y/4 + Z/2} \tag{2.51}$$

where it is now assumed that for metals the ratio between their proton to total nucleon number is 1/2, a well-justified assumption because the most abundant isotopes of O, Ne, C, and N satisfy this condition. In the solar core, appropriate values for X, Y, and Z are 0.35, 0.63, and 0.02 so $\mu_{\rm CI} = 0.846$.

In the intermediate regime, the partial ionization of elements needs to be determined to account for the electron contribution to the EoS. This can be done using the Boltzmann–Saha equations that give the population of an ionization state $p + 1$ with respect to the population of the ionization state p. In general, for species i, the population ratio between ionization levels $p + 1$ and p, regardless of the excitation state, is given by

$$\frac{n_{i,p+1}}{n_{i,p}} = 2\frac{g_{i,p+1}}{g_{i,p}}\left(\frac{2\pi m_e kT}{h^2}\right)^{3/2}\frac{1}{N_e}{\rm e}^{-\psi_{i,p+1}/kT} \tag{2.52}$$

Here, $g_{i,p}$ and $g_{i,p+1}$ are statistical weights of the ground states of atoms in ionization states p and $p + 1$, respectively, the factor 2 is the statistical weight of a free electron, N_e is the electron density, and $\psi_{i,p+1}$ is the ionization energy of the ionization state $p + 1$. All other quantities have their usual meaning. As an example, if a composition of only H and He would be considered, a system of three such equations is necessary to compute $f_{\rm H,1}$, the fraction of ionized hydrogen, and $f_{\rm He,1}$ and $f_{\rm He,2}$, the fractions of helium singly and doubly ionized helium. These equations are complemented with the condition of charge neutrality that links the ionization fractions to N_e. As it will be shown below, H and He are the dominant elements in the Sun and determine the most relevant characteristics of the EoS. For them, ionization energies are $\psi_{\rm H,1} = 13.6$ eV, $\psi_{\rm He,1} = 26.6$ eV, and $\psi_{\rm He,2} = 54.4$ eV. These correspond to temperatures of the order of 1.5, 2.7, and $6.0{\times}10^5$ K respectively, which give an approximate idea of the temperatures at which we expect the different ionization states to be dominant. In this case,

$$\mu = \frac{1}{(1 + f_{\rm H,1})X + (1 + f_{\rm He,1} + 2f_{\rm He,2})Y/4 + Z/2} \tag{2.53}$$

where for simplicity it has been assumed that metals are fully ionized.

It should be noted that the Boltzmann–Saha equations are valid as long as the separation between atoms is large and interaction among them is negligible.

With increasing pressure, the Coulomb potentials of atoms overlap and lower the continuum level. Bound levels, starting from the higher excitation states, disappear and enhance ionization. This effect is known as pressure ionization. At the conditions in the solar center, even the ground state in a H atom has disappeared (see, e.g. [2]).

Realistic equations of state must account for pressure ionization, as well as nonideal corrections from many-body effects and Coulomb interactions. The latter, in particular, give the largest correction to the ideal gas equation, with pressure corrections of the order of −1% in the solar core but of order −8% in the outer convection zone. For very accurate models, corrections due to relativistic electrons in the solar core need to be considered as well. In addition, although metals play a minor role in comparison to H and He, at least the most abundant ones – carbon, nitrogen, oxygen, and neon – must be included in detail. Some examples of this class of equations of state appropriate for detailed solar models are the OPAL EoS [21], the MHD EoS [22, 23], and the FreeEOS [24].[3]

Several thermodynamic quantities such as

$$\nabla_{\rm ad} = \left(\frac{\partial \log T}{\partial \log P}\right)_{\rm ad} \qquad \delta = -\left(\frac{\partial \log \rho}{\partial \log T}\right)_P$$

$$\Gamma_1 = \left(\frac{\partial \log P}{\partial \log \rho}\right)_{\rm ad} \qquad c_P = \left(\frac{\partial u}{\partial T}\right)_P - \frac{P}{\rho^2}\left(\frac{\partial \rho}{\partial T}\right)_P$$

need to be obtained from an EoS to solve the equations of stellar structure and evolution Section 2.1.4. Figure 2.1 shows their behavior in the solar interior as a function of temperature. At the lowest temperatures, μ is very close to μ_0. As temperature increases, ionization increases as well and more free electrons become available, leading to a decrease of μ. The minimum μ values correspond to the regions where H is the dominant element and both H and He are fully ionized. Close to the center, in the region $\log_{10} T > 7$, μ increases because part of the H has been transformed into He due to nuclear burning.

At $\log_{10} T \gtrapprox 5.5$, H and He are almost fully ionized, as shown by $f_{\rm H,1}$, $f_{\rm He,1}$, and $f_{\rm He,2}$. At higher temperatures, the behavior of all thermodynamic quantities

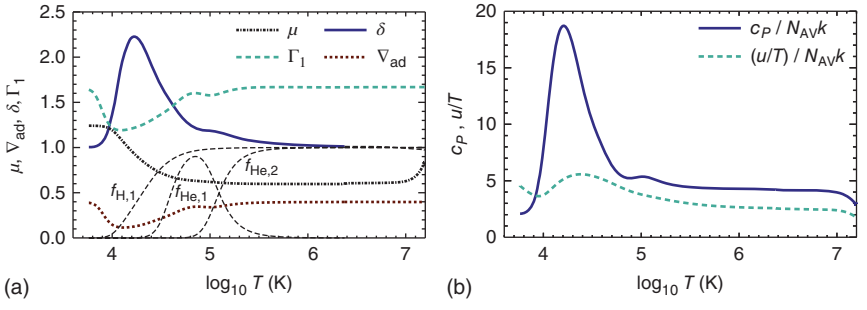

Figure 2.1 (a) $\nabla_{\rm ad}$, δ, and Γ_1 in the solar interior as a function of temperature. Fractional population of ionization levels of H and He and the mean molecular weight μ are also shown. (b) c_P and u/T in units of the gas constant $\mathcal{R}$.

3 http://freeeos.sourceforge.net/.

approach that of an ideal monoatomic fully ionized gas: $\nabla_{ad} = 0.4$, $\Gamma_1 = 5/3$, $\delta = 1$, $c_P = 5/(2\mu)$, and $u/T = 3/(2\mu)$. Here c_P and u/T are given in units of $\mathcal{R} = k/m_u$, the gas constant. In the $\log_{10} T$ range from 4.5 to 5.5, He partial ionization becomes important and affects the behavior of thermodynamic quantities. Of particular relevance is the depression in Γ_1 at $\log_{10} T \sim 5.1$ due to the second helium ionization because it has important consequences for helioseismology. This will be discussed to larger extent in Section 2.6. Below $\log_{10} T \sim 4.5$ partial ionization of H becomes very important, leading to strong variations in all quantities. The peak in c_P (and in u/T) around this temperature occurs because heat is used to ionize H instead of increasing the temperature of the gas. Energy is stored as ionization energy without much variation of T. Similarly, δ increases strongly because, at constant P, ρ decreases rapidly with increasing ionization (the mean molecular weight of the gas decreases) even with small changes in T. Analogous arguments apply to ∇_{ad}, Γ_1, and other thermodynamic quantities not shown in Figure 2.1.

Finally, partial ionization of metals extends much deeper than that of H and He. This is shown in some detail in Figure 2.2 for the most important metals in the Sun.[4] The impact of partial ionization of metals is small in the EoS because even oxygen, the most abundant metal, is less abundant in number density by more than three orders of magnitude compared to hydrogen. However, the detailed atomic configuration of metals in the solar interior is of central importance in the calculation of radiative opacities κ_r.

A complete discussion of thermodynamic quantities and their relations can be found in classical works such as [2, 3, 25].

2.2.2 Radiative Opacities

The temperature gradient in the radiative regions of a star is proportional to the opacity κ of matter to radiation (Eq. (2.9)). Therefore, κ regulates the rate at which a star radiates its energy and it is a fundamental quantity for determining accurate stellar models. In the Sun, electron conduction is highly inefficient because the mean free path of free electrons is very short, resulting in $\kappa \approx \kappa_r$, where κ_r is the Rosseland mean opacity that has been defined in Eq. (2.13).

The actual computation of radiative opacities appropriate for stellar models poses a very challenging problem. The interaction of atoms with the radiation field occurs in a hot high density plasma. Detailed models of atomic structure are required for all abundant elements. Here, unlike in the case of the EoS, metals play a very important role. A detailed discussion of the theory of opacity calculations is well beyond the scope of this book can be found in the authoritative reference [26]. Here, the more relevant physical processes that contribute to radiative opacities are only briefly commented upon and placed in the context of solar models.

Bound–bound (bb) transitions imply the absorption of a photon by a bound electron, with the corresponding transition to a state of higher excitation. It is the process that gives rise to spectral lines. It is a dominant effect close to the

4 Ionization fractions have been obtained with the EoS developed by F. Timmes http://cococubed.asu.edu/code_pages/eos_ionize.shtml.

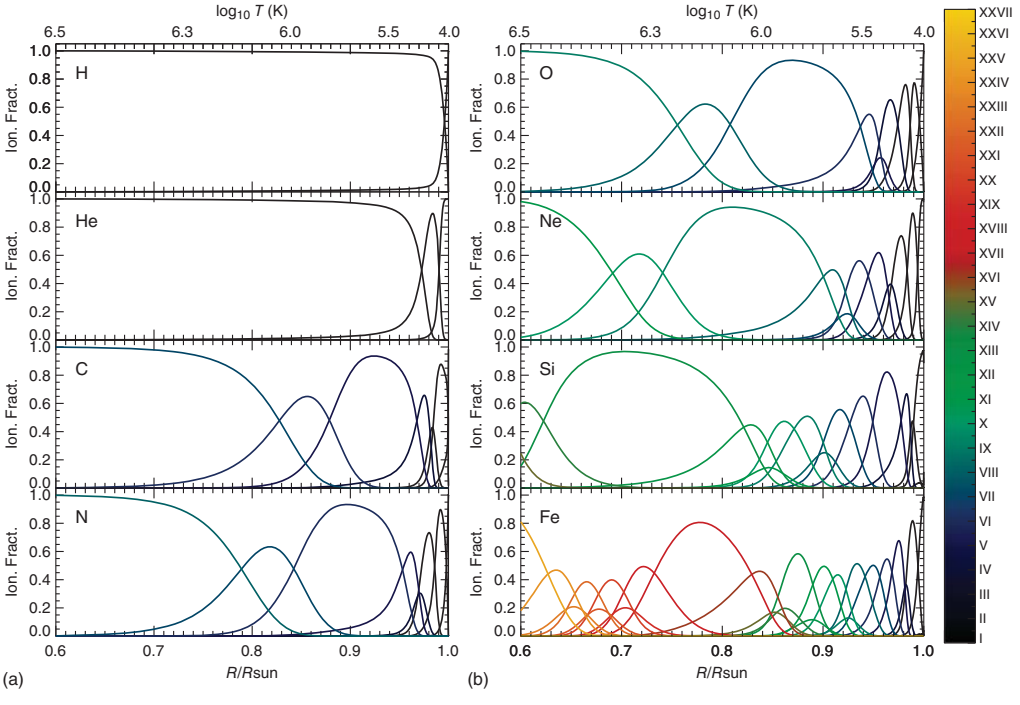

Figure 2.2 Ionization fraction of all ionization states for H, He, and the most abundant metals in a solar model given as a function of radius. Temperature values are also given on top for reference. Ionization states are colored according to the scale in the bar, where *I* indicates the neutral state.

solar surface, where atoms retain most of their electrons. But it is also present in the interior, where it is more important for elements with larger atomic number. There are several effects that broaden the lines with respect to their natural width and Lorentzian shape that need to be accounted for in detail and enhance the importance of bb opacity in the solar interior.

Bound–free (bf) transitions involve the transition of an electron from a bound to a continuum (free) state. The absorption coefficient depends approximately on $Z_i^4 \nu^{-3}$, where Z_i is the atomic number of species i and ν is the frequency of radiation. The ionization energy $\psi_{i,p}$ imposes a minimum frequency $\nu_{i,p} = \psi_{i,p}/h$ below which the bf transition cannot occur. This leads to the formation of ionization edges at $\nu_{i,p}$ that decay as ν^{-3} at higher frequencies.

Free–free (ff) transitions involve the absorption of a photon by an electron in an unbound state, i.e. inverse bremsstrahlung. Unlike the case of bb and bf transitions, ff transitions occur for any frequency and lead to a continuous behavior of opacity with frequency. Classical approximation to ff opacity shows that, for a species i, it behaves as $\kappa_{\nu,\mathrm{ff},i} \propto Z_i^2 \nu^{-3}$. For an ff transition to occur, it is necessary that an additional electron or ion is present to conserve energy and momentum. Therefore, the ff transition probability is proportional to the time the electron and the additional particle are close to each other, i.e. inversely proportional to the thermal velocity of electrons, or $T^{1/2}$. Combining these dependences, the Rosseland mean opacity from ff transitions follows the relation $\kappa_{\mathrm{ff},i} \propto Z_i^2 \rho T^{-7/2}$, a relation known as the Kramers' law.

Free single electrons cannot absorb a photon but can oscillate in the electric field of the incident photon. In the non-relativistic limit, appropriate for the solar interior, electron scattering (es) of photons is simply Thomson scattering. Its cross section is $\sigma_T = 8\pi r_{\mathrm{ec}}^2/3$, with $r_{\mathrm{ec}} = e^2/m_e c^2$ as the classical electron radius. Opacity due to es is then $\kappa_{\mathrm{es}} = \sigma_T N_e$ or, in the case of a fully ionized gas, $\kappa_{\mathrm{es}} = 0.2(1 + X)\ \mathrm{cm}^2/\mathrm{g}$.

Radiative opacities are generally provided as tables computed for a specific chemical composition as function of T and R. The latter quantity is defined as $R = \rho/T_6^3$, with $T_6 = T/10^6$. Figure 2.3 represents the Rosseland mean opacity for a composition appropriate for solar models as a function of T and R. The black line represents the T–R profile of the solar structure. Solid parts of the line correspond to the two solar regions where κ_r is important: (i) the radiative interior, corresponding the $\log_{10} T > 6.3$ or $r < 0.7 R_\odot$, where κ_r regulates energy transport and strongly determines solar structure and (ii) the near-surface layers where convection is not adiabatic and the radiative layers above the photosphere. The dashed part of the line indicates the region where energy transport is done by adiabatic convection, so $\nabla = \nabla_{\mathrm{ad}}$ and κ_r becomes irrelevant.

Figure 2.4 shows the fractional contribution of different chemical elements to κ_r at three different locations in the Sun as indicated in each plot. The contribution of the four different classes of processes is also broken down for each element. In solar core, where the plasma is almost completely ionized, es and ff transitions dominate the opacity. H and He are important simply because they are the most abundant electron donors. Among the metals, iron is important because it combines a relatively large abundance and a large nuclear charge so it still preserves bound electrons that provide a large bf opacity (photons are too energetic for bb

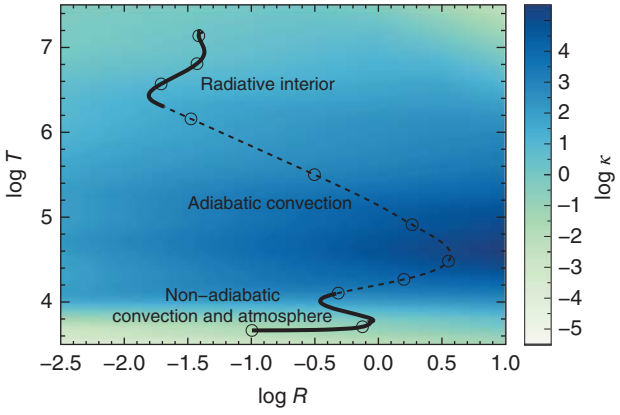

Figure 2.3 Rosseland mean opacity as a function of $\log_{10}T$ and $\log_{10}R$. The T–R profile of the solar interior is showed as a line. Regions where radiative opacities play a relevant role in determining the solar structure are indicated in solid line. Open circles correspond to locations in the Sun where $\log_{10}\rho = -8, -7, \ldots, 1, 2$ with ρ expressed in g/cm^3.

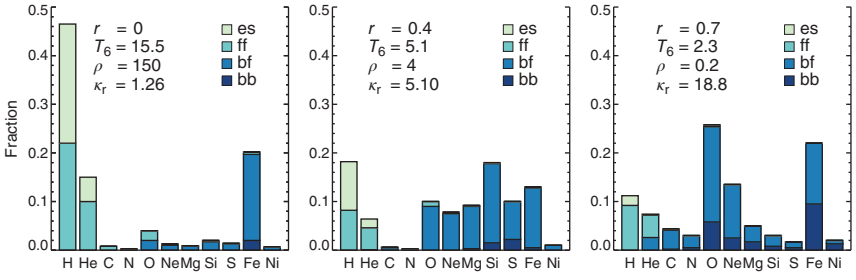

Figure 2.4 Fractional contribution of individual chemical elements to κ_r at three locations in the solar interior as indicated in each plot. Radius r is given in solar units, T in 10^6 K, ρ in g/cm^3, and κ_r in cm^2/g. Relative contributions of electron scattering (es), free–free (ff), bound–free (bf), and bound–bound (bb) transitions are indicated by colors. Source: Data courtesy of F. Delahaye.

transitions to be too relevant). At $r = 0.4\ R_\odot$, the relative importance of metals increases because the lower temperature bf transitions are strongly enhanced. Metals in the intermediate range, between O and S, contribute more than half the total κ_r. At the base of the convective zone, $r = 0.7\ R_\odot$, metals strongly dominate κ_r, with light metals now also being important. Note that at these lower temperatures, bb transitions account for about 20% of the total opacity.

It is clear from Figure 2.4 that metals are very important in determining the radiative opacity in the solar interior, dominating through bf and bb transitions. This implies that models of atomic structure need to be very accurate. But, also, plasma effects leading to broadening of spectral lines need to be modeled correctly because bf and bb opacity depend crucially on this [27].

The calculation of solar models requires very detailed radiative opacity calculations, for which several sources are available. The most widely used radiative opacities are: OPAL opacities [28], the Opacity Project (OP) [29]. More recently,

a new generation of the Los Alamos Opacities (formerly LAOL, now OPLIB) has been developed [30]. Other recent activity in theoretical calculations include the OPAS [31, 32] and the STAR efforts [27, 33]. The combination of large temperatures and high densities makes experimental work on radiative opacities at solar conditions very difficult. To date, the only experimental result available is for iron and it has been obtained with the Z-facility at the Sandia Laboratory [34]. The conditions are $T_6 = 2.3$ and electron densities about a factor of 4 lower than those found at that temperature in the solar interior. Experimental results point toward a higher monochromatic iron opacity than predicted by all available theoretical calculations by up to a factor of 2, which, if confirmed, would be clear evidence of a fundamental deficiency in currently available opacity calculations, as already put forward in [35]. The curious reader can consult those references for detailed information on what opacity calculations and experiments entail.

2.2.3 Nuclear Reaction Rates

In the Sun, as in any other star in a hydrogen burning stage, the net nuclear transformation that determines its energetics and drives its evolution is

$$4\mathrm{p} \longrightarrow {}^4\mathrm{He} + 2e^+ + 2\nu_e \tag{2.54}$$

The energy released in the process is $Q = c^2(4m_{\mathrm{H}} - m_{^4\mathrm{He}}) = 26.7$ MeV, with neutrinos carrying away a small fraction of it that depends on the specific channel by which hydrogen burning proceeds. There are two main sets of nuclear reactions through which hydrogen is fused into helium: the pp chains and CNO-bicycle. Figure 2.5 shows the complete set of reactions involved in the pp chains. There are three different branches or chains that take place, identified in Figure 2.5 at the ending reaction. The relative importance of the different branches depends primarily on the temperature at which reactions take place. The numbers given in Figure 2.5 show the branching ratios in the present-day Sun. The reactions that produce neutrinos are highlighted in boxes. Figure 2.6 illustrates the CNO-bicycle. The branching point occurs at the proton capture by ^{15}N. In the Sun, the α+^{12}C channel is dominant by several orders of magnitude so in practice the CNO-bicycle is reduced to the CN-cycle, with a marginal contribution from the NO-cycle. Note that in each of the cycles, CNO elements are produced and destroyed, but the total number of CNO nuclei is not altered. Reactions that produce neutrinos are also highlighted in the figure. This will be discussed in more detail in Section 2.5, in the context of the energetics and production of neutrinos in the Sun.

Thermal nuclear reactions in the pp chains and the CNO-bicycle occur between two charged nuclei. Densities and temperatures are large enough that all nuclear species are in thermal equilibrium, i.e. obey Maxwellian distributions. Under these conditions, the Maxwellian averaged cross section in Eq. (2.38) between two species can be written as

$$\langle \sigma v \rangle = \left[\frac{(8/\pi)^{1/2}}{\mu^{1/2}(kT)^{3/2}} \right] f^e \int_0^\infty \sigma(E) E \exp(-E/kT) \mathrm{d}E \tag{2.55}$$

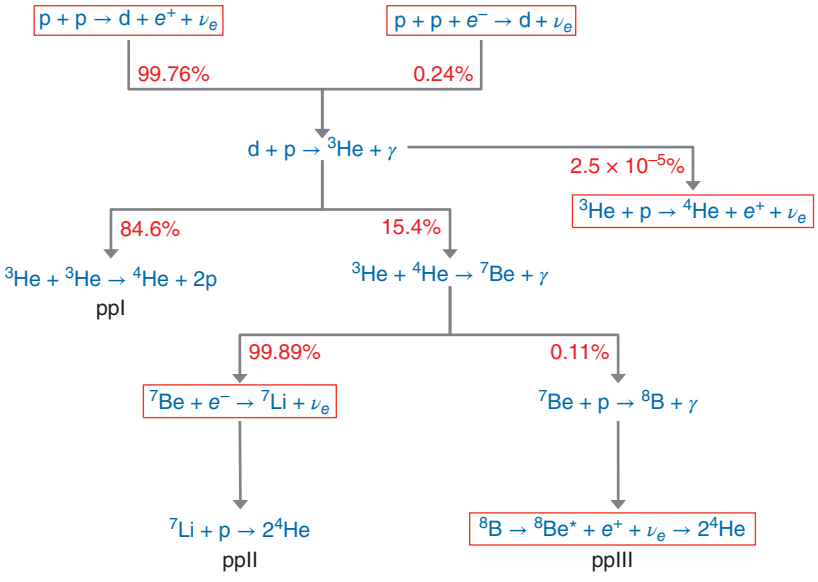

Figure 2.5 Complete set of reactions in the three pp chains (ppI, ppII, ppIII) including the additional ^{3}He + p reaction. Each branch is identified at the end reaction. Reactions identified with boxes are those producing neutrinos.

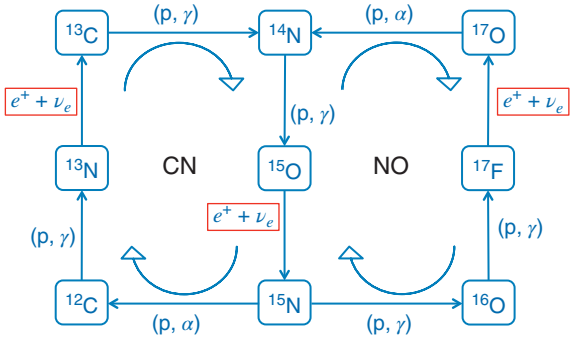

Figure 2.6 Complete set of reactions in the CNO-bicycle. Branching occurs at the p+^{15}N reaction, but for solar conditions only the CN-cycle is effective.

where v is the relative velocity between the interacting nuclei, E is the energy in center of mass system of the interacting particles, μ is the reduced mass of the pair of particles, and $\sigma(E)$ is the reaction cross section at energy E. Electron screening f^e is treated separately, at the end of this section.

The interaction between two charged nuclei is dominated by Coulomb repulsion at long distances. At the typical temperatures of the solar interior, $T \sim 10^7$ K (or 1 keV), the distance between two approaching nuclei at the classical turning point is

$$r_c = \frac{2e^2 Z_1 Z_2}{\mu v^2} \tag{2.56}$$

of the order of $r_c = 1.7 \times 10^{-10} Z_1 Z_2$ cm, with Z_1 and Z_2 as the atomic numbers of the interacting nuclei and e as the elementary charge. The nuclear potential becomes attractive only at distances of the order of a few femtometers, $\sim 10^{-13}$ cm. At this short range, the Coulomb energy E_c is several orders of magnitude larger than the kinetic energy of nuclei, i.e. $E_c \sim 1.5 Z_1 Z_2$ MeV $\gg E$. As a result, nuclear reactions occur in the solar interior only due to the tunneling effect through the Coulomb barrier [36, 37].

It is convenient to express $\sigma(E)$ as

$$\sigma(E) = \frac{S(E)}{E} \exp(-2\pi\eta) \tag{2.57}$$

where $\eta = Z_1 Z_2 (e^2/\hbar v)$ and $v = (2E/\mu)^{1/2}$. The exponential factor is the penetration factor in the limit $E_c \gg E$, and it accounts for the tunneling probability. This factor decomposition of $\sigma(E)$ is useful because $S(E)$, known as the astrophysical factor, contains all the nuclear physics involved in the reaction. Moreover, in the absence of resonances, $S(E)$ is a smoothly varying function of E. The integrand of Eq. (2.55) is then proportional to

$$g(E) = \exp\left(-\frac{(2\mu)^{1/2} \pi Z_1 Z_2 e^2}{\hbar E^{1/2}} - \frac{E}{kT} \right) \tag{2.58}$$

that has a maximum at

$$E_0 = \left(\frac{\mu}{2}\right)^{1/3} \left(\frac{\pi e^2 Z_1 Z_2 kT}{\hbar}\right)^{2/3} = 5.69 (Z_1^2 Z_2^2 A T_7^2)^{1/3} \text{ keV} \tag{2.59}$$

Here $A = \mu/m_u$ is the reduced atomic mass in atomic units and T_7 is the temperature expressed in 10^7 K. Then, $g(E)$ can be approximated as a Gaussian function around E_0 with full width at $1/e$:

$$\Delta E_0 = 4(E_0 kT/3)^{1/2} = 5.11 (Z_1^2 Z_2^2 A)^{1/6} T_7^{5/6} \text{ keV} \tag{2.60}$$

E_0 and ΔE_0 describe what is known as the Gamow peak. Because $S(E)$ is usually a slowly varying function of E, the Gamow peak provides a good characterization of the energy range at which a reaction actually takes place in stellar interiors for a given temperature T. In the solar interior, E_0 is always larger than kT, by a factor of a few (e.g. for the proton–proton reaction) up to more than 20 for proton captures by CNO elements. The different contributions to $g(E)$ are illustrated in Figure 2.7a for the important p(p, $\nu_e e^+$)d, ^{3}He (^{4}He, γ)^{7}Be, and ^{14}N(p, γ)^{15}O reactions. The number of available pairs of interacting nuclei decreases rapidly with energy following the Maxwell distribution, whereas the tunneling probability increases with E and decreases with larger $Z_1 Z_2$. The Gamow peak described by $g(E)$ is a strongly peaked function of E as shown in Figure 2.7b. The analytic approximation based on the Gaussian function is shown with dashed lines.

In practice, nuclear reaction rates require the complete knowledge of $S(E)$ and the evaluation of Eq. (2.55) at all temperatures T. $S(E)$ can be determined from experimental data or theoretical calculations when data is not available or incomplete. The measurement of nuclear reaction rates in laboratories is difficult because the Gamow peak energies in the Sun are very low and, at such energies, the reaction rates that can be achieved in the labs are negligible for all but a

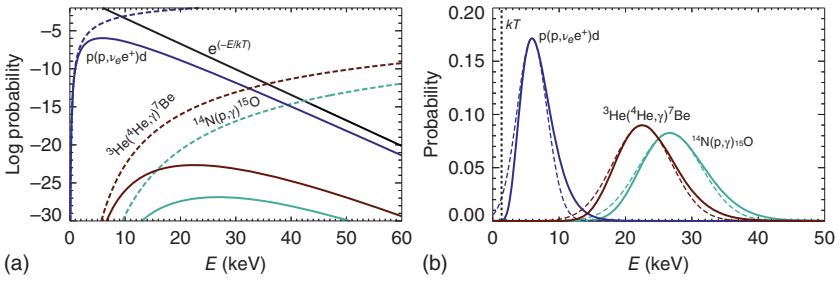

Figure 2.7 (a) Penetration factors (dashed lines), Maxwell distribution (dashed-dotted line), and probability factors ($g(E)$ in Eq. (2.58), solid lines) afor three important reactions in solar interiors. Dashed-dotted line shows the Maxwell distribution. (b) Probability factors in linear scale where the concept of Gamow peak is evident (solid lines) and Gaussian approximation using E_0 and ΔE_0 (dashed lines). Vertical dashed line is $kT = 1.33$ keV at the solar center. Probabilities given in arbitrary units.

very limited number of nuclear reactions. One important exception relevant for solar models is the ^{3}He(^{3}He, 2p)^{4}He reaction that, for the central temperature of the Sun, $T_7 = 1.55$, has $E_0 = 22.0 \pm 6.2$ keV. The Laboratory of Underground Nuclear Astrophysics (LUNA) experiment has provided the only available measurement of this rate at Gamow peak energies [38]. Experimental measurements for all other nuclear reactions have been carried out at energies higher than E_0. Methods based on theoretical nuclear models have been developed and are used to extrapolate the measured rates down to the relevant Gamow peak energies. Using $S(E)$ to express the rates is here an advantage because it is simpler to device extrapolation methods to work with a smoothly varying quantity. A very extensive discussion on the topic can be found in the specialized literature, e.g. [39].

The smoothness of $S(E)$ and the existence of the Gamow peak allow the possibility of treating nuclear reaction rates analytically to a good level of accuracy. We provide this without demonstration, which can be found, for example, in [40]. Using Eq. (2.57), the integrand in Eq. (2.55) can be expanded in the inverse of the parameter $\tau = 3E_0/kT \gg 1$ and the resulting integrals can be solved analytically. This requires a second order expansion of $S(E)$ that can be performed either around E_0 or $E = 0$. The latter case is most widely used in the literature and leads to the final expression:

$$\langle \sigma v \rangle = 2.802 \times 10^{-14} \left(\frac{Z_1 Z_2}{A T_7^2} \right)^{1/3} S_{\rm eff} \exp(-\tau) f^e \ {\rm cm}^3/{\rm s} \tag{2.61}$$

with

$$S_{\rm eff} = S(0) \left(1 + \frac{5kT}{36E_0} \right) + S'(0) E_0 \left(1 + \frac{35kT}{36E_0} \right) + \frac{1}{2} S''(0) E_0^2 \left(1 + \frac{89kT}{36E_0} \right) \tag{2.62}$$

Expression in Eq. (2.61) can be used to determine a simple scaling between nuclear reaction rates and temperature. If the rate is approximated as a power

law dependence around a reference temperature value T_0:

$$\frac{\langle \sigma v \rangle}{\langle \sigma v \rangle_0} = \left(\frac{T}{T_0} \right)^n \tag{2.63}$$

then

$$n = (\tau - 2)/3 = \frac{E_0}{kT} - 2/3 \tag{2.64}$$

where the first term is the ratio between the central energy of the Gamow peak and the thermal energy, and the latter term comes from the explicit $T^{-2/3}$ dependence of the rate on temperature. From Figure 2.7 it can then be inferred that, in the solar center where $kT = 1.33$ keV, $n \approx 4$, 16, and 20 for the proton–proton, ^{3}He + ^{4}He, and p+^{14}N reactions, respectively. For a given temperature, n scales with $(Z_1^2 Z_2^2 A)^{1/3}$.

Very often, nuclear reactions rates for solar models are provided through $S(0)$, $S'(0)$ and $S''(0)$. Table 2.1 lists $S(0)$ for the complete set of reactions in the pp chains and the CNO-bicycle that account for nuclear energy generation in the solar interior and for the production of solar neutrinos. For decays of unstable nuclei the mean lifetime, λ_c^{-1} in Eq. (2.41), is provided. The table also includes the energy released in each reaction and the average energy carried away by neutrinos. Note that pep and ^{7}Be neutrinos are mono-energetic: i.e. their energy spectrum is given by a line, broadened only by thermal effects.

There are two electron capture reactions in the pp chains. For these, reaction rates depend on the temperature and the electron density. These rates are given by

$$\lambda(\text{pep}) = 3.573 \times 10^{-5} (\rho/\mu_e) \times T_6^{-1/2} [1 + 0.2 T_7] \lambda(\text{pp}) \tag{2.65}$$

and, for the unstable ^{7}Be, by

$$\lambda(^7\text{Be} + e^-) = 1.77 \times 10^9 (\rho/\mu_e) \times T_7^{-1/2} [1 + 0.04(T_7 - 1.6)] \text{s}^{-1} \tag{2.66}$$

Electron capture by ^{7}Be can occur to the ^{7}Li ground state or to the first excited state, at 478 keV, followed by a radiative decay to the ground state. In both cases, the ν_e will carry away all the energy produced during the electron capture, but the radiative decay contributes to the thermal energy in the Sun in the second case.

Finally, it is necessary to consider that the Coulomb repulsion between charged nuclei in stellar interiors is partially screened by electrons, which leads to a lowering of the Coulomb barrier and, consequently, to an enhancement of the reaction rates that would otherwise occur between isolated nuclei. In the Sun, for all reactions in the pp chains and CNO-bicycle, the interaction energy between nuclei is lower than their kinetic energy and electron screening can be treated is the so-called weak screening or Salpeter approximation [44]. In this limit, the modified Coulomb potential is

$$V_S(r) = \frac{e^2 Z_1 Z_2}{r} \mathrm{e}^{-r/R_D} \tag{2.67}$$

where the Debye–Hückel radius R_D is a measure of the size of the electron cloud surrounding the nucleus:

$$R_D = \frac{1}{\zeta} \left(\frac{kT}{4\pi e^2 \rho} \right)^{1/2} \tag{2.68}$$

Table 2.1 Astrophysical factors $S(0)$, energy release Q, and average neutrino energy loss $\langle Q_{\nu_e} \rangle$ for reactions in the pp chains and CNO-bicycle.

Reaction	$S(0)$ (keV b)	Q (MeV)	$\langle Q_{\nu_e} \rangle$ (MeV)
^{a}p(p, $e^+\nu_e$)d	$(4.03 \pm 0.04) \times 10^{-22}$	1.442	0.265 (pp)
p(pe^-, ν_e)d	—	1.442	1.442 (pep)
d(p, γ)^{3}He	$(2.14 \pm 0.16) \times 10^{-4}$	5.493	—
^{3}He(3He, 2p)^{4}He	$(5.21 \pm 0.27) \times 10^3$	12.86	—
^{3}He(4He, γ)^{7}Be	0.56 ± 0.03	1.586	—
^{7}Be(e^-, ν_e)^{7}Li	—	0.862(90%)	0.862(90%) (^{7}Be)
^{7}Be(e^-, ν_e)^{7}Li	—	0.862(10%)	0.384(10%) (^{7}Be)
^{7}Li(p, α)^{4}He	52 ± 10	17.347	—
^{b}^{7}Be(p, γ)^{8}B	$(2.13 \pm 0.10) \times 10^{-2}$	0.137	—
$^8B(e^+\nu_e)2^4$He†	0.77 s	17.98	6.710 (^{8}B)
^{3}He(p, $e^+\nu_e$)^{4}He	$(8.6 \pm 2.6) \times 10^{-20}$	19.80	9.625 (hep)
^{12}C(p, γ)^{13}N	1.34 ± 0.21	1.944	—
^{13}N($e^+\nu_e$)^{13}C†	863 s	2.221	0.707 (^{13}N)
^{13}C(p, γ)^{14}N	7.6 ± 1.0	7.551	—
^{c}^{14}N(p, γ)^{15}O	1.59 ± 0.12	7.297	—
^{15}O($e^+\nu_e$)^{15}N†	176 s	2.754	0.996 (^{15}O)
^{15}N(p, α)^{12}C	$(7.3 \pm 0.5) \times 10^4$	4.966	—
^{15}N(p, γ)^{16}O	36 ± 6	12.128	—
^{16}O(p, γ)^{17}F	10.6 ± 0.8	0.602	—
^{17}F($e^+\nu_e$)^{17}O†	93 s	2.759	0.999 (^{17}F)
^{17}O(p, α)^{14}N	10.6 ± 0.8	1.191	—

For decays, indicated by †, the mean lifetime is given. Astrophysical factors are taken from [40] except for ^{a} [41], ^{b} [42], and ^{c} [43].

and

$$\zeta = \left[\sum_i \left(\frac{X_i}{A_i} Z_i^2 \right) + \theta_e \sum_i \left(\frac{X_i}{A_i} Z_i \right) \right]^{1/2} \tag{2.69}$$

Here, θ_e is the degeneracy parameter and is close to unity for solar conditions. For energies around E_0 for which reactions are effective, $r_c \ll R_D$, so

$$V_S(r) \approx e^2 Z_1 Z_2 \left(\frac{1}{r} - \frac{1}{R_D} \right) = V_c - U_0 \tag{2.70}$$

with V_c the Coulomb potential and $U_0 = e^2 Z_1 Z_2 / R_D$. In the weak screening limit, the effect of electron screening is to enhance the tunneling probability by the factor:

$$f^e = \exp(U_0/kT) = \exp(5.95 \times 10^{-3} Z_1 Z_2 \zeta \rho^{1/2} T_7^{-3/2}) \tag{2.71}$$

This expression for electron screening is a first-order approximation but it is accurate for conditions in the solar interior to better than 2% [45]. For these conditions, the enhancement factor f^e is about 1.05 for the proton–proton reaction, and it rises as the product $Z_1 Z_2$ to about 1.2 for He–He or p+^{7}Be reactions and between 1.35 and 1.45 for reactions in the CNO-bicycle.

2.3 Calibrating Standard Solar Models

2.3.1 Observational Constraints

2.3.1.1 Age, Mass, Radius, and Luminosity

Solar Age One of the defining characteristics of an SSM is that the present-day solar model is a snapshot in the evolution of a 1 $M_\odot$ star obtained by integrating the full set of Eq. (2.43). Therefore, the age of the Sun, i.e. the moment at which this snapshot is taken, must be known. The age of the solar system can be obtained with high precision and accuracy from radioactive dating of the most primitive constituents found in meteorites, formed in the very early epochs of the formation of the solar system. Particularly useful are the so-called calcium–aluminum-rich inclusions (CAIs). The most robust method relies on the time evolution of the abundance ratio of the ^{207}Pb–^{206}Pb pair of lead isotopes that are the endpoints of the decay of ^{235}U and ^{238}U, respectively. Other pairs of isotopes such as ^{26}Al–^{26}Mg, ^{53}Mn–^{53}Cr, and ^{182}Hf–^{182}W are also used and allow a check for systematic deviations that could go unnoticed otherwise. Current best estimates give a solar system age $\tau_\odot = 4568$ Myr with a scatter of only ~ 2 Myr among different measurements. Pedagogical explanations of the concept behind radioactive dating can be found in [7, 46]. For a more detailed and technical presentation, [47] is a good reference.

Solar Mass The present-day solar mass is determined from the orbital motion of the Earth. A very precise determination of $GM_\odot$ is obtained from Earth's orbital period and semi-major axis. The ultimate precision with which $M_\odot$ can be obtained is then limited by the precision with which G is known, currently 0.05%. There are two sources of mass loss occurring in the Sun, the conversion of mass to energy by nuclear reactions and the solar wind. In the first case, the total mass lost through the solar history is of the order of a few $10^{-4}\ M_\odot$. In the second case, current mass loss rate is estimated to be of the order or $10^{-14}\ M_\odot\ \mathrm{yr}^{-1}$, leading to a total mass loss again of around $10^{-4}\ M_\odot$ during the solar lifetime. It is not known if the solar mass loss rate was higher in the past. Observations of younger stars of mass similar to the Sun (solar analogues) [48] indeed suggest higher mass loss rates for younger stars, but based on those inferred values, the integrated mass loss over the solar evolution does not amount to more than a few $10^{-3}\ M_\odot$. Based on these considerations, SSMs assume that these mass loss sources are negligible: i.e. the Sun, once formed, has evolved at a constant mass equal to its present-day value. The currently adopted value by the International Astronomical Union (IAU) is $M_\odot = 1.9891 \times 10^{33}$ g.

Solar Radius Several techniques are used to measure the solar radius $R_\odot$. Some are based on precise timing of the motion of the Sun and other celestial bodies. This is the case of solar meridian transits, solar eclipses, and transits of Mercury or Venus. Alternatively, direct measurements of the angular diameter can be carried out by means of astrolabes, heliometers, or solar sextants. Helioseismology, the study of solar oscillations, can also be used for this purpose because the frequencies of the surface f-mode scale as $R_\odot^{-2}$ [49]. The precise meaning of solar radius depends to some extent on the measurement technique and even on the wavelength in which observations are made. Therefore, it is natural that an intrinsic scatter is present in the values quoted in the literature. The current IAU value is $R_\odot = 6.957 \times 10^{10}$ cm.

Solar Luminosity It is determined from measurements of the total solar irradiance (TSI), the power in the solar radiation integrated across the electromagnetic spectrum. Such measurements are carried out with radiometers both from the ground and from space. The TSI is subject to variations over the solar 11-year cycle, with variations of 0.07% [50]. Most recent results from the total irradiance monitor in the SORCE satellite yield a TSI, during solar minimum, of 1360.8 ± 0.5 W/m^2 [51], somewhat lower than 1365.4 ± 1.3 W/m^2, a widely accepted value since the 1990s. The IAU recommends 1361 W/m^2 which translates to a solar luminosity $L_\odot = 3.828 \times 10^{33}$ erg/s.

2.3.1.2 Surface Composition

Spectroscopic Abundances The abundance of almost all chemical elements can be determined from the analysis of absorption lines formed in the solar atmosphere and observed in the solar spectrum. The intensity of a given spectral line depends on the abundance of the chemical element or molecule producing it and it is measured with respect to the background continuum. In the solar atmosphere, this continuum is set by the negative hydrogen ion H^-. As a result, it is the relative abundance of a given element with respect to hydrogen that can be measured. In astronomical notation, the abundance of a given element i is usually expressed as $\log \epsilon_i = \log(n_i/n_H) + 12$.

But, to complicate matters, the intensity of a spectral line depends on the detailed physical conditions present in the region of the solar atmosphere where the line forms. Temperature, pressure, electron density, and even the detailed radiation field must all be known accurately throughout the solar atmosphere. This information is provided by models of the solar atmosphere. With such models as a background, detailed radiative transfer calculations are carried out for the different chemical elements to produce synthetic spectra that are matched to observations. From this matching element, abundances are ultimately determined.

Traditionally, spectroscopic determination of solar abudances have relied on one-dimensional (1D) models of the solar atmosphere. Such models rely on approximate convection theories such as the MLT to model the solar near-surface convection. Examples of these models are MARCS or ATLAS [52, 53].

Other widely used alternatives are the semiempirical models such as that from Holweger–Müller model [15].

A leap forward in spectroscopic studies has occurred with the development of 3D radiation hydrodynamic (3D-RHD) models of the solar atmosphere. In these simulations, the set of conservation equations, analogous to those derived in Section 2.1, are coupled to radiative transport equations and solved in full 3D [54]. Convection is driven by the radiative cooling of gas in the outermost layers of the atmosphere, so the coupling between hydrodynamics and radiative transfer is a fundamental aspect in a physically consistent model. Figure 2.8 illustrates the behavior of temperature and density as a function of depth in a solar model atmosphere model [17]. Color intensity shows the temporally averaged frequency with which a given temperature or density value is realized at a given depth. The surface of the Sun is defined here as the surface where the average temperature equals the solar effective temperature. The temperature and density distributions show not only fluctuations around mean values but also that there are regions in the atmosphere where the contrast between convective upflows and downflows leads to a markedly bimodal distribution, especially right below the surface. None of these features can be captured by 1D models.

The most recent works on spectroscopic solar abundances include further complexities related to line formation. In the rarefied solar atmosphere, LTE breaks down and non-local effects must be taken into account in detailed line formation studies. Non-LTE (NLTE) effects depend on an element-by-element basis and even on which spectral lines of a given element are considered. A general discussion on the so-called NLTE effects can be found in [55], and a detailed discussion of the physics and relevance of NLTE effects for spectroscopic abundances is presented in [56]. Solar abundances based on 3D models and including NLTE effects can be found in [57, 58].

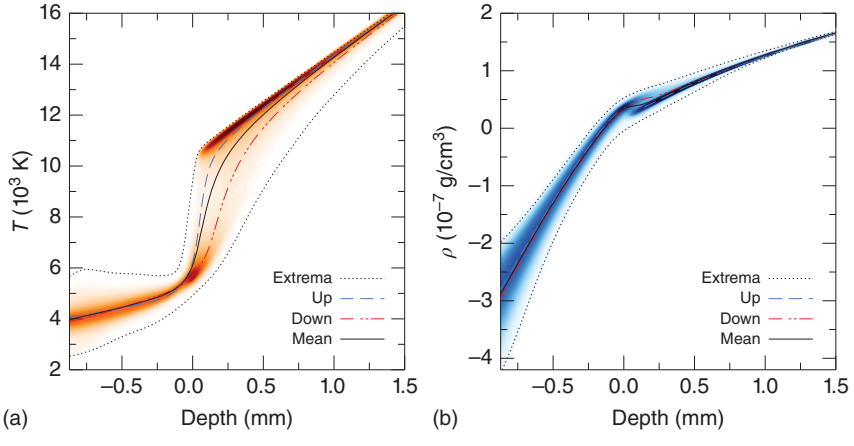

Figure 2.8 Histogram of temperature and density as a function of depth in a 3D-RHD solar atmosphere model. Solid black lines show averaged quantities over surfaces of constant depth, and the dashed blue and dashed-dotted red lines the average values in upflows and downflows, respectively. Source: Courtesy of Z. Magic.

Meteoritic Abundances An important alternative source to determine the primordial abundances of the solar system is provided by the most primitive meteorites, in particular the so-called CI-chondrites, recovered on Earth. The relative abundance of elements with high condensation temperatures, refractories, determined in chondrites agrees extremely well with spectroscopic determinations. Thus, the abundances of these refractory elements in CI-chondrites are thought to represent the primordial distribution of these elements in the solar system. Five meteorites of the CI-chondrite type have been recovered and are used for solar abundance determination. The great advantage over spectroscopic abundances is that abundances are determined directly through laboratory measurements. Abundance measurements are carried out with respect to a reference element, typically Si. To place meteoritic abundances in the same scale as spectroscopic measurements, which correspond to abundances in the solar photosphere, a reference element (e.g. Si) or group of elements is used as an anchor to both scales. A very extensive discussion about this topic is [59]. Meteoritic abundances are not reliable for elements with low condensation temperatures (volatiles) such as C, N, and O, for which spectroscopy is the only available source.

Other Sources Abundance of noble gases in particular cannot be determined from spectroscopic observations for lack of useful photospheric lines, and they are also not locked efficiently in meteorites. The most important elements, as a function of their abundance are He, Ne, and Ar. For Ne and Ar, in particular, combinations of solar wind measurements and spectral lines formed in the solar corona are used. It is not simple to relate chemical abundances determined in this way to values that are representative of the element abundances in the solar photosphere [57]. For He, the most robust measurements are obtained with helioseismic techniques [60]

Tables of Solar Abundances Table 2.2 gives a list of the most abundant metals in the Sun and their abundances according taken from two widely used reference values. Abundances of volatile elements are from spectroscopic observations, while for refractories, abundances are from meteoritic measurements. The so-called AGSS09 solar composition has been obtained by using the most sophisticated spectroscopic analysis, including 3D-RHD models of the solar atmosphere and NLTE line formation for many elements. They represent the state-of-the-art in spectroscopic analysis. The older GS98 composition was determined with previous generation of solar atmospheres and less sophisticated line formation modeling. However, both sets are provided here because, as it will be discussed in Section 2.6, when the AGSS09 composition is used to calibrate SSMs, the resulting model does not reproduce well the solar structure that is inferred from the analysis of helioseismic data. On the other hand, if the older GS98 composition is used, the resulting SSM reproduces solar properties with a high degree of accuracy. The incompatibility of results obtained with the state-of-the-art solar atmosphere and solar interior calculations is known as the solar composition or solar modeling problem. It will be discussed to some extent in Section 2.6. We note that other solar composition determinations, based on

Table 2.2 Recommended abundances of the most abundant metals in two widely used solar mixtures, [61] and [57], given as $\log \varepsilon_i = \log(n_i/n_H) + 12$.

Element	GS98	AGSS09	Element	GS98	AGSS09
C	8.52 ± 0.06	8.43 ± 0.05	Si	7.56 ± 0.01	7.51 ± 0.01
N	7.92 ± 0.06	7.83 ± 0.05	S	7.20 ± 0.06	7.15 ± 0.02
O	8.83 ± 0.06	8.69 ± 0.05	Ar	6.40 ± 0.06	6.40 ± 0.13
Ne	8.08 ± 0.06	7.93 ± 0.10	Ca	6.35 ± 0.01	6.29 ± 0.02
Na	6.32 ± 0.02	6.27 ± 0.02	Fe	7.50 ± 0.01	7.45 ± 0.01
Mg	7.58 ± 0.01	7.53 ± 0.01	Ni	6.25 ± 0.01	6.20 ± 0.01
Al	6.47 ± 0.01	6.43 ± 0.01	$(Z/X)_\odot$	0.0229 ± 0.0017	0.0178 ± 0.0011

The last entry is the present-day total metal-to-hydrogen mass ratio in the solar photosphere.

comparable techniques as those in AGSS09, are also available, particularly from [58]. However, that work does not provide measurements for all elements needed in SSM calculations.

2.3.2 Adjusting the Free Parameters

Two free parameters in the calibration of an SSM are the initial mass fractions of helium $Y_{\rm ini}$ and metals $Z_{\rm ini}$. In order to specify the initial abundances for all elements in the solar model, a solar mixture needs to be chosen in advance, e.g. GS98 or AGSS09. This choice fixes the relative abundances of metals: i.e. if i and j are two metals, the mass fraction ratios Z_i/Z_j are fixed by the mixture. The initial abundance of hydrogen is obtained from $X_{\rm ini} + Y_{\rm ini} + Z_{\rm ini} = 1$.

The third and final free parameters in an SSM is the mixing length parameter $\alpha_{\rm mlt}$.[5] The value of $\alpha_{\rm mlt}$ is constrained primarily by the solar radius.

The calibration of a solar model consists in finding the set $\{\vec{p}\} \equiv \{\alpha_{\rm mlt}, Y_{\rm ini}, Z_{\rm ini}\}$ of free parameters that, when used to compute the evolution of a $1\ M_\odot$ initially homogeneously mixed standard stellar model, starting at the pre-main sequence up to the solar age $\tau_\odot$, reproduces the set of observational constraints $\{\vec{c}\} \equiv \{L_\odot,\ R_\odot,\ (Z/X)_\odot\}$.

The model predictions for $\vec{c}$ dependence on the input parameters can be represented by the partial derivatives:

$$m_{ij} = \frac{\partial \log c_i}{\partial \log p_j}$$

which take the approximate values given in the matrix below:

$$\begin{array}{c|ccc} & \alpha_{\rm mlt} & Y_{\rm ini} & Z_{\rm ini} \\ \hline L_\odot & 0.06 & 2.35 & -0.73 \\ R_\odot & -0.19 & 0.56 & -0.14 \\ (Z/X)_\odot & 0.06 & 0.08 & 1.11 \end{array} \tag{2.72}$$

5 Other models of convection may contain different free parameters, but there is always at least one free parameter equivalent to $\alpha_{\rm mlt}$.

A suitable initial guess $\{\vec{p}_0\}$ will allow the calculation of a model that, at $\tau_\odot$, will miss $\{\vec{c}\}$ by some margin. Iteratively, e.g. using a Newton–Raphson scheme with derivatives m_{ij} such as those in Eq. (2.73), it is straightforward to find the correct set of free parameters $\{\vec{p}\}$ that satisfy the constraints $\{\vec{c}\}$ to a prescribed accuracy. Accuracies of order one part in 10^{-4} or 10^{-5} are usually enough for most purposes such as studies of solar neutrinos. An SSM is then determined by the choice of the solar mixture of chemical elements and the calibrated $\{\vec{p}\}$.

2.4 Standard Solar Models

2.4.1 Previous and Future Evolution

In studies of standard solar models, it is customarily to neglect the phase of proto-star formation, i.e. the short-lived phase during which the star is initially assembled in its birth gas cloud. Instead, it is assumed that the initial configuration already has 1 $M_\odot$, is fully convective, but central temperatures are still low enough such that nuclear energy generation is absent. Under these conditions, newly formed stars populate the so-called Hayashi line in a Hertzsprung–Russell diagram (HRD). In Figure 2.9 this is illustrated for the evolutionary track of 1 $M_\odot$ stellar model as the dotted line that runs almost vertically for more than 2 dex in luminosity at low temperatures, roughly below 4500 K. Here, typical convective timescales are of the order of 1 year and evolutionary timescales are of the order of 1 Myr, which ensures the star is homogeneously mixed due to convective mixing. During this phase, the star contracts and becomes more gravitationally bound. Half of the gravitational energy is used by the star to increase its internal energy, heating up, while the other half is radiated away, as can be shown using the virial theorem [2]. In the absence of nuclear energy generation, it is the

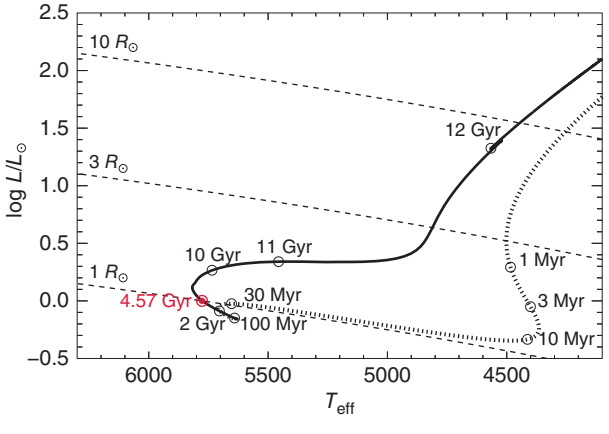

Figure 2.9 Hertzsprung–Russell diagram showing the evolution of a 1 $M_\odot$ stellar model. Curves of constant stellar radii are shown with dashed lines and the age of the model is indicated at several locations. The location of the present-day Sun is indicated with the ⊙ symbol, at $\tau_\odot = 4.57$ Gyr. Pre-main sequence evolution is indicated with dashed lines.

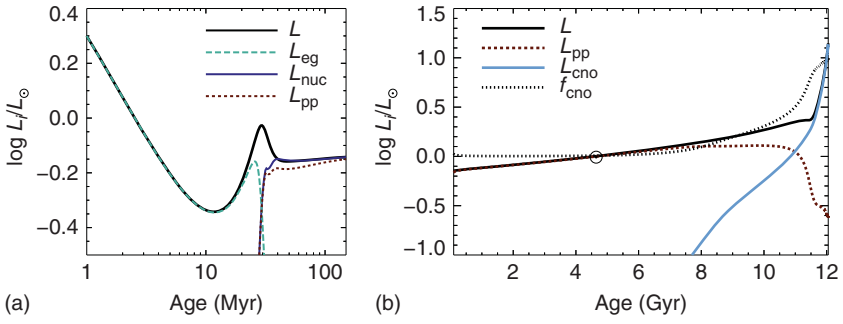

Figure 2.10 (a) Time evolution of energy sources and stellar luminosity, as indicated in the labels. The present-day Sun is shown at $\tau_\odot = 4.57$ Gyr. (b) f_{CNO} shows the fraction of the total nuclear energy that is generated by the CNO-bicycle.

gravothermal energy, ϵ_{gr} in Eq. (2.43c), that dominates the energetics of the contracting star. The time evolution of the luminosity and different energy sources during the first evolutionary stages in Figure 2.10a shows that up to an age of approximately 20 Myr the gravothermal energy supplies the totality of the stellar luminosity.

As the core temperature rises above a few 10^6 K, a radiative core develops and the star moves away from the Hayashi line, toward higher T_{eff} values. The core continues to contract and heat up, and nuclear energy generation increases rapidly due to the steep dependence of nuclear reaction rates with temperature. When the central temperature exceeds 10^7 K, at about 30 Myr, nuclear energy becomes the dominant energy source. Figure 2.10 shows this transition. Energy from the pp chains dominate the total nuclear energy output and, between 30 and 40 Myr, L_{nuc} increases from begin only a marginal contribution to completely dominating the energetics of the star, accounting for all the stellar luminosity. At that point, evolutionary timescales start being dictated by the slow pace at which hydrogen burning proceeds in the core. Rapid contraction or expansion phases are absent and gravothermal energy becomes negligible; the star enters the main sequence phase.

During the main sequence, the stellar luminosity increases slowly, but steadily, as shown in Figure 2.10. This can be understood qualitatively in rather simple terms by considering the equations of hydrostatic equilibrium and radiative energy transport, Eqs. (2.43b) and (2.43d) (the latter with $\nabla = \nabla_{rad}$). From Eq. (2.43b) it follows that a typical pressure in the star scales as $P \propto M^2/R^4$, where M and R are the stellar mass and radius, respectively, and the scaling $\rho \propto M/R^3$ has been used. The EoS is close to that of an ideal gas, so the typical temperature scales as $T \propto (M^2/R^4)(\mu/\rho)$, where μ and ρ are typical values of the mean molecular weight and density. An analogous scaling for the stellar luminosity, using Eqs. (2.43d) and (2.11) to express ∇_{rad}, leads to $L \propto (T^4R^4)/(M\kappa)$. Here κ represents an average opacity value. Combining the two relations,

$$L \propto \mu^4 M^3/\kappa \tag{2.73}$$

This relation, albeit derived in a very approximate way, captures the relevant dependencies between stellar luminosity and basic properties of stars in the main

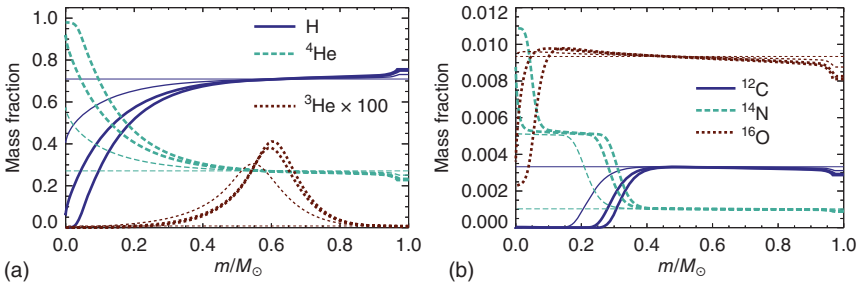

Figure 2.11 Internal chemical composition profiles for relevant nuclear species as a function of mass coordinate. Profiles are shown at ages τ =1, 3904, 7904, and 9904 Myr in order of increasing line thickness. Note the different *y*-axis scale in (a) and (b).

sequence. As hydrogen is converted into helium, μ increases leading to a steady luminosity increase by virtue of Eq. (2.73).

The internal profile of important chemical species, as a function of mass coordinate, at different evolutionary times is illustrated in Figure 2.11. Starting from a homogeneous composition, ^{4}He is produced at the expense of H and, as evolution proceeds, the temperature in the central regions increases and nuclear burning slowly moves outward. The characteristic peaked shape of the ^{3}He profile results because the sequence of reactions that create it, i.e. $p(p, \nu_e e^+)D$ followed by $D(p, \gamma)^3$He, are active at lower temperatures than the reaction that destroys it, ^{3}He$(^3$He, 2p$)^4$He. Then, outward from the peak, ^{3}He is created but not destroyed and its abundance increases. Inward from the peak, the destruction rate increases more steeply with temperature than ^{3}He creation and its abundance drops. The ^{3}He thus created is dredged up toward the stellar surface by envelope convection in the red giant branch (RGB) phase that follows after the main sequence and it is eventually shed to the interstellar medium through stellar winds. Low mass stars such as the Sun are net creators of ^{3}He during the main sequence; they are the main contributors to the evolution of ^{3}He in the universe.

Figure 2.11b shows the profiles of the most important species associated with the CNO-bicycle. For most of the main sequence, the core temperature is only high enough for the CN-cycle to be active. In this cycle, the slowest reaction is ^{14}N$(p, \gamma)^{15}$O, which then acts as a bottleneck and regulates the rate at which the CN-cycle operates. For the same reason, the net effect of the CN-cycle on the CN elements is to convert most of the ^{12}C and ^{13}C (not shown in Figure 2.11) into ^{14}N. The NO-cycle becomes active at higher temperatures, in the latest phases of main sequence evolution, and only then ^{16}O conversion to ^{14}N becomes important. This is seen in the profiles corresponding to 7.90 Gyr and especially at 9.90 Gyr, very close to the end of main sequence evolution. Note that in the CNO-bicycle, CNO elements act as catalyzers. The total number of CNO nuclei is not changed but there is a strong redistribution of the relative abundances, with a net production of ^{14}N at the expense of all other CNO nuclei.

The effect of microscopic diffusion, in particular gravitational settling, is evident in the outermost regions, where a moderate increase in the H abundance and a decrease for all other elements can be seen at $m/M_\odot \gtrapprox 0.95$. Gravitational

settling also produces a moderate gradient in the profiles in the radiative interior, most clearly seen in the profiles of ^{16}O. Changes induced by microscopic diffusion are subtle but are important in understanding the detailed properties of the structure of solar models, as it is described in Section 2.4.2.

All along the main sequence, the dominant channel of hydrogen fusion is through the pp chains. At the solar age, 4.57 Gyr, the CN-cycle contributes just about 1% of the total nuclear energy. Only when the central temperature reaches 2×10^7 K, the CNO-bicycle starts to be the dominant channel for nuclear energy production. This occurs at about 11 Gyr and by that time hydrogen in the core has already been depleted and the star has evolved off the main sequence (Figure 2.10). After the main sequence, the star develops an inert helium core and nuclear burning proceeds in a hydrogen shell surrounding the ever growing helium core. The star becomes an RGB star and the temperature in the burning shell is high enough the CNO burning drives the subsequent evolution. In Figure 2.9 the RGB phase corresponds approximately to the evolution posterior to the star becoming larger than 3 $R_\odot$. On the RGB the luminosity of the star is not controlled by μ as it happens on the main sequence, but by the size of the helium core, that becomes supported by pressure exerted by electron degeneracy. This is the well-known core mass–luminosity (M_c–L) relation that is stated here without proof:

$$L \propto M_c^\beta \tag{2.74}$$

where M_c is the mass of the degenerate helium core and β is approximately in the range of 7–8 [62]. A consequence of the M_c–L relation is that the evolution speeds up as the star climbs the RGB. Consider a given change in luminosity ΔL. According to the M_c–L relation, it follows that $\Delta L \propto M_c \Delta M_c$. But $\Delta M_c = \dot{M}_c \Delta t$, where $\dot{M}_c$ is the rate at which M_c increases due to nuclear burning, that is, $\dot{M}_c \propto L$. Therefore, the time Δt it takes an RGB star to change its luminosity by ΔL scales as

$$\Delta t \propto \frac{\Delta L}{L^{2-1/\beta}} \sim \frac{\Delta L}{L^2} \tag{2.75}$$

This approximate relation helps understand the time evolution of the stellar luminosity after the main sequence. In Figure 2.10 this can be seen around 11.5 Gyr as a sudden change in the time derivative of L. A detailed account of the subsequent evolutionary phases of the future Sun, considered as a typical low mass star, is quite outside the scope of this book and can be found in textbooks dedicated to stellar evolution (e.g. [2, 63]).

2.4.2 The Sun Today: An Overview

The Sun is today approximately halfway its main sequence evolution. The internal profile of the most important thermodynamic quantities and most important chemical species are shown as a function of the mass coordinate in Figure 2.12a,b for an SSM based on the GS98 solar mixture of metals. Central temperature, density, and pressure are $T_c = 15.6 \times 10^7$ K, $\rho_c = 151$ g/cm^3, and $P_c = 2.34 \times 10^{17}$ g/(cm s^2). At $m/M_\odot = 0.5$ they drop to 50%, 13%, and 9% of their central values, respectively. The steep profile of density implies that most

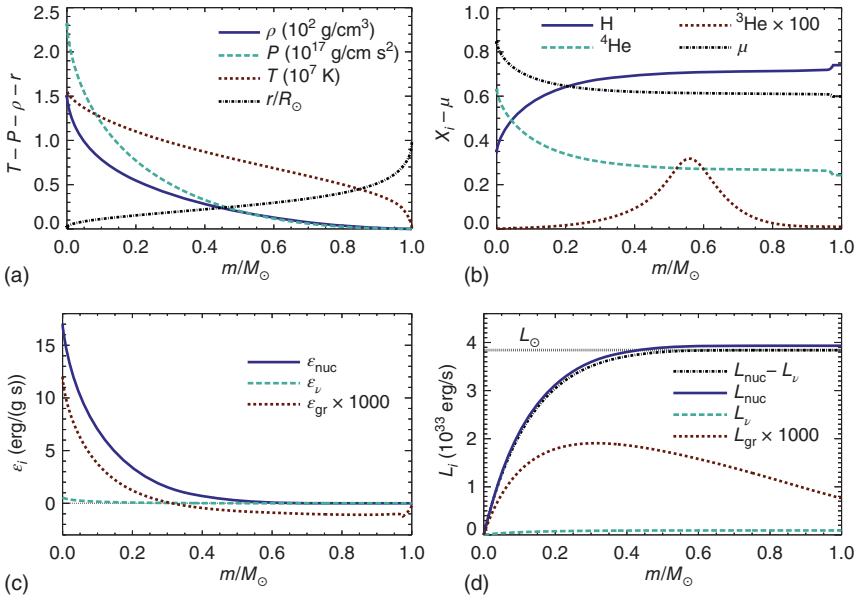

Figure 2.12 Internal profiles for physical quantities and composition for the present-day Sun predicted by SSMs as a function of mass coordinate $m/M_\odot$. (a) Density, pressure, temperature, and radius. (b) Mean molecular weight, hydrogen, ^{4}He, and ^{3}He (multiplied by a factor 100). (c) Local production of nuclear energy, neutrino energy loss, and gravothermal energy (enhanced by a factor 1000). (d) Cumulative contributions of different energy sources shown in (c)). Solar luminosity is shown as a horizontal line $L_\odot$.

of the mass of the Sun is concentrated in a small volume, so at $m/M_\odot = 0.5$ the radius is 0.26 $R_\odot$, i.e. less than 2% of the solar volume. The hydrogen mass fraction of hydrogen at the center is $X_c = 0.347$, which, compared to the initial value $X_{\rm ini} = 0.709$, can be considered as a proxy of how much of its main sequence lifetime the Sun has already spent.

Energetics of the Sun is illustrated in Figure 2.12c,d. Figure 2.12c shows the local production rates of different energy sources or sinks, while Figure 2.12d shows the profiles of the cumulative distributions. Nuclear energy generation $\varepsilon_{\rm nuc}$ happens inside $m/M_\odot = 0.5$. In fact, 90% of the total nuclear energy release takes place within $m/M_\odot = 0.28$, corresponding to $r/R_\odot = 0.18$, just 0.6% of the solar volume. The steepness of $\varepsilon_{\rm nuc}$ with mass is the result of the approximate temperature dependence, $\varepsilon_{\rm nuc} \propto T^4$, of hydrogen burning dominated by pp chains. Production of neutrinos in hydrogen burning implies that some of the energy produced in the conversion of hydrogen into helium does not contribute to the solar luminosity because it is carried away by neutrinos (Eq. (2.54)), which is shown as ε_ν. In the Sun, approximately 85% of the production of ^{4}He happens through the ppI chain, implying that two pp neutrinos are produced per ^{4}He nucleus created. The average energy loss per pp neutrino is 0.265 MeV (Table 2.1): i.e. a fraction of $2 \times 0.265/26.7$ or about 2% of the nuclear energy production is

lost through neutrinos and contributes to the cosmic neutrino background. As a result,

$$L_{\rm nuc} = \int_0^{M_\odot} \varepsilon_{\rm nuc}\, {\rm d}m > L_\odot \tag{2.76}$$

as illustrated in Figure 2.12d.

There is one more source of energy in the Sun to be considered, the gravothermal energy $\varepsilon_{\rm eg}$ (see Eq. (2.43c)), associated with changes in the internal structure. The contribution of $\varepsilon_{\rm gr}$, as shown in Figure 2.12c,d is negligible because main sequence stars change very slowly. It is instructive to note however that $\varepsilon_{\rm gr}$ is positive in the central regions, for $m/M_\odot < 0.3$, and becomes negative outward. The central regions are slowly contracting, while the zone outside the energy generation region slowly expands. The total contribution $L_{\rm gr}$ to the solar energetics is less than 0.02%. Therefore, nuclear energy is the only relevant energy source in the present-day Sun according to results of SSMs.

The temperature gradients in the solar interior are shown in Figure 2.13 as a function of solar radius. Note that in the figure quantities are shown against radius to show better the outer low density regions. In the solar interior energy transport is radiative and the actual temperature gradient is $\nabla = \nabla_{\rm rad}$. This is typical of stars dominated by hydrogen burning through pp chains. The temperature dependence of $\varepsilon_{\rm nuc} \propto T^4$ is that of the proton + proton reaction, and it is not strong enough to lead to a highly localized energy release. The ratio l/m in the solar core is low enough such that $\nabla_{\rm rad} < \nabla_{\rm ad}$ (Eq. (2.11)). The opacity κ is typically low in the solar interior as well, as also shown in Figure 2.13. But, as temperature and density decrease toward the outside, κ increases steeply, as bf and bb transitions become increasingly dominant. This was already shown in the T–R plane, in Figure 2.3. $\nabla_{\rm rad}$ scales linearly with κ so it also increases rapidly and, at $r/R_\odot = 0.713$, $\nabla_{\rm rad} = \nabla_{\rm ad}$. This condition sets the location of the inner boundary of the solar convective envelope. At larger radii, energy transport is dominated by convection. The convective region in the SSM is indicated by the cross-hatched

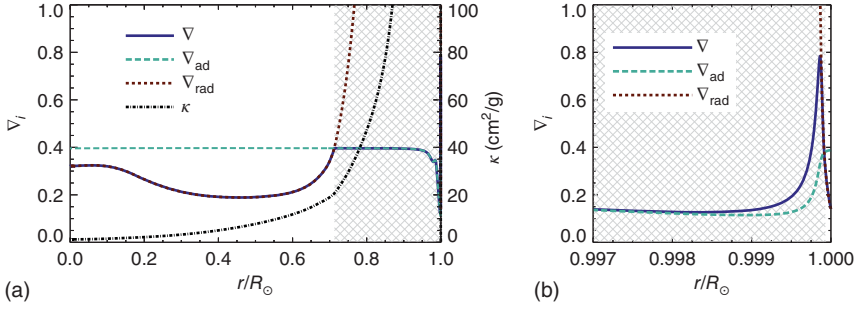

Figure 2.13 (a) Temperature gradients and (b) radiative opacity in the solar interior. The convective envelope is indicated as the cross-hatched region. The transition between radiative and convective energy transport occurs at $r/R_\odot = 0.713$. In the radiative interior $\nabla = \nabla_{\rm rad}$, in the convective envelope $\nabla = \nabla_{\rm ad}$ except in the outermost layers, enhanced in (b).

region. In most of the convective envelope ∇ is almost equal to ∇_{ad}: i.e. convection is almost adiabatic because a very small overadiabaticity is enough to account for the energy flux. Figure 2.13b zooms in the region close to the solar photosphere. There, the departure of convection from near adiabaticity increases and ∇ is noticeably larger than ∇_{ad}. At $r/R_\odot > 0.99975$ the opacity decreases sharply and then ∇_{rad} drops below ∇_{ad}, giving rise to a very thin radiative, formally stable region. In reality, overshooting convective bubbles rising from the interior penetrate this layer and keep it well mixed, thus chemically homogeneous, with the convective envelope.

The actual value of ∇ in the outermost, non-adiabatic region depends critically on the treatment of convection in the models. Employing phenomenological descriptions of convection, such as the MLT, forces the introduction of free parameters that need to be adjusted with observational constraints as explained in Section 2.3.2. Ideally, 3D-RHD simulations of near surface convection, like those used in the determination of the solar composition (Section 2.3.1.2) should be used in modeling this region of the Sun, as they provide the most physically accurate description that can be currently achieved. However, the secular evolution of the Sun cannot be followed with such simulations due to the very different timescales involved: minutes for convection and millions of years for structural changes in the Sun. As a palliative, 3D RHD can serve as a guide for the development of more realistic, albeit still phenomenological, descriptions of convection that can be implemented into stellar evolution 1D codes [64, 65]. A detailed modeling of the outer layers of the Sun is not critical to the production of solar neutrinos, but it is fundamental for studies of solar oscillations.

2.5 Solar Neutrinos

The nuclear reactions that produce neutrinos in the Sun are highlighted in Figures 2.5 and 2.6. There are eight such reactions in the pp chains and CNO-bicycle and the nomenclature given in the last column of Table 2.1 will be used to refer to each of them. If the reaction between species 1 and 2 produces neutrinos, the integrated production rate can be computed in an SSM as

$$\Phi = \int_0^{R_\odot} \frac{4\pi r^2}{1+\delta_{12}} \frac{X_1 X_2}{A_1 A_2} \frac{\rho^2}{m_u^2} \, r_{12} \, \mathrm{d}r \tag{2.77}$$

where the reaction rate r_{12}, the mass fraction X_i of species i and the density ρ are functions of radius r. This expression can be simplified accordingly in the case that neutrinos are produced by decays such as in the case of neutrinos from the CNO-bicycle.

Figure 2.14 shows the distribution of the neutrino production, i.e. the integrand in Eq. (2.77), for all solar neutrinos in the pp chains. Distributions have been normalized to integrate to 1. Differences in the distributions originate in the quantity $X_1 X_2 r_{12}$. The location and width of the peak reflect primarily the temperature dependence of the production rate and to a lesser extent the underlying distribution of X_1 and X_2 (Figure 2.12). These distributions can be understood as the

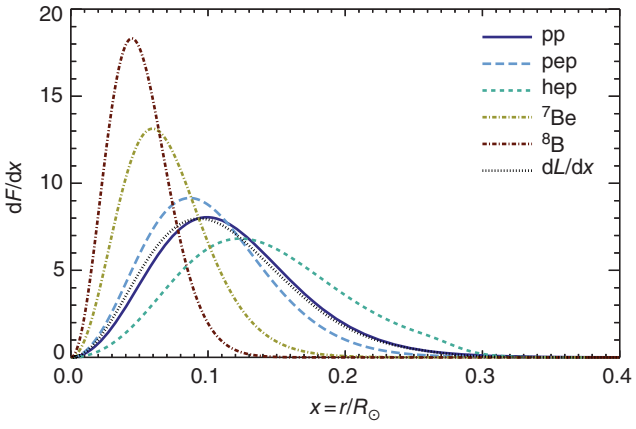

Figure 2.14 Distribution functions of the production of neutrinos in the pp chains and of the solar total luminosity.

probability distributions of the neutrino productions and are important when studying neutrino oscillations. The electron density is very well described in the solar interior as

$$N_e = \rho \frac{(1+X)}{2m_u} \tag{2.78}$$

where X is the hydrogen mass fraction. The location where neutrinos are produced then determines the electron density N_e profile that neutrinos will traverse on their way to the laboratory. Together with the neutrino energy, this will determine if neutrino oscillations will be dominated by matter effects as it is the case for the high energy ^{8}B neutrinos or by vacuum oscillations such as for pp neutrinos. Figure 2.14 also shows the distribution of the generation of the solar luminosity $\mathrm{d}L/\mathrm{d}x$, that very closely resembles that of pp neutrinos and shows that energetics in the Sun is dominated by this reaction.

The distribution functions for neutrinos in the CNO-bicycle are shown in Figure 2.15a. The similitude in the shape occurs because the temperature dependence of the production of CNO neutrinos is very similar. The production region is also very similar to that of ^{8}B neutrinos, but the energy of CNO neutrinos is lower so oscillations are not dominated by matter effects. They are, in fact, in a transition region between matter dominated and vacuum oscillations. The production of ^{13}N neutrinos shows two peaks. The outer peak is the result of the operation of the $^{12}\mathrm{C}(\mathrm{p},\gamma)^{13}\mathrm{N}$ reaction at $T \approx 10^7$ K ($r/R_\odot \approx 0.17$) followed decay of the ^{13}N. Figure 2.15b shows the mass fraction profile for the three most important CNO isotopes, where it can be seen that the outer peak in the ^{13}N neutrinos production coincides with the location where ^{12}C is transformed into ^{13}C and then ^{13}C into ^{14}N. At this relatively low temperature, proton captures by ^{14}N is not efficient and the CN-cycle is choked. At higher temperatures, all proton capture reactions in the CN-cycle become active and the CN-cycle reaches a steady state. As a result, the same total number of ^{13}N and ^{15}O neutrinos are produced in the inner $r/R_\odot \leq 0.12$ region. Note this is not apparent

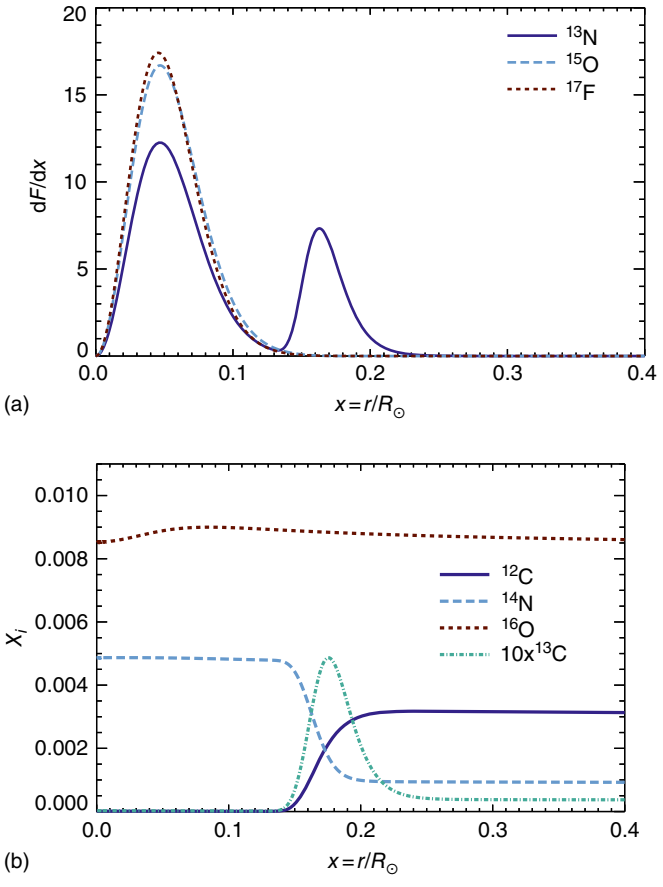

Figure 2.15 (a) Distribution functions of the production of neutrinos in the CNO-bicycle. (b) Mass fraction profiles of most important CNO isotopes.

in Figure 2.15 because of the normalization of the distribution functions. The distribution functions of neutrino production are robust to changes in the SSMs. The uncertainties in the physical inputs, e.g. nuclear reactions rates, solar composition, do not affect the shape of these functions in any appreciable manner.

The integrated neutrino production rate depends on the detailed physical inputs in the models. Table 2.3 lists the solar neutrino fluxes on Earth[6] for two SSMs that are calibrated using the solar surface compositions GS98 and AGSS09 that have been presented in Section 2.3.1.2 [66]. The solar neutrino fluxes determined from a joint analysis of all data from neutrino experiments [67] are also listed in Table 2.3. Data include results from chlorine and gallium radiochemical experiments, water and heavy water Cherenkov detectors, and liquid scintillator detectors (see Chapter 4).

6 Total production rate in Eq. (2.77) is divided by $4\pi 1$ AU^2, where 1 AU = 1.495 98 $\times 10^{13}$ cm is the astronomical unit, or mean Sun–Earth distance.

Table 2.3 Solar neutrino fluxes on Earth. Predicted by two solar models based on GS98 and AGSS09 solar compositions [66] and the solar fluxes determined from a global analysis of all available experimental results [67].

Flux	B16-GS98	B16-AGSS09	Solar fluxes
Φ(pp)	$5.98(1 \pm 0.006)$	$6.03(1 \pm 0.005)$	$5.97(1 \pm 0.006)$
Φ(pep)	$1.44(1 \pm 0.01)$	$1.46(1 \pm 0.009)$	$1.45(1 \pm 0.009)$
Φ(hep)	$7.98(1 \pm 0.30)$	$8.25(1 \pm 0.30)$	$19(1 \pm 0.55)$
$\Phi(^7\text{Be})$	$4.93(1 \pm 0.06)$	$4.50(1 \pm 0.06)$	$4.80(1 \pm 0.048)$
$\Phi(^8\text{B})$	$5.46(1 \pm 0.12)$	$4.50(1 \pm 0.12)$	$5.16(1 \pm 0.021)$
$\Phi(^{13}\text{N})$	$2.78(1 \pm 0.15)$	$2.04(1 \pm 0.14)$	≤ 13.7
$\Phi(^{15}\text{O})$	$2.05(1 \pm 0.17)$	$1.44(1 \pm 0.16)$	≤ 2.8
$\Phi(^{17}\text{F})$	$5.29(1 \pm 0.20)$	$3.26(1 \pm 0.18)$	≤ 85
χ^2 (σ)	6 (0.5)	7 (0.6)	—

Units are 10^{10} for Φ(pp), 10^9 for $\Phi(^7\text{Be})$, 10^8 for Φ(pep), $\Phi(^{13}\text{N})$, and $\Phi(^{15}\text{O})$, 10^6 for $\Phi(^8\text{B})$, $\Phi(^{17}\text{F})$, and 10^3 for Φ(hep), always in $\text{cm}^{-2}\ \text{s}^{-1}$. The last row shows the level of agreement between both B16 SSMs and solar neutrino fluxes.

The fluxes $\Phi(^8\text{B})$ and $\Phi(^7\text{Be})$ are currently determined with very good precision, driven by SuperKamiokande and SNO in the first case and by Borexino in the second. Φ(pp) and Φ(pep) are determined to better than 1%, but this is possible only when the so-called solar luminosity constraint is included in the analysis of experimental data. This constraint assumes that only nuclear energy is responsible for the generation of all $L_\odot$ and allows to build a linear relation between the neutrino fluxes and $L_\odot$ [68]. As it was shown in Section 2.4.2, SSMs give a strong support to this hypothesis, as only nuclear energy is a relevant source of energy in the SSM. About 99% of the nuclear energy is produced either by ppI and ppII chains. This implies that the precise measurement of $\Phi(^7\text{Be})$ provided by Borexino [69, 70], can be used to fix the ppII contribution to $L_\odot$, automatically fixing the ppI fraction, that is, the value of Φ(pp) and the closely related Φ(pep). If the luminosity constraint is not used in the analysis of neutrino data, then Φ(pp) and Φ(pep) are currently determined experimentally to 8% [67]. Current solar neutrino experiments yield, independently of solar models:

$$\frac{L_\odot(\text{neutrino-inferred})}{L_\odot} = 1.04 \pm 0.08 \tag{2.79}$$

This is the most accurate and precise anwser, with current experimental evidence, to the question "How does the Sun shine?".

There are differences in the fluxes predicted by the two different SSMs. The model calibrated with the higher $(Z/X)_\odot$, B16-GS98, predicts larger $\Phi(^7\text{Be})$ (ppII chain) and $\Phi(^8\text{B})$ (ppIII chain) fluxes, and lower fluxes for those in the ppI chain. The higher metallicity in the model leads to higher opacity (see Section 2.2.2 for the role of metals in opacity) and this in turn leads to slightly larger temperatures in the solar core. A power-law scaling $\Phi \propto T_c^n$ between

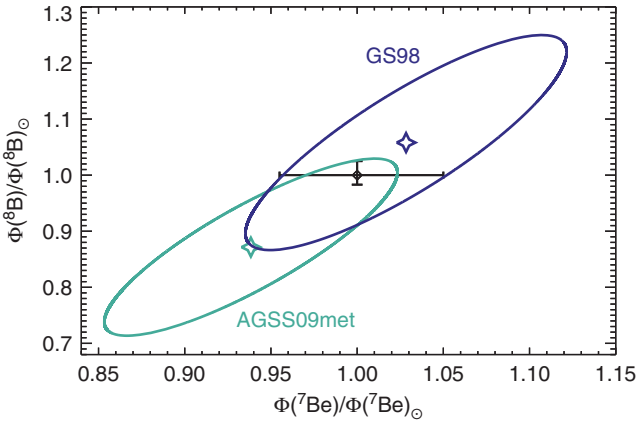

Figure 2.16 $\Phi(^8\mathrm{B})$ and $\Phi(^7\mathrm{Be})$ normalized to solar values. Black circle and error bars: solar values determined from neutrino experiments as listed in Table 2.3. Stars and ellipses show model predictions and 1σ uncertainties.

fluxes and the central temperature in SSMs [71] yields $n \approx -1, -2.5, 10$, and 24 for $\Phi(\mathrm{pp})$, $\Phi(\mathrm{pep})$, $\Phi(^7\mathrm{Be})$, and $\Phi(^8\mathrm{B})$ respectively.[7] Therefore, changes in the solar core temperature alters the balance between the pp chains, increasing those with higher temperature sensitivity. As a result, $\Phi(^7\mathrm{Be})$ and $\Phi(^8\mathrm{B})$ fluxes are about 10% and 21% higher in B16-GS98 than in B16-AGSS09. The fluxes predicted by both SSMs are, however, well in agreement with the solar values. This is summarized in the last row of Table 2.3, where the corresponding χ^2 values and level of agreement in number of σ are given. On the other hand, it is unfortunate that solar neutrino data of pp chain fluxes, the ones that can be measured to good precision with current experiments, cannot separate models with different solar composition. Figure 2.16 shows the comparison between SSMs and experimental determinations of $\Phi(^7\mathrm{Be})$ and $\Phi(^8\mathrm{B})$. Note that model predictions for these two fluxes are correlated; this is the reason of the tilted error ellipses.

Current solar neutrino experiments have not been able to measure the neutrino fluxes from the CNO-bicycle. The potential targets of such measurements are $\Phi(^{13}\mathrm{N})$ and $\Phi(^{15}\mathrm{O})$ because the expected $\Phi(^{17}\mathrm{F})$ value is too low. Neutrinos from the CN-cycle have a very interesting scientific potential. They are sensitive to the solar composition through the effect that metals have on the stellar opacity in a very similar way as $\Phi(^8\mathrm{B})$. But, in addition, when the CN-cycle is operating steadily as it happens in the solar inner core, $r/R_\odot \leq 0.12$, the catalyzing action of carbon and nitrogen implies that the rate of production of these two neutrino fluxes scales linearly with the total abundance of carbon and nitrogen. This is clear from Table 2.3, from which $\Phi(^{13}\mathrm{N})$ and $\Phi(^{15}\mathrm{O})$ are 36% and 42% higher for the B16-GS98 model. A measurement of $\Phi(^{13}\mathrm{N})$ and $\Phi(^{15}\mathrm{O})$, constrained by the

7 The negative exponents in $\Phi(\mathrm{pp})$ and $\Phi(\mathrm{pep})$ follow from the constraint that SSMs must satisfy $L = L_\odot$.

available high precision measurement of $\Phi(^8\mathrm{B})$ can be used to directly determine the abundance of C + N in the solar core. Details of the method can be found in [72, 73]. A direct measurement of elemental abundances in the core of the Sun would be a stunning result. It could help understanding the origin of the solar abundance problem (Section 2.7), but it would also contribute to test chemical mixing in stars by comparing the core and surface abundances, and eventually the conditions under which the planets in the solar system formed [74].

There are other sources of neutrinos in the Sun that are related to the CNO-bicycle. ^{13}N, ^{15}O, and ^{17}F decay predominantly by β^+ decay, but electron captures on these species are also possible, e.g. $^{13}\mathrm{N} + e^- \rightarrow {}^{13}\mathrm{C} + \nu_e$, leading to the electron capture CNO fluxes $\Phi^e(^{13}\mathrm{N})$, $\Phi^e(^{15}\mathrm{O})$, and $\Phi^e(^{17}\mathrm{F})$. The expected fluxes for these electron capture neutrinos are about three orders of magnitude smaller than their β^+-decay counterparts, but the spectrum is monochromatic, which enhances the detection possibility. The energy of these neutrinos is the endpoint energy of their β^+ decay counterparts plus 1.022 MeV because of the electron capture instead of the positron emission. Neutrinos from the electron capture by ^{13}N in particular are potentially very interesting for testing the electron neutrino survival probability in the transition region from matter dominated to vacuum neutrino oscillations [75].

Figure 2.17 shows the energy spectrum for all solar neutrino fluxes, normalized to total fluxes from the B16-GS98 SSM. Neutrinos from the pp chains and CNO-bicycle are shown in dark and light colors, respectively. Neutrinos with a continuous spectrum are indicated with solid lines, while spectral lines are shown with dashed trace. Note that spectral lines from electron captures are in reality broadened by thermal effects, but this is not seen at this scale.

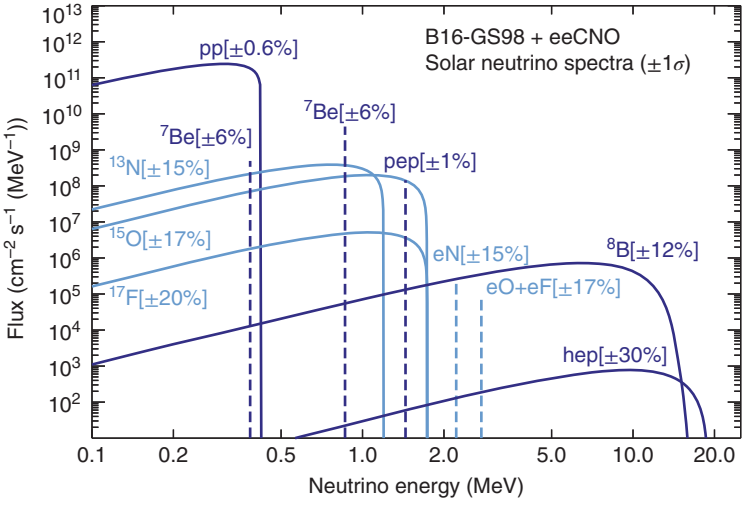

Figure 2.17 Individual contributions to the solar neutrino spectra. Fluxes and uncertainties correspond to the B16-GS98 SSM.

2.6 Helioseismology

2.6.1 Overview

Helioseismology is the study of the oscillations present in the Sun that can be measured in its surface. They were discovered in 1962 [76] using time series of maps of radial velocity shifts (Dopplergrams) of the solar surface. Observations revealed the presence of coherent variations in the velocity field with periods of around 300 seconds, 5 minutes, and lifetimes of a few periods. These oscillations were first interpreted by Ulrich [77], Leibacher and Stein [78] as standing acoustic waves, or pressure modes (p-modes), occurring in the solar convective envelope and trapped below the photosphere. The global nature of the oscillations was established a few years later. Soon, it was found that power was concentrated in ridges in a wavenumber–frequency diagram [79, 80], according to predictions made by Ulrich [77], establishing firmly that oscillations corresponded to non-radial p-modes.

In what follows, the presentation of the topic includes the basic concepts needed to understand the most important results of helioseismology in the context of SSMs. A detailed accont of the theory of solar oscillations can be found in specialized literature [81].

Solar oscillations have small amplitudes. Observed in radial velocity, the amplitude of the velocity field is ∼500 m/s [82]. This is the result of the random superposition of $\sim 10^7$ oscillation modes, each with typical amplitudes of $\sim\sqrt{500^2/10^7}$ m/s ∼0.15 m/s. Observed in brightness, oscillation amplitudes are just a few parts per million. The small amplitudes of the oscillations, both in the surface and in the solar interior, allows to consider them as small linear perturbations to a background reference state that is itself not affected by the oscillations. Solar oscillations can be decomposed as a superposition of individual modes, each of which can be characterized by a wave function with a radial component and an angular component, the latter given by a spherical harmonics Y_m^ℓ. Each eigenmode is then identified by the triplet (n, ℓ, m) where n denotes the radial order, i.e. the number of nodes of the radial eigenfunction, ℓ is the angular degree and m, the azimuthal number, can take any value $-\ell, -\ell+1, \ldots, \ell-1, \ell$.

When the background model is spherically symmetric, mode frequencies depend only on n and ℓ and form a degenerate multiplet of $(2\ell+1)$ components. Figure 2.18 shows the frequencies of over 2000 eigenmodes in the Sun that have been obtained with the Michelson Doppler Imager (MDI), on board of the SOHO mission [82] and by the Birmingham Solar Oscillations Network (BiSON) [84]. Each ridge corresponds to a different radial order n. The measurement errors have been enhanced by a factor 1000 to make them visible at low ℓ high ν corner. Figure 2.18 also shows in dots the theoretical spectrum of frequencies corresponding to the B16-GS98 SSM.

The typical timescales of solar oscillations are much shorter than the radiative timescales associated with heat exchange. This implies that oscillations are to a very good approximation adiabitic. Then, only linear perturbations of the mechanical structure equations, Eqs. (2.2) and (2.3), need to be considered.

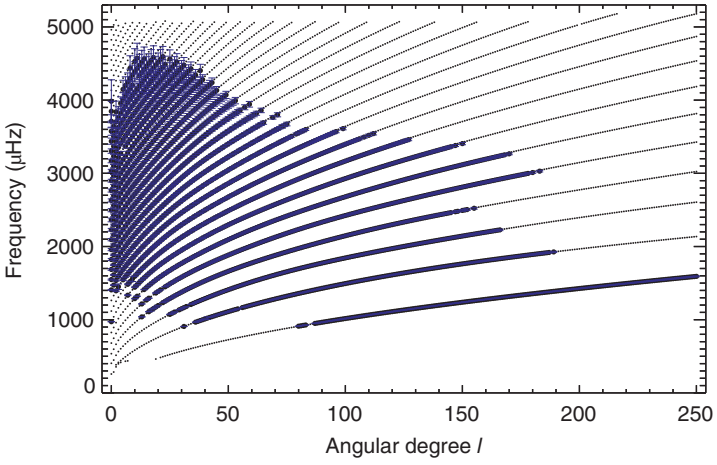

Figure 2.18 Spectrum of solar oscillations. Large symbols: data from the Michelson Doppler Imager (MDI) on board of SOHO and from the Birmingham Solar Oscillations Network (BiSON). Error bars are increased by a factor 1000 to make them visible. They are shown in blue but are only visible at high frequency and low ℓ. Small dots: theoretical frequencies of the B16-GS98 SSM. Source: Data courtesy of Sarbani Basu et al. [83].)

A further simplification can be introduced with the so-called Cowling approximation, which neglects the perturbation of the gravitational potential due to the oscillations. Under these conditions, a simplified form of the equations of solar oscillations, given here without demonstration, can be written as [85, 86]:

$$\left[\frac{\mathrm{d}^2}{\mathrm{d}r^2} + \frac{\omega_{\mathrm{eff}}^2}{c_s^2}\right] \Psi_\ell(r) = 0 \tag{2.80}$$

Here $\Psi_\ell(r) \equiv c_s^2 \sqrt{\rho}\ \vec{\nabla} \cdot \delta\vec{r}$, where $\delta\vec{r}$ is the displacement vector around the spherically symmetric background state and

$$\omega_{\mathrm{eff}}^2 = \omega^2 \left[1 - \frac{\omega_{\mathrm{ac}}^2}{\omega^2} - \frac{S_\ell^2}{\omega^2}\left(1 - \frac{N^2}{\omega^2}\right)\right] \tag{2.81}$$

Several quantities need to be defined. The eigenfrequency of the mode is ω, the buoyancy frequency N (also known as Brunt–Väisälä frequency) is

$$N^2(r) = g\left(\frac{1}{\Gamma_1}\frac{\mathrm{d}\log P}{\mathrm{d}r} - \frac{\mathrm{d}\log\rho}{\mathrm{d}r}\right) \tag{2.82}$$

S_ℓ is the acoustic (or Lamb) frequency:

$$S_\ell^2(r) = \frac{\ell(\ell+1)c_s^2}{r^2} \tag{2.83}$$

where c_s the adiabatic sound speed given by

$$c_s^2 = \frac{\Gamma_1 P}{\rho} \tag{2.84}$$

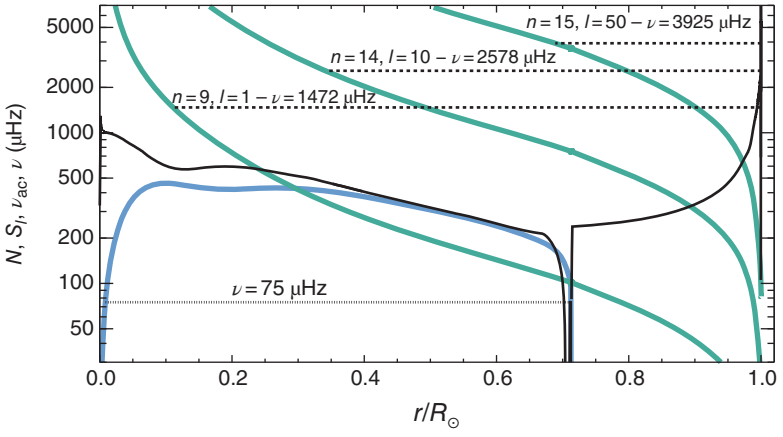

Figure 2.19 Propagation diagram of oscillations for a solar model.

Finally, $\omega_{\rm ac}$ is the acoustic cutoff frequency that can be approximated as[8]:

$$\omega_{\rm ac} = \frac{c_s}{2H_P} \tag{2.85}$$

From Eqs. (2.80)–(2.85) it can be seen that the properties of adiabatic solar oscillations are completely determined by P, ρ, Γ_1, and g but only two of these quantities are independent.

The expression in Eq. (2.80) is very useful because it allows to perform a local stability analysis. If Ψ_ℓ is expressed locally as $\Psi_\ell(r) \propto e^{iK(r)r}$, the local dispersion relation is

$$K^2(r) = \frac{\omega^2_{\rm eff}}{c_s^2} \tag{2.86}$$

Solutions in the form of trapped waves exist only in the regions where $K(r)$ is real, i.e. when $\omega^2_{\rm eff} \geq 0$. These are the propagating regions, or resonant cavities, of solar oscillations. Their boundaries, or turning points, are located where $\omega^2_{\rm eff} = 0$. Figure 2.19 represents the propagation diagram of an SSM. The buoyancy frequency is shown with a light blue line, the green lines show the acoustic frequencies for $\ell = 1,\ 10,\ 50$, and the thin black line is $\omega_{\rm ac}$. Note that for the p-modes observed in the Sun (Figure 2.18), $\omega \gg N$ and $\omega \gg \omega_{\rm ac}$ in the solar interior. In this limit, $\omega^2_{\rm eff} \simeq \omega^2 - S^2_\ell(r)$ and the inner turning point r_t is given by the condition $\omega = S_\ell(r_t)$. In the outermost regions of the Sun, $S_\ell(r) \ll \omega$ even for large ℓ values. The outer boundary of the propagating cavity is then set by the rapid increase of $\omega_{\rm ac}$ in the solar atmosphere, around $R_\odot$, when the condition $\omega = \omega_{\rm ac}$ is fulfilled. The analysis presented here is approximate. A more detailed determination of the propagating cavities in the solar interior can be found in [81].

---

8 The complete expression is $\omega^2_{\rm ac} = \frac{c_s^2}{4H^2}\left(1 - 2\frac{{\rm d}H}{{\rm d}r}\right)$, with $H = \left(\frac{{\rm d}\log\rho}{{\rm d}r}\right)^{-1}$ as the density scale height. In an isothermal atmosphere this expression reduces to Eq. (2.85).

Figure 2.19 shows with dashed lines the propagating region of several nonradial ($\ell > 0$) p-modes that are identified according to their frequency ($\nu = \omega/2\pi$) and angular degree ℓ. For each mode, the inner turning point is given by

$$r_t = \frac{\sqrt{\ell(\ell+1)}c_s}{\omega} \tag{2.87}$$

Different oscillation modes are sensitive to the structural properties in different regions of the Sun, depending on their frequency and angular degree. This property can be exploited to determine the localized properties of the solar interior.

2.6.2 Global Structure Inversions

A range of helioseismic techniques exists for determining solar properties. Global inversions of the solar structure are particularly powerful. Consider a reference solar model and its set of theoretical frequencies $\omega^r_{n\ell}$. A localized change in the model structure will lead to variations in oscillation frequencies. If changes in the structure are small, they can be treated in a linear approximation and then, frequency variations can be expressed as

$$\frac{\delta\omega_{n\ell}}{\omega_{n\ell}} = \int_0^{R_\odot} \mathcal{K}^{n\ell}_{c_s^2,\rho}(r)\frac{\delta c_s^2}{c_s^2}(r)\mathrm{d}r + \int_0^{R_\odot} \mathcal{K}^{n\ell}_{\rho,c_s^2}(r)\frac{\delta\rho}{\rho}(r)\mathrm{d}r + F(\omega_{n\ell}) \tag{2.88}$$

where $\delta\omega_{n\ell}$ is the change of frequency with respect to the reference model value, $\delta c_s^2/c_s^2$ and $\delta\rho/\rho$ are the changes (as a function of r) in c_s^2 and ρ with respect to the reference model, and $\mathcal{K}^{n\ell}_{c_s^2,\rho}(r)$ and $\mathcal{K}^{n\ell}_{\rho,c_s^2}(r)$ are the kernels that represent the response of $\omega_{n\ell}$ to local changes in c_s^2 and ρ, respectively. The kernels are computed using solar models and are known functions. The function $\mathcal{F}$ accounts for departures from adiabaticity in the solar atmosphere and it is of no relevance for the following discussion.

Equation (2.88) can be considered from a different perspective. Instead of expressing the difference between two models, it can be thought of as the difference between the Sun and a reference model. In this case, $\delta\omega_{n\ell} = \omega_{n\ell,\odot} - \omega_{n\ell,r}$. Now the functions $\delta c_s^2/c_s^2$ and $\delta\rho/\rho$ are unknown but they are determined by solving the set of integral equations given by Eq. (2.88) for a large set of frequencies $\omega_{n\ell}$. This is the global inversion of solar properties. The resulting functions $\delta c_s^2/c_s^2 = (c_{s,\odot}^2 - c_{s,r}^2)/c_{s,r}^2$ and $\delta\rho/\rho = (\rho_\odot - \rho_r)/\rho_r$ express the difference between the Sun and the reference model. Given that the model c_s^r and ρ^r are known, inversions allow to reconstruct the interior properties of the Sun. Note that other quantities can be used for inversion instead of c_s^2 and ρ, for example, the adiabatic index Γ_1, or even the helium abundance of the Sun.

Figure 2.20 shows the results of global inversions using $\delta c_s^2/c_s^2$ and $\delta\rho/\rho$ for the B16-GS98 and B16-AGSS09 SSMs presented in Section 2.5. Inversions have been obtained using the set of frequencies shown in Figure 2.18 [83]. Differences are shown in the sense (solar model) and show the level of agreement between SSM predictions and the actual solar interior structure. The observational uncertainties in inversions of solar structure are shown with error bars. They are very small due to the very high precision with which oscillation frequencies are measured. The colored band in each plot shows fractional variations due to uncertainties

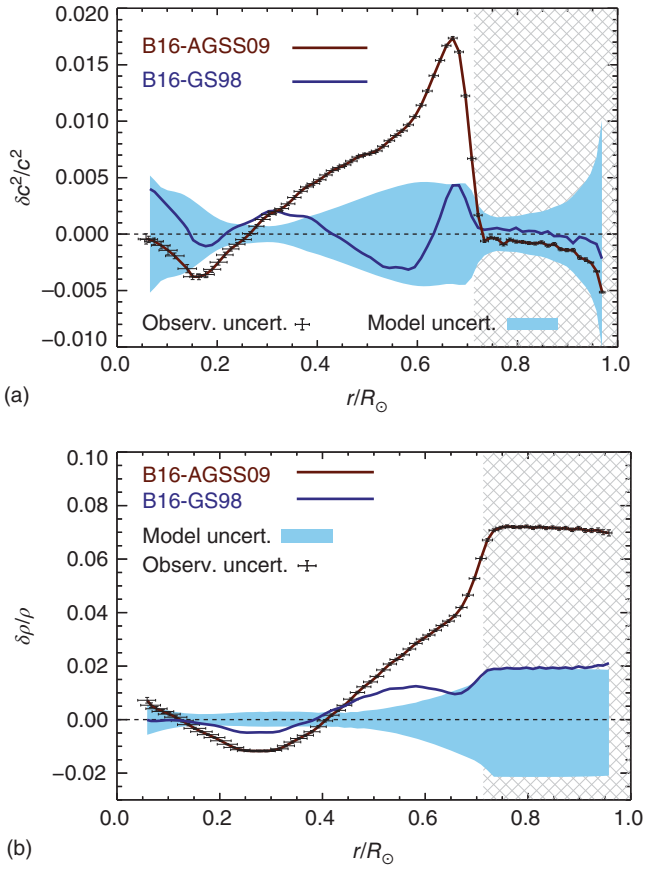

Figure 2.20 (a) Sound speed inversion results for B16-GS98 and B16-AGSS09 SSMs. (b) Density inversion results. In (a) and (b), uncertainties due to frequency measurement errors are shown with error bars. Model uncertainties are shown as a colored area. The hatched area denotes the convective envelope.

in the SSMs originating in the solar composition, nuclear reaction rates, and all other physical inputs in SSM calculations. It is noteworthy that, in particular for c_s^2, the agreement between SSMs and the Sun is about 1.5% at worst, or a factor of 2 lower if c_s is considered instead of c_s^2. The average or root mean square discrepancy of c_s is 0.4% for the B16-AGSS09 model and 0.1% for B16-GS98. SSMs are remarkably good in reproducing the sound speed profile of the solar interior. For the density the situation seems less clear because B16-AGSS09 shows differences of more than 7%. Density inversions, however, are more difficult to interpret than sound speed results because results at different depths are very strongly correlated. The reason is that for density inversions the integrated mass of the Sun needs to match the known solar mass $M_\odot$. This implies that a small difference between the Sun and an SSM in the solar core, where density is very large, needs to be compensated by a large difference of opposite sign in the outer layers, of much smaller density. This is the reason that a large density difference is seen

in the outer regions. Sound speed inversions provide more robust information than density inversions.

2.6.3 Other Constraints

Helioseismology can be used to perform other tests of solar models. Among the most important observables that can be determined from helioseismology are the depth of the convective envelope $R_{\rm CZ}$ and the helium abundance Y_S in the convective envelope.

The location of $R_{\rm CZ}$ is determined by the condition $\nabla_{\rm ad} = \nabla_{\rm rad}$. The temperature gradient is continuous across $R_{\rm CZ}$ but its derivative is discontinuous, as illustrated in Figure 2.13a. The EoS is very close to an ideal gas, i.e. $c_s^2 \simeq RT/\mu$, and this implies that the second derivative of c_s is discontinuous at $R_{\rm CZ}$. The properties of the propagation cavity of p-modes changes abruptly at $R_{\rm CZ}$ and this can be exploited to determine $R_{\rm CZ}$. Figure 2.21a shows the sound speed difference of a solar model with $R_{\rm CZ} = 0.713 R_\odot$ relative to other models that have different $R_{\rm CZ}$ values as indicated in the figure. The sensitivity of the sound speed profile to the location of $R_{\rm CZ}$ is clearly seen in the plot. The magnitude of these differences is much larger than uncertainties in the sound speed profile obtained from inversions. This implies that the sound speed difference between models and the Sun can be used to determine $R_{\rm CZ}$ very precisely. Using this and other techniques [87–89], the helioseismic measurement yields $R_{\rm CZ} = (0.713 \pm 0.001) R_\odot$.

The EoS in the solar interior is very close to that of a fully ionized gas because its composition is dominated by hydrogen and helium. However, as shown in Figure 2.1, the adiabatic index Γ_1 shows depressions from 5/3, the value corresponding to a fully ionized gas. At $T \approx 10^5$ K (or $r/R_\odot \approx 0.98$), hydrogen is fully ionized but a large fraction of the helium atoms still have a bound electron (Figure 2.2; HeII). The depth of the deviation of Γ_1 from 5/3 due to HeII ionization depends on the abundance of helium linearly for relatively small variations of the helium abundance. Figure 2.21b shows the Γ_1 profiles for models with different helium mass fractions. The changes in Γ_1 due to variations in the helium abundance are much larger than the precision of helioseismic inversions of Γ_1 and allow to determine the helium abundance by adjusting it such that a solar model reproduces the depth of the Γ_1 dip. It should be noted that for transforming a Γ_1 measurement into a helium abundance value, it is necessary to rely on an EoS. Uncertainties in the EoS will affect the determined helium abundance. The EoS is the main uncertainty source in the helium determination [60]. The HeII region is located in the convective envelope. Due to the very short convective timescale for chemical mixing, the helium abundance determined at this depth is the same abundance in all the convective envelope, and it is for this reason also the solar surface helium abundance Y_S. Typical measured values of Y_S range between 0.242 and 0.255, with some dependence on the helioseismic method employed for its determination [60, 90]. The result $Y_S = 0.2485 \pm 0.0034$ [60] is widely used as a reference value. A wealth of literature has been devoted this topic, but it is well beyond the scope of this book to describe these methods (see [89] for a good review).

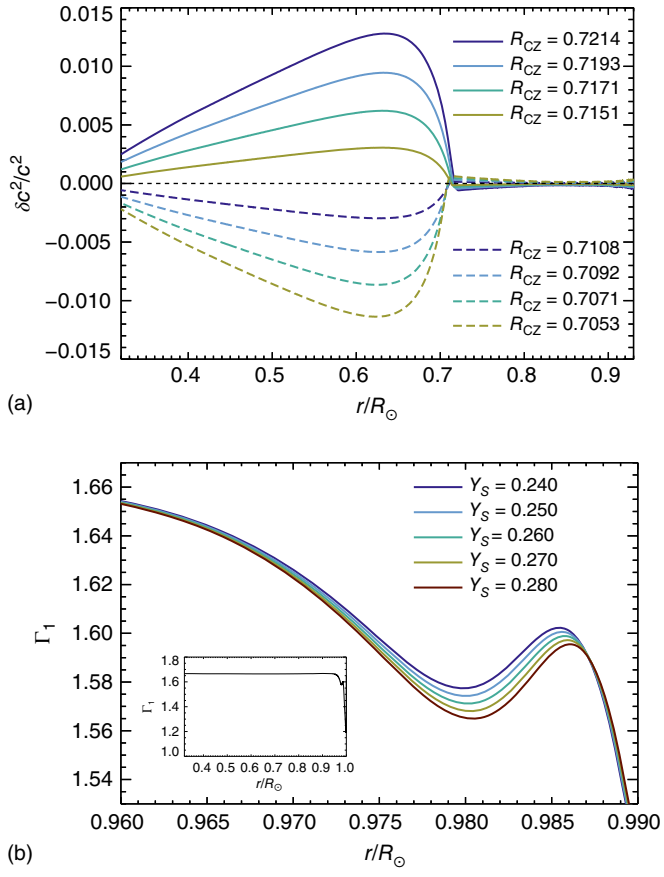

Figure 2.21 (a) Sensitivity of sound speed with respect to the R_{CZ}, the location of the base of the convective envelope. It is illustrated by the fractional c_s^2 differences of solar models with different R_{CZ} values with respect to a solar model with $R_{CZ} = 0.713R_\odot$. (b) Variation of depth of the Γ_1 depression in the HeII region as a function of the helium abundance Y_S of the solar envelope. The inset shows that $\Gamma_1 \simeq 5/3$ in most of the solar interior.

2.7 Solar Abundance Problem

Table 2.4 summarizes some properties of the B16-SSMs. It includes the constraints used in the calibration; results of the calibrated quantities $Y_{\rm ini}$, $Z_{\rm ini}$, and $\alpha_{\rm mlt}$; helioseismic results; and a characterization of the central conditions of the SSM.

The difference between the two SSMs lies only on the use of GS98 or AGSS09 solar surface compositions for the $(Z/X)_\odot$ constraint and in the distribution of metals. CNO elements and Ne are particularly lower in AGSS09 compared to GS98, between 30% and 40% (Table 2.2). As a result, the calibration of the free parameters is affected, and changes in $Y_{\rm ini}$ and $Z_{\rm ini}$ have direct observational consequences that appear in the helioseismic results.

Table 2.4 Summary of properties of B16 SSMs and solar quantities.

	B16-GS98	B16-AGSS09	Solar value
Constraints			
$\tau_\odot$ (Gyr)	4.57	4.57	4.57
$R_\odot$ (10^{10} cm)	6.9598	6.9598	6.9598
$L_\odot$ (10^{33} erg/(cm^2 s))	3.8418	3.8418	3.8418
$(Z/X)_\odot$	0.0229	—	0.0229
$(Z/X)_\odot$	—	0.0178	0.0178
Calibration			
$\alpha_{\rm mlt}$	2.18 ± 0.05	2.11 ± 0.05	—
$Y_{\rm ini}$	0.2718 ± 0.0056	0.2613 ± 0.0055	—
$Z_{\rm ini}$	0.0187 ± 0.0013	0.0149 ± 0.0009	—
Helioseismic results			
Maximum $\delta c_s^2/c_s^2$	0.0042	0.0175	0
$\langle \delta c_s^2/c_s^2 \rangle$	0.0010 ± 0.0008	0.0042 ± 0.0012	0
$R_{\rm CZ}$ ($R_\odot$)	0.712 ± 0.005	0.722 ± 0.005	0.713 ± 0.001
$Y_{\rm S}$	0.2426 ± 0.0059	0.2317 ± 0.0059	0.2485 ± 0.0034
Central conditions			
X_C	0.347	0.362	—
Y_C	0.633	0.622	—
Z_C	0.020	0.016	—
T_C (10^7K)	1.560	1.544	—
ρ_C (g/cm^3)	150.8	148.9	—

The lower metallicity in the B16-AGSS09 model leads to a lower radiative opacity κ in the solar interior. The temperature gradient in the radiative interior: i.e. $r < R_{\rm CZ}$, is proportional to κ. Therefore, a lower metallicity in the model leads to a reduction in the radiative gradient in the B16-AGSS09 compared with that in the B16-GS98 model. This is shown in Figure 2.22, which illustrates the reduction in κ and $\nabla_{\rm rad}$ from the high-Z model to the low-Z model. In both models $\nabla_{\rm ad} = 0.4$, corresponding to a fully ionized gas. Then, the Schwarzschild condition $\nabla_{\rm rad} = \nabla_{\rm ad}$, i.e. the location of $R_{\rm CZ}$, is satisfied at a shallower radius in B16-AGSS09, as also shown in the Figure 2.22. The comparison between SSM predictions and the helioseismic measurement of $R_{\rm CZ}$ shows that B16-GS98 is in agreement with the helioseismic value whereas B16-AGSS09 is not. The shallower $R_{\rm CZ}$ also leads to the discrepancy in the sound speed profile that has been shown in Figure 2.20. The large peak in the $\delta c_s^2/c_s^2$ below the convective envelope present in the B16-AGSS09 model can now be understood by considering the impact on the sound speed profile produced by a mismatch in the $R_{\rm CZ}$ value (Figure 2.21a). The sound speed mismatch is about four times larger for the

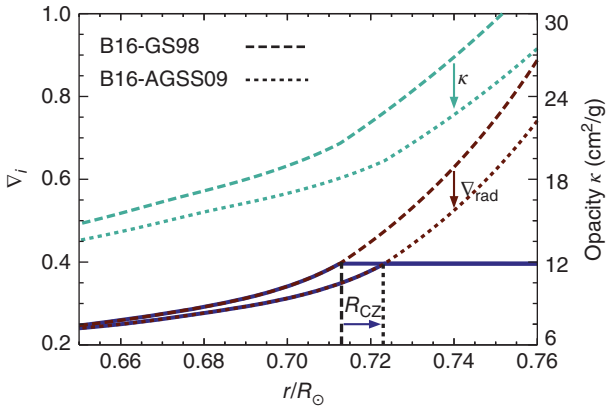

Figure 2.22 Comparison of temperature gradients and opacity in B16-GS98 and B16-AGSS09 SSMs. The decrease in κ, which follows from the lower metallicity corresponding the AGSS09, lowers ∇_{rad} and shifts R_{CZ} toward a shallower position. The solid line shows the actual temperature gradient in the models, which matches ∇_{rad} below R_{CZ} and ∇_{ad} above it (horizontal segment).

B16-AGSS09 model than for B16-GS98, both in its maximum value and its root mean squared difference.

The lower $(Z/X)_\odot$ leads to a decrease in Y_{ini}. This is represented in Eq.(2.73). Physically, it occurs because a lower metallicity produces a solar model with a lower central temperature T_C in B16-AGSS09, by about 1%. The temperature dependence of the pp cycle, dominated by the p + p rate, is about T^4, but nuclear energy must account for $L_\odot$ in both models. Then, the lower temperature in the B16-AGSS09 must be compensated by a larger hydrogen abundance, for which the central value X_C can be considered a proxy. Nuclear energy production through the pp chains scales with the square of the hydrogen abundance, so a 1% lower T is roughly compensated by a ∼2% higher hydrogen mass fraction. More hydrogen implies a lower helium content in the model, i.e. a lower Y_{ini}. Observationally, this has its counterpart in a lower Y_S in the SSM today. The comparison with the helioseismic value in Table 2.4 shows again that B16-GS98 fares much better than B16-AGSS09.

The discrepancy between SSMs that are calibrated using low $(Z/X)_\odot$ abundances such as AGSS09 and the Sun are much larger than those based on a higher solar $(Z/X)_\odot$ such as GS98. Solar abundances determined by AGSS09 are based on qualitatively and quantitatively better solar atmosphere models, better atomic data to account for line strengths in the solar spectrum, detailed atomic physics models to account for departures from local thermodynamic equilibrium. SSMs are based on the best available physical inputs to stellar models. Currently, there is a conflict between our understanding of the physics and radiative transport in solar atmospheres and that of solar interiors. This conflict is a general result, i.e. not restricted to the B16 models, and have been found by all authors working in the topic. There is an extensive literature on this so-called solar abundance, or solar modeling, problem. Some references are [74, 91–97].

What is the solution to the solar abundance problem? There are alternative determinations of solar abundances based on comparable physics as that from AGSS09. Most relevant is the work by the CO^{5}BOLD group [58]. The CNO abundances determined by CO^{5}BOLD are halfway between AGSS09 and GS98, so SSMs calibrated to the CO^{5}BOLD abundances would have a smaller discrepancy when compared to helioseismic diagnostics of the solar properties. Therefore, the robustness of the determination of CNO abundances might be called into question, particularly in the final step of the process: the choice of spectral lines used to determine abundances and the detailed radiative transport used to obtain the synthetic solar spectrum. However, it seems clear that the better physics used in modern spectroscopic analysis rules out with some level of confidence CNO abundances as high as those in the GS98 composition.

Within the framework of SSMs a possible solution to the solar abundance problem is that present-day models of radiative opacity κ_r in the solar interior underestimate the true radiative opacity value. The accurate evaluation of κ_r requires complex atomic models and a detailed account of interactions with the radiation field and stellar plasma. The lower metallicity in SSMs based on the AGSS09 composition leads to a κ_r reduction of about 20% at R_{CZ} compared to models with GS98 composition. This reduction reduces to a few percent toward the solar core. It is possible that current opacity models such as OP or OPAL underestimate the actual opacity by comparable amounts. Only recently, with the first ever experimental results on iron opacity under conditions similar to those at R_{CZ} [34], has there been an empirical check for atomic opacity calculations appropriate for the solar interior. The results obtained with the Z-experiment at Sandia Labs hint at the iron opacities being underestimated theoretical models by about 40%, and when this is propagated into the total Rosseland mean opacity the increase is about 7%. This is not by itself enough to solve the solar abundance problem, but it is certainly a clear indication that opacity models would benefit from a full revision.

At this point, it has to be noted that, albeit the discrepancy between low-Z solar models and helioseismic results arises because of a deficit in the radiative opacity, it is not possible to use these helioseismic diagnostics to determine whether the origin of the problem lies in the low-Z abundances or in that radiative opacity calculations underestimate the true opacity in the Sun. There is an almost complete degeneracy between these two possibilities in helioseismic diagnostics. The same argument applies to solar neutrinos generated in the pp chains. All these quantities are affected by the metal content of the Sun only through their interplay with opacity. The only direct way to break this degeneracy, that is, to have a diagnostics that is directly dependent on the metal content of the Sun is through the measurement of CNO solar neutrinos. In particular, $\Phi(^{13}\mathrm{N})$ and $\Phi(^{15}\mathrm{O})$ can be used for this purpose. In Section 2.5 it was shown that these fluxes show the largest difference between the predicted values by the high- and low-Z SSMs.[9] This is due to the catalyzing role of C and N in the CN-cycle, which leads to a linear dependence of these fluxes on the added C + N abundance. It is possible to relate a hypothetical measurement of any of these fluxes and a precise measurement of $\Phi(^{8}\mathrm{B})$ to the present-day abundance of C + N in the solar core. It has

9 $\Phi(^{17}\mathrm{F})$ has a larger difference but its flux is too low to be measurable in any foreseeable future.

been shown [72, 73] in a semianalytical way that

$$\frac{\Phi(^{13}\mathrm{N})}{\Phi(^{13}\mathrm{N})^{\mathrm{SSM}}} \Big/ \left[\frac{\Phi(^{8}\mathrm{B})}{\Phi(^{8}\mathrm{B})^{\mathrm{SSM}}}\right]^{0.576} = \left[\frac{n_C + n_N}{n_C^{\mathrm{SSM}} + n_N^{\mathrm{SSM}}}\right] \times [1 \pm 0.03(\nu) \pm 0.10(\mathrm{nuc})] \tag{2.89}$$

The interpretation of this relation is that, provided that experimental results for $\Phi(^{13}\mathrm{N})$ and $\Phi(^{8}\mathrm{B})$ are available, they can be scaled to SSM fluxes and the ratio of abundances in the right-hand side of Eq. (2.89) will match the ratio between the actual solar abudance $n_C + n_N$ and the corresponding SSM values. The uncertainties indicated come from uncertainties in current neutrino oscillation parameters and in the uncertainties of nuclear reactions affecting fluxes predictions in SSMs. A similar relation can be obtained for $\Phi(^{15}\mathrm{O})$, with the only difference is that the exponent is 0.785. In the likely case that neutrino experiments measure a combination of both fluxes, it is possible to construct an equivalent relation accounting for any specific experiment [73].

Finally, it has to be kept in mind that SSMs offer a representation of the Sun that is incomplete. Several important phenomena are not included in SSMs that might have an influence in the predicted solar structure and affect the comparison with helioseismic diagnostics. An account of non-SSMs is presented in Section 2.9.

2.8 Uncertainties in SSMs

Results from SSMs are affected by a variety of uncertainties related to the constraints used in the solar calibration and also in the physical inputs such as nuclear reaction rates. The quantification of SSM uncertainties is important to be able to make quantitative statements that involve SSM results such as neutrino fluxes or helioseismic quantities. The problem needs to be separated into two different parts. The first aspect to consider is the determination of uncertainties in each input quantity in solar model calculations and constraints. The second one is how to combine all these uncertainty sources and produce a meaningful assessment of uncertainties in solar model predictions.

2.8.1 Uncertainties in SSM Inputs

2.8.1.1 Nuclear Reaction Rates

The complete list of nuclear reaction rates entering the calculation of SSMs is listed in Table 2.1. Not all nuclear reaction rates have a direct impact on properties of solar models that can be measured. An example is $\mathrm{D}(\mathrm{p},\gamma)^3\mathrm{He}$. The production of ^{3}He depends on this reaction, but its rate is many orders of magnitude larger than the rate of any of the two reactions that produce D such that ^{3}He production can be considered to follow immediately after either of the $\mathrm{p}(\mathrm{p}, e^+\nu_e)\mathrm{d}$ or the $\mathrm{p}(\mathrm{p}e^-, \nu_e)\mathrm{d}$ reactions occur, regardless of the actual $\mathrm{D}(\mathrm{p},\gamma)^3\mathrm{He}$ rate. After this type of considerations is applied to all nuclear reactions, the ones that have a measurable impact in the solar structure and/or solar neutrino production are seven. The corresponding astrophysical factors are identified here

with subindices: p(p, $e^+\nu_e$)d (S_{11}), ^{3}He(^{3}He, 2p)^{4}He (S_{33}), ^{3}He(4He, γ)^{7}Be (S_{34}), ^{7}Be (p, γ)^{8}B (S_{17}), ^{7}Be (e^-, ν_e)^{7}Li (S_{e7}), ^{14}N(p, γ)^{15}O (S_{114}), and ^{3}He (p, $\nu_e e^+$)^{4}He ($S_{\rm hep}$). All uncertainties at the 1σ level are listed in Table 2.1, except for S_{e7}, for which it is 2%. The rate of ^{16}O(p, γ)^{17}F (S_{116}) can also be included in the list if it is necessary to have a proper assessment of $\Phi(^{17}\mathrm{F})$.

2.8.1.2 Microscopic Diffusion

The uncertainty in the microscopic diffusion rate for all elements cannot be computed from first principles nor tested experimentally. It is estimated by considering results from different authors that compute the binary collision rates between nuclear species under different assumptions. Based on this approach, the uncertainty is considered to be 15% at 1σ.

2.8.1.3 Radiative Opacities

Atomic opacity calculations do not include a determination of uncertainties. Here, a possible approach is to compare two independent sets of opacities, for example, OPAL and OP, obtained for the same composition and along a $T - \rho$ profile corresponding to a solar model. Such a comparison yields differences not larger than 3% in the radiative solar interior. However, based on the results of the Z-facility experiment on iron opacity that hints at a 7% increase of the radiative opacity at $R_{\rm CZ}$, this seems to underestimate the true uncertainty. Current B16 SSMs use an opacity uncertainty that increases linearly from 2% at the solar center up to 7% at $R_{\rm CZ}$, all at a 1σ level. But this is an ad hoc assumption, based on current knowledge as much as possible, but that could be very well underestimating the true uncertainty.

2.8.1.4 Solar Radius, Luminosity, and Age

The uncertainty in solar radius is very small and has a negligible impact in solar models, especially regarding solar neutrino predictions. The uncertainty in the solar luminosity is 0.4% and it is simply of experimental origin. For the age, the value is also 0.4% at 1σ, and it represents a dispersion from individual determinations as well as uncertainties related to the very early phases of the solar system formation.

2.8.1.5 Solar Composition

Individual elements need to be considered on a one-by-one basis. Current uncertainties are those provided by the spectroscopic analysis. In the light of the solar abundance problem, it is apparent that quoted errors are smaller than differences between central values of high- and low-Z solar metallicities. This could call into question the validity of the spectroscopic uncertainties. It is preferred, however, to consider SSMs based on the high-Z or the low-Z compositions as two different groups of solar models and adopt the spectroscopic uncertainties as the actual uncertainties. Out of all the elements listed in Table 2.2, only C, N, O, Ne, Mg, Si, S, Ar, and Fe need to be considered as relevant sources of uncertainty for SSMs. This is because other elements have low abundances that, when combined with their uncertainties, produce negligible variations in the opacity profile and thus do not alter SSM predictions at a measurable level.

2.8.1.6 Equation of State

The EoS is very well known for solar interiors and is not usually considered a meaningful source of uncertainty, except maybe in the case of the determination of the solar surface helium abundance with helioseismic techniques.

2.8.2 Global Uncertainties in SSMs

Two different methods have been used to compute the resulting global uncertainties in SSMs starting from the 20 individual sources listed in the Section 2.8.1. The first method is based on treating all sources individually. In this approach, a given input paramter p_j is varied and an SSM is recalibrated with the varied value. If variations in p_j are not large, the response of the SSM will be linear. In fact, a power law expression describes the SSM response very well, especially for solar neutrino fluxes. This can be expressed as a logarithmic derivative such as

$$\frac{\partial \log \Phi_i}{\partial \log p_j} = \alpha_{ij} \tag{2.90}$$

where α_{ij} is the power-law exponent. In practice, α_{ij} can be computed from a set of SSMs calibrated with different values of p_j around the value $p_j(0)$. From this,

$$\Phi_i = \Phi_i(0)\left[\frac{p_j}{p_j(0)}\right]^{\alpha_{ij}} \tag{2.91}$$

The exponents α_{ij} represent the physical response of the SSM to a change in the input parameters and thus are quantities that are to first order constant, i.e. independent of the reference SSM or reference $p_j(0)$ values. As a result, the dependence of observables on input parameters can be considered as the product:

$$\Phi_i = \Phi_i(0)\prod_j \left[\frac{p_j}{p_j(0)}\right]^{\alpha_{ij}} \tag{2.92}$$

where the product extends over the complete set of input parameters j. Under this approximation, the total uncertainty of neutrino fluxes can be obtained by generating probability distribution functions for each parameter p and computing resulting distribution for Φ_i using Eq. (2.92). This type of expressions was initially developed in [98] and has been widely used in the literature. The same procedure can be applied to all helioseismic quantities of interest such as R_{CZ} or Y_S, or the sound speed at a given depth r. Examples of power-law expansions are

$$\Phi(\mathrm{pp}) = \Phi_0(\mathrm{pp}) \times \left(S_{11}^{0.09}\, S_{33}^{0.03}\, S_{34}^{-0.06}\, \tau_\odot^{0.09}\, D^{-0.01}\, L_\odot^{0.82}\, \kappa^{-0.08}\right.$$
$$\left. \mathrm{C}^{-0.004}\, \mathrm{O}^{-0.005}\, \mathrm{Ne}^{-0.004}\, \mathrm{Si}^{-0.012}\, \mathrm{S}^{-0.007}\, \mathrm{Fe}^{-0.019}\right) \tag{2.93}$$

$$\Phi(^8\mathrm{B}) = \Phi_0(^8\mathrm{B}) \times \left(S_{11}^{-2.71}\, S_{33}^{-0.43}\, S_{34}^{0.86}\, S_{e7}^{-1.00}\, S_{17}^{1.03}\, \tau_\odot^{1.37}\, D^{0.28}\right.$$
$$\left. L_\odot^{7.05}\, \kappa^{2.86}\, \mathrm{O}^{0.11}\, \mathrm{Ne}^{0.09}\, \mathrm{Mg}^{0.12}\, \mathrm{Si}^{0.20}\, \mathrm{S}^{0.14}\, \mathrm{Fe}^{0.51}\right) \tag{2.94}$$

$$\Phi(^{15}\mathrm{O}) = \Phi_0(^{15}\mathrm{O}) \times \left(S_{11}^{-2.94}\, S_{34}^{-0.04}\, S_{114}^{1.05}\, \tau_\odot^{1.30}\, D^{0.39}\, L_\odot^{6.00}\, \kappa^{2.22}\right.$$
$$\left. \mathrm{C}^{0.82}\, \mathrm{N}^{0.21}\, \mathrm{O}^{0.09}\, \mathrm{Ne}^{0.06}\, \mathrm{Mg}^{0.09}\, \mathrm{Si}^{0.15}\, \mathrm{S}^{0.11}\, \mathrm{Fe}^{0.39}\right) \tag{2.95}$$

These expressions offer a very flexible tool to analyze the impact of input parameters because the contribution of each input parameter to SSM predictions can be considered separately. Moreover, once the α_{ij} coefficients are known, it is not necessary to perform any SSM calibration, and these coefficients are provided in the literature, e.g. a complete set of α_{ij} can be found in [66]. Power-law expansions also allow a simple way of studying correlations among SSM predictions without the need to compute any SSM.

There is an alternative approach to modeling global SSM uncertainties based on Monte Carlo simulations of SSMs. This approach is more formally correct than power-law expansions, which are justified only as long as uncertainties in the input parameters are not large and logarithmic perturbations can be linearly added. While this is usually the situation, there are cases in which the assumption of small input uncertainties might not be entirely justified. In particular, the 1σ uncertainties of O and Ne are 0.06 and 0.10 dex, i.e. 15% and 26% respectively. It is not guaranteed that variations in these parameters will propagate linearly into SSM results. The validity that the α_{ij} coefficients are constant breaks down if input paramters deviate by a large fraction from the reference values. Therefore, under some conditions, the power-law expansions need to be replaced by a more general method. This can be achieved by performing large sets calculations in which all input parameters are varied simultaneously and SSMs are calibrated for the varied parameters. The first set of this class of Monte Carlo simulations was carried out with 1000 SSMs [99]. Modern versions are based on sets with 10 000 models [66]. The advantage of the Monte Carlo approach is that nonlinearities in the SSM response are accounted for by construction. They can arise from a large variation range for a given parameter or by the cummulative effect of several input parameters. Monte Carlo simulations allow for a thorough determination of uncertainties and correlations in SSM predictions. The disadvantage over the power-law approach is that it requires calibrating a very large set of SSMs and it is thus computationally very expensive. Fortunately, power-law expansions are, for most practical purposes, accurate enough.

Which are the dominant sources of uncertainty in SSMs? This is summarized in Table 2.5 for all neutrino fluxes as well as for R_{CZ} and Y_S where, for each quantity, the five dominant uncertainty sources are listed with their respective contribution. This type of information is relevant because it allows to identify possibilities for improvement in solar models. Three classes of sources can be identified.

2.8.2.1 Nuclear Reaction Rates

A direct example is given by nuclear rate uncertainties, such as S_{34} for $\Phi(^7\mathrm{Be})$, S_{114} for $\Phi(^{13}\mathrm{N})$, and $\Phi(^{15}\mathrm{O})$, or S_{17} for $\Phi(^8\mathrm{B})$, for which more precise experimental determinations are required to improve SSM predictions.

2.8.2.2 Constitutive Physics

Among the constitutive physics, a difficulty arises because κ and the microscopic diffusion rates are important sources of uncertainty for several observables. Improved opacity calculations, preferrably constrained by experimental data, will be required to reduce the impact of opacity uncertainties in SSMs. In relation to microscopic diffusion, the problem is even more complex because it

Table 2.5 Dominant theoretical error sources for neutrino fluxes and the main characteristics of the SSM.

Quantity	Dominant theoretical error sources (%)							
Φ(pp)	$L_\odot$:	0.3	S_{34}:	0.3	κ:	0.2	Diff:	0.2
Φ(pep)	κ:	0.5	$L_\odot$:	0.4	S_{34}:	0.4	S_{11}:	0.2
Φ(hep)	S_{hep}:	30.2	S_{33}:	2.4	κ:	1.1	Diff:	0.5
$\Phi(^7\text{Be})$	S_{34}:	4.1	κ:	3.8	S_{33}:	2.3	Diff:	1.9
$\Phi(^8\text{B})$	κ:	7.3	S_{17}:	4.8	Diff:	4.0	S_{34}:	3.9
$\Phi(^{13}\text{N})$	C:	10.0	S_{114}:	5.4	Diff:	4.8	κ:	3.9
$\Phi(^{15}\text{O})$	C:	9.4	S_{114}:	7.9	Diff:	5.6	κ:	5.5
$\Phi(^{17}\text{F})$	O:	12.6	S_{116}:	8.8	κ:	6.0	Diff:	6.0
Y_S	κ:	2.2	Diff:	1.1	Ne:	0.6	O:	0.3
R_{CZ}	κ:	0.6	O:	0.3	Diff:	0.3	Ne:	0.2

is not possible to perform experiments and its efficiency in the Sun is also linked to other physical processes that are not included in SSM calculations. Some of these processes are presented in Section 2.9, which includes a summary of non-SSMs.

2.8.2.3 Element Abundances

Carbon and oxygen are relevant uncertainty sources for the neutrino fluxes in the CNO-bicycle. In the case of C, its abundance, added to that of N, catalyzed the CN-cycle and $\Phi(^{13}\text{N})$ and $\Phi(^{15}\text{O})$ depend almost linearly on the added abundance of C and N. Oxygen dominates the uncertainty of $\Phi(^{17}\text{F})$ because its abundance determines the efficiency of the $^{16}\text{O}(\text{p}, \gamma)^{17}\text{F}$ reaction. For helioseismic quantities, O and Ne are important through their contribution to the opacity, particularly at the base of the convective zone (see Figure 2.4).

2.9 Solar Models Beyond the SSM

The SSM provides a description of the solar interior that is accurate, as reflected by the level of agreement with helioseismic diagnostics of solar interior properties and solar neutrino fluxes. The solar abundance problem might be an indication of the limitations of the framework defined by SSMs, but it might have a solution within this framework as well if, for example, new calculations show that the radiative opacities currently used in solar models underestimate the true opacity in the solar interior.

But there are still strong motivations for considering solar models beyond the framework defined by SSMs. First, SSMs are based on a simplified physical description of the Sun. Some of the simplifications adopted are spherical symmetry, neglect of rotation and magnetic fields, and modeling of convection.

Second, the sheer size of the Sun, the conditions at the solar interior that cannot be reproduced in terrestrial laboratories, and the tight constraints imposed by solar neutrino fluxes and helioseismology on our knowledge of the solar properties set the scene for using the Sun as a laboratory for particle physics. It is not possible to present a full account of all non-SSMs in this book, but some cases are discussed below.

2.9.1 Nonstandard Solar Physics

Among the well-known limitations of SSMs is the neglect of rotation. The solar surface rotates at the equator with a period of about 24.5 days and a longer period around 28 days at the poles. Using the rotational splittings of (n, ℓ) multiplets, helioseismic analysis has shown that the convective envelope sustains this differential rotation. The radiative interior, on the contrary, rotates as a rigid body at least down to $r/R_\odot \approx 0.2$, the region over which rotation can be probed in detail with p-modes [100]. There are also suggestions that the solar core rotates about four times faster [101]. The rotation rate is low and centrifugal forces in the solar interior are always negligible compared to the local gravity. But rotation induces meridional circulation in the solar interior. These are slow currents that transport angular momentum and chemicals, affecting the solar structure. Global timescales linked to meridional circulation are of the order of 10^{12} year, much larger than $\tau_\odot$, but it is still possible that they produce measurable changes in helioseismic tests or in the predicted solar neutrino fluxes.

Solar evolutionary models that include the effects of rotation and other dynamical effects in simplified and parametrized ways have been developed for a long time [102–104]. Given that the SSM reproduces well the available helioseismic diagnostics and solar neutrino results, the changes in the solar structure induced by rotation cannot be large. But this class of models is necessary to understand primarily the evolution of angular momentum in the solar interior. Rotating solar models are usually constructed such that they reproduce the average surface rotation velocity of 2 km/s, but the rigid body rotation in the radiative interior poses a serious challenge to the models. Without exception, all rotating solar models lead to a present-day rotation radial profile in which the solar radiative interior rotates differentially and at much larger angular velocities than determined from helioseismology [104]. A fundamental textbook dedicated to stellar models and rotation, including the Sun, is [5]. A more formal theoretical presentation of rotating stars is the classical reference [105].

An additional important problem with SSMs is the lithium depletion observed in the Sun. The lithium in the solar photosphere today is $\log \varepsilon_{\rm Li} = 1.05 \pm 0.10$ but the abundance in primitive meteorites is $\log \varepsilon_{\rm Li} = 3.26 \pm 0.05$ [57]. Lithium has been depleted in the Sun by more than a factor of 100 with respect to the primordial solar system value. SSMs however predict a much smaller lithium depletion factor because the temperature at the base of the convective envelope is too low to burn lithium efficiently. SSMs cannot reproduce the observed abundance. Lithium depletion can be explained if there is an additional mixing process that brings the convective envelope into contact with deeper regions where the temperature is about 3×10^6 K, high enough to burn lithium [106, 107].

Phenomenologically, this can be achieved by introducing a mixing diffusive coefficient D_x, below the convective envelope, and extending the application of Eq. (2.24) such that below the convective envelope:

$$\left(\frac{\partial X_i}{\partial t}\right)_x = \frac{\partial}{\partial m}\left((4\pi r^2\rho)^2 D_x \frac{\partial X_i}{\partial m}\right) \tag{2.96}$$

Several authors have proposed physical processes that can induce the needed extra mixing and provided parametrizations for D_x and calibrations on its efficiency by forcing models to reproduce the observed lithium depletion. Two different parametrizations of the diffusion coefficient are given here as examples. For overshooting [106], that is, penetration of convective bubbles beyond the formal boundary set of the Schwarzschild criterion (Eq. (2.17)):

$$D_{\rm ov}(r) = D_c \exp\left[\frac{-2(|R_{\rm CZ} - r|)}{fH_p}\right] \tag{2.97}$$

where D_c is the diffusion coefficient in the convective envelope and the overshooting mixing efficiency decays exponentially with the distance from $R_{\rm CZ}$ over a distance scale that is controled by the free parameter f. Another proposed mechanism is related to extra mixing linked to turbulence generated by shear occuring at the interface between the convective envelope and the radiative interior, a region known as the tachocline. Here, the diffusion coefficient is parametrized as [108]:

$$D_t = D_0\left(\frac{\rho}{\rho_{\rm CM}}\right)^{-3} \tag{2.98}$$

Here, the diffusion coefficient decays toward the radiative interior with the cube power of ρ and D_0 is a free parameter that sets the overall efficiency of the extra mixing and, as f in the case of overshooting, is calibrated to reproduce the lithium depletion. Figure 2.23 shows the lithium profiles for an SSM and solar models

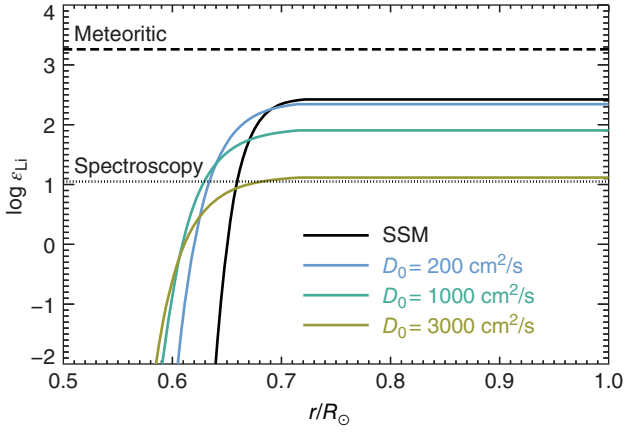

Figure 2.23 Lithium depletion in solar models of increasing amount of turbulent mixing. The dashed and dotted lines denote the initial lithium abundance in the solar system and the present-day photospheric value, respectively.

including turbulent mixing for different D_0 values. The SSM reduces the initial meteoritic value by less than one order of magnitude. By increasing D_0 more lithium is depleted, and for $D_0 = 3000$ cm^2/s solar models match the lithium abundance observed today in the solar photosphere. The physical process that is responsible for this extra mixing has not been identified unequivocally and, much less, understood in a quantitative way.

A qualitative step forward in solar modeling requires an approach different from what 1D solar models, standard or nonstandard, provide. It is necessary to resort to sophisticated multidimensional simulations, tailored to tackle specific problems. One example is that of 3D-RHD models of the solar atmosphere and near-surface convection mentioned in connection to spectroscopic abundances (see Section 2.3.1.2). Deeper in the Sun, spatial and temporal scales become larger and longer, and the need for global models also becomes mandatory. The coupling between the convective envelope and the radiative interior, the generation of magnetic fields, transport of angular momentum, stochastic generation of internal gravity waves are all problems that require this type of hydrodynamic and magnetohydrodynamic simulations. Such simulations can cover only a very short period of time compared to solar evolution, and it cannot be expected that anytime in the midterm future the complete evolution of the Sun can be computed with such type of simulations. Instead, what this class of simulations can offer is a detailed understanding of physical phenomena and guide the way toward phenomenological models that can be implemented in solar evolutionary calculations as nonstandard extensions of SSMs. Interesing references in this line of research are [109–111]).

2.9.2 Nonstandard Particle Physics

A very important motivation for considering nonstandard solar models has its origin in the realm of particle physics.

In a series of works, [112–115] considered the possibility that the Sun, during its motion through the Milky Way and its dark matter halo, could accrete weakly interacting massive particles (WIMPs) that would constitute the galactic dark matter. These hypothesized particles, with masses of the order of a few giga electron volts and interacting with baryonic matter only very weakly, would thermalize and move in bounded orbits in the solar core. Then, with a very low probability, they would scatter from time to time to outer regions of the Sun, carrying away thermal energy from the hotter solar core to the cooler outer regions, providing an additional energy transport mechanism to radiative transport by photons. At that time, this class of models was considered as a possible solution to the solar neutrino problem. The effect of WIMPs would be to lower the solar core temperature in comparison to SSMs, and a few percent reduction would then lead a much larger change in the $\Phi(^8\mathrm{B})$ predicted by models, bringing it into agreement with results from the radiochemical experiments available at the time.

Non-SSMs can be constructed to include such effects by including an extra term in the equation of conservation of energy, as in Eq. (2.43c):

$$\frac{\partial l}{\partial m} = \varepsilon_{\mathrm{nuc}} - \varepsilon_{\nu} + \varepsilon_{\mathrm{eg}} + \varepsilon_{x} \tag{2.99}$$

Here, ε_x represents a generic energy source or sink, depending on whether it is positive or negative. The specific form of ε_x is determined by which class of exotic particles is considered. Consider for example the case of asymmetric dark matter massive particles (ADM), which do not self-annihilate. In this case, ADM will contribute to the energy transport as discussed above but will not have a net contribution to the energetics of the Sun. ADMs will extract energy from the solar core, i.e. $\varepsilon_x < 0$ in those regions, and will deposit it in outer layers, where $\varepsilon_x > 0$, with the additional constraint that $\int_{\rm sun} \varepsilon_x {\rm d}m = 0$. This constraint is dropped when DM particles self-annihilate or they can escape from the Sun if their scattering velocity is larger than the escape velocity and mean free path is large enough.

Still, the specific form of ε_x depends on the properties of the ADM particles and the type of interaction with baryons that is assumed. Recent works providing a detailed account of implementation of energy transport in the Sun by massive dark matter particles are [116–118]. A typical application of this class of models consists in computing solar models that include dark matter effects across the parameter space that defines the particle properties, typically mass and cross section. These non-SSMs are calibrated in the same manner as SSMs, and their predictions, solar neutrinos and helioseismic diagnostics, are compared with the available data. In this way, limits to the particle properties can be placed based on solar constraints.

The appeal of using that Sun for this type of tests is that their sensitivity is higher under conditions different than those of terrestrial experiments. ADMs offer again a good example. If ADMs form the galactic halo of cold dark matter, the Sun will preferentially accrete those with the lowest relative velocity with respect to the Sun. Contrary to this, terrestrial experiments for direct detection of dark matter are based on techniques, e.g. measuring the recoil energies of the active matter in the detector, that are more sensitive to the high velocity tail of the dark matter velocity distribution in the Milky Way.

Another intersting application of solar models to particle physics is related to low mass weakly interacting particles that can be produced thermally in the solar core. A good example is that of axions, a light pseudoscalar particle introduced to solve the strong CP problem. Depending on the models, axions can couple with photons (hadronic axions) or electrons [119] and are candidate particles for dark matter. Axions, or more generically axion-like particles (ALPs), can be produced thermally and then stream away unimpeded, much as neutrinos do. In the hadronic model, axions are produced by the Primakov effect and the energy loss rate by axions in the Sun is given by [120]:

$$\varepsilon_{a\gamma} = \frac{g_{a\gamma}^2}{4\pi} \frac{T^6}{\rho} F(\lambda^2) \tag{2.100}$$

where F is a smooth function of the chemical composition, $g_{a\gamma}$ is the unknown coupling constant between axions and photons. A solar model modified in this way still has to produce the observed solar luminosity $L_\odot$. Then,

$$\int_{\rm sun} (\varepsilon_{\rm nuc} - \varepsilon_\nu + \varepsilon_{\rm eg} - \varepsilon_{a\gamma}) {\rm d}m = L_\odot \tag{2.101}$$

The negative sign in the last term has been added because $\varepsilon_{a\gamma}$ has been defined as a positive quantity in Eq. (2.100) but it is an energy sink for the Sun. Such model is also very close to hydrostatic equilibrium, in the same way as SSMs are. Then, $\varepsilon_{\rm gr} \simeq 0$. Comparing the integral above with the SSM case, it is concluded that

$$\int_{\rm sun,axions} (\varepsilon_{\rm nuc} - \varepsilon_\nu) {\rm d}m > \int_{\rm sun,ssm} (\varepsilon_{\rm nuc} - \varepsilon_\nu) {\rm d}m \tag{2.102}$$

Neutrino losses are those from nuclear reactions in the pp chains (and marginally from the CNO-bicycle), so they are to a very good approximation proportional to $\varepsilon_{\rm nuc}$, which leads to the final conclusion that including an extra energy loss in solar models must be compensated by an increase in the production of nuclear energy. This argument is general to any free streaming light particle produced in the solar interior.

The origin of the solar luminosity and how much energy is being produced by nuclear reactions in the Sun today can be answered by solar neutrino experiments. This is summarized by Eq. (2.79), which shows that the nuclear energy production, as measured by neutrino experiments, is consistent with the solar luminosity. Therefore, solar neutrino experiments alone constrain energy losses not accounted for in SSMs such as those from axions or other ALPs to be smaller than 8% (at 1σ) of $L_\odot$. That is, the left-hand side in Eq. (2.102) cannot exceed the right-hand side by more than 8%. This limit is improved when helioseismic constraints are used to compare predictions of non-SSMs. In this case, and depending on the specific ALP considered [121, 122]:

$$\frac{\int_{\rm sun} \varepsilon_{\rm ALP} {\rm d}m}{L_\odot} \leq 0.02 - 0.03 \tag{2.103}$$

Further improvements in this limit will require new solar neutrino experiments that can measure the pp neutrino flux to about 1% at a 1σ level or better. This is a challenging task, as discussed in Chapters 4 and 5 of this book.

3

Neutrino Physics

In this chapter we give a brief overview about the status of neutrino physics today. We will start with an introduction of neutrinos in the standard model of elementary particles. Then we will see how neutrino oscillations are motivated theoretically and we derive the most important oscillation formulas including matter effects, which play an important role especially for solar neutrinos. Finally, the leading experiments on neutrino physics will be described and their results are reconsidered within the theoretical framework derived beforehand. We close the chapter discussing about open questions in neutrino physics and possible ways to answer them in the future.

3.1 Neutrinos in the Standard Model

We know two types of elementary particles, which build up matter in the standard model of particle physics: quarks and leptons. Both are fermions with spin 1/2[1] and they show up in three so-called families or flavors as shown in Table 3.1.

Every particle has its antiparticle, which is not shown here. The forces between quarks and leptons are conveyed by spin 1 bosons. These exchange bosons are photons for electromagnetic interactions; W^+, W^-, and Z^0 bosons for weak interactions; and gluons for strong interactions. The neutral Higgs boson H^0 (spin 0) has couplings to the bosons and fermions as well, causing them to acquire mass.

Quarks do not exist as free particles; they rather appear in bound states of three quarks (baryons) or quark–antiquark pairs (mesons). Baryons and mesons form together the group of hadrons. The up- and down-quarks are constituents of the well-known proton and neutron, the lightest baryonic states, which build up the nuclei of the atoms. The proton is the only hadron, which is known to be stable[2] with a lifetime, at the level of the present sensitivity, greater than the order of 10^{34} years (the age of the universe is of the order of 10^{10} years).

Three active neutrino flavors exist in the standard model of particle physics. This three flavor nature of elementary particle has been determined experimentally from the Z^0-width measurement at the large electron positron (LEP) collider at CERN, where the number of light neutrinos (with masses $mc^2 < 45$ GeV)

1 In this chapter we use natural units, i.e. $c \to 1$ and $h \to 1$.
2 On the contrary, free neutrons decay via weak interaction; only neutrons bound in nuclei can be stable.

Solar Neutrino Physics: The Interplay between Particle Physics and Astronomy,
First Edition. Lothar Oberauer, Aldo Ianni, and Aldo Serenelli.

Table 3.1 Elementary particles in the standard model.

Quarks			
$q = +2/3e$	**u**	**c**	**t**
	up	charm	top
$q = -1/3e$	**d**	**s**	**b**
	down	strange	bottom
Leptons			
$q = 0$	ν_e	ν_μ	ν_τ
	$e-$ neutrino	$\mu-$ neutrino	$\tau-$ neutrino
$q = -e$	e	μ	τ
	electron	muon	τ

a) The three flavor structures of quarks and leptons and their electric charges are shown. Neutrinos are neutral and underlie only weak interactions. Not shown are the antiparticles.

was determined to be $N_\nu = (2.9840 \pm 0.0082)$ [123]. In addition all three neutrino flavors have been detected directly in charged current (cc) weak interactions of the type $\nu_\alpha + X \rightarrow \alpha + Y$, where α is either a charged electron, muon, or τ-lepton ($\alpha = e, \mu, \tau$) and X, Y are some hadronic states. For instance, the very first direct neutrino detection by F. Reines and C. Cowan in 1956 succeeded via the so-called inverse β decay $\overline{\nu}_e + p \rightarrow e^+ + n$ [124], after the neutrino was postulated by W. Pauli in 1930 as an almost desperate attempt to rescue energy and angular momentum conservation in nuclear physics (see, e.g. [125]). In the experiment of Reines and Cowan, a nuclear reactor was used as an intensive antineutrino source and the feature of the experiment was the detection of the positron and the neutron in a delayed coincidence measurement. With this newly developed technique, the background rate due to radioactive elements in detector materials and cosmogenic generated signals could be lowered to acceptable levels. The first experimental evidence of neutrino detection was awarded the Nobel Prize in 1995 [126].

Neutrinos are unique among elementary particles as they do not carry an electric charge. As neutral leptons, neutrinos only undergo weak interaction (we neglect the forces of gravity here). Generally, leptons are described in the standard model in the frame of SU(2) × U(1) group theory. Lepton families can be arranged in so-called left- and right-handed (index l, r) isospin groups. For instance, we can write down for the electron and electron neutrino (ν_e):

$$\begin{pmatrix} \nu_e \\ e \end{pmatrix}_l \quad I = \frac{1}{2}; \quad \begin{matrix} I_3 = +\frac{1}{2} & Q = 0 \\ I_3 = -\frac{1}{2} & Q = -1 \end{matrix};$$

$$(e)_r \quad I = 0; \quad Q = -1$$

Left-handed leptons are grouped in doublets, the right-handed charged leptons in singlets. The same structure holds for muon and τ-leptons, which will be discussed below.

How are left- and right-handed neutrinos states described in quantum physics? The wave function ψ of a spin 1/2 fermion is obtained by solving the Dirac equation:

$$(i\gamma_\mu \partial^\mu - m)\psi = 0 \tag{3.1}$$

where ψ is a four-component spinor and γ_μ are the 4×4 Dirac matrices. One may use the Dirac representation:

$$\gamma_0 = \begin{pmatrix} I & 0 \\ 0 & -I \end{pmatrix} \quad \gamma_k = \begin{pmatrix} 0 & \sigma_k \\ -\sigma_k & 0 \end{pmatrix} \tag{3.2}$$

where I is the identity matrix and σ_k ($k = x, y, z$) are the two-dimensional Pauli matrices:

$$\sigma_x = \begin{pmatrix} 0 & 1 \\ 1 & 0 \end{pmatrix} \quad \sigma_y = \begin{pmatrix} 0 & -i \\ i & 0 \end{pmatrix} \quad \sigma_z = \begin{pmatrix} 1 & 0 \\ 0 & -1 \end{pmatrix} \tag{3.3}$$

The solutions are plane wave functions with

$$\psi(x) \propto \begin{pmatrix} \hat{u} \\ (\eta\sigma)\hat{u} \end{pmatrix} \mathrm{e}^{-ipx} + \begin{pmatrix} (\eta\sigma)\hat{v} \\ \hat{v} \end{pmatrix} \mathrm{e}^{+ipx} \tag{3.4}$$

with the four momentum vectors $p = (E, \mathbf{p})$, the four space–time vectors $x = (t, \mathbf{x})$, $E = \sqrt{p^2 + m^2}$, and $\eta = \mathbf{p}/E + m$.[3]

The first and second terms are describing positive and negative energy states, respectively. The first is interpreted as the particle state, and the second corresponds to the antiparticle state. The spin direction is given by the normalized two-component spinors $\hat{u}$ and $\hat{v}$.

The wave function can be written as sum of a left-handed state and a right-handed state:

$$\psi = \psi_l + \psi_r \tag{3.5}$$

with

$$\psi_{l,r} = \frac{1 \mp \gamma_5}{2} \cdot \psi \tag{3.6}$$

where $\gamma_5 = \begin{pmatrix} 0 & I \\ I & 0 \end{pmatrix}$.

In the case of massless particles, like neutrinos in the standard model, left- or right-handedness is equivalent to the definition of helicity $h := \mathbf{sp}/|\mathbf{sp}| = \pm 1$, which measures the projection of the spin to the momentum vector of a particle. In this sense right- and left-handedness means parallel and antiparallel adjustment of the spin to the momentum.

Left-handed leptons form isospin doublets $I = 1/2$ with the isospin components $I_3 = \pm 1/2$, and the charged right-handed particles in addition to isospin singlets. Right-handed neutrinos do not exist in the standard model.[4] This is the consequence of maximal violation of parity conservation in cc weak interaction.

---

3 In this chapter three-dimensional vectors are described in bold characters.

4 In contrary antineutrinos only exist as right-handed states.

The nonexistence of right-handed neutrinos implies that neutrinos are massless in the standard model of particle physics. With the definition of a hypercharge Y as $Y = 2(Q - I_3)$, one obtains

$$Y\begin{pmatrix}\nu_e\\ e\end{pmatrix}_l = -1 \quad Y(e)_r = -2 \tag{3.7}$$

cc weak interaction occurs only within the isospin doublets with constant hypercharge Y. This implies conservation of the lepton number L, which is defined to be $L = +1$ for all left-handed leptons and $L = -1$ for its antiparticles. In addition there exists individual lepton number conservation for each lepton family. Quarks are particles that do not carry lepton number, i.e. $L = 0$ for all quarks. Lepton number conservation has consequences for weak processes. For instance, consider the following weak decays, which are all allowed kinematically but separated between lepton number conserving and violating processes:

$$\begin{aligned}
\text{Muon decay:}\quad & \mu^- \to e^- + \overline{\nu}_e + \nu_\mu \qquad \text{allowed}\\
& \mu^- \to e^- + \gamma \qquad \text{not allowed}\\
\text{Neutron } (\beta) \text{ decay:}\quad & n \to p + e^- + \overline{\nu}_e \qquad \text{allowed}\\
& n \to p + e^- \qquad \text{not allowed}\\
\text{Double } \beta \text{ decay:}\quad & (A,Z) \to (A,Z+2) + 2e^- + 2\overline{\nu}_e \qquad \text{allowed}\\
& (A,Z) \to (A,Z+2) + 2e^- \qquad \text{not allowed}
\end{aligned}$$

Here, (A, Z) denotes a nucleus with atomic number A and Z protons. The search for lepton number violating processes like the radiative μ-decay is a lively and an important sector in subatomic physics today. So far, no violation of the global lepton number has been observed. However, within the standard model also individual lepton number should be preserved, and neutrino flavor transitions like $\nu_e \to \nu_\mu$ as they occur in neutrino oscillations[5] are forbidden as well.

The weak exchange bosons $W^\pm$ and Z^0 carry hypercharge Y as the leptons do, and the fundamental neutrino couplings to the charged and neutral bosons can be depicted as shown in Figure 3.1.

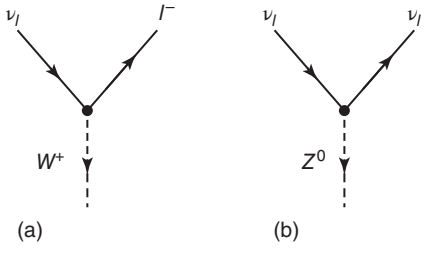

Figure 3.1 Fundamental couplings of neutrinos. The index l stands for a specific lepton family, i.e. $l = e, \mu, \tau$. (a) cc reaction, (b) nc reaction.

5 For description of ν-oscillations, see below.

Neutrino interactions are described within the unified electroweak theory of Glashow, Weinberg, and Salam. The general Lagrange density function[6] is written as:

$$\mathcal{L} = \frac{g}{\sqrt{2}}(J_\mu^- W_\mu^- + J_\mu^+ W_\mu^+) + \frac{g}{\cos\theta_W}(J_\mu^3 - \sin^2\theta_W J_{e,m})Z_\mu + g\sin\theta_W J_{e,m} A_\mu \tag{3.8}$$

with the weak $W_\mu^\pm$, Z_μ, and electromagnetic A_μ gauge currents, the weak coupling constant g, and the Weinberg angle θ_W, which links the electromagnetic and weak coupling constants e and g via

$$e = g\sin\theta_W. \tag{3.9}$$

The first term of $\mathcal{L}$ describes cc neutrino reactions with the charged leptonic fermion currents:

$$J_\mu^+ = \overline{\nu}_\alpha \gamma_\mu \frac{1+\gamma_5}{2}\alpha \tag{3.10}$$

$$J_\mu^- = \overline{\alpha}\gamma_\mu \frac{1-\gamma_5}{2}\nu_\alpha \tag{3.11}$$

with γ_μ, γ_5 as 4×4 Dirac matrixes given above and α and ν_α as four-component Dirac spinors, representing the charged leptonic and neutrino states. The cc-currents describe the absorption of a charged lepton α and the generation of its hypercharged neutrino partner ν_α (and vice versa). The electric charge transfer is conveyed by the $W^\pm$-bosons and the $(1+\gamma_5)/2$-operator takes into account parity violation, because it projects the left-handed part of the four-component spinor α or ν_α.

The second term of $\mathcal{L}$ describes neutral current (nc) neutrino reactions with the nc:

$$J_\mu^3 = \overline{\nu}\gamma_\mu \frac{1+\gamma_5}{2}\nu \tag{3.12}$$

For completeness the third term of $\mathcal{L}$ is shown. It describes electromagnetic interactions, which are not relevant in neutrino physics.

Now, the weak matrix element M_{cc} for cc–neutrino interactions for low q-momentum transfer (i.e. $q^2 \ll M_W^2$) can be calculated. The propagator term is not dynamic in this low energy approximation and introduces a constant factor proportional to $1/M_W^2$. We get

$$M_{\mathrm{cc}} = \left(\frac{g}{\sqrt{2}}\right)^2 \frac{1}{M_W^2}\left[\overline{\alpha}\gamma_\mu \frac{1+\gamma_5}{2}\nu_\alpha\right]\left[\overline{\nu}_\alpha\gamma_\mu \frac{1+\gamma_5}{2}\alpha\right] \tag{3.13}$$

$$= \frac{G_F}{\sqrt{2}}[\overline{\alpha}\gamma_\mu(1+\gamma_5)\nu_\alpha][\overline{\nu}_\alpha\gamma_\mu(1+\gamma_5)\alpha] \tag{3.14}$$

The last term was introduced (without the γ_5 factor, as parity violation was not known yet) by Fermi already in 1934 [127]. G_F is the Fermi constant, well known

6 The integral over all space gives the Lagrangian L, which is equal to the difference of the kinetic and potential energies of a system.

experimentally from β decays and the lifetime measurement of muons. Here we obtain the link between G_F and the weak coupling constant g and the mass of the weak exchange bosons $W^{\pm}$:

$$\frac{G_F}{\sqrt{2}} = \frac{g^2}{8M_W^2} \tag{3.15}$$

With $e = g \sin\theta_W$, one obtains

$$M_W = \left(\frac{e^2\sqrt{2}}{8G_F \sin^2\theta_W} \right)^{\frac{1}{2}} \simeq \frac{37.4 \text{ GeV}}{\sin\theta_W} \tag{3.16}$$

In addition the theory of the unification of weak and electromagnetic forces delivers the link between the masses of the $M^{\pm}$ and Z^0 bosons:

$$M_{Z^0} = \frac{M_W}{\cos\theta_W} \tag{3.17}$$

The masses of the $W^{\pm}$- and Z^0-bosons have been measured at the LEP collider at CERN. Furthermore, the Weinberg angle has been measured in elastic neutrino electron scattering experiments. As the electromagnetic coupling constant is of course also known, we have a redundant set of equations. Today, the Glashow–Salam–Weinberg theory has been proven to an impressive accuracy and the actual values of the parameter are

- $\theta_W \simeq 28.74°$
- $e \simeq \frac{1}{2}g$
- $M_W = (80.399 \pm 0.023)\frac{\text{GeV}}{c^2}$
- $M_Z = (91.1876 \pm 0.0021)\frac{\text{GeV}}{c^2}$

Note that weak interaction is only "weak" in the low energy approximation regime due to the constant $1/M_W^2$-term in the weak interaction of matrix element. In fact g is even slightly larger than e, and "weak" interaction becomes as large in size as electromagnetic interaction for momentum transfer $q^2 > M_W^2$. However, for solar neutrinos, we are very well within the low energy approximation regime and we will use the Fermi constant when we derive equations for neutrino generation and detection reactions.

Neutrinos are massless in the standard model of particle physics. However, the discovery of neutrino oscillations showed, in contrast, that neutrinos do have mass and hence the standard model has to be extended. Evidence for neutrino oscillations was first found in 1998 by analyzing atmospheric neutrinos in the large underground water detector Super-Kamiokande (SK) in Japan [128], although the first hints for this phenomenon were provided by solar neutrino experiments beforehand. Later, neutrino oscillations have been observed and confirmed in many experiments using solar, atmospheric, reactor, and accelerator-generated neutrinos.

At present, neutrino oscillations are a well-understood phenomenon based on quantum mechanics, and the basic parameters, namely, the neutrino mass differences and mixing angles, have been measured with impressive accuracy. However, not all parameters are known yet and it is the aim of current and future

experiments to determine these quantities and scrutinize our understanding of neutrino physics. Neutrinos gave us many surprises so far; they showed us the way beyond the standard model of particle physics.

Later in the chapter we will describe in detail the phenomenon of neutrino oscillations in vacuum and derive the most important formulas. Moreover, in the framework of solar neutrinos, because the dense matter in the solar interior modifies the neutrino propagation, we will discuss matter effects on neutrino oscillation probabilities. Experimental findings will be reported.

3.2 Neutrino Oscillations

The phenomenon of neutrino oscillations is a fascinating example of how a quantum mechanics effect can manifest in a macroscopic way. It was first Bruno Pontecorvo who suggested neutrino–antineutrino oscillations [129] as explanation of the observed deficit of solar neutrinos as seen in the Homestake experiment by R. Davis and coworkers [130], in close analogy to $K^0 - \overline{K}^0$-oscillations in the hadronic sector. Later he and others imposed neutrino flavor oscillations, a periodic transition in time of the probability to observe a distinct neutrino flavor. However, it took many years until the evidence for neutrino oscillations could be proven experimentally. In 2015 Takaaki Kaija and Arthur McDonald were honored with the Nobel Prize for their discovery of neutrino oscillations and the inevitable consequence of massive neutrinos. We will describe the way how neutrino oscillations have been discovered experimentally in the Section 3.4.

Preconditions for neutrino oscillations are existing neutrino mass eigenstates ν_i with mass eigenvalues m_i ($i = 1, 2, 3$), which determine the propagation of neutrinos in vacuum. Flavor neutrinos are created and detected in cc weak interactions. For example, the ν_μ is the particle that is produced in the decay $\pi^+ \to \mu^+ + \nu_\mu$. The flavor eigenstates ν_α ($\alpha = e, \mu, \tau$) can be linear superpositions of the mass eigenstates:

$$\nu_\alpha = \sum_{i=1}^{3} U_{\alpha i}\, \nu_i \tag{3.18}$$

This means that the flavor neutrinos ν_e, ν_μ, and ν_τ have no definite mass. Assume, in a hypothetical experiment, one would be able to measure the kinematics of a weak process, like the pion decay given above, with an accuracy high enough to observe the impact of neutrino masses, what would the observer see? In each individual event of the pion decay, one would observe a definite neutrino mass m_i with a certain *probability*, which is given in this example by $|U_{\mu i}|^2$. As the total probability to observe any neutrino mass must be equal to one, we have the condition $\sum |U_{\mu i}|^2 = 1$ which holds for any flavor α and is therefore nothing else but the unitary condition on the neutrino mixing matrix defined below.

With this hypothesis of neutrino mixing, the conservation of lepton numbers is only approximate. It is violated if there are nonzero neutrino masses and nontrivial neutrino mixing parameter $U_{\alpha i}$. For three flavors, the left-handed flavor fields are superpositions of the left-handed components of the fields with definite

masses. The link between flavor and mass eigenstates can be written in matrix form:

$$\begin{pmatrix} \nu_e \\ \nu_\mu \\ \nu_\tau \end{pmatrix} = \begin{pmatrix} U_{e1} & U_{e2} & U_{e3} \\ U_{\mu 1} & U_{\mu 2} & U_{\mu 3} \\ U_{\tau 1} & U_{\tau 2} & U_{\tau 3} \end{pmatrix} \times \begin{pmatrix} \nu_1 \\ \nu_2 \\ \nu_3 \end{pmatrix} \tag{3.19}$$

In this scenario the matrix $U_{\alpha i}$ is unitary and $\nu_i = U^{\dagger}_{\alpha i}\nu_\alpha$. Here, we define the assignment ν_α to ν_i in such a way that the absolute values of the diagonal elements of the mixing matrix are maximal. Hence, no mass ordering in the sense $m_j > m_i$ for $j > i$ is assessed a priori.

The mixing matrix $U_{\alpha i}$ (sometimes called Pontecorvo–Maki–Nakagawa–Sato matrix) has three real free parameters, which can be interpreted as rotation angles and one imaginary phase δ, which can cause CP violation in the leptonic sector. In case the neutrino is its own antiparticle (a so-called Majorana particle), additional imaginary phases may occur. The matrix can be parameterized in the form

$$\begin{pmatrix} \nu_e \\ \nu_\mu \\ \nu_\tau \end{pmatrix} = \begin{pmatrix} 1 & 0 & 0 \\ 0 & c_{23} & s_{23} \\ 0 & -s_{23} & c_{23} \end{pmatrix} \begin{pmatrix} c_{13} & 0 & s_{13}\mathrm{e}^{i\delta} \\ 0 & 1 & 0 \\ -s_{13}\mathrm{e}^{i\delta} & 0 & c_{13} \end{pmatrix} \begin{pmatrix} c_{12} & s_{12} & 0 \\ -s_{12} & c_{12} & 0 \\ 0 & 0 & 1 \end{pmatrix} \begin{pmatrix} \nu_1 \\ \nu_2 \\ \nu_3 \end{pmatrix} \tag{3.20}$$

Here, $s_{ij} = \sin\theta_{ij}$ and $c_{ij} = \cos\theta_{ij}$ with the rotation angles θ_{ij}. The origin of neutrino oscillations is easy to see: the evolution in space and time of the mass eigenstates $\nu_i(t) = \nu_i(0)\exp(-i(E_i t - p_i x))$ will differ if E_i and p_i do not coincide and this will create interference effects leading to neutrino flavor oscillations. Here E_i and p_i are the energy and momentum of the eigenstate ν_i, respectively. Therefore a neutrino with a determined flavor at $t = 0$ (e.g. in the solar fusion reaction $p + p \to d + e^+ + \nu_e$) will rotate into another flavor, if the differences in the mass eigenvalues of ν_i do not vanish and if the unitary matrix is not diagonal.

Usually, the basic formula for obtaining the oscillation probabilities is based on the assumption of plane waves, where the momenta are all equal, i.e. $p_i = p$. Hence, the energies determine the propagation of the different mass eigenstates $E_i = (p^2 + m_i^2)^{1/2}$ in time differ, if the m_i differ. For simplicity we will use this formalism with two neutrino states, say, $\nu_{e,\mu}$ and $\nu_{1,2}$. Then the mixing matrix is reduced to one real parameter, the mixing angle θ, and we can write

$$\nu_e(0) = \cos\theta\ \nu_1 + \sin\theta\ \nu_2 \tag{3.21}$$

$$\nu_\mu(0) = -\sin\theta\ \nu_1 + \cos\theta\ \nu_2 \tag{3.22}$$

The mass eigenstates evolve in time as $\nu_i(t) = \mathrm{e}^{-iE_i t}\ \nu_i$. We omit the momentum part, as they evolve exactly in the same way for all mass eigenstates. A particle generated at $t = 0$ as electron neutrino ν_e therefore evolves in time as

$$\nu_e(t) = \cos\theta\ \mathrm{e}^{-iE_1 t}\ \nu_1 + \sin\theta\ \mathrm{e}^{-iE_2 t}\ \nu_2 \tag{3.23}$$

In order to determine the flavor content of this state, we should express it in terms of $\nu_e(0)$ and $\nu_\mu(0)$. We may use the inverse equations

$$\nu_1 = \cos\theta\ \nu_e - \sin\theta\ \nu_\mu \tag{3.24}$$

$$\nu_2 = \sin\theta\ \nu_e + \cos\theta\ \nu_\mu \tag{3.25}$$

and get for the time development of the state $\nu_e(t)$ the expression

$$\nu_e(t) = (\cos^2\theta\ \mathrm{e}^{-iE_1 t} + \sin^2\theta\ \mathrm{e}^{-iE_2 t})\ \nu_e(0) + \sin\theta\cos\theta(\mathrm{e}^{-iE_2 t} - \mathrm{e}^{-iE_1 t})\ \nu_\mu(0) \tag{3.26}$$

The probability $P_{e\mu}(t)$ for the state $\nu_e(t)$, generated as electron neutrino at $t = 0$, to be observed as a muon neutrino at time $t > 0$, is the absolute square of the amplitude before $\nu_\mu(0)$. Hence, we get

$$P_{e\mu}(t) = 2\sin^2\theta\cos^2\theta[1 - \cos(E_2 t - E_1 t)] \tag{3.27}$$

Here, the oscillatory behavior in time of the probability to see the "wrong" flavor ν_μ becomes very clear. Note at $t = 0$ this probability equals to zero and $P_{e\mu}(t) = 0$ for all values of t for "trivial" mixing angles $\theta = 0$ and $\theta = \pi/2$.

Usually, neutrinos are highly relativistic particles. Therefore, we can write $E_i \simeq p + m_i^2/2p$ and get

$$P_{e\mu}(t) = \frac{1}{2}\ \sin^2(2\theta)\ [1 - \cos((m_2^2 - m_1^2)t/2p)] \tag{3.28}$$

Using trigonometric relations and $\Delta m_{21}^2 := m_2^2 - m_1^2$, we get

$$P_{e\mu}(t) = \sin^2(2\theta)\ \sin^2\left(\frac{\Delta m_{21}^2 t}{4\ p}\right) \tag{3.29}$$

The probability $P_{ee}(t)$, which the particle remains an electron neutrino, is

$$P_{ee}(t) = 1 - P_{e\mu}(t) \tag{3.30}$$

Again, the oscillatory behavior is clearly seen. Neutrino oscillations occur if $\theta \neq 0$ or $\pi/2$ and if $\Delta m_{21}^2 \neq 0$. So, for flavor oscillations to occur, it is not only necessary for the neutrinos to have masses, but the eigenvalues also have to differ: i.e. the masses must not be degenerate.

After the period or length L_{osc}, the oscillation pattern repeats:

$$L_{osc} = 2\pi\ \frac{2p}{\Delta m_{21}^2} \tag{3.31}$$

In an experiment this oscillation length is usually expressed as a distance in space (relativistic neutrinos travel basically with the speed of light, i.e. $v \simeq c$). If we measure the neutrino energy $E_\nu \simeq pc$ in MeV and the mass difference Δm_{21}^2 in eV^2, we get for the oscillation length in meters:

$$L_{\mathrm{osc}}\ \simeq\ 2.48\ m\ \frac{E_\nu/\mathrm{MeV}}{\Delta m_{21}^2/(\mathrm{eV})^2} \tag{3.32}$$

In Figure 3.2 the generic behavior of neutrino oscillations in case of two neutrino states is shown.

The same formalism can be applied for the general case of three neutrinos, where the full mixing matrix has to be taken into account. We assume the generation of a neutrino flavor ν_α at time $t = 0$ at $x = 0$. The state $\psi(x, t)$ is then given by

$$\psi(x, t) = \sum_i U_{\alpha i}\ \mathrm{e}^{-i(E_i t - px)}\ \nu_i \tag{3.33}$$

$$\psi(x, t)\ \simeq\ \mathrm{e}^{ipx}\ \sum_i U_{\alpha i}\ \mathrm{e}^{-i(m_i^2 t/2p)}\ \nu_i \tag{3.34}$$

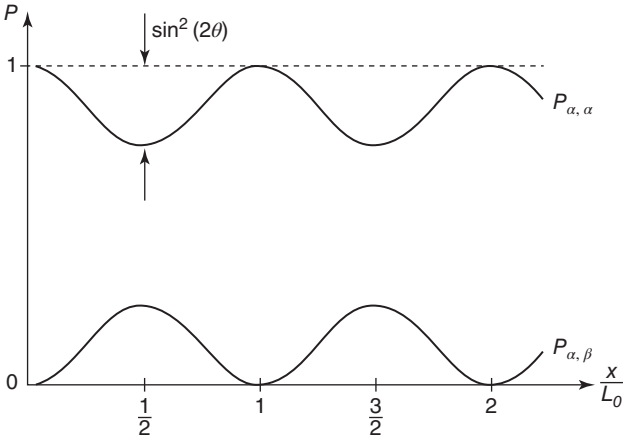

Figure 3.2 Oscillation probabilities as function of the distance between source and detector in units of the oscillation length L_{osc}. The neutrino is generated in $x = 0$ as flavor "α." The upper curve shows the "survival probability" $P_{\alpha,\alpha}$, the lower the appearance probability $P_{\alpha,\beta}$ for the "wrong" flavor β. The oscillation strength is determined by the mixing angle Θ, the oscillation wavelength by the neutrino energy, and the mass splitting Δm^2 that enter into the expression for L_{osc}.

The probability $P_{\alpha\beta}(x,t)$ for a neutrino, generated as flavor α, to be found in a new flavor β after the distance x, is (see, e.g. [131])

$$P_{\alpha\beta}(x,t) = |\psi(x,t)|^2 \tag{3.35}$$

$$P_{\alpha\beta}(x,t) = \left| \sum_i U_{\alpha i} U^*_{i\beta} \, \mathrm{e}^{-i(m_i^2 t/2p)} \right|^2 \tag{3.36}$$

This expression can be expanded to

$$P_{\alpha\beta}(x,t) = \sum_{i=1}^{3} |U^*_{\beta i}|^2 U^*_{\alpha i}|^2 + 2 \sum_{i>j} |U^*_{\beta i} U_{\alpha i} U_{\beta j} U^*_{\alpha j}| \cos\left(2\pi \frac{x}{L_{ij}}\right) \tag{3.37}$$

where we neglected a possible CP violating phase. Again, L_{ij} is the oscillation length between ν_i and ν_j:

$$L_{ij} = 2\pi \frac{2p}{m_i^2 - m_j^2} \tag{3.38}$$

These equations describe the basic features of neutrino oscillations correctly. However, many conceptual problems arise with the assumption of plane waves with a common, sharp momentum. In reality the neutrino source and the detector are localized. Hence, also the neutrino states are localized and the uncertainty principle then implies that neutrinos must be in a superposition of different momentum states. Therefore, the neutrino wave function cannot be a plane wave but must be a wave packet (see, e.g. [132] and references therein). An overview about the theoretical background as well as the actual experimental status of neutrino oscillations can be found, e.g. in [133].

As the neutrino propagates, the wave packets will become separated in space and time due to their different group velocities. Hence, after a certain distance, there will be no overlap between corresponding mass eigenstates and coherence will be lost. The flavor change will then no longer depend on distance. Calculations for the oscillation probability for wave packets [131] yield

$$P_{\alpha\beta}(x) = \sum_{i=1}^{3} |U^*_{\beta i}|^2 U^*_{\alpha i}|^2 + 2 \sum_{i>j} |U^*_{\beta i} U_{\alpha i} U_{\beta j} U^*_{\alpha j}| \cos\left(2\pi \frac{x}{L_{ij}}\right) \times \mathrm{e}^{-(x/L^{\mathrm{coh}}_{ij})^2} \tag{3.39}$$

with the coherence length

$$L^{\mathrm{coh}}_{ij} = \frac{4\sqrt{2}E^2_\nu}{|\Delta m^2_{ij}|}\sigma_x \tag{3.40}$$

where σ_x is an effective wave packet width depending on the spatial uncertainty of source and detector. The oscillatory pattern is damped by the exponential factor $\mathrm{e}^{-(x/L^{\mathrm{coh}}_{ij})^2}$ and the coherence length is enlarged at higher energies and becomes smaller for larger mass differences. It is interesting to calculate the coherence length in practical units [132]. One obtains

$$L^{\mathrm{coh}}_{ij} \simeq 57 \times 10^3 \text{ m} \left(\frac{E_\nu}{\mathrm{MeV}}\right)^2 \left(\frac{\mathrm{eV}}{\Delta m^2_{ij}}\right) \left(\frac{\sigma_x}{\dot{A}}\right) \tag{3.41}$$

The actual known values in Δm^2_{ij} are in the range well above 10^{-5} (eV) ^{2}, and we see that neutrinos from astrophysical sources, including our sun, arrive to Earth as completely incoherent mixtures of mass eigenstates.[7] Still the flavor content of the neutrinos will be altered, but the oscillation pattern would be not observable as function of time and distance. On the other hand, for basically all known terrestrial experiments, using neutrinos from nuclear reactors or accelerators coherence is established.

Basically there are two types of experiments searching for neutrino oscillations, appearance and disappearance experiments. In the former the appearance of neutrino interactions with a "strange" flavor is searched for. A typical example is accelerator experiments, where the neutrino energies are high enough to produce all flavors in cc weak processes. The advantage of appearance experiments is their high sensitivity for the oscillation amplitude. Typical examples of disappearance experiments are reactor and solar neutrino experiments. In both cases one is looking for a deficit in the neutrino flux and for a distortion in the energy spectrum. In disappearance experiments (with solar or reactor neutrinos, as an example), the neutrino energies are not sufficient to produce charged muons or τ-leptons. However, with such experiments, one can be very sensitive to small values of the mass splitting Δm^2, especially at long baselines L.

Sometimes the oscillation of neutrinos can be described approximately with the simple two-oscillation formula. This is, for instance, the case for reactor neutrino experiments at rather short distances ($x \ll 10$ km), when the slow

7 For a detailed description of the actual Δm^2_{ij} values, see later.

component due to Δm^2_{21} is still negligible. We will discuss this in more detail later. If the dimensions of either the neutrino source or the detector are much larger in comparison with the oscillation length, the effect of neutrino oscillation will wash out. In this case no dependence on the distance will be observed and only an average oscillation probability

$$P_{\text{osc,aver}} = \frac{1}{2}\sin^2 2\theta \tag{3.42}$$

will be measured.

So far, neutrino oscillations in vacuum have been considered. If neutrinos are going through matter, additional effects have to be taken into account. These effects will be discussed in the section 3.3.

3.3 Matter Effects

Neutrinos going through matter undergo coherent forward scattering off particles like electrons via the neutral weak interaction. This results in a refractive index, or in an effective mass term, which depends on the neutrino flavor and energy, and as a consequence, matter may modify neutrino oscillations significantly. As solar neutrinos are generated in a dense environment, they traverse matter at varying densities until they leave the sun. It turns out that matter effects are indeed important and its consequences were first discussed in papers of Wolfenstein, Smirnov, and Mikheyev [134–136]. Therefore, the effect is often referred to by the acronym Mikheyev-Smirnov-Wolfenstein (MSW).

The refractive index n_l for a neutrino with flavor l is $n_l = 1 + (2\pi N/p^2) f_l(0)$, where N is the number density of particles, p is the momentum, and $f_l(0)$ is the real part of the forward scattering amplitude. Contributions to the forward scattering in solar matter come from nucleons and electrons. The part from nucleons is via neutral interaction only and therefore identical for all neutrino flavors. However, ν_e scatter off electrons via neutral and charged interactions, all other flavors only via neutral interaction. This leads to a net difference between the refractive indices of electron neutrinos and all other flavors and influences neutrino oscillation probabilities.

In order to discuss these effects, it is useful to remind about the time evolution of mass eigenstates in vacuum:

$$\nu_i(x) = \mathrm{e}^{-i\frac{m_i^2}{2p}x}\nu_i \tag{3.43}$$

These functions are solution to the following equation of motion ($x = t$):

$$i\frac{\mathrm{d}\nu_i}{\mathrm{d}t} = \frac{m_i^2}{2p}\nu_i \tag{3.44}$$

In matrix notation, we can write

$$\begin{pmatrix}\nu_1(t)\\ \vdots \\ \nu_n(t)\end{pmatrix} = \underbrace{\frac{1}{2p}\begin{pmatrix}m_1^2 & & 0\\ & \ddots & \\ 0 & & m_n^2\end{pmatrix}}_{=:H^i}\begin{pmatrix}\nu_1\\ \vdots \\ \nu_n\end{pmatrix} \tag{3.45}$$

In vacuum, the Hamiltonian H^i is diagonal and the differential equations for the time evolving mass states decouple. Hence, the mass states are stable, when neutrinos travel through vacuum. The Hamiltonian H^α in the flavor basis is connected via H^i via

$$H^\alpha = UH^iU^\dagger \tag{3.46}$$

Contrary to H^i, the Hamiltonian H^α is not diagonal and additional terms in the Hamiltonian have to be considered. However, only relative differences are important, because this part of the refractive index, which is common for all neutrino flavors, modifies the phase development in the exact same way.

In the following we will describe matter effects in the two-neutrino approach. In the flavor basis, the additional cc interaction of electron neutrinos can be written as

$$H^\alpha_{\text{mat}} = H^\alpha + \begin{pmatrix} V_{\text{cc}} & 0 \\ 0 & 0 \end{pmatrix} \tag{3.47}$$

with $V_{cc} = \sqrt{2}G_F N_e$ where G_F is the Fermi constant and N_e the electron density in the medium. We transform now the Hamiltonian H_{mat} into the basis of mass eigenstates and get

$$H^i_{\text{mat}} = U^\dagger H^\alpha_{\text{mat}} U = H^i + U^\dagger \begin{pmatrix} V_{cc} & 0 \\ 0 & 0 \end{pmatrix} U = \frac{1}{2p} \begin{pmatrix} m_1^2 + Ac^2 & Asc \\ Asc & m_2^2 + As^2 \end{pmatrix} \tag{3.48}$$

with $A = 2\sqrt{2}G_F N_e p$, $c = \cos\theta$, and $s = \sin\theta$.

Note that H^i_{mat} is no longer diagonal if $A \neq 0$. We can find the new, relevant parameter in matter by diagonalizing and obtain for the mixing angle in matter the equation:

$$\tan(2\theta_{\text{mat}}) = \frac{\sin 2\theta}{\cos 2\theta - A/\Delta m^2} \tag{3.49}$$

From this expression one can calculate the oscillation amplitude in matter as

$$\sin^2(2\theta_{\text{mat}}) = \frac{\sin^2(2\theta)}{(A/\Delta m^2 - \cos(2\theta))^2 + \sin^2(2\theta)} \tag{3.50}$$

where $A/\Delta m^2 = 1.526 \times 10^{-7} \left(\frac{n_e}{\text{mol/cm}^3}\right) \left(\frac{E}{\text{MeV}}\right) \left(\frac{\text{eV}^2}{\Delta m^2_{21}}\right)$ and for the new mass differences squared

$$(m^{\text{mat}}_{1,2})^2 = \frac{1}{2}\left((m_1^2 + m_2^2 + A) \mp \sqrt{A - \Delta m^2 \cos^2(2\theta) + \Delta m^2 \sin^2(2\theta)}\right) \tag{3.51}$$

The effective oscillation length L_{mat} in matter is given by

$$L_{\text{mat}} = L_{ij} \cdot \frac{\sin 2\theta_{\text{mat}}}{\sin 2\theta_{ij}} \tag{3.52}$$

Note that one gets the results obtained above in case of vacuum, i.e. for $N_e \to 0$.

Generally, matter is suppressing oscillation probabilities. Indeed, in the case $N_e \to \infty$ (which is equivalent to $A \to \infty$), we get $\tan(2\theta_{\text{mat}}) \simeq \sin(2\theta)\Delta m^2/(-A)$

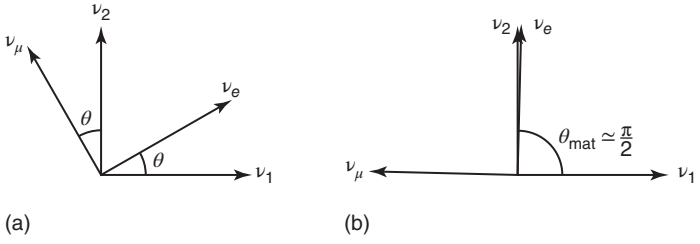

Figure 3.3 Neutrino mixing and rotation scheme in case of vacuum (a) and in case of matter dominance for $A/\Delta m^2 \gg 1$ (b), when ν_e becomes very close to the state ν_2.

and hence $\theta_{\text{mat}} \simeq \pi/2$, which means that mass and flavor eigenstates are almost aligned to each other. This case is shown schematically in Figure 3.3.

However, there exists a value $A = \Delta m^2 \cos(2\theta)$, which leads to a maximum oscillation amplitude $\sin^2(2\theta_{\text{max}}) = 1$, independent of how large or small this amplitude is in vacuum. This resonance is realized, if the neutrino energy E_ν and the matter electron density N_e fulfill the condition:

$$E_\nu = \frac{\Delta m^2 \cos(2\theta)}{2\sqrt{2} G_F N_e} \tag{3.53}$$

An interesting question is this: Can solar neutrinos meet this resonant condition? Well, if one takes the value for the electron density in the solar center $N_e = \rho N_A Z/A$ with $\rho \approx 150$ g/cm^3, N_A the Avogadro number, and Z/A being the average charge to mass ratio of the solar plasma, one obtains for the resonant energy E_{res}

$$E_{\text{res}} \simeq 6 \times 10^4 \frac{\text{MeV}}{\text{eV}^2} \cos(2\theta) \Delta m^2 \tag{3.54}$$

Considering a two-neutrino scenario, we use $\Delta m^2 = \Delta m^2_{21} = m_2^2 - m_1^2 \simeq 8 \times 10^{-5}(\text{eV})^2$ and $\cos 2\theta \simeq 0.38$. We see that $E_{\text{res}} \simeq 2$ MeV and the resonance condition is met indeed, because the solar neutrino spectrum reaches ≈ 15 MeV. Note that the resonance condition depends on the sign of Δm^2_{21}. Only for $m_2 > m_1$ the resonance condition will be fulfilled.

As solar neutrinos travel through a medium with variable density, one has to solve the system of coupled differential equations numerically [135, 137–139]. In addition there exist approximate analytical solutions to this problem (see, e.g. [140]). Let us follow the fate of a neutrino that is generated in the solar center and propagates through the star toward the solar surface. For $E_\nu > 2$–3 MeV, forward scattering will dominate over the vacuum mass splitting at the solar center and the electron neutrino ν_e will be close to ν_2. This is schematically shown in Figure 3.3.

Thus, the situation is inverted with respect to the vacuum, where ν_e is closer to ν_1. As the neutrino traverses through the sun, the orthogonal vectors $\nu_{1,2}$ slowly rotate. When the resonance region is reached, full mixing (i.e. $\theta_{\text{mat}} = 45°$) will occur. If the neutrino remains in the same state, it will leave the star being still closer to ν_2. This is the scenario of the so-called adiabatic solution of the MSW effect, where the solar density variation is slow, such that it can be considered

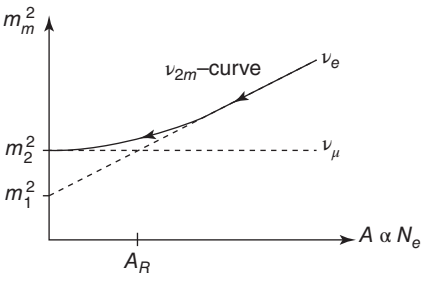

Figure 3.4 Adiabatic conversion of ν_e to ν_μ in solar matter. High energy electron neutrinos have a higher effective mass in the solar center due to matter effects (high values of A). If they stay on their curve (adiabatic behavior), they will leave the sun dominantly in another flavor state (here denoted as ν_μ). The conversion only works for $m_2 > m_1$.

to be constant over the oscillation length L_{mat} in matter. In Figure 3.4 the adiabatic conversion of an electron neutrino in the solar center to a muon neutrino is depicted.

The resonance energy is dividing the solar spectrum into two parts. Low energy neutrinos well below E_{res} are not very much influenced by matter effects, whereas high energy neutrinos are dominated by them. Therefore, pp- and ^{7}Be-neutrinos are in the so-called vacuum regime, whereas ^{8}B-neutrinos above ≈2–3 MeV are dominated by the matter effect. The transition region between both regimes can be probed by measuring the energy spectrum of solar ^{8}B-neutrinos over their whole spectrum. Also, mono-energetic pep-neutrino measurement yield interesting information in order to determine the transition region experimentally, because the theoretical uncertainty on its flux is very small in contrast to what we know about solar CNO neutrinos. From a theoretical point of view, the exact course of the transition region between vacuum and matter-dominated regimes depends not only on neutrino mixing parameter values but also on the knowledge of the solar electron density as a function of the solar radius. Here, information gained from helioseismology delivers important details.

Taking into account the known actual mixing parameter, one obtains a specific energy-depending curve for the probability of an electron neutrino to remain in its state when it reaches the solar surface. This so-called survival probability P_{ee} is about 0.6 in the low energy region and drops to about 0.3 for high energy neutrinos, as it is depicted in Figure 3.5. As mentioned above P_{ee} can be probed by solar neutrino spectroscopy. Currently, observational data are consistent with prediction. Indeed, the flux of the high energy part of solar ^{8}B-ν_e is stronger suppressed than that of low energy neutrinos (e.g. ^{7}Be-ν_e and pp-ν_e). This confirmation of the

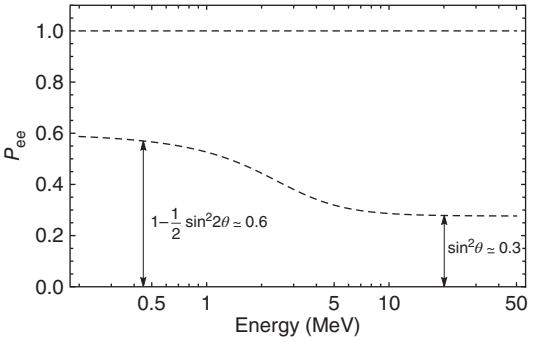

Figure 3.5 Schematic view of the survival probability P_{ee} for an electron neutrino created in the solar interior to remain in its state as a function of its energy. For low energies (vacuum regime), P_{ee} is significantly higher as in the high energy (matter) regime. Actual known values of the neutrino mixing matrix are used here.

solar MSW effect is a clear evidence for the so-called normal ordering in the ν_1, ν_2 sector, i.e. $m_2 > m_1$.

However, there exist not yet direct observational data from the transition region between the vacuum and matter dominated regimes. This could be achieved in the future by a precise measurement of the solar ^{8}B-ν-spectrum also at low energies. Theories beyond the standard model of particle physics predict deviations from the normal survival probability curve in the transition region. This is the case for flavor changing neutral currents (FCNCs) in weak interaction (see, e.g. [141]) and for the hypothetical admixture of so-called sterile neutrinos to the known active flavors [142]. It can be shown that the survival probabilities for the vacuum as well as the matter dominated regimes are not altered. However, one expects significant deviations of P_{ee} within the transition region, say, between ≈1 and ≈5 MeV, and future solar neutrino experiments may have the chance to probe this field of new physics.

3.4 Neutrino Oscillation Experiments

There are two types of neutrino oscillation experiments in general. In so-called appearance experiments, one searches for a new flavor to show up, and in disappearance experiments one looks for a deficit in the flux of a given neutrino flavor. Often the two neutrino approximation can be applied for estimating the effect of neutrino oscillations. In this special case, we get from the formulas developed within Section 3.2 the following expression for the probability $P_{\alpha\beta}$ for observing the new flavor β, when starting with flavor α

$$P_{\alpha\beta} = \sin^2(2\theta)\sin^2(\Phi(E_\nu, L)) \tag{3.55}$$

with the oscillation phase in useful units

$$\Phi(E_\nu, L) = \left(\frac{1.27\ \Delta m^2/\mathrm{eV}^2}{E_\nu/\mathrm{GeV}} \cdot L/\mathrm{km}\right) \tag{3.56}$$

Then, the survival probability $P_{\alpha\alpha}$ for the original neutrino flavor to get observed is $P_{\alpha\alpha} = 1 - P_{\alpha\beta}$. The amplitude of neutrino oscillations is determined by the mixing angle θ, and the oscillation phase is assigned by $\Delta m^2 \cdot L/E_\nu$. We will use this simple formula in the Section 3.4 in order to understand better the experimental results on neutrino oscillation parameters.

An impressive development has been demonstrated in neutrino physics within the last two decades. First hints on neutrino oscillations came from early solar neutrino experiments, where a significant lower neutrino flux has been measured with respect to theoretical predictions. A detailed description of solar neutrino experiments and the discovery as well as the manifestation of neutrino oscillations is given in the Chapter 4. In this section we report about the development and actual status of atmospheric-, reactor-, and accelerator-based experiments.

3.4.1 Atmospheric Neutrinos

The first direct evidence for neutrino oscillations was coming from atmospheric neutrino observations. So-called atmospheric neutrinos are created in the upper

atmosphere of the Earth via the constant bombardment of charged cosmic rays, predominantly formed by high energetic protons. Unstable mesons, especially the lightest pions (π^+, π^0, π^-) are generated in strong interactions of cosmic protons with nitrogen and oxygen nuclides. The charged mesons decay via weak interactions, e.g. $\pi^+ \to \mu^+ + \nu_\mu$, thus forming a natural source of high energetic neutrinos. A part of the charged muons will decay before reaching the Earth's surface (the lifetime at rest for muons $\tau_\mu \simeq 2.2\ \mu s$) via $\mu^+ \to e^+ + \overline{\nu}_\mu + \nu_e$ and add to the total atmospheric neutrino flux. Similar decay chains are present for negative mesons and the heavier charged kaons K^+, K^-. In total, one expects to observe two muon-like neutrinos for one electron-like type, when we do not distinguish between neutrinos and antineutrinos. However, if the muon reaches the Earth's surface before it decays, the muon will lose energy very efficiently. Therefore, the ratio $r = \nu_\mu : \nu_e \sim 2$ is valid only approximatively. As the probability for reaching the Earth's surface is increasing with energy due to the effect of relativistic time dilation, the approximation for r holds only for $E_\nu \lesssim 3\ GeV$ and is increasing for higher energies significantly. Today the distribution of r as a function of E_ν can be calculated with a quite high accuracy.

In Figure 3.6 the production of atmospheric neutrinos is shown as a sketch, and in Figure 3.7 the expected energy spectrum for the ratio between muon and electron neutrinos. For a detailed discussion, one may see, e.g. [145] and references therein.

The atmospheric neutrino energy spectrum reaches a maximum at around 1 GeV and is decreasing with a power law similar as that of the cosmic protons. For water Cherenkov detectors like Super-Kamiokande (**SK**) in Japan the useful energy region is between ∼0.1 GeV and several GeV. Therefore, the typical

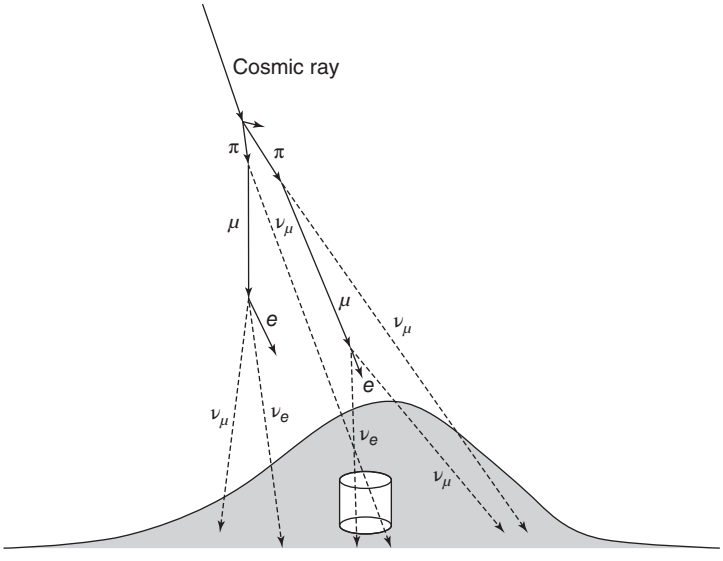

Figure 3.6 Scheme of neutrino production in the upper atmosphere due to strong interactions of cosmic particles and succeeding weak decays of charged mesons. Source: Kajita 2010 [143]. Reproduced with permission of The Japan Academy.

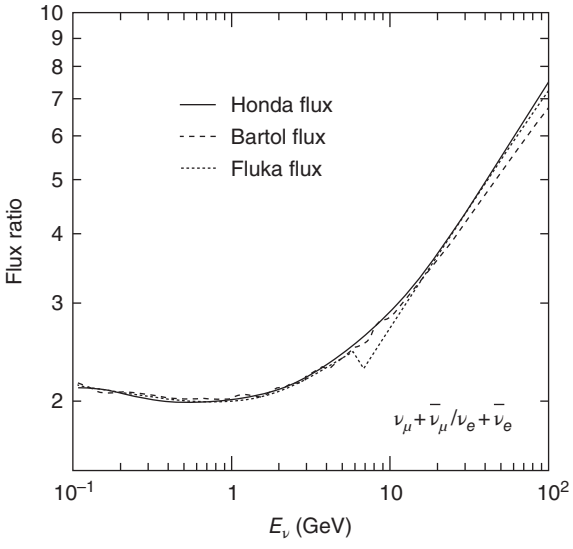

Figure 3.7 Calculated flux ratio between muon and electron neutrinos produced in the atmosphere as a function of energy. Three distributions from independent groups Honda et al. [144], Barr et al. (Bartol) [145], and Battistoni et al. (Fluka) [146] are shown.

baseline between source and detection is between ∼20 and ∼12 000 km and atmospheric neutrino experiments are sensitive to a wide variety of the neutrino oscillation parameter Δm^2. The SK experiment, for instance, covers very well the mass range between $\Delta m^2 \sim 0.1$ eV^2 and $\Delta m^2 \sim E/L \sim 10^{-4}$ eV^2. Neutrino detection and flavor separation occur in atmospheric neutrino experiments via cc reactions on a nucleon X (proton or neutron):

$$\nu_e + X \rightarrow e + Y \tag{3.57}$$

$$\nu_\mu + X \rightarrow \mu + Y \tag{3.58}$$

where Y is an arbitrary hadronic final state. The charge leptons are emitted dominantly in forward direction and are detected by their Cherenkov light. Besides these quasi-elastic scattering processes also single and coherent meson production as well as deep inelastic scattering will take place. For energies below ∼1 GeV, the quasi-elastic scattering processes are dominant, whereas meson production (predominantly pions) is important for energies around 1 GeV and inelastic scattering off quarks is paramount for even higher energies. Above ∼1 GeV the neutrino–nucleon interaction cross-section scales almost linearly with E_ν.

Therefore, the neutrino interaction rate decreases with $\sim E_\nu^{-2}$ as the atmospheric neutrino flux scales approximately with E_ν^{-3}. Figure 3.8 shows the cc neutrino and antineutrino cross sections as function of energy [143].

SK is using a large water Cherenkov detector with a cylindrical shape and a total mass of 50 kt. About 11 200 photomultiplier (PMT) with 50 cm diameter and about 1900 with 20 cm diameter are used for the inner and outer detectors, respectively. The outer part is detecting penetrating charged particles, like cosmic muons, and the inner detector is used for neutrino analysis. Figure 3.9 shows the schematic of the SK detector. More on the SK detector is discussed in Chapter 4.

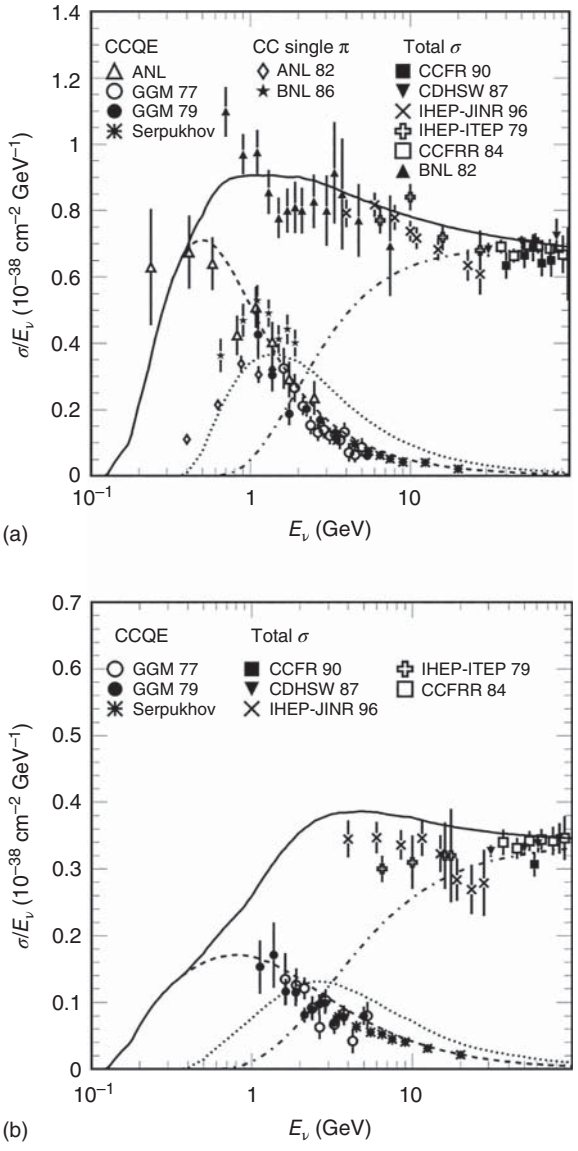

Figure 3.8 Charged current cross sections for (a) neutrino and (b) antineutrino interactions. Solid line shows the calculated total cross sections [147]. The dashed, dotted, and dash-dotted lines show the calculated quasi-elastic, Single meson, and deep inelastic scattering cross sections, respectively. Data points from various experiments are also shown. Source: Ashie et al. 2005 [147]. Reproduced with permission of American Physical Society.

If the energy is not too high the charged leptons are stopped within the detector volume and from the total amount of light the neutrino energy can be deduced, when the neutrino interaction vertex is inside the so-called fiducial volume. Events which exhibit such a topological structure are called "fully-contained events." SK is large enough to register them: for instance, a muon with 1 GeV kinetic energy will travel around 5 m in water before it gets stopped. The data analysis on neutrino oscillations is based mainly on the fully contained events. However, also the distributions of so-called partially contained, upward stopping muon and upward through-going muon events has been analyzed in the SK

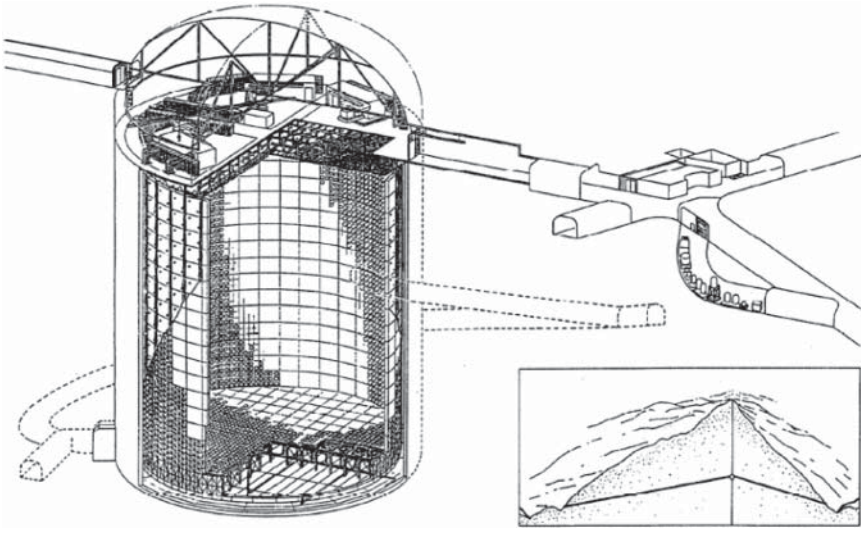

Figure 3.9 Schematic of the 50 kt Super-Kamiokande water Cherenkov neutrino detector in the Kamioka mine in Japan. Source: Kajita 2010 [143]. Reproduced with permission of The Japan Academy.

experiment and are used as important cross-checks for testing the oscillation hypothesis.

From the position of the Cherenkov ring, the direction of the neutrino can be determined and so also the baseline length between neutrino generation and detection. The correlation between the directions of the incoming neutrino and the charged lepton is strongest for quasi-elastic scatter interactions, which show up as fully contained events with single Cherenkov ring structure inside the fiducial volume of the detector. Of course the correlation is energy dependent and is increasing with neutrino energy due to the relativistic Lorentz boost factor. For $E_\nu \gtrsim 1$ GeV, the angular resolution is around 20° or better. This uncertainty has to be taken into account for the oscillation analysis.

As electrons undergo much more deflections as muons until they are finally stopped, their Cherenkov ring appears to be much more smeared out and this feature can be used to distinguish between muon- and electron-like events with high sensitivity. This important experimental feature is illustrated in Figure 3.10, where the local distribution of fired photosensors of a muon-like event and an electron-like event with energies around 0.5 GeV are shown for comparison. The cylindrical wall is rolled out and also shown are the top and bottom parts of the detector. The color code is used to show the timing, whereas the circle sizes indicate the intensities of the registered photons. It is evident that the electron-like event exhibits a smeared PMT-distribution with respect to the muon-like event.

Early observations done by the smaller water Cherenkov experiments **IMB** [148] and **Kamiokande** [149] showed a ratio between the number of ν_μ- and ν_e-events, which was significantly lower as the expected value ∼2. This was not confirmed by other experiments like **Frejus** [150] and **NUSEX** [151]

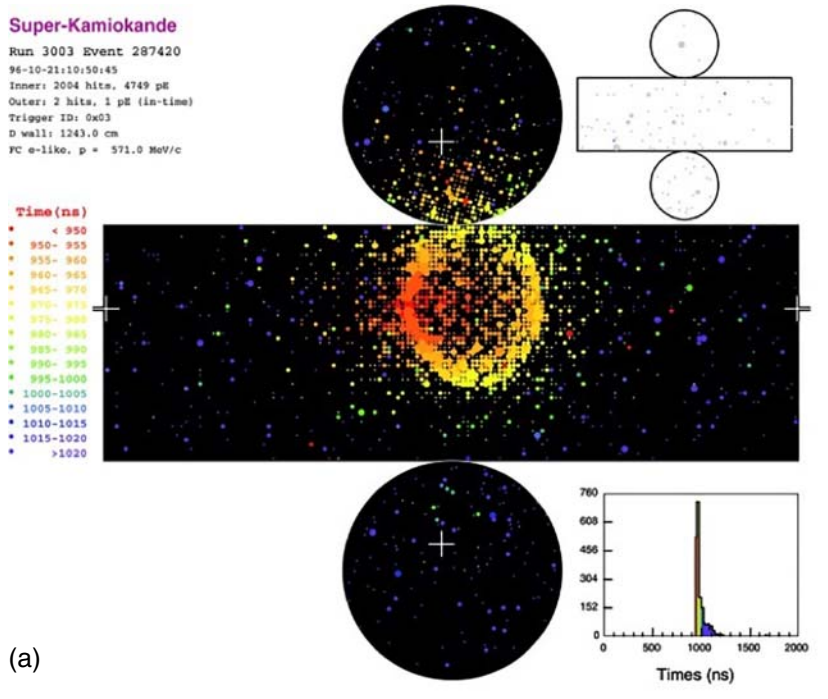

(a)

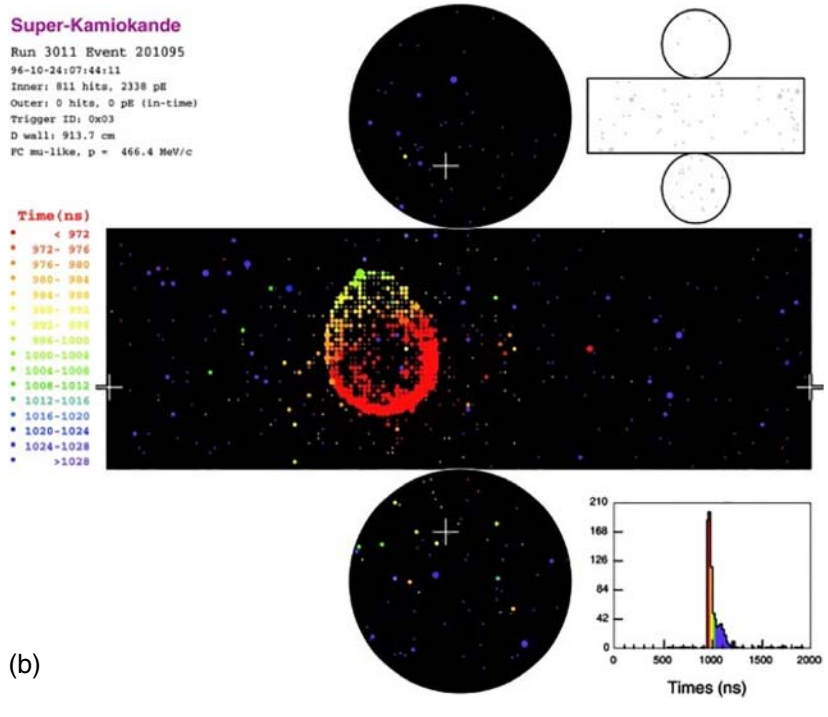

(b)

Figure 3.10 Electron- (a) and muon (b)-like neutrino interaction visible as single Cherenkov rings. The colors indicate the photon timing and the size of the dots shows the registered intensities in each photomultiplier. Reconstructed energies are 571 and 466 MeV, respectively. The distribution of fired photomultipliers is sharper for the muon-like event. Source: Kajita 2010 [143]. Reproduced with permission of The Japan Academy.

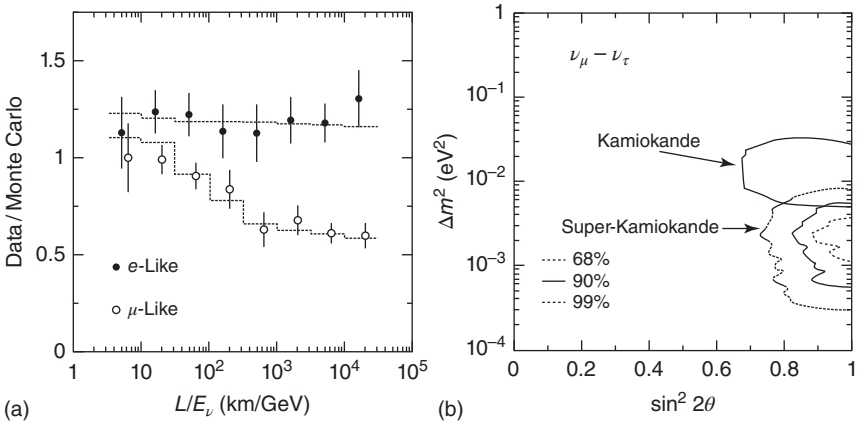

Figure 3.11 First evidence for neutrino oscillations in the atmospheric data of Super-Kamiokande [152]. (a) Ratio of ν_μ– and ν_e–like events over Monte Carlo calculated values as function of L/E_ν. The dashed line shows the expected shape for $\nu_\mu \to \nu_\tau$ oscillations with $\Delta m^2 = 2.2 \times 10^{-3}$ eV^2 and full mixing. (b) Confidence contours for Δm^2 over $\sin^2 2\theta$. Also shown are data from the former Kamiokande experiment for comparison. Source: Fukuda et al. 1998 [152]. Reproduced with permission of American Physical Society.

using the technology of iron calorimeter with track capabilities. However, these detectors were much smaller and therefore their statistical uncertainties much larger. Evidence for neutrino oscillations was first reported in the neutrino conference 1998 in Takayama, Japan, by the SK collaboration. In Figure 3.11 the L/E-dependence of ν_μ- and ν_e-like constraint events is shown [152].

A significant deficit of and ν_μ-events is visible, which is in good agreement with the assumption of neutrino oscillations with full mixing, i.e. $\sin^2 2\theta \sim 1$. In addition the SK data show a clear evidence for $\nu_\mu \Leftrightarrow \nu_\tau$-oscillations, because the ν_e-distribution over L/E_ν is flat. If the oscillation would have been predominantly of the type $\nu_\mu \Leftrightarrow \nu_e$ a significant *increase* of the ν_e-spectrum at larger L/E_ν-values would have been observed. Also shown are the corresponding contour plots Δm^2 over $\sin^2 2\theta$ in comparison with the older Kamiokande results, which showed indication for larger values of the mass splitting. Not shown are the exclusion limits from Frejus, which were in conflict with the upper part of Kamiokande, but not with SK, as the sensitivity of Frejus was constrained on $\Delta m^2 \gtrsim 3 \times 10^{-3}$ eV^2, which is just above the actual allowed parameter range.

Today the precision of the data is much higher and atmospheric neutrino oscillation measurements have entered the era of high accuracy. In Figure 3.12 the actual ν_μ-spectrum above L/E_ν is shown [153].

The ν_μ-flux divided by the Monte Carlo prediction is plotted versus L/E_ν. In case of no oscillations, the data should scatter around a value of 1. The disappearance of ν_μ above $L/E_\nu \sim 3 \times 10^2$ km/GeV will manifest. The solid line shows the best fit to the spectrum for $\nu_\mu \Leftrightarrow \nu_\tau$ oscillations. The fit is fully compatible with data. Other hypothetical approaches like neutrino decay or neutrino decoherence (dashed and dotted lines) can be excluded by the significant dip around

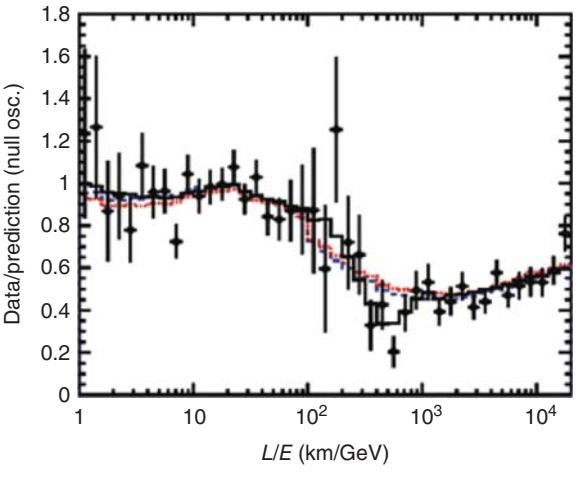

Figure 3.12 L/E-Analysis of atmospheric neutrino data obtained by Super-Kamiokande and published in [153]. Source: Ashie et al. 2004 [153]. Reproduced with permission of American Physical Society.

$L/E_\nu \sim 5 \times 10^2$ km/GeV. The actual best fit values for oscillation parameters[8] from SK [154] are

$$0.518 < \sin^2\theta_{23} < 0.623 \tag{3.59}$$

$$2.19 \times 10^{-3} < \Delta m^2_{32}/\ \mathrm{eV}^2 < 2.63 \times 10^{-3} \tag{3.60}$$

at 68% confidence level (CL). The collaboration studied interactions of oscillation-generated τ-neutrinos within the 22.5 ton fiducial volume of the SK detector for 2806 days of data taking and is excluding the non-tau hypothesis on a 3.8σ-level [155]. If the oscillations are indeed from the type $\nu_\mu \rightarrow \nu_\tau$, it should be possible to observe ν_τ cc events in the SK detector. However, the observation of charged τ-leptons produced from atmospheric neutrino oscillations is very difficult because of several reasons. First, the event rate is small, due to the heavy τ-mass of 1.78 GeV/c^2 and a resulting energy threshold of 3.5 GeV: only one event per kilo-ton target is expected within one year of measurement. Second, the τ-lepton is very short living and only the decay products are visible. It decays into an invisible neutrino and many hadrons in 65% of all cases. However, similar topological structures are generated in nc interactions of all neutrino flavors and these events form a considerable large background for the search of cc-ν_τ-events in a water Cherenkov detector like SK. The search for ν_τ-events is carried out in SK by analyzing various kinematical variables using advanced statistical methods such as maximum likelihood and artificial neural network methods in order to separate candidate events from background signals. This is not possible on an event-to-event basis but it is giving a statistical hint that indeed τ-neutrinos are observed in the atmospheric data set of SK. This is shown in Figure 3.13, where the zenith angle distribution of events, which are considered as ν_τ candidates (i.e. events, which survived all relevant analysis cuts) with an excess above background for up-going events is visible. This plot is based on data of the SK Phase-I data-taking period.

8 Neutrino mass ordering (NMO) is left open as a free parameter.

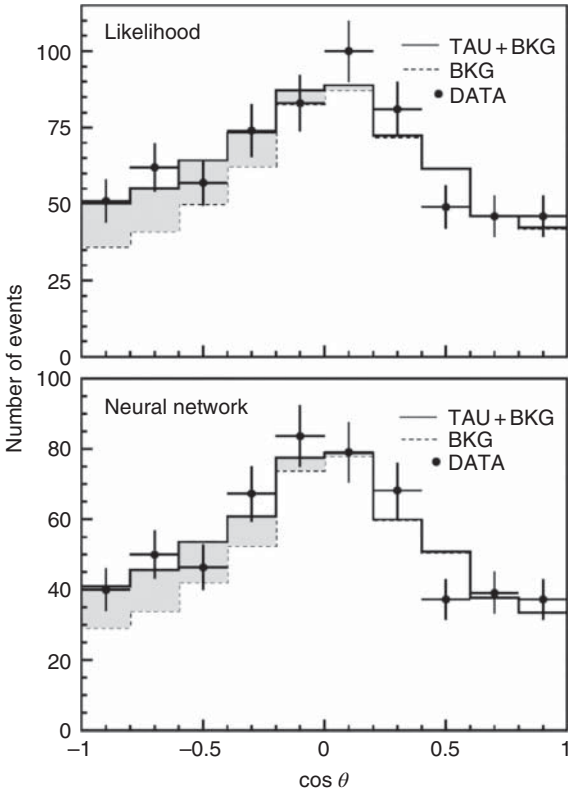

Figure 3.13 Zenith angle distribution of ν_τ candidates in Super-Kamiokande (Phase-I). Both maximum likelihood and neural network method results are shown. An excess above background is visible for up-going events. The data agree with the hypothesis of $\nu_\mu \rightarrow \nu_\tau$ oscillations. Source: Kajita 2010 [143]. Reproduced with permission of The Japan Academy.

In 2013 observation of atmospheric neutrino oscillations has been observed also by the **IceCube** neutrino observatory at the south pole [156]. IceCube consists of a huge array of photo-sensing modules, deposited deep inside the Antarctic ice shield, and is searching for cosmic neutrinos at extremely high energies. The measurement of atmospheric neutrino oscillations became possible, thanks to the so-called DeepCore detector, an extension of IceCube with a denser matrix of optical sensors and hence a lower energy threshold of about 20 GeV. The non-oscillation scenario can be excluded by IceCube data at 5σ significance. The data are best described by the oscillation parameters $\sin^2\theta > 0.93$ and $1.8 \times 10^{-3} < \Delta m^2/\ \mathrm{eV}^2 < 2.9 \times 10^{-3}$, which are in agreement with SK results.

3.4.2 Long Baseline Accelerator Neutrinos

The test and finally the verification of atmospheric neutrino oscillations with an independent source of neutrinos was extremely important. This was accomplished by the use of high energy neutrinos produced by accelerators. There, neutrinos are produced in a similar way as atmospheric neutrinos: protons, accelerated to high energies hit a target, where charged mesons are generated via hadronic interactions. These mesons are focused in a set of magnetic horns and

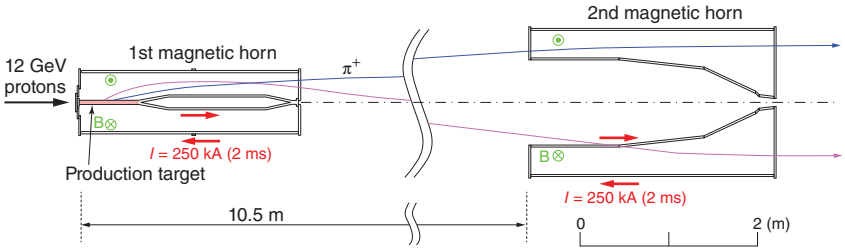

Figure 3.14 Schematic view of the neutrino gun used in the K2K experiment. A beam of 12 GeV protons is lead to an aluminum target. An electric current of 250 kA is supplied to both horns, creating a toroidal magnetic field inside the horns. The pions are focused in this way, and a narrow neutrino beam appears due to the weak decays of the pions in the decay channel. Source: Ahn et al. 2006 [157]. Reproduced with permission of American Physical Society.

led to a vacuum decay tunnel. In Figure 3.14 the schematic view of the experimental setup as used in the **K2K** experiment to form the neutrino beam with the help of two magnetic horns is shown.

Muon neutrinos are produced in the pionic decays $\pi \to \mu + \nu_\mu$ and both neutrinos and their antiparticles can be produced, depending on the sign of the pion charge. The muonic branching ratio of charged pion decay is almost 100% and the length of the tunnel is adjusted in such a way that by far most of the muons are dumped into a beam stopper at the very end of the tunnel and so no further contamination of the almost purely ν_μ-beam occurs.

In the K2K experiment in Japan, a 12-GeV pulsed proton beam was used, producing muon neutrinos in the GeV range. The ν_μ-beam was directed to the SK detector, 250 km away. The neutrino flux was monitored by a smaller near detector and in SK the disappearance of the ν_μ-flux was measured. In Figure 3.15a the energy spectrum of ν_μ-events is shown. The data scatter due to the limited statistics, but a significant disappearance of neutrinos with energies $E_\nu \sim 0.7$ GeV is observed [157]. On Figure 3.15b, the corresponding contour plots for the mixing parameters obtained in the K2K experiment are shown. It is evident that atmospheric neutrino oscillations have been confirmed by the K2K experiment.

Perhaps it is worthwhile to mention one peculiar aspect here, which goes beyond neutrino oscillations. With K2K for the very first time, neutrinos have been used by mankind as information carriers for long distances. It is easy to think about methods to modulate the pulsing of the neutrino beam and it is evident that information can be transported from the source to its destination, which is a neutrino detector. Of course this method seems to be very elaborate and costly, but as strange as it may appear at the first glance it might exhibit also some advantages: one can send neutrinos through dense matter like the Earth without any noticeable attenuation and no magnetic or electric fields may change the direction of theses elusive particles. It will be also quite difficult to intercept a neutrino beam. Future will tell us if this may be an interesting technological application of neutrino physics.

The **main injector neutrino oscillation search (MINOS)** experiment in the United States measured neutrino oscillations with accelerator neutrinos at

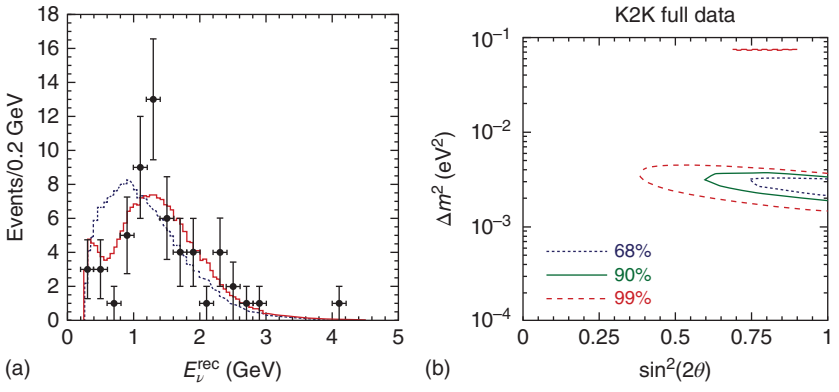

Figure 3.15 Energy spectrum (a) and oscillation contour plots (b) obtained in the long baseline accelerator experiment K2K as published in [157]. The solid line on (a) represents the best fit to the data with oscillations; the dashed line shows the expected shape for no oscillations. Panel (b) shows the allowed parameter islands for 1, 2, and 3σ contours. Source: Ahn et al. 2006 [157]. Reproduced with permission of American Physical Society.

higher energies and with a baseline of 735 km [158]. Instead of a Cherenkov detector, a large iron and scintillator calorimeter with tracking capabilities was used. The accelerator at Fermilab, close to Chicago, can produce a π^+- as well as a π^--meson-beam by changing the polarity of focusing magnets. Therefore, MINOS is able to study not only the ν_μ-disappearances but also $\overline{\nu}_\mu$-disappearances as function of the energy and with this method CPT invariance can be probed. In addition MINOS is capable to use atmospheric neutrinos as well to study oscillation parameters. The MINOS experiment has been operating since 2005 and is still taking data. A near detector is used for beam monitoring and the far detector is located in the Soudan Underground Laboratory. In Figure 3.16 the combined analysis of MINOS disappearance experiment is shown [159].

Long baseline neutrino as well as antineutrino data and also MINOS atmospheric neutrino data are in agreement and are used in a combined analysis. Figure 3.16 shows the allowed oscillation parameter space and compares the MINOS ν_μ only result (red line) with the combined (ν_μ and $\overline{\nu}_\mu$ plus atmospheric-ν) analysis (black line). Also shown are results from SK atmospheric data analysis and from the K2K long baseline experiment. All experimental data are consistent with neutrino oscillations and with MINOS an era of high precision measurements of the mass splitting Δm^2 has been opened.

K2K as well as MINOS are so far disappearance experiments, considering $\nu_\mu \Leftrightarrow \nu_\tau$ oscillations, because the neutrino energy is not high enough to create $\tau^\pm$-leptons at high rates. The energy threshold for charged τ-lepton production is at about 3.5 GeV. Therefore, ν_τ-appearance experiments require very long baselines, as the oscillation length scales linearly with the neutrino energy. Another problem in ν_τ-appearance experiments is the fact that $\tau^\pm$-leptons are particles with a very short lifetime. Therefore, a very fine-segmented but nonetheless also large detector has to be constructed to be able to observe a

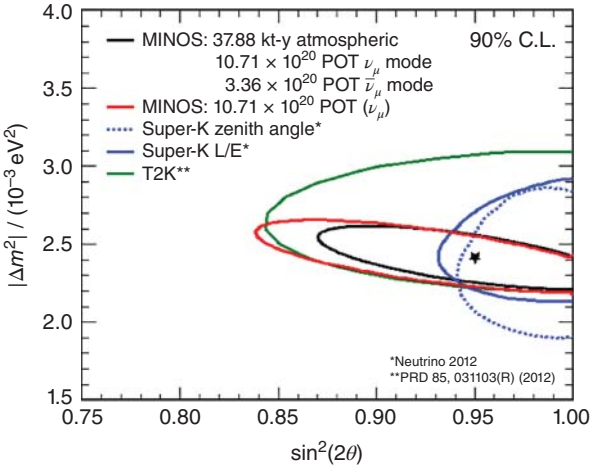

Figure 3.16 Allowed oscillation parameter space by MINOS as published in [159] in comparison with Super-Kamiokande atmospheric and K2K long baseline results. Source: Adamson et al. 2013 [159]. Reproduced with permission of American Physical Society.

ν_τ-track with succeeding decay products. Within the CERN Neutrinos to Gran Sasso (CNGS) project a pulsed ν_μ-beam with an average energy of about 17 GeV was sent from CERN at Geneva down to the Gran Sasso underground laboratory.

There, the **oscillation project with emulsion tracking apparatus (OPERA)** detector has been constructed to observe ν_τ-events. OPERA is a hybrid detector, consisting of 1.3 kton of lead bricks acting as target, which are equipped with emulsion layers. The bricks are arranged in planes and adjacent to them scintillating plates with good position resolution are placed. The scintillator planes allow to select neutrino candidates and are used to identify the brick, in which the neutrino interaction was registered and a large muon spectrometer allows to measure the muon charge and momentum.

The baseline of 732 km between CERN and Gran Sasso is not optimized for ν_τ-appearance observations at that high energies, as the oscillation phase is small: $\Phi(E_\nu, L) = \Delta m^2 L/4E_\nu \sim 0.083 \cdot (\pi/2)$ for $\Delta m^2 \sim 2.4 \times 10^{-3}$ eV^2 and hence far away from the expected oscillation maximum $\pi/2$. In Eq. (3.61) the appearance probability is reported:

$$P_{\mu\tau} = \sin^2 2\theta_{23} \cos^4 \theta_{13} \sin^2 \left(\frac{\Delta m^2_{31} L}{4E} \right) \tag{3.61}$$

In spite of the fact that the baseline is not optimized, the experiment has finally observed ν_τ-events. In a total of 10 ν_τ-events have been found between 2008 and 2012 [160]. The ν_τ appearance has been confirmed with a significance level of 6.1σ [160]. This result is consistent with expectations from actual neutrino oscillation parameters taking into account the total neutrino luminosity, detection efficiencies, and the expected oscillation probability. For the first time, the appearance of

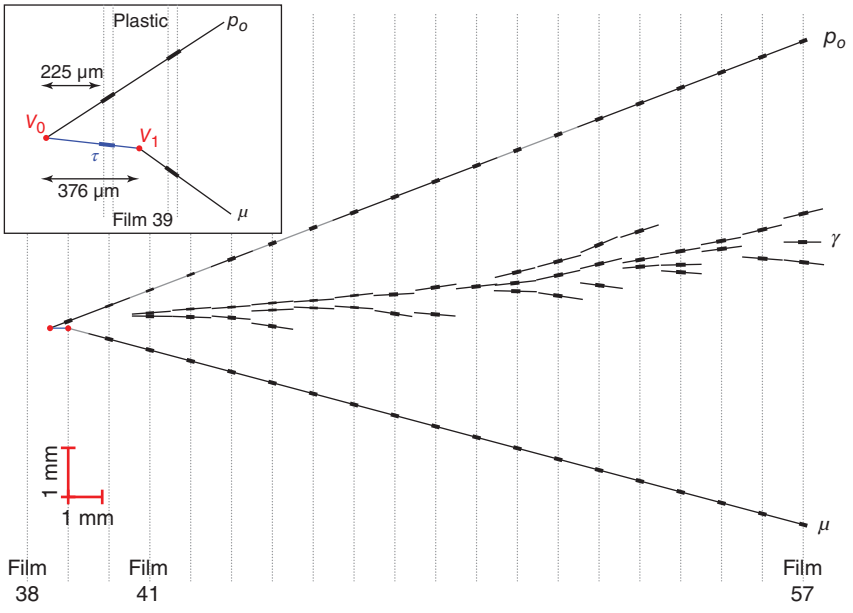

Figure 3.17 The third ν_τ candidate in OPERA in projected topography. In the insert the kink of $\tau - \mu$-track is shown. Source: Agafonova et al. 2018 [160]. Reproduced with permission of American Physical Society.

$\nu_\mu \Leftrightarrow \nu_\tau$ oscillations was observed directly. In Figure 3.17 the projected topology of the third ν_τ-candidate is depicted.

Here one can clearly see the signature for a τ-event the collaboration was looking for. The oscillated ν_τ produces a charged τ-lepton in a cc reaction of the type $\nu_\tau + X \to Y + \tau$, where X and Y are some hadronic states. The τ-lepton decays after a path length of about ~ 400 µm via $\tau \to \mu + \nu_\tau + \nu_\mu$. The neutrinos leave the detector without interaction, but carry away momenta, and therefore a kink between the τ- and μ-tracks is observed.

In Japan the **T2K** experiment has been installed as successor of the pioneering K2K project. A 30-GeV proton beam provided by the proton synchrotron at JPARC is used to create high energy pions, which are led into a decay tunnel. Again, the ν_μ-beam is sent to the SK detector at a distance of 295 km. T2K is a new generation accelerator experiment with a significantly increased neutrino luminosity. In addition, a highly advanced near detector with tracking capabilities has been set up in order to monitor the neutrino beam. It is designed for precision measurement and identification of charged particles and neutral pions. With this setup the beam intrinsic electron neutrino component could be determined experimentally [161], which forms an irreducible background to the appearance signal in the T2K experiment. This feature is important for the measurement of the mixing angle θ_{13} and for future plans to get hands on the CP parameter δ_{CP}. Also new is the fact that the SK detector as well as the near detector are not at the center of the neutrino beam but centered off-axis by c. 2.5°. The off-axis beam is more similar to a monoenergetic neutrino beam. The beam intensity is somehow

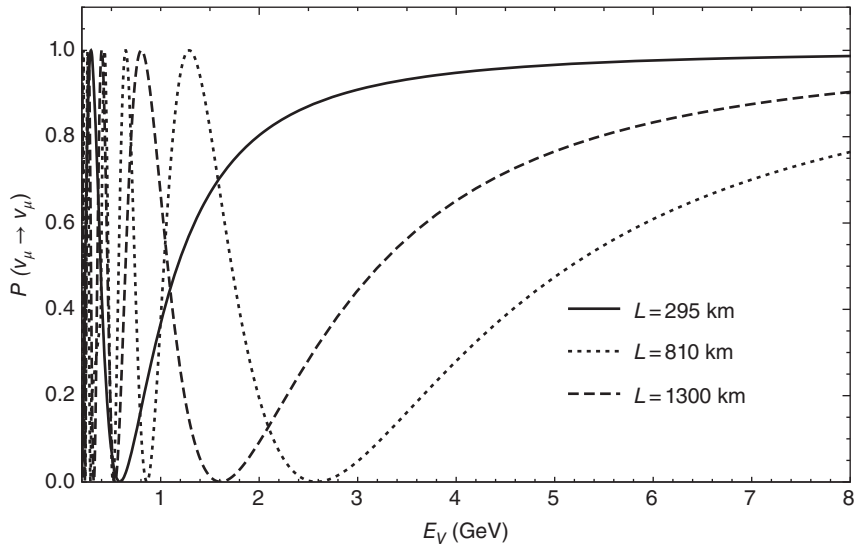

Figure 3.18 Disappearance oscillation probability, $P_{\mu\mu}$, for T2K, NOνA, and DUNE baselines and mean energies (0.6 GeV for T2K and 2 GeV for NOνA and DUNE).

lower in the off-axis position, but this disadvantage is more than compensated by the fact that the neutrino energy distribution is much narrower. The neutrino energy is peaked at about 0.6 GeV, which optimizes the oscillation length, $L_{\text{osc}} \sim 310$ km with $\Delta m^2 = 2.5 \times 10^{-3}$ eV^2. The T2K experiment has observed ν_μ-disappearance with very high statistics [162]. In Eq. (3.62) the oscillation probability for ν_μ-disappearance is reported.

$$P_{\mu\mu} = 1 - (\cos^2\theta_{13}\sin^2 2\theta_{23} + \sin^2\theta_{23}\sin^2 2\theta_{13})\sin^2\left(\frac{\Delta m^2_{32} L}{4E}\right) \tag{3.62}$$

In Figure 3.18 the oscillation probability $P_{\mu\mu}$ for $\Delta m^2 = 2.5 \times 10^{-3}$ eV^2 for the T2K baseline is shown. Figure 3.18 shows how T2K is optimized for a ν_μ-disappearance experiment with an almost monoenergetic neutrino beam. In the same figure we anticipate a similar plot for the NOνA and Deep Underground Neutrino Experiment (DUNE) baselines. The result for T2K from 2013, as an example, is shown in Figure 3.19. Here, the 58 μ-like events, which produced single Cherenkov rings in the SK detector, are plotted. The observed effect is tremendous and in very good agreement with former measurements performed by SK atmospheric, K2K, and MINOS. Besides this success the real importance of T2K is in its potential to explore ν_e appearance effects. This is important, because in this way the coupling provided by the mixing angle θ_{13} can be explored and a first glance on the term, which leads to CP-violating effects may be gained.

3.4.2.1 Long Baseline Experiments and θ_{13}

The already mentioned long baseline experiment T2K is the first that can observe the appearance of electron neutrinos in a muon neutrino beam due to

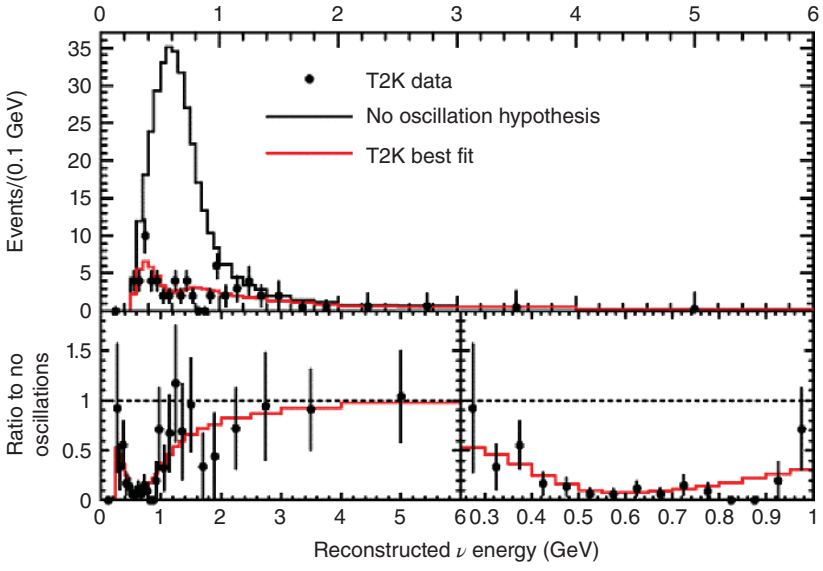

Figure 3.19 T2K disappearance ν_μ measurement at high statistics. Upper plot: the observed spectrum with the best fit is compared with the no-oscillation expectation. Lower plot: the ratio between data and no-oscillation expectation is shown in two energy bands. Source: Abe et al. 2013 [162]. Reproduced with permission of American Physical Society.

a nonvanishing mixing angle θ_{13} [163]. A total of 28 electron neutrino events were detected with an energy distribution consistent with an appearance signal, corresponding to a significance of 7.3σ when compared to 4.92 ± 0.55 expected background events. As mentioned before the determination of the irreducible contamination of the beam with electron neutrinos by a near detector was crucial for this measurement. The appearance signal depends on several parameters of the mixing matrix. In Eq. (3.63) the appearance probability is reported at first order in the matter effects.

$$
\begin{aligned}
P_{\mu e} \approx\ & 4c_{13}^2 s_{13}^2 s_{23}^2 \sin^2 \Delta_{31} \\
& + 8c_{13}^2 s_{12} s_{13} s_{23} (c_{12} c_{23} \cos\delta_{\mathrm{CP}} - s_{12} s_{13} s_{23}) \cos\ \Delta_{32}\ \sin\ \Delta_{31}\ \sin\ \Delta_{21} \\
& - 8c_{13}^2 c_{12} c_{23} s_{12} s_{13} s_{23} \sin\ \delta_{\mathrm{CP}}\ \sin\ \Delta_{32}\ \sin\ \Delta_{31}\ \sin\ \Delta_{21} \\
& + 4s_{12}^2 c_{13}^2 (c_{12}^2 c^2 23 + s_{12}^2 s_{23}^2 s^2 13 - 2c_{12} c_{23} s_{12} s_{23} s_{13} \cos\ \delta_{\mathrm{CP}}) \sin^2 \Delta_{21} \\
& - 8c_{13}^2 s_{13}^2 s_{23}^2 \frac{aL}{4E_\nu} (1 - 2s_{13}^2) \cos\ \Delta_{32}\ \sin\ \Delta_{31} \\
& + 8c_{13}^2 s_{13}^2 s_{23}^2 \frac{a}{\Delta m_{31}^2} (1 - 2s_{13}^2) \sin^2 \Delta_{31}
\end{aligned}
\tag{3.63}
$$

where $c_{ij} = \cos\theta_{ij}$, $s_{ij} = \sin\theta_{ij}$, $\Delta_{ij} = \Delta m_{ij}^2 / 4E_\nu$, and $a = 2\sqrt{2} G_F N_e E_\nu$. We have used $N_e = N_A \rho \langle Z/A \rangle$, with $\rho \sim 4$ g/cm^3 and $\langle Z/A \rangle \sim 0.5$. In Figure 3.20 the expected oscillation probability in the $\nu_\mu \to \nu_e$ appearance channel for two δ_{CP} values and for the T2K baseline is shown. We notice that on this baseline matter effects are negligible. On the contrary, above 1000 km they become significant.

Under the assumption of $\delta_{\mathrm{CP}} = 0, \theta_{23} = 45^\circ$ and normal mass ordering a best-fit value of $\sin^2 2\theta_{13} = 0.140^{+0.038}_{-0.032}$ is obtained. In Figure 3.21 the allowed 1-σ and 90%

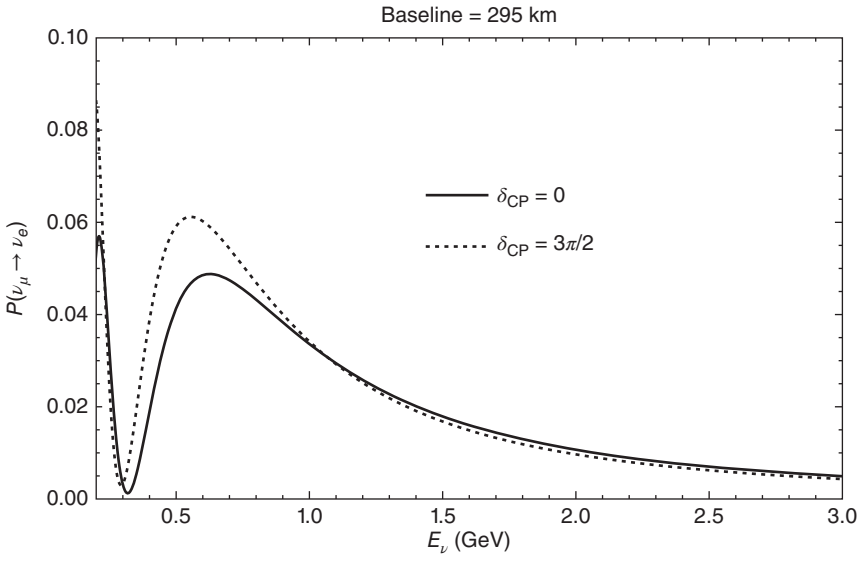

Figure 3.20 Oscillation probability $P_{\mu e}$ for T2K and for two δ_{CP} values in the normal mass ordering scenario.

CL regions for $\sin^2 2\theta_{13}$ as a function of δ_{CP} and the NMO are shown. The values of θ_{23} and Δm^2_{32} are varied within their constraints. For comparison the average value from all experiments on θ_{13} is shown as well.

The goal of measuring θ_{13} via electron appearance is followed by the long baseline **NOνA** experiment in the United States. The intensive ν_μ beam, which is supplying MINOS at the Soudan mine and is sent from Fermilab, is now also used off axis by a new, large neutrino detector placed at Ash River at a distance of 810 km. The scientific program of the experiment encompasses ν_μ disappearance as well as ν_e appearance modes, both in the neutrino and the antineutrino channels. Two functionally identical detectors, optimized for ν_e-identification, are used. A ∼14 kt liquid scintillator far detector in Ash River, which has only 3 m of overburden as shielding, and a ∼300 t near detector at Fermilab at a distance of 1 km from the accelerator. Both detectors are placed 14 mrad off-axis to the neutrino beam and has been operational since August 2014. The geometrical displacement provides the experiment with a nicely centered neutrino flux around 2 GeV. The far detector consists of a horizontal ashlar with 60 m length and a quadratic cross section of 15.6×15.6 m^2. It is segmented into 928 layers with plastic cells, which are filled with scintillator and the light is read out by wavelength shifting fibers and avalanche photodiodes (APDs). Neutrino separation against cosmic muon events in the huge far detector is a challenge due to the shallow overburden and is performed via neural net evaluation and an analysis of event topologies. The main scientific goals of the experiment are connected with the open questions of the neutrino ordering and the CP value in the neutrino mixing matrix. In August 2015, first results of the NOνA experiment were published at summer conferences. The muon neutrino spectrum of 33 candidate events is shown in Figure 3.22 and compared to the no-oscillation prediction [164]. Again a clear evidence for neutrino oscillation is being demonstrated. In addition, new

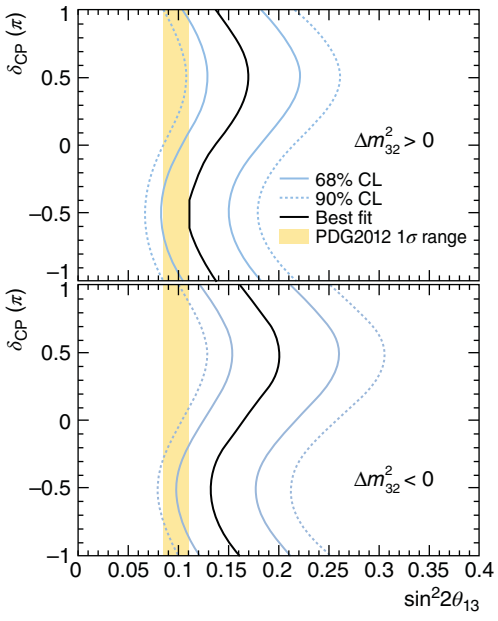

Figure 3.21 The 68% and 90% CL allowed regions for $\sin^2 2\theta_{13}$ as a function of δ and the neutrino mass ordering. The shadowed band corresponds to the averaged value on θ_{13} and is shown for comparison. Source: Abe et al. 2014 [163]. Reproduced with permission of American Physical Society.

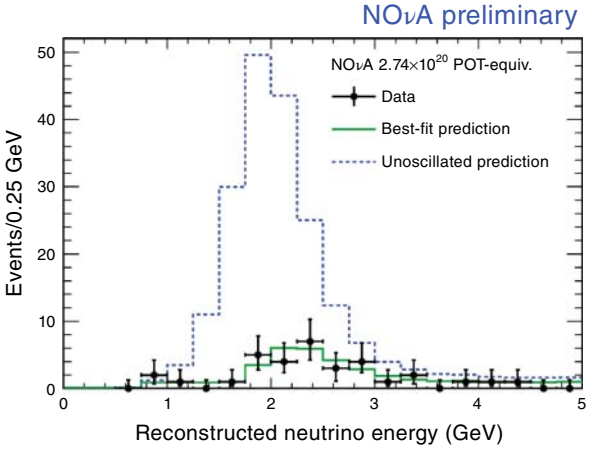

Figure 3.22 Preliminary ν_μ spectrum with 33 events as obtained in the long baseline NOνA off-axis experiment and made open to the public in August 2015. The disappearance of ν_μ is evident. Source: From Sanchez 2015 [164].

input for a higher precision on the mixing angles θ_{13} and on the octant of θ_{23} is expected from NOνA for the future. As of 2019, T2K and NOvA have measured $\sin^2\theta_{23}$ at the level of about 7% (still consistent with maximal mixing), shown a clear ν_e appearance, probed at 2σ level CP violation in lepton sector, and explored mass ordering with an initial preference for normal ordering.

3.4.3 Reactor Neutrinos

Nuclear reactors emit electron antineutrinos $\overline{\nu}_e$ at very high intensities. A 1-GW reactor will produce about 2×10^9 $\overline{\nu}_e/\text{cm}^2/\text{s}$ at 1 km distance from the core.

Therefore, neutrino experiments at nuclear reactors have a long history. Indeed, it was the famous experiment "Poltergeist" installed close to the reactor core at Savannah river, where C. Cowan and F. Reines have measured neutrinos for the very first time in 1956 [124].

The neutrino sources are β decays of neutron-rich isotopes, which are products from the fission of ^{235}U, ^{238}U, ^{239}Pu, and ^{241}Pu. In commercial, light-enriched nuclear reactors, all U- and Pu-isotopes contribute to the total spectrum, in some special cases like research reactors with highly enriched ^{235}U content the contributions from ^{238}U and the Pu-isotopes are negligible. The total energy spectrum is the sum of all β spectra. About 10 000 individual β decays from ~800 isotopes, weighted with their fission yields and their transition strengths contribute to the total spectrum, which has a continuous shape and reaches maximal values at ~10 MeV.

An exact calculation of the total spectrum *ab initio* is very difficult due to the high number of β decays and considering the fact that not all fission yields, intensity distributions, and β decay shape factors are known at high precision. Systematic effects and missing information in nuclear databases lead to final relative uncertainties in the 10–20% range [165]. However, the total $\overline{\nu}_e$ spectrum can be derived by measuring the cumulative β spectra from the main fuel isotopes listed above, followed by an algorithm that converts the β to a neutrino spectrum. Cumulative β spectra from ^{235}U, ^{239}Pu, and ^{241}Pu have been measured at the high resolution iron-core electron spectrometer at Institute-Laue-Langevin (ILL) (BILL) spectrometer at the ILL research reactor already in the 1980s [166–169]. Recently, also the cumulative spectrum of ^{238}U, which undergoes fission only with fast neutrons was measured [170]. Also the conversion method has its systematic uncertainties and recently a more accurate approach has been developed by combining information from nuclear databases and β spectra associated with the fission of the main contributing isotopes [165]. While the shapes of the spectra and their uncertainties are comparable to that of the previous analysis of the BILL data, the normalization is shifted by about +3% on average. Possible implications on the interpretation of former oscillation experiments will be discussed later.

Neutrino detection occurs always via the so-called inverse β decay:

$$\overline{\nu}_e + p \rightarrow e^+ + n \tag{3.64}$$

The target as well as detecting material is usually an organic, liquid scintillator with a high number of free protons. The charged positron produces a prompt light signal, whereas the neutron slows down until it is captured by a nucleus. The typical time constant for this process is in the range of $\sim 2 \times 10^2$ μs for neutron capture on a proton. This feature of a *delayed coincidence* is used experimentally to distinguish neutrinos from background signals with high efficiency. Neutron capture by a proton leads to a 2.2 MeV γ emission, due to the reaction $p + n \rightarrow {}^2\mathrm{H} + \gamma$. It is possible to add chemical elements[9] to the liquid scintillator in order to increase the visible energy of the delayed event and to lower the average capture

9 For instance, Gd-isotopes have a very high neutron capture cross section and emit a γ-cascade with an average energy close to 8 MeV.

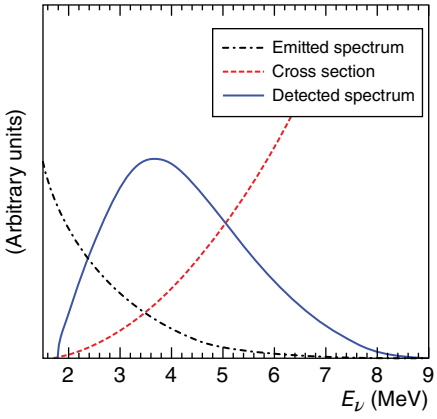

Figure 3.23 Shape of a non-oscillated reactor neutrino spectrum observed via the inverse β decay on free protons as a function of the emission spectrum and the interaction cross section. Arbitrary units are used. Source: Mueller et al. 2011 [171]. Reproduced with permission of American Physical Society.

time to values below $\sim 10^2$ µs, which may improve the signal to background ratio significantly, if the experiment is suffering due to a high accidental background level.

Only neutrinos with energies above the reaction threshold $Q = ((m_n + m_e)^2 - m_p^2)/2m_p \simeq 1.806$ MeV can contribute to the event rate. The visible energy E_{vis} of a neutrino event is enhanced by the positron annihilation energy of ~1 MeV and is therefore $E_{\text{vis}} \simeq E_\nu - 0.8$ MeV. The kinetic energy of the neutron is below ~0.1 MeV and is usually neglected. The cross section of the inverse β decay can be expressed in terms of the neutron lifetime τ_n and the phase space factor f_{ps} as

$$\sigma_\nu = \frac{2\pi^2/m_e^5}{\tau_n f_{\text{ps}}} E_e p_e \sim 0.98 \times 10^{-43} \text{ cm}^2 \ (E_e p_e/\text{MeV}^2) \tag{3.65}$$

where E_e and p_e are the positron energy and momentum, respectively. The non-oscillated neutrino spectrum is a continuous distribution with a broad peak around 4 MeV. This is the result of the exponentially decreasing reactor flux folded with the neutrino cross section, which increases at these energies effectively with E_ν^2 (see Figure 3.23).

Alternatively the cross section can be of course expressed via the weak coupling constant. With the expression used above uncertainties of the weak coupling constant, the Cabibbo angle and nuclear effects can be avoided, but it couples the cross section to the reciprocal value of the neutron lifetime. Therefore, systematic uncertainties on the neutron lifetime have an impact on the accuracy of absolute reactor neutrino experiments using the inverse β decay as detection reaction. In order to avoid these systematic effects, relative measurements make use of a so-called near detector, which uses the same target liquid and has the task to monitor the nuclear reactor status. The later aspect is important, because the different nuclear fuel contributions from the U- and Pu-isotopes vary with time during reactor operation.

Reactor experiments are always of the disappearance types, because the neutrino energies are too low to produce charged muons or τ-leptons. Neutrino oscillations can be observed in reactor experiments by analyzing the measured neutrino spectrum and the total neutrino flux or event rate at the detector

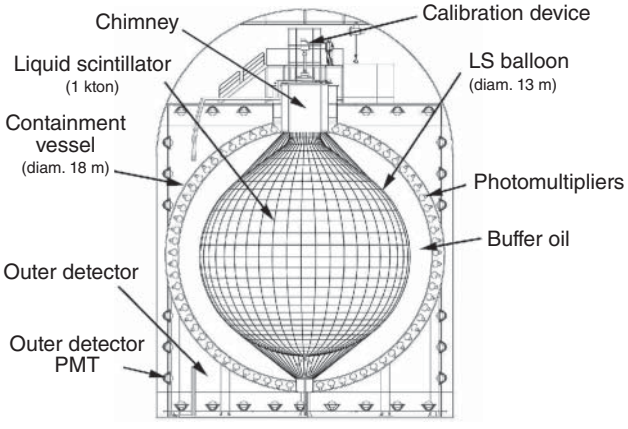

Figure 3.24 Schematic scheme of the 1 kt liquid scintillator detector used in the KamLAND reactor neutrino experiment in Japan.

location. For a long baseline (>1 km) reactor neutrino experiment, the electron antineutrino survival probability is reported in Eq. (3.66):

$$P_{ee} = \cos^4\theta_{13}\left(1 - \sin^2 2\theta_{12}\sin^2\left(\frac{\Delta m^2_{21}L}{4E}\right)\right) + \sin^4\theta_{13} \tag{3.66}$$

where L is the distance between the reactor and the detector.

For a short baseline reactor neutrino experiment, the electron antineutrino survival probability is reported in Eq. (3.67):

$$P_{ee} = 1 - \sin^2 2\theta_{13}\sin^2\left(\frac{\Delta m^2_{31}L}{4E}\right) - \cos^4\theta_{13}\sin^2 2\theta_{12}\sin^2\left(\frac{\Delta m^2_{21}L}{4E}\right) \tag{3.67}$$

with the assumption that $\Delta m^2_{31} \simeq \Delta m^2_{32}$. An interesting aspect is the comparison of solar and reactor neutrino disappearance experiments, for the former are observing electron neutrinos (i.e. ν_e), while the latter are observing electron antineutrinos (i.e. $\overline{\nu}_e$). In case of CPT invariance,[10] effects on oscillation probabilities should be the same in both cases.

The **KamLAND** experiment in the Kamioka underground laboratory in Japan performs an absolute reactor neutrino experiment using a 1 kt liquid scintillator detector. A scheme of the detector is shown in Figure 3.24.

KamLAND measures the integral neutrino flux coming from about 70 nuclear reactors located in Japan and Korea. Most of the reactors have distances to KamLAND between 150 and 200 km. As the neutrino detection cross section increases with energy and the reactor neutrino flux decreases with E_ν, the expected no-oscillation e^+-spectrum has a maximum at around 3 MeV. In Figure 3.25 this expected spectrum is shown together with experimental data as published in [172].

10 C, charge conjugation; P, parity transformation; T, time reversal.

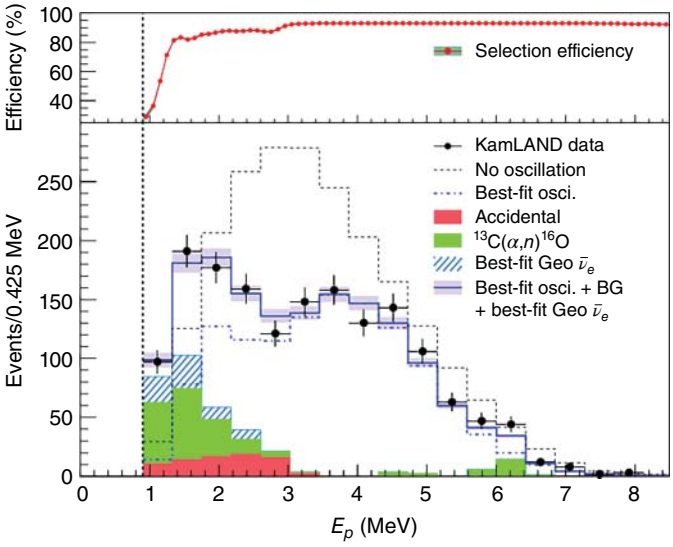

Figure 3.25 Prompt event energy spectrum of electron antineutrino candidate events. On top the energy dependent selection efficiency is shown. The data show statistical, the blue band systematic uncertainties. Contributions due to background and caused by terrestrial (geo-) neutrinos are also shown. Evident is the clear energy dependent deviation from the no-oscillation expectation, shown as dashed curve. Source: Abe et al. 2008 [172]. Reproduced with permission of American Physical Society.

Evident is an energy dependent deviation of the experimental data from the no-oscillation expectation. The measured energy distribution is in very good agreement with neutrino oscillations. The systematic uncertainties are shown as blue band around the full line, which shows the best-fit oscillation expectation in Figure 3.25. In addition the plot shows background contributions from radioactivity in the scintillator, from geo-neutrinos, and due to spallation events of cosmic muons. The recent long-term shutdown of Japanese nuclear reactors as a consequence of the earthquake and tsunami in March 2011 has resulted in a significantly reduced reactor flux at the KamLAND site. This gave the opportunity to check and to confirm the background model used for the KamLAND $\overline{\nu}_e$ oscillation analysis [173].

Neutrino oscillation were not yet proved when the KamLAND detector was constructed. The experiment was motivated by the status of solar neutrino physics at that time. KamLAND was built to probe the so-called "large mixing angle" solution, which was one parameter set compatible with solar neutrino results. It turned out that this solution is indeed the correct one. Furthermore, KamLAND data could be used to constrain the neutrino mass differences with unprecedented accuracy. How well the data correspond to neutrino oscillations is demonstrated when plotted over E_ν/L, as shown in Figure 3.26. From the same plot one can see that at the average distance, weighted over thermal power, between source and detector of about 200 km at mean energies of about 3 MeV, $L/E \sim 70$ km corresponds to the second oscillation maximum.

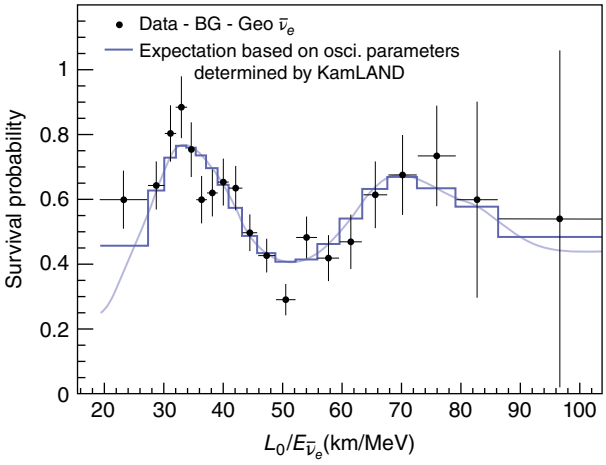

Figure 3.26 KamLAND reactor neutrino data as function over E_ν/L in comparison with the oscillation expectation using the best-fit parameters. Error bars are statistical only. Source: Abe et al. 2008 [172]. Reproduced with permission of American Physical Society.

In the assumption of CPT invariance, the KamLAND and solar neutrino data can be combined. The oscillation parameters derived from a global analysis including solar and reactor neutrino data are [174]

$$0.291 < \sin^2\theta_{12} < 0.318 \tag{3.68}$$

$$7.20 \times 10^{-5} < \Delta m^2_{21}/\ \mathrm{eV}^2 < 7.51 \times 10^{-5} \tag{3.69}$$

within 1-σ limits. Yet, a remark is in order, for there is a tension at 2σ level on the value of Δm^2_{21} between the best fit including only solar data ($4.82^{+1.20}_{-0.60} \times 10^{-5}$ eV^2) and the one including solar and KamLAND data ($7.54^{+0.19}_{-0.18} \times 10^{-5}$ eV^2) [175]. This yet unsolved discrepancy could be a sign of a subleading effect due to new physics.

It is evident that ν_e disappearance experiments provide different parameter sets with respect to ν_μ experiments. Both mixing angles are quite large, but they differ. Even more pronounced is the difference between the mass splitting squared, which is at a factor ∼30. One can assign the mixing angle θ_{12} to the value measured by solar experiments and KamLAND, and θ_{23} to the value measured with atmospheric neutrinos and confirmed by accelerator long baseline experiments. As far as θ_{13} is concerned, as reported above, the first hint on this mixing angle came from T2K; however, the definitive answer was provided by reactor experiments.

The **Double Chooz**, **Daya Bay**, and **RENO** experiments measure reactor $\overline{\nu}_e$ spectra at a baseline between 1 and 2 km. Hence, they are sensitive to mass differences $\Delta m^2 \sim 2.5 \times 10^{-3}$ eV^2 at 3 MeV average energy. At this baseline the dominant oscillation pattern is driven by θ_{13} and Δm^2_{31}, as it is shown in Eq. (3.67).

Former experiments at this short baseline performed by **Chooz** and **Palo Verde** did not observe oscillations, and from their analysis it became clear that θ_{13} is

small with respect to the other mixing angles. The limit derived at the end of the last century by Chooz is $\sin^2\theta_{13} < 0.039$ at $\Delta m^2 \sim 2.5 \times 10^{-3}$ eV^2 [176].

The sensitivity on the mixing angle in disappearance experiments is limited by systematic uncertainties. Therefore, the following generation experiments, namely, Double Chooz, Daya Bay, and RENO are all using at least two detectors in order to improve their sensitivity on small neutrino oscillation amplitudes. A second so-called near detector, very close to the reactor core, with basically the same structure as the far detector is used to monitor the nuclear reactors. The distances for the close detectors are chosen such that the influence of oscillation due to θ_{13} is negligible. Systematics besides reactor-based problems are uncertainties on the cross section, background conditions, and detection efficiencies. It is the aim of the new generation experiments to minimize these effects by using the same target material, detector sizes, and by providing similar shielding conditions.

All three experiments have a comparable setup: they are using Gd-loaded liquid scintillators as inner targets and they use so-called γ-catcher volumes without Gd-loading in order to obtain high efficiencies for detecting γ-rays from Gd-excited nuclei. The γ catcher is also useful to reconstruct the original neutrino energy with better accuracy, because it will also detect the 511 keV γ-rays from positron annihilation with high efficiency, even when the annihilation takes place close to the surface of the target container. A non-scintillating buffer region shields the inner parts against external radioactivity. In addition outer detectors are used as muon veto systems in order to get control over cosmogenic generated background events and those stemming from fast neutrons, which can be produced as secondaries in spallation processes inside and outside the target volume. In Figure 3.27 the experimental setup of the Double Chooz far detector is shown as an example, which is using even two external muon veto systems.

All three experiments observe a clear disappearance signal in the integral counting rate as well as in the spectral distribution due to a nonvanishing θ_{13} value. The amplitude of the deficit delivers $\sin^2(2\theta_{13})$ and the position of the dip in the spectrum can be used to determine Δm^2_{31}. The most significant result is obtained so far by the Daya Bay experiment, which has been running eight antineutrino detectors simultaneously since October 2012. The first sign of a nonvanishing θ_{13} value was coming from the Double Chooz experiment [177]. In combination with the accelerator T2K experiment, already a three sigma signal could be obtained and soon Daya Bay [178] and RENO [179] confirmed this result with significantly improved accuracy.

In Figure 3.28 the measured positron energy spectrum of the far detector of the Daya Bay experiment in China is shown in comparison with the expected distribution for the no-oscillation scenario based on the data taken by the near detectors. This result was published in 2015 after a total exposure of 6.9×10^5 GW-ton-days corresponding to a 404-day lasting measurement period with eight detectors, combined with 217 days of data acquisition with six detectors [180]. The statistical power of this experiment is impressive. In Figure 3.29 the oscillation hypothesis is tested by showing the neutrino survival probability as a function of L/E_ν. The solid line represents the expected distribution using

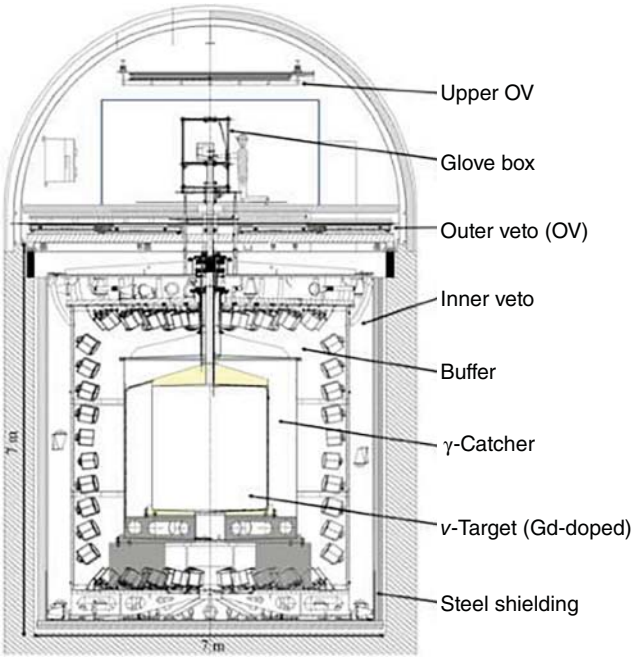

Figure 3.27 Schematically view of the Double Chooz far detector. As neutrino target a Gd-loaded scintillator is used, followed by a γ-catcher and a non-scintillating buffer liquid. Outside an inner and outer muon veto detect penetrating cosmic muons. Source: Abe et al. 2012 [177]. Reproduced with permission of American Physical Society.

the best-fit oscillation parameters, whereas the dashed line shows the no-oscillation case.

The best-fit oscillation parameters obtained by the Daya Bay experiment in 2015 are $\sin^2 2\theta_{13} = 0.084 \pm 0.005$ and $\Delta m^2_{13} = (2.42 \pm 0.11) \times 10^{-3}$ eV^2 [180]. One may compare this result with Double Chooz as obtained in 2014 after 467.9 days of data taking with one detector at a distance of 1050 m from two reactor stations with 8.5 GW$_{\text{th}}$ thermal power in total. Since the end of 2014, Double Chooz has been running with two detectors and so far is the only reactor experiment that could measure the background during a period, where both reactors are shut down. Due to the low background achieved, it was possible to add an analysis, where the neutron capture on hydrogen in the γ-catcher is used as a signal. A similar analysis was later repeated by Daya Bay successfully. The Double Chooz value for the oscillation amplitude with one detector is $\sin^2 2\theta_{13} = 0.090^{+0.032}_{-0.029}$ [181]. In 2014 RENO published $\sin^2 2\theta_{13} = 0.101 \pm 0.008_{\text{stat}} \pm 0.010_{\text{syst}}$ [182]. This result is using neutrino data from two detectors running for $\sim$ 800 days and is based on a rate analysis only. All results obtained in the three reactor experiments are so far in agreement within their statistical and systematic uncertainties. Daya Bay has published a Δm^2 result as shown in Figure 3.30.

In Figure 3.30 the Daya Bay result from 2015 is depicted in a Δm^2 versus $\sin^2 2\theta_{13}$ diagram. Shown are the 1-, 2-, and 3-σ allowed regions as well as the

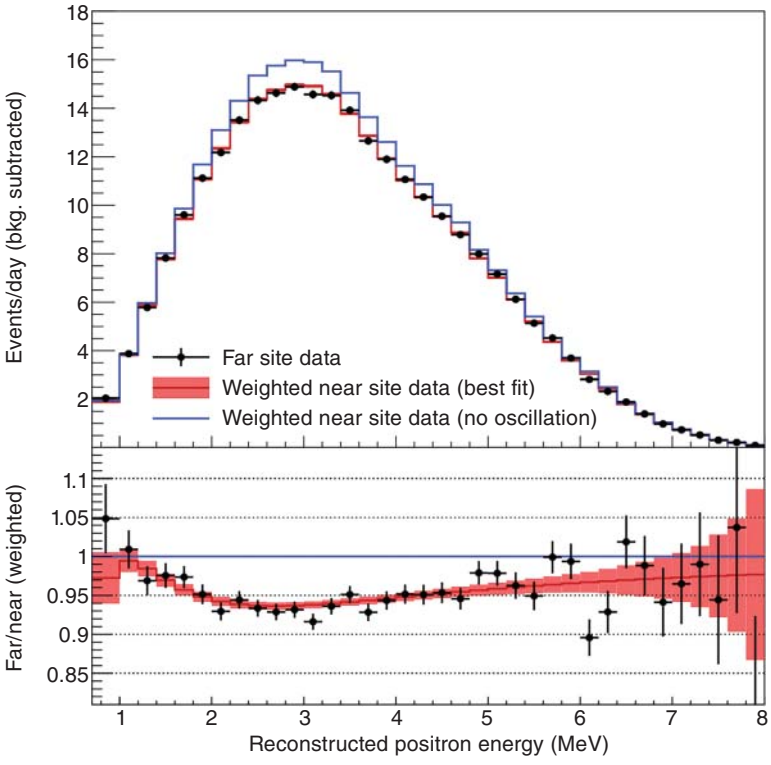

Figure 3.28 Background subtracted positron spectrum of the Daya Bay far detector in comparison with the expected distribution from the near sites. The error bars are statistical. Below the ratio of the spectrum to the no-oscillation case is shown. Source: An et al. [180]. Reproduced with permission of American Physical Society.

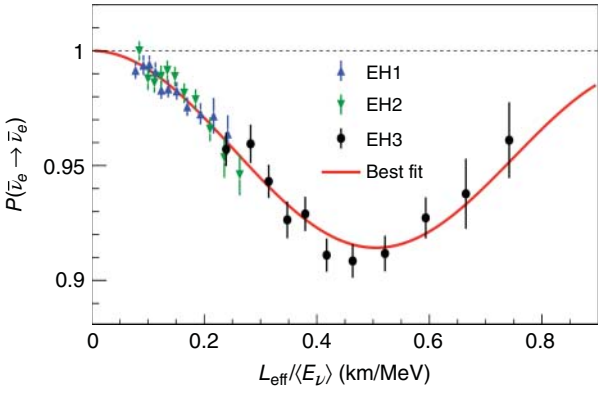

Figure 3.29 The antineutrino survival probability as a function of the effective propagation distance divided by the average neutrino energy. Error bars are statistical. The labels EH1 and EH2 are used for near-site detectors, whereas EH3 stands for the far distance detector. The full line represents the expected distribution for the best-fit oscillation parameters. Source: An et al. [180]. Reproduced with permission of American Physical Society.

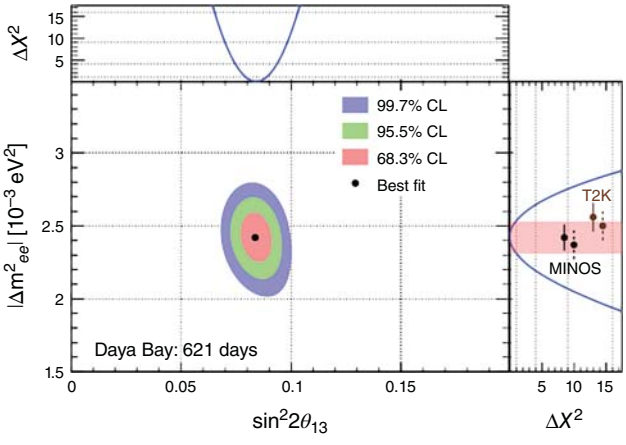

Figure 3.30 Regions of the oscillation parameter space allowed in the Daya Bay experiment. Shown are the 1-, 2-, and 3-σ contours together with the best-fit value. Also shown are the normalized $\Delta\chi^2$ distributions. The Daya Bay result on Δm^2 is in agreement with MINOS and T2K accelerator experiments. Source: An et al. [180]. Reproduced with permission of American Physical Society.

best-fit values [180]. In addition the $\Delta\chi^2$-distributions for the two oscillation parameters are shown in the adjoining panels. The 1-σ band from Daya Bay is consistent with results from the accelerator based experiments MINOS and T2K. The value Δm^2_{ee} used here is an effective parameter, which depends on the still open question of the neutrino mass ordering. With reference to Eq. (3.67), one can replace $\sin^2\delta_{31}$ with $\sin^2\delta_{ee} = \cos^2\theta_{12}\sin^2\delta_{31} + \sin^2\theta_{12}\sin^2\delta_{32}$. This definition removes the small difference between Δm^2_{31} and Δm^2_{32}. The measured value yields $\Delta m^2_{32} = (2.37 \pm 0.11) \times 10^{-3}$ eV^2 under the assumption of a normal ordering (i.e. $m_3 > m_2$) and $\Delta m^2_{32} = -(2.47 \pm 0.11) \times 10^{-3}$ eV^2 and vice versa.

3.5 Conclusions and Open Questions

Results from neutrino experiments performed within the last two decades revealed the phenomenon of neutrino oscillations clearly and opened the window to physics beyond the standard model. At the beginning anomalies were found in the data of solar and atmospheric experiments, which puzzled scientists. With the large and high resolution experiment by SK, the first clear evidence for oscillation of atmospheric neutrinos was found. With Sudbury Neutrino Observatory (SNO) the transition of solar electron neutrinos to other active flavors has been demonstrated. The experiment KamLAND observed an energy dependent deficit of reactor neutrinos and only neutrino oscillations with a large mixing angle were left over as an explanation for this and all solar experiments. With Borexino the solar pp-chain was explored in detail and the matter effect, originally already detected by SNO was fostered by measurement of low energy solar neutrinos. This important result implies $m_2 > m_1$ as otherwise the solar MSW effect would not have been observed.

Table 3.2 Overview about past and actual main neutrino oscillation experiments.

Type of experiment	ν-source	Mode	$\Delta m^2/\text{eV}^2$	Comment
Atmospheric (Kam, IMB, SK)	$\nu_\mu,\overline{\nu}_\mu,\nu_e,\overline{\nu}_e$	ν_μ-dis.	$\pm 2.5\times 10^{-3}$	L/E analysis
Solar (RC, SNO, SK, BX)	ν_e	ν_e-dis.	$+8\times 10^{-5}$	MSW effect
Reactor-LB (KL)	$\overline{\nu}_e$	$\overline{\nu}_e$-dis.	$\pm 8\times 10^{-5}$	L/E analysis
Accel. (K2K, MINOS, T2K)	$\nu_\mu,\overline{\nu}_\mu$	ν_μ-dis.	$\pm 2.5\times 10^{-3}$	E analysis
Accel. (T2K, MINOS)	$\nu_\mu,\overline{\nu}_\mu$	ν_e-app.	$\pm 2.5\times 10^{-3}$	E analysis
Accel. (OPERA)	$\nu_\mu,\overline{\nu}_\mu$	ν_τ-app.		
Reactor-SB (DC, DB, RENO)	$\overline{\nu}_e$	$\overline{\nu}_e$-dis	$\pm 2.5\times 10^{-3}$	L/E analysis

a) KAM, Kamiokande; SK, Super-Kamiokande; RC, Radiochemical (Homestake, GALLEX/GNO, SAGE); BX, Borexino; Reactor-LB/SB, Reactor long baseline/short baseline; KL, KamLAND; DC, Double Chooz; DB, Daya Bay.

The oscillation of atmospheric neutrinos was confirmed by the long baseline accelerator experiments K2K, MINOS, and T2K. Precise measurements of oscillation parameters commenced with these experiments and OPERA could demonstrate the appearance of ν_τ from a high energy ν_μ-beam. All these results can be explained in the frame of neutrino mixing and two different mixing angles θ_{12} and θ_{23} with quite large values were measured. It became also clear that two different mass splitting values have been observed, which are $\sim 2.5\times 10^{-3}$ eV^2 and $\sim 8\times 10^{-5}$ eV^2, respectively. Evidence for a nonvanishing third mixing angle θ_{13} was found first in a common analysis of T2K and the reactor experiment Double Chooz. Soon, this oscillation parameter was determined at high precision by Daya Bay and RENO, again using nuclear reactors as neutrino sources. The actual experimental situation is summarized in Table 3.2.

Global fits of all available neutrino data can be found in Refs. [174, 183–185]. They all show a consistent picture of neutrino masses and mixing. Here, we show the results (Figure 3.31) of the work from F. Capozzi et al. [174, 183]. As the difference between $|m_3^2 - m_1^2|$ and $|m_3^2 - m_2^2|$ cannot be resolved, the authors have been analyzing all available data as function of $\delta m^2 := m_2^2 - m_1^2$ and $\Delta m^2 := m_3^2 - (m_1^2 + m_2^2)/2$, following the definitions in [174, 183]. We already know that $\delta m^2 > 0$ from solar neutrino experiments. The cases $\Delta m^2 > 0$ and $\Delta m^2 < 0$ correspond to normal ordering (NO) and inverted ordering (IO), respectively. At present, as shown in Figure 3.31, the IO is disfavored at 3σ level. Probably the most intriguing feature of this analysis is the trend to see a nonzero value for $\delta \sim 1.4\pi$. If the current indication would become more robust, the CP violation in the leptonic sector would be quite large.

However, there are still open important questions. We do not know the absolute mass scale. We do not know the nature of the neutrino (see below). We do not know the complete mass ordering: i.e. it could be either $m_3 > m_1$ (NO) or $m_1 > m_3$ (IO), and we do not know the value of the imaginary phase(s).[11]

11 In case of Majorana neutrinos up to three phases may exist.

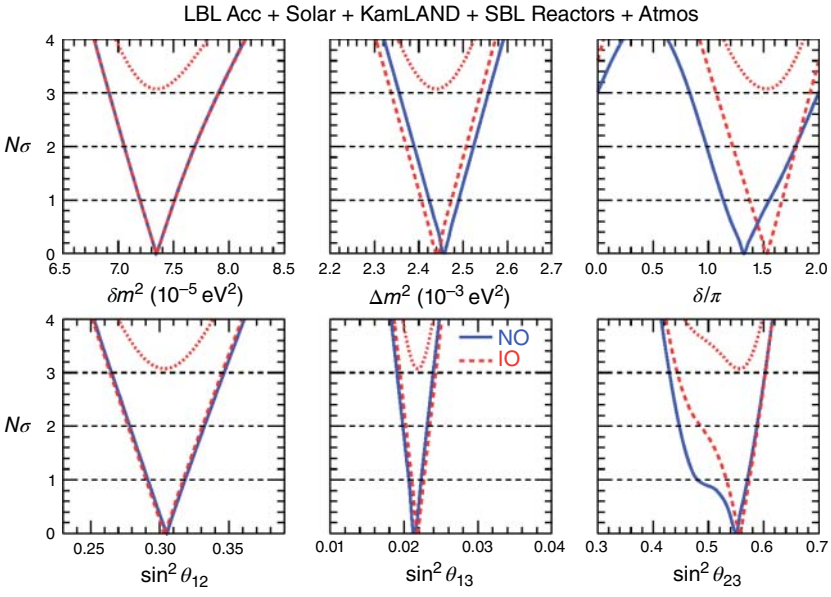

Figure 3.31 Combined oscillation analysis of all neutrino data available. The horizontal dotted lines mark the $1, 2, 3\sigma$ levels for each oscillation parameter. Solid blue lines refer to normal ordering (NO) and dashed red lines to inverted ordering (IO), respectively. Dotted red lines show bounds for IO with respect to the absolute χ^2_{min} for NO. Source: Capozzi et al. [174]. Reproduced with permission of Elsevier.

3.5.1 What Is the Absolute Neutrino Mass Scale?

The perhaps most evident open question is the absolute **neutrino mass scale**. Oscillation experiment can only provide information about mass differences. In order to search for the absolute neutrino mass, the kinematics of weak decays, where neutrinos are involved, is studied experimentally. The most advanced experiments in this field are those that measure the shape of the electron spectrum very precisely at the endpoint of the β decay of tritium ^{3}H. In the decay $^3\text{H} \rightarrow {}^3\text{He} + \overline{\nu}_e + e^-$, the maximal kinetic energy of the electron is at 18.6 keV. A nonzero value of the neutrino mass would change the maximal available kinetic β energy and consequently also deform the electron spectrum close to the endpoint. Now we know that neutrino masses are carried by neutrino mass eigenstates and due to kinetic reasons only the neutrino masses squared show up as observables in these experiments. Actually the sum of β decays with different mass eigenstates in the end channel is observed experimentally. The probability for a mass eigenstate ν_i to participate in the decay is $|U_{ei}|^2$. According to Fermi's golden rule, the differential β decay rate $\mathrm{d}N/\mathrm{d}E$ for an allowed transition is given by

$$\frac{\mathrm{d}N}{\mathrm{d}E} = \frac{G_F^2}{2\pi^3\hbar^7} \cdot M_c^2 \cdot F(E, Z+1) \cdot p \cdot (E+m) \cdot \epsilon \cdot \sqrt{\epsilon^2 - m^2(\nu_e)} \qquad (3.70)$$

with G_F the Fermi constant, M_c^2 the absolute value squared of the nuclear matrix element multiplied with $\cos^2\theta_c$ (the cosine squared of the Cabibbo

angle), $F(E, Z+1)$ the Fermi function of the daughter nucleus,and p, m, and E the electron momentum, mass, and kinetic energy. Further $\epsilon = E_0 - E$, with E_0 as the endpoint energy. The effective neutrino mass squared $m^2(\nu_e)$ is the incoherent mass term:

$$m^2(\nu_e) = \sum_i |U_{ei}|^2 m_i^2 \tag{3.71}$$

This equation holds for the decay of a bare nucleus. For more realistic cases, possible excitations of the atoms involved have to be taken into account.

The search for $m^2(\nu_e)$ is being performed with high resolution β-spectrometer. So far only upper limits on this quantity have been derived. The actual lowest values of $m_\beta > 2.2(3)$ eV (95% CL) could be obtained in the Troitsk [186] and Mainz experiments [187], respectively. β-Spectroscopy has been performed in both cases with electrostatic filters in combination with an electron optics based on the principle of magnetic adiabatic collimation. Electrons are transported from the source to a detector by spiraling along the lines of a magnetic field, allowing a wide acceptance angle of almost 2π. An electrostatic filter potential U in between can be passed only then, when the longitudinal energy along the guiding magnetic line is larger than eU.

The momenta of the electrons are aligned to the magnetic lines in the plane where the electrostatic potential is applied. This is achieved by lowering the magnetic field strength from a very high value $B_{\max}$ at the entrance of the spectrometer to a small value B_a in the region of the so-called analyzing potential. Thereby the transverse energy of the cyclotron motion is transferred adiabatically to a longitudinal kinematic energy. The electron spectrum can be scanned by varying the electrostatic potential U and counting the electrons in a detector at the end of the spectrometer as function of $E - E_0$, where E_0 is the endpoint of the tritium decay. This technique is called MAC-E (magnetic–adiabatic collimation electrostatic) filter and details can be found in [188].

In Figure 3.32 the fundamental requirements and challenges of these experiments is demonstrated. In Figure 3.33 the principles of a spectrometer with

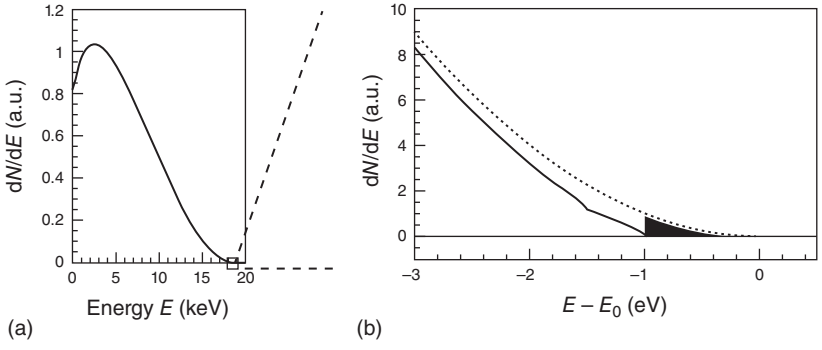

Figure 3.32 Schematic view of a β spectrum and the impact of neutrino masses and mixing. (a) The full spectrum of tritium decay is shown and (b) the expanded region close to the endpoint without (dashed line) a neutrino mass and with a hypothetical combination of two neutrino mass eigenstates with $m_1 = 1$ eV, $|U_{e1}|^2 = 0.7$ and $m_2 = 1.5$ eV, $|U_{e1}|^2 = 0.3$, respectively. Source: From C. Weilheimer 2002 [189].

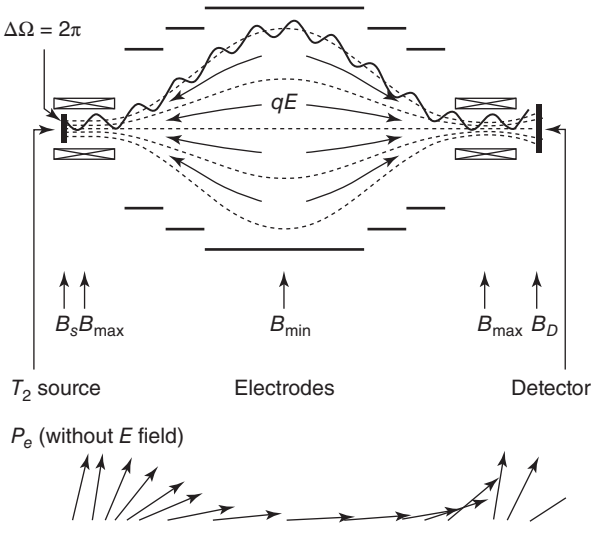

Figure 3.33 Principle of a β-spectrometer with MAC-E filter. At the top the experimental setup is shown. At the bottom the adiabatic alignment of the electron momentum within the varying magnetic field. Source: From C. Weilheimer 2002 [189].

electrostatic filter and adiabatic magnetic aligning are shown. A very small change of the spectral shape due to the neutrinos in the region just below the endpoint E_0 where the counting rate is going down to zero has to be resolved. As the actual limits are in the ∼eV region, molecular excitation and other effects of condensed matter that play a role in this energy region have to be taken into account. In principle the contribution of the different mass eigenstates could be observed as kinks in the sum spectrum, as shown in a hypothetical example in Figure 3.32, provided the instrumental resolution is good enough.

Figure 3.34 shows the endpoint region as obtained in several measurement campaigns in the Mainz experiment between 1994 and 2001. During that time an improvement of the signal to background ratio by a factor ∼10 has been achieved as well as a significant enhancement of the statistical quality. The main systematic uncertainties on this experiment originate from the physics of the condensed tritium film, which is used as β source. Inelastic scattering of electrons within the solid film, the excitation of molecules in the vicinity of the β decay, and the electrical charging of the film due to the radioactive decays play important roles here. The spectral shape is in agreement with a vanishing neutrino mass, taking into account the systematic effects. Therefore, the Troitsk and Mainz experiments set the upper limit on the absolute neutrino mass of about ∼2.2 eV, whereas the neutrino oscillation experiments yield a lower limit on this quantity.

In order to improve the sensitivity for the direct search of a neutrino mass by roughly 1 order of magnitude, the **KATRIN** experiment [190] has been built, using a new, larger spectrometer with MAC-E filter technique. In June 2018 the experiment has been inaugurated and a commissioning run started. A gaseous, molecular windowless tritium source with an activity of $\sim 10^{10}$ s^{-1} will be used. The tritium activity is monitored by an X-ray detector and its purity is measured via Raman laser spectroscopy. The electrons are transported through a system of differential and cryo-pumping sections toward a pre-spectrometer, before they enter the main spectrometer, which has dimensions of 10 m in

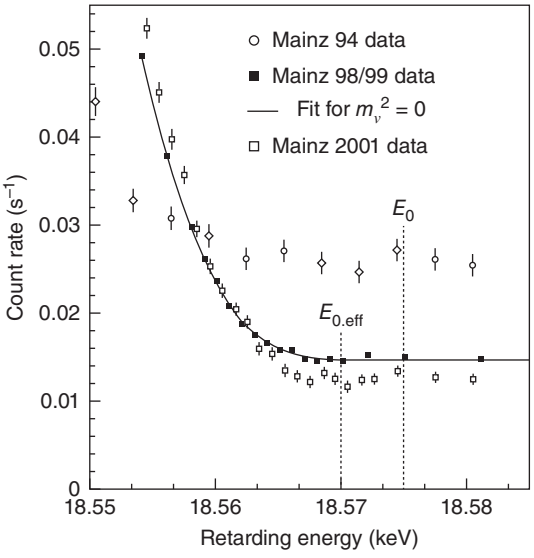

Figure 3.34 Averaged counting rate from the Mainz experiment using a frozen tritium film as β source as function of the retarding potential close to the endpoint. The effective endpoint $E_{0,\mathrm{eff}}$ takes into account the width of the response function of the spectrometer and mean rotation vibration excitation energies of the electronic ground state of the daughter molecule. Source: Kraus et al. [187]. Reproduced with permission of Springer Nature.

diameter and 24 m in length. The KATRIN collaboration is facing a number of challenges such as the maintenance of an ultrahigh vacuum with $\sim 10^{-11}$ mbar, of an extremely precise high voltage in the ppm range, and the achievement of an energy resolution around 1 eV. The electrons are detected with a Si-PIN diode, 90 mm in diameter, equipped with a 50 nm thin entrance window. It consists of a segmented wafer with 148 pixels, which allows to record the azimuthal and radial profile of the flux tube. This technique allows to compensate field inhomogeneities and helps to reduce systematic effects. KATRIN is an experiment set up in Karlsruhe, Germany. Secondary electrons generated by cosmic muons in the wall of the spectrometer may enter the vacuum tank and produce a dangerous background to the measurements. In order to reduce this effect, a double layer electrode system with 23 000 thin wires are located close to the inner wall of the main spectrometer. A slightly negative potential with respect to the wall will deflect such secondary electrons back and hinder them to enter the main vacuum tank. Background due to emanation of radioactive radon atoms is strongly reduced by material screening and selection. Electrons from radioactive nuclei like radon may get trapped in the main spectrometer quite efficiently, as it works basically as a magnetic bottle. Therefore, stored particles can be removed actively by electric dipole and magnetic zeroing, which is achieved by electromagnetic pulses. A sketch of the spectrometer together with source and transport section is shown in Figure 3.35.

The KATRIN experiment started a commissioning run in June 2018. First tritium data with a full beamline were expected by the end of 2018. The aimed sensitivity of KATRIN is 0.2 eV (90% CL), whereas the discovery potential is 0.3 eV for a 3-σ measurement. More details about KATRIN can be found, e.g. in [189]. At TAUP 2019 in Toyama, Japan, results from the first 4-week run carried out in spring 2019 have been reported by the KATRIN Collaboration using a high-purity (97.5%) and high intensity (2.45×10^{10} Bq) tritium source. A four free parameters fit (normalization, end-point energy, neutrino mass, and background rate) to the measured β spectrum provide $m_{\nu_e}^2 = -1.0^{+0.9}_{-1.1}$ eV^2 at 90% C.L. From

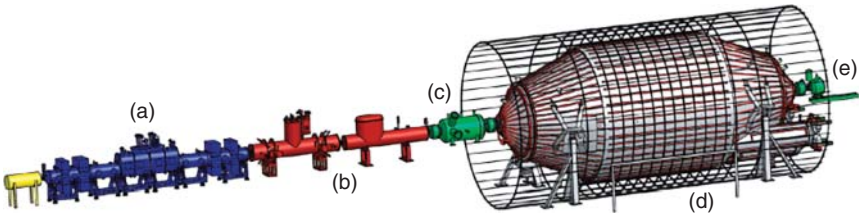

Figure 3.35 Schematic view of the KATRIN experiment with a windowless gaseous tritium source (a), differential pumping and cryotrapping section (b), a pre-spectrometer (c), the main spectrometer (d), and the electron detector (e). In total the experimental setup is 70 m long. Source: From C. Weilheimer 2002 [189].

the present data (32 days) an upper limit on the neutrino mass equal to 0.8 eV (90% C.L.) is determined using Feldman-Cousins confidence belts. A sensitivity at the level of 0.2 eV (90% C.L.) is expected with 1000 days of measurement.

Future projects on kinematic tests on the neutrino mass by studying weak decays are planned with different technologies. Here, we would like to mention Project 8 [191], ECHo [192], HOLMES [193], and MARE [194], which aim to explore the sub-eV region. In Project 8 a new type of electron energy spectroscopy should improve the measurement of the tritium endpoint. Here, the coherent cyclotron radiation emitted by an electron in a magnetic field will be detected. The ECHo and HOLMES projects will use electron capture of ^{163}Ho ($Q_{\mathrm{EC}} \sim 2.8$ keV) and new developed cryogenic detectors to perform calorimetric measurements of the characteristic X-ray and auger electron spectrum. The MARE collaboration is developing microcalorimeter arrays for investigating the β decay of ^{187}Re, which has the lowest known endpoint of 2.47 keV.

The compelling evidence for nonzero neutrino masses from oscillation experiments stimulates ideas to determine the absolute neutrino mass scale beyond the usual laboratory scales. An intriguing example is the possibility to extract a neutrino mass from the observation of a neutrino burst from a core collapse supernova. Supernova modeling predicts that about 99% of the total energy in such an event is released in the form of neutrinos. This scenario was basically confirmed by the observation of the neutrino burst of the core collapse supernova SN1987a in the Large Magellanic Cloud, about 51 kpc away from Earth (Figure 3.36). On 23 February 1987, a total of 24 neutrino events have been registered by Kamiokande (Japan) [195], IMB (United States) [196], and Baksan (Russia) [197] during a time period of about 13 seconds. The main detection reaction in all these detectors was the inverse β decay on free protons $\overline{\nu}_e + p \rightarrow e^+ + n$. The neutrino energies measured via this reaction showed a distribution from a few MeV to about 40 MeV, with an average value of about 12 MeV. Taking into account the well-known detection cross section for this process, the detector sizes and the different thresholds, the total neutrino emission of SN1987a in the form of $\overline{\nu}_e$ was determined to be $\sim 2 \times 10^{57}$. Under the assumption that all neutrino flavors are emitted during a gravitational collapse due to adiabatic[12] compression and successive thermal neutrino emission via $\gamma + \gamma \rightarrow \nu + \overline{\nu}$, the total neutrino energy emitted in SN1987a was estimated to be of the order of 10^{46} J and found to be in agreement with basic supernova assumptions.

12 For a short time when nuclear densities are reached during the collapse, even neutrinos are trapped inside the supernova and no cooling can occur.

(a) (b)

Figure 3.36 Supernova 1987a optical observation (a) in the Large Magellanic Cloud and the corresponding star field before the explosion was observed (b). Source: Courtesy of David Malin/Anglo-Australian Observatory.

Neutrino masses will lead to a time dispersion of the neutrino front during its time of flight as high energy neutrinos will travel faster than low energetic ones. The time difference Δt between a massless neutrino and a species with mass value m can be calculated in relativistic approximation to be

$$\Delta t \approx \frac{r}{c} \left(1 + \frac{1}{2}\frac{m^2}{E^2}\right) \tag{3.72}$$

with r as the travel distance, c the speed of light in vacuum, and E the neutrino energy. In the case of SN1987a, the travel time $r/c \approx 160\,000$ years and a 10-MeV neutrino with mass $m \sim 1$ eV will therefore induce a time delay $\Delta t \approx 0.27$ seconds. One can look for a correlation between neutrino arrival time and neutrino energy, as both quantities are detectable. If the neutrino emission could be described by a sharp delta function, the effect of a finite neutrino mass could be directly seen by this correlation. However, the time spectrum of the neutrino emission after a gravitational collapse is model dependent and should take a period up to ∼10 seconds. In the case of SN1987a, also the statistics was quite limited and therefore only an upper bound of ∼11 eV for a neutrino mass could be derived. For present large detectors like SK, a gravitational collapse in our galaxy would generate many thousands of neutrino events and one would expect a sensitivity $m \sim 1$ eV for the neutrino mass. In order to reach sensitivities in the sub-eV range, our astrophysical knowledge of a gravitational collapse has to be improved significantly.

Besides an upper limit on the neutrino mass, other interesting neutrino parameters could be deduced from the SN1987a signal. For instance, the neutrino

arrival time and the optical image of SN1987a are known to be in coincidence within a few hours. From this a limit on the deviation of the neutrino speed versus the speed of light $|v - c|/c < 2 \times 10^{-9}$ can be deduced [198]. It is more stringent by many orders of magnitude as any actual limit obtained in terrestrial neutrino experiments using pulsed accelerators. The fact of a neutrino burst observation compatible with the basic assumptions sets also a lower bound on the neutrino lifetime. This limit becomes even more restrictive, if special decay modes are considered. For instance, radiative neutrino decay $\nu_j \to \nu_i + \gamma$ of a massive ν_j to a lighter ν_i would lead to a γ-signal coincident with the neutrino burst. From the non-observation of such a signal with γ-detectors on board of the "solar maximum mission" satellite, a lifetime limit $\tau > 8.3 \times 10^{14}$ s/eV could be derived [199]. In addition other interesting constraints on electromagnetic neutrino properties could be deduced from SN1987a. A review about this topic can be found at Ref. [200].

Cosmology provides information on the absolute scale of neutrino masses, too. Although the Big Bang relic neutrino background has not been observed yet, its presence is indirectly proven by the observation of the abundances of light elements produced in the first minutes of the universe, which agrees very well with theoretical Big Bang calculations. In addition, other cosmological observables as the accurate measurement of the cosmic microwave background (CMB) are providing strong evidence for the existence of a cosmic neutrino background. In the scenario of the Big Bang, neutrinos decouple from the rest of particles after roughly 1 second, when their weak interaction rate falls below the expansion rate of the universe. In a temperature or energy scale, this corresponds to about 1 MeV. As we know that neutrinos have mass values below ∼2 eV, neutrinos were highly relativistic when they decoupled from nuclei and electrons. Since then neutrinos are believed to stream freely through the universe and their energies should have red-shifted as it is the case for photons, as long as neutrinos are still relativistic. Today at least two of the neutrino states are non-relativistic. This we know from the oscillation results as $\sqrt{|\Delta m^2_{31}|} \sim 50$ meV as well as $\sqrt{\Delta m^2_{21}} \sim 9$ meV are both larger than their temperature $T_\nu \sim 1.96$ K ~ 0.17 meV. The time between the relativistic and non-relativistic transition depends on the absolute values of the neutrino masses, and their present number density is calculated to be ∼113 neutrinos and antineutrinos of each flavor per cm^3. The corresponding energy density as a function of the evolution of the universe can be calculated in the frame of an expanding universe, which is described by the Friedman–Robertson–Walker metric with $a(t)$ as a scale factor, which is normalized to unity for today and related to the redshift z as $a = 1/(1 + z)$. The relation between the metric and matter as well as energy density is provided by the Einstein equations, which leads to the time-dependent Friedmann equation:

$$\left(\frac{\dot{a}}{a}\right)^2 = H^2 = \frac{8\pi G}{3}\rho \tag{3.73}$$

with H the Hubble constant, G the gravitational constant, and ρ as the total energy density. In our current understanding of the evolution of the universe, the contributions to ρ are carried by the Cosmic Microwave Background (CMB), by cold

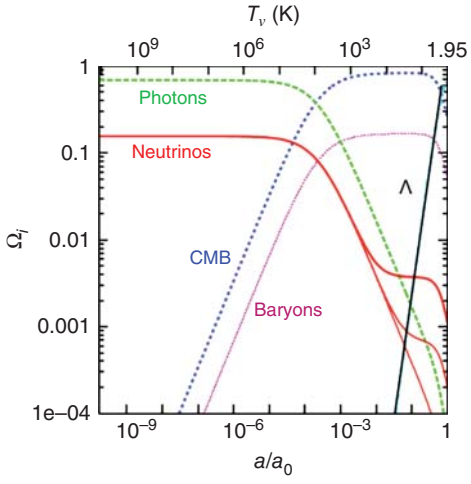

Figure 3.37 Evolution of the CMB, ν, dark matter, baryonic and Λ energy densities during the expansion of the universe from $T = 1$ MeV until now. For the neutrinos mass values of 0, 9, and 50 meV have been assumed. Source: Lesgourgues and Pastor 2014 [201]. https://iopscience.iop.org/article/10.1088/1367-2630/16/6/065002/meta. Licenced under CC BY 3.0.

dark matter, by baryons, by neutrinos, and by the cosmological constant. The evolution can be calculated under the assumptions of different neutrino masses.

For instance, in Figure 3.37, the contributions of all species to the total energy density are shown from the time of the decoupling of the neutrino until today [201]. At the beginning radiation in form of photons and highly relativistic neutrinos dominate, then non-relativistic matter takes over, and finally the cosmological constant density starts to dominate. In Figure 3.37 three neutrino masses with $m_1 = 0$, $m_2 = 9$ meV, and $m_3 = 50$ meV have been assumed.

Neutrinos, together with photons, determine the expansion rate, while the universe is dominated by radiation. Therefore, also the expansion rate during Big Bang nucleosynthesis (BBN) is fixed by these particles and BBN itself determines the abundances of light elements, especially that of ^{4}He. We know that the number of light, active neutrinos is ∼3 from the Z-width measurement at CERN [123]. Neutrino decoupling and $e^\pm$ annihilations are very close in time, and for a certain period, relic interactions between $e^\pm$ and ν_e as well as $\overline{\nu}_e$ persist. Therefore, the effective number of neutrinos contributing to the total energy density of the universe is expected to be $N_\nu \approx 3.046$ [201]. Any deviation of N_ν from this value would indicate the existence of nonstandard neutrino features or to the contribution of other, yet unknown, relativistic species. In a recently published analysis, BBN constrains an additional relativistic contribution to $\Delta N_\nu < 1$ at 95% CL [202]. The analysis is conservative in the sense that the astrophysical determination of ^{4}He has presumably systematic uncertainties, which are difficult to estimate at high accuracy.[13] In addition to BBN, observables from the CMB would be affected by a nonstandard N_ν value. The damping envelope of the acoustic peaks at low angular scales (or high multipole order) would be shifted with respect to the standard scenario. For a minimal cosmological model with a cosmological constant and cold dark matter (ΛCDM), the CMB data alone yield $N_\nu = 3.36^{+0.68}_{-0.64}$ [203] at 95% CL taking into account the data released by the Planck mission [204]. This value is in good agreement with the standard scenario but is still allowing

13 For other analysis on BBN and extra radiation, see references within [202].

the existence of an additional relativistic species. It is interesting to see how additional astrophysical and cosmological observables influence this result. Data from the Hubble Space Telescope (HST) used to determine the recent Hubble parameter H_0 show a tension with respect to Planck data as HST favors larger values of the expansion factor. As an increase of H_0 correlates positively with an increased value of N_ν a combined analysis (Planck + HST) yields $N_\nu = 3.62^{+0.54}_{-0.48}$. On the other hand the recent expansion history can also be inferred from the luminosity of type-Ia supernova and from the angular scale of baryonic acoustic oscillations (BAO). Now, if one performs a global analysis with Planck plus BAO, the best-fit value decreases to $N_\nu = 3.30^{+0.54}_{-0.51}$. It is interesting to note that a free parameter N_ν relaxes the tension between the different data sets. Therefore, it makes sense to combine CMB data with HST and BAO, which gives $N_\nu = 3.52^{+0.48}_{-0.45}$ and would still favor the existence of an enhanced radiation.

The relic neutrinos form a diffuse background and they contribute to the energy density of the universe in units of the critical value with

$$\Omega_\nu = \frac{\sum m_i}{93.14\ h^2\ \text{eV}} \tag{3.74}$$

where $\sum m_i$ includes all masses of non-relativistic neutrino states today and with the normalized value of the actual Hubble parameter $h = H_0/(100\ \text{km/(s Mpc)})$. If we demand that neutrinos should not be heavy enough to overclose the universe (i.e. $\Omega_\nu < 1$), an upper bound $M_\nu = \sum m_i < 45$ eV can be derived, when we use $h = 0.7$. Moreover we know from CMB that the matter contribution is in total $\Omega_m \approx 0.3$, which yields $M_\nu < 15$ eV. For non-relativistic neutrinos at the time of decoupling (i.e. for $m_\nu \geq 1$ MeV), ν-annihilation has to be taken into account. The more massive neutrinos are, the longer the time they require to undergo annihilation, and as a consequence the number density of heavy neutrinos surviving this destructive era is decreasing exponentially with its mass. For this reason there exists also a lower limit on neutrinos masses in the range $m_\nu > 2$–5 GeV, depending on whether neutrinos are from the Dirac or Majorana type ("Lee–Weinberg limit" [205]). These limits hold for stable neutrino states, or at least for neutrinos that have lifetimes significantly longer than the age of our universe. Now, neutrino mixing does introduce neutrino decay: for instance, a massive state ν_j may decay radiatively into a lighter ν_i and a photon via $\nu_j \to \nu_i + \gamma$. This process occurs on loop level and its decay width is

$$\Gamma = \frac{G_F^2 m_j^5}{128\pi^3}(\alpha/\pi)(9/16)\left(\sum_k U_{kj}U_{ki}^*(m_l/M_W)^2\right)^2 \tag{3.75}$$

(e.g. [200]), with G_F as the Fermi constant, α the electromagnetic coupling constant, m_l the mass of the virtual charged lepton, and M_W the W-boson mass. In scenarios of massive neutrinos with standard interactions, the lifetime is exceeding the age of the universe by far. Therefore, fast decays modes beyond the model of standard neutrino interactions have to be introduced to overcome cosmological constraints.

An alternative way to solve this problem can be provided by sterile neutrinos with masses in the keV range. The hypothesis of sterile neutrinos in this mass range gained much attention recently, because it can be used to explain the evidence for dark matter in our universe. Sterile neutrinos can be produced in the

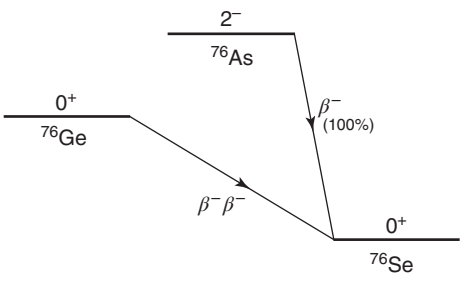

Figure 3.38 Scheme of the double β decay of ^{76}Ge to ^{76}Se. The single β decay to ^{76}As is kinematically forbidden.

early universe by oscillations. In order not to violate the cosmological limits given above, the mixing strength to the well-known active flavors has to be very small. Alternatively, sterile neutrinos might be produced in decays of heavy bosons, for instance, via Higgs decays at the era of electroweak scale. In these scenarios sterile keV neutrinos form "warm dark matter" and this can be helpful in solving some problems in structure formation at small scales, which occur in models with cold dark matter alone. Also sterile neutrinos will decay radiatively as they mix weakly to active flavors. As discussed above the decay rate is expected to be very small, but large lumps of dark matter still should emit photons with an energy that is half of the neutrino mass. This can be a path to detect sterile neutrinos indirectly via satellite-based X-ray telescopes. Indeed, in the last years some X-ray observations from both galaxy and galaxy clusters have been discussed if a weak hint of a mono-energetic line at ∼3.5 keV could be a sign for the existence of a 7 keV sterile neutrino. These observations are however questioned within the astrophysical community, and today it is not clear if we can speak from a real signal, because a vigorous search has ensued in the last two years and this resulted in a respectable number of non-detections as well. Finally, it is interesting to note that the upcoming KATRIN experiment has some sensitivity to search for the admixture of keV neutrinos to ν_e, as this would be seen as kinks in the spectral shape of the tritium β decay [206].

3.5.2 Are Neutrinos Majorana or Dirac Particles?

An additional method to search for neutrino masses are experiments looking for so-called "neutrinoless" double β decays, often denoted as $0\nu\beta\beta$. The quest for these processes is especially interesting, because of aspects that reach beyond the scope of the neutrino masses. Besides probing the absolute mass scale $0\nu\beta\beta$ experiments may reveal the nature of neutrinos: are they four-component Dirac particles with a conserved Lepton number L, or two-component truly neutral Majorana particles without electric and leptonic charge?

Some even–even nuclei (i.e. nuclei with both even numbers of protons and neutrons) can decay into a nucleus with lower mass via double β decay only, because the normal single β decay is forbidden kinematically. One example of such a nucleus is ^{76}Ge with and endpoint energy of 2039 keV. The decay via the isotope ^{76}As is kinematically forbidden and its decay scheme $^{76}\mathrm{Ge} \rightarrow {}^{76}\mathrm{Se} + 2e^- + 2\overline{\nu}_e$ is depicted in Figure 3.38.

Double β decaying nuclei have been experimentally confirmed for about a dozen of elements. These decays with neutrinos of the type $(A, Z) \rightarrow (A, Z+2) + 2e^- + 2\overline{\nu}_e$ are weak processes of second order with lifetimes much longer than the age of the universe. On the contrary, neutrinoless double β decays of the type $(A, Z) \rightarrow (A, Z+2) + 2e^-$ are forbidden in the standard model of particle physics as the total lepton number is violated by two units. The process of $0\nu\beta\beta$ is only possible if the neutrino that is exchanged virtually is a Majorana particle, i.e. if the neutrino and its antiparticle are identical. In this case neutrinos can be described as two-component spinors, in contrast to the usual four-component Dirac particle description. There exist several mechanisms that may introduce $0\nu\beta\beta$ decays, but they all have in common the Majorana nature of the neutrino.[14] The discovery of $0\nu\beta\beta$ decay would have severe consequences for our understanding of the standard model of elementary particles, because of both absolute lepton number violation and the Majorana type of the neutrino. A review about the phenomenon on $0\nu\beta\beta$ decay and especially on the meaning of lepton number violation in the context of the standard model and its extensions can be found in [208]. Neutrino oscillation experiments cannot solve the question about the Majorana nature of the neutrinos, because in the oscillation transitions the total lepton number L is always conserved, and to our knowledge today the search for $0\nu\beta\beta$ decays is the by far most sensitive way to probe the Majorana type of the neutrino. It was S. Weinberg who first pointed out that there is only one dimension.[15] Lagrangian term that can be constructed with standard model fields, which violated the total lepton number L [209]. If this mechanism is realized in nature, small Majorana neutrino masses and neutrino mixing would have been generated by this term after spontaneous electroweak symmetry breaking in the early phase of the universe. As a counterpart ("seesaw mechanism") to these light neutrinos, the generation of heavy Majorana leptons would be the consequence of such a term and it is speculated that fast CP-violating decays of these extremely massive particles could be the origin of the baryon asymmetry of the universe through the so-called leptogenesis mechanism (see, e.g. [210, 211]). In this way the fact of the smallness of neutrino masses and matter–antimatter asymmetry could have a common explanation. However, neutrino masses can be also generated by the standard Higgs mechanism with extremely small Yukawa couplings. Then neutrinos would be Dirac particles and as a consequence $0\nu\beta\beta$ decays could not be observed. It is open to experiments to answer this fundamental question.

Among all discussed possibilities the presumably best motivated way for introducing $0\nu\beta\beta$ decays are neutrino masses, because we know they have to have finite values due to our observations from oscillation experiments. In Figure 3.39 the Feynman diagram for a $0\nu\beta\beta$ decay via exchange of a massive Majorana neutrino is shown.

Note that the neutrino that is emitted with left-handed chirality has to be absorbed in a right-handed chiral state. This can be induced by a nonzero

14 This has been proven by a famous theoretical paper from J. Schechter and J. Valle [207], called "Valle–Schechter theorem"

15 A Lagrangian term with total energy dimension five. Products of fields with total energy dimension of four or smaller do not violate L.

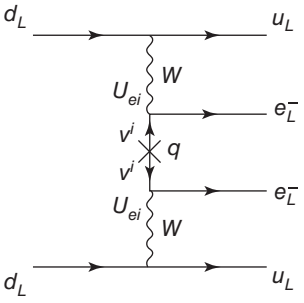

Figure 3.39 Feynman diagram for the neutrino mass mechanism of neutrinoless double β decay. The process is only possible if the neutrino is a Majorana particle. In total lepton number conservation is violated by two units. The decay width depends on the coupling parameter U_{ei} of the massive neutrino to the electron. Source: Päs 2015 [212]. https://iopscience.iop.org/article/10.1088/1367-2630/17/11/115010/pdf. Licenced under CC BY 3.0.

neutrino mass term. In the usual description of neutrino mixing, all three mass eigenstates, coupled with U_{ei}^2 to the electron neutrino, contribute to this process. Hence, the amplitude for the $0\nu\beta\beta$ decay can be written as

$$m_{\beta\beta} = \left| \sum_{i=1}^{3} U_{ei}^2 m_i \right| \tag{3.76}$$

Let us note that U_{ei}^2 can contain imaginary phases. Indeed, the unitary mixing matrix allows for an imaginary phase in general, but as we have to assume here to deal with Majorana neutrinos, two additional degrees of freedom enter the mixing matrix. In total we have nine physical parameters: three masses m_i ($i = 1, 2, 3$), three mixing angles $\theta_{12}, \theta_{13}, \theta_{23}$, and three phases δ, α, β. The effective double β mass $m_{\beta\beta}$ is a function of these parameters and can be calculated to be

$$m_{\beta\beta} = |c_{12}^2 c_{13}^2 m_1 + s_{12}^2 c_{13}^2 m_2 \mathrm{e}^{i\alpha} + s_{13}^2 m_3 \mathrm{e}^{i\beta}| \tag{3.77}$$

with the denotations $c_{ij}^2 = \cos^2\theta_{ij}$ and $s_{ij}^2 = \sin^2\theta_{ij}$. α and β in Eq. (3.77) are referred to as Majorana CP-violating phases.

In $m_{\beta\beta}$ only two phases enter, because only the differences between them are relevant. As described above we currently do not know the values of the lightest neutrino mass and the phases and the mass ordering is not completely known, too. One can calculate the space of values which are still possible for $m_{\beta\beta}$, taking into account all our knowledge from neutrino oscillation experiments. The clearest scenario can be found for inverted mass ordering, because in this case m_2 and m_1 would give the largest contributions to the sum and even negative contributions from the other term would not derogate the final value substantially. A simple example may illustrate this: let us assume $m_{\min} = m_3 \to 0$, then it follows that $m_2 = \sqrt{m_3^2 + \Delta m_{13}^2 + \Delta m_{21}^2} \simeq m_1 \simeq 50$ meV, and the lowest value for the effective double β mass would be $m_{\beta\beta} \simeq c_{13}^2(c_{12}^2 - s_{12}^2)m_1 \simeq 0.385 \cdot 50$ meV $\simeq 19$ meV, even in the most unfortunate situation $\alpha \to \pi$. Here, we used the actual best-known mixing angles from [174] yielding $\cos^2\theta_{12} \simeq 0.697$ and $\cos^2\theta_{13} \simeq 0.978$.

For normal mass ordering, the situation can be completely different. Then cancellations can play an important role and diminish $m_{\beta\beta}$, even for the case of quite large values for the individual mass eigenvalues m_i. In Figure 3.40, $m_{\beta\beta}$ is shown as a function of the lightest neutrino mass for both mass ordering scenarios by sampling 2×10^5 times the oscillation parameters and CP-violating phases involved

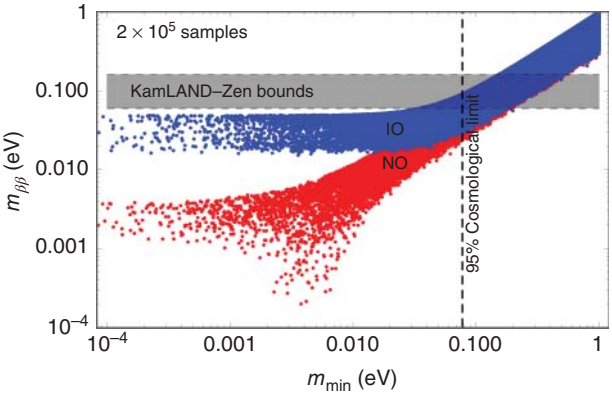

Figure 3.40 Allowed values for the effective Majorana neutrino mass $m_{\beta\beta}$ as a function of the lightest mass eigenvalue in the two scenarios of normal (NO) and inverted (IO) mass ordering. Dots show the output of a 2×10^5 random sampling from Eq. (3.77), using global best-fit values for parameters. Also shown are experimental and cosmological limits.

in Eq. (3.77). Note that the lower edge of the IO region is equal to the limit derived above. In addition, Figure 3.40 shows that very small values for $m_{\beta\beta}$ in the NO scenario have a low occurrence probability.

Figure 3.40 shows constraints on $m_{\beta\beta}$, which are coming from $0\nu\beta\beta$ experiments and limits on m_{min} stemming from cosmology. The latter has to be considered as model dependent[16] and its actual value is under discussion. Figure 3.40 shows that the ultimate $0\nu\beta\beta$ experiment should aim to 1 meV sensitivity. Up to now, $0\nu\beta\beta$ decay has not been observed experimentally. The most stringent limits obtained so far are in the range between 0.2 and 0.6 eV for $m_{\beta\beta}$. A not negligible uncertainty raises due to theoretical calculations for the nuclear matrix elements, which have to be used in order to derive values or limits on $m_{\beta\beta}$, as experimental results only can deliver results on the lifetime of the $0\nu\beta\beta$ decay investigated. The half-life $T^{0\nu}_{1/2}$ is linked with $m_{\beta\beta}$ via the formula:

$$m_{\beta\beta} = (1/M^{0\nu})(\ T^{0\nu}_{1/2}\ G(Q,Z))^{-1/2} \tag{3.78}$$

where $M^{0\nu}$ denotes the nuclear matrix element and $G(Q,Z)$ is the phase space factor for the neutrinoless double β decay, which depends on the endpoint energy Q and the atomic number Z. Unfortunately, the matrix elements can be only calculated in the frame of nuclear models, which try to take into account many-body interactions of the nuclei bound inside the nucleon. There is no way to determine the matrix elements experimentally and the calculations rely on numerical approximations, mostly performed with nuclear shell models and with the method of quasi-particle random phase approximation. In experiments the number $N_{\beta\beta}$ of $0\nu\beta\beta$ decays is counted during a measuring time T_m. It can be written as

$$N_{\beta\beta} = (\ln 2\ /\ T^{0\nu}_{1/2})\ N_n\ T_m\ \epsilon \tag{3.79}$$

16 See our discussion about cosmological limits on neutrino masses above.

with N_n being the number of nuclei that can undergo $0\nu\beta\beta$ decay and ϵ as the detection efficiency. The number of candidate nuclei scales with the total detector mass M_{det}, and we can write $N_n = y_a \cdot M_{\text{det}}$, where y_a can be considered as an effective yield of isotope abundance, being $y_a = a \cdot N_A/A$, with N_A the Avogadro's number, A the nucleus atomic number, and a the isotopic abundance of the nucleus which undergoes $0\nu\beta\beta$ decay. In order to achieve a high exposure, it can be important to take into account the isotopic abundance of the $0\nu\beta\beta$ nuclei, and for this reason some experiments are working with enriched samples. $0\nu\beta\beta$ experiments can be divided into two groups: some are using the nuclear material as a detection medium and others are separating them.

Examples for the former group are experiments using ^{76}Ge as candidate isotope in Ge-semiconductor detectors with high energy resolution (Heidelberg-Moscow, GERDA, IGEX) or ^{136}Xe in a liquid xenon noble gas as the medium of a time projection chamber (EXO) or dissolved in a liquid scintillator (KamLAND-Zen). In the CUORE experiment crystals with ^{130}Te are cooled down to cryogenic temperatures of order 10 mK and the energy deposition is measured via the amount of heat released in these processes. The second technique is used, e.g. in the NEMO experiment, where the source is defined by a thin membrane and the two electrons are going to be observed in a tracking detector. All $0\nu\beta\beta$ projects have in common to be rare event experiments, quite similar to solar neutrino experiments. Background rejection and the achievement of an exposure and detection efficiency as high as possible are the major corner pieces for a successful $0\nu\beta\beta$ experiment. Background events may occur due to radioactivity inside or in the vicinity of the detector or due to activation by cosmic muons and because of the latter point all experiments are located in deep underground laboratories. In a $0\nu\beta\beta$ decay, the sum of the kinetic energies of both electrons is fixed by the endpoint energy Q. Therefore, the signature of each $0\nu\beta\beta$ experiment is a peak-like structure in the energy spectrum at position Q. This is illustrated schematically in Figure 3.41 for the case of ^{76}Ge, and it is evident that a high energy resolution is necessary in order to minimize background events in the energy region around Q, which originate from allowed $2\nu\beta\beta$ decays. In the GERDA experiment, Ge-detectors enriched with ^{76}Ge are immersed into a tank filled with liquid argon, which acts as a cooling medium and shields against background stemming from external radioactivity. In the second phase of GERDA, the argon tank has been turned into an active veto detector utilizing the scintillation properties of the liquid argon. In 2013 the collaboration published the first result with a total exposure of 21.6 kg yr with a background level at the endpoint of the order of 10^{-2} cts/(keV kg yr).

No hint on $0\nu\beta\beta$ decays has been found as it is illustrated in Figure 3.42 and an upper limit $T^{0\nu}_{1/2} > 2.1 \times 10^{25}$ year could be set at a CL of 90%. In Figure 3.42a, the spectrum is superimposed by the curve one would expect if this limit would be the real value (blue, solid line) and for $T^{0\nu}_{1/2} = 1.19 \times 10^{25}$ year, which is a value coming from a claim [214] based on an analysis of the former Heidelberg-Moscow experiment, which was supported by a part of the collaboration. With the new GERDA data, this claim is now clearly disfavored.

In a second phase, 30 BEGe detectors (20 kg total mass) were deployed together with the first phase coaxial detectors. A total mass of 35.6 kg germanium, enriched at 87%, has been available in GERDA during the second phase. The second phase data taking started in December 2015. The total

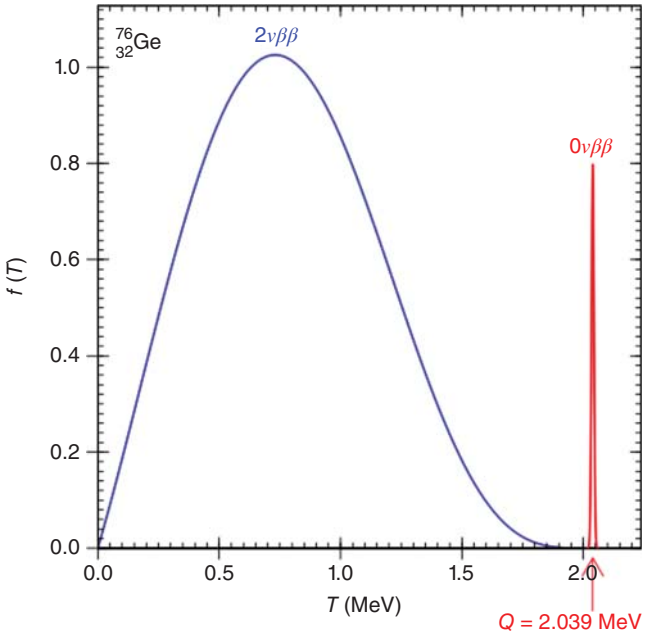

Figure 3.41 Spectrum of the total kinetic energy of ^{76}Ge originating from the $2\nu\beta\beta$ decay, which is allowed in the standard model, and a hypothetical peak at $Q = 2.039$ keV, which is searched for in a $0\nu\beta\beta$ experiment. Source: From S. Bilenky and C. Giunti 2014 [208].

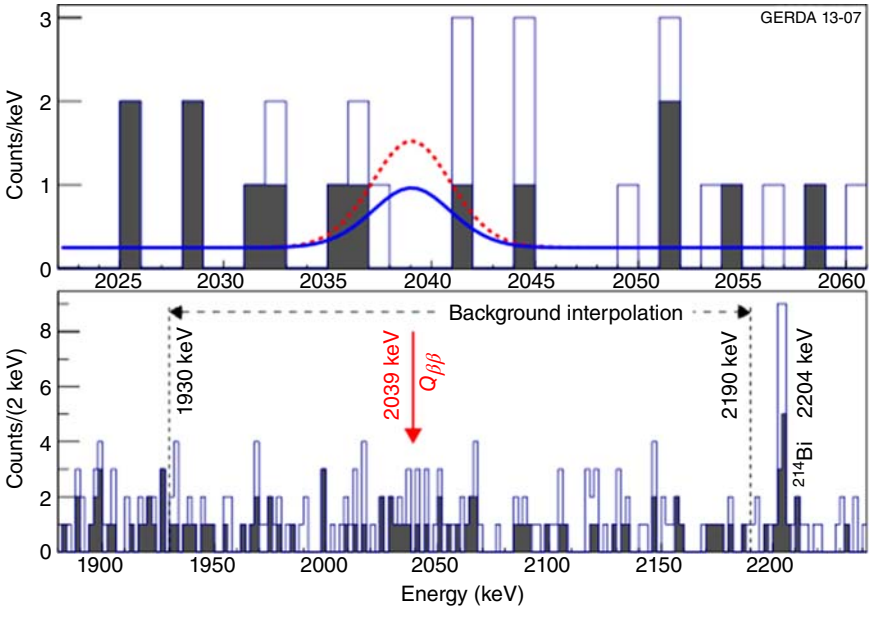

Figure 3.42 Energy spectrum shown by the GERDA experiment after an initial exposure of 21.6 kg·yr around the endpoint of 2039 keV. The zoom of the upper panel shows the data distribution before (open Histogram) and after pulse shape discrimination has been applied. Source: Agostini et al. 2013 [213]. Reproduced with permission of American Physical Society.

exposure collected till April 2017 is equal to 23.2 kg yr. The background index is determined to be $1.0^{+0.6}_{-0.4} \times 10^{-3}$ cts/(keV kg yr) and a frequentist analysis provides a lower limit at 90% CL of $T^{0\nu}_{1/2} > 8.0 \times 10^{25}$ year on the decay half-life [215]. As of 2017, a background index of $0.7^{+1.1}_{-0.5} \times 10^{-3}$ cts/keV kg yr has been achieved [215a].

In the case of a background counting rate r_b (measured e.g. in counts per keV, per kg, and per year), the 1σ fluctuation ΔN_b of the registered number of background events N_b is

$$\Delta N_b = \sqrt{N_b} = \sqrt{r_b \, M_{\text{det}} \, T_m \, \Delta E} \tag{3.80}$$

with M_{det} as the detector mass and ΔE the relevant energy window, provided the background scales with the detector mass linearly. This is the case if, for instance, the internal radioactivity, which is distributed homogeneously over the detector, is the dominant source of background. Setting ΔN_b equal to $N_{\beta\beta}$ gives the 1σ limit half-life limit

$$T^{0\nu}_{1/2} = \ln 2 \cdot \sqrt{\frac{M_{\text{det}} \, T_m}{r_b \, \Delta E}} \; y_a \, \epsilon \tag{3.81}$$

The importance of a high levels on the detection efficiency and on the isotope yield are evident: the experimental sensitivity grows with the square root of the exposure and with the inverse square root of the background level times the energy resolution, but linearly with the detection efficiency times the yield of the isotope abundance. The situation is different in the case of negligible background. Then the sensitivity on the lifetime scales linearly with the exposure, i.e. $\propto M_{\text{det}} \, T_m$.

A high Q-value can be advantageous, because it shifts the region of interest further away from naturally occurring radioactivities. However, this can be compensated by a careful passive and active background rejection, as it was demonstrated in Ge experiments. Even more subtle is the question about uncertainties connected with theoretical calculations for the nuclear matrix elements, which are necessary to get a bound or value for the effective neutrino mass. Systematic errors are, for instance, enhanced when the nucleus considered shows deformation from a spherical shape. Actual $\beta\beta$ experiments are successful in measuring the allowed $2\nu\beta\beta$ decay. From these measurements the nuclear matrix elements for $2\nu\beta\beta$ decays can be derived. However, these quantities do not correlate automatically with the $0\nu\beta\beta$ matrix elements, because the former underly the known selection rules for weak processes in the standard model, which have not been applied for the case of Majorana neutrinos. It is also interesting to note that a large matrix element for the allowed $2\nu\beta\beta$ decay may generate background if the energy resolution is not high enough to exclude the events close at the endpoint from data analysis. In sum the quest for finding $0\nu\beta\beta$ decays is an interesting multiparameter game in search for the ideal isotope and the optimal technique and the question about costs and availability is of course important as well.

We summarize the actual experimental situation in Table 3.3 where we note the limits on $m_{\beta\beta}$ have reached the sub-eV regime. The claim in Ref. [214] about evidence of $0\nu\beta\beta$ decay in ^{76}Ge is disfavored not only by GERDA but indirectly also by the limits obtained in the xenon-based experiments EXO and KamLAND-Zen.

Table 3.3 Overview about double β-experiments, their techniques, and achieved 90% cl-limits.

Isotop	Experiment	Technik	$T^{0\nu}_{1/2}$ (y) >	m_{ee} (eV) <
^{76}Ge	Heidelberg-Moscow [216]	Ge high-resolution	1.9×10^{25}	0.23–0.67
	IGEX [217]	Ge high-resolution	1.6×10^{25}	0.25–0.73
	Majorana [217a]	Ge high-resolution	1.9×10^{25}	0.24–0.53
	GERDA-I [213]	Ge high-resolution	2.1×10^{25}	0.22–0.64
	GERDA-II [217b]	Ge high-resolution	5.3×10^{25}	0.15–0.33
	GERDA-II [215]	Ge high-resolution	8.0×10^{25}	0.12–0.26
^{136}Xe	EXO [218]	Xenon-TPC	1.1×10^{25}	0.17–0.49
	KamLAND-Zen [219, 220]	Xenon in LSc	1.1×10^{26}	0.05–0.16
^{128}Te	CUORICINO [221]	TeO cryo-det.	2.8×10^{24}	0.32–1.20
^{128}Te	CUORE [222]	TeO cryo-det.	1.5×10^{25}	0.11–0.50
^{100}Mo	NEMO-3 [223]	Tracking	2.1×10^{25}	0.32–0.88

a) The allowed ranges for the limits on $m_{\beta\beta}$ accounts for the uncertainties of the corresponding nuclear matrix elements.

The current constraints on $m_{\beta\beta}$ vary around 0.2 eV and values just below the 1 eV limit. The next generation of $0\nu\beta\beta$ experiments aim for values well below 0.1 eV with the purpose to explore the region given by the inverted mass ordering scenario. If future oscillation experiments would find that indeed this scenario is realized in nature; next-generation $0\nu\beta\beta$-project could really find out whether neutrinos are Majorana particles or not. However, the whole situation may change completely, if some hints on sterile neutrinos, which mix to the normal neutrino states, would be confirmed. Then, the search for $0\nu\beta\beta$ decays may become even more promising, if the sterile neutrino (i.e. not weakly interacting neutrinos) is quite massive and if its coupling to ν_e is not too small.[17]

3.5.3 What Is the Neutrino Mass Ordering and How Large Is CP-δ?

From solar neutrino experiments and the matter effects involved, we have evidence that $m_2 > m_1$. This type of mass ordering, or sometimes named NMO, is considered to be the "normal" scenario, because it corresponds to the nature of charged leptons, where the mass sequence is clearly hierarchical with $m_\tau > m_\mu > m_e$. However, for neutrinos this picture may be somehow different. As we have discussed above, it might be the case that the neutrino mass generation is not realized like for the other charged elementary particles (i.e. via the Higgs mechanism). Therefore, one has to be open minded and base conclusions only on experimental results. Two scenarios are possible: normal mass ordering with $m_3 > m_2 > m_1$ or the so-called inverted mass ordering with $m_2 > m_1 > m_3$. Both are shown schematically in Figure 3.43.

17 Sterile neutrinos with ~eV masses and quite large mixing amplitudes are discussed currently.

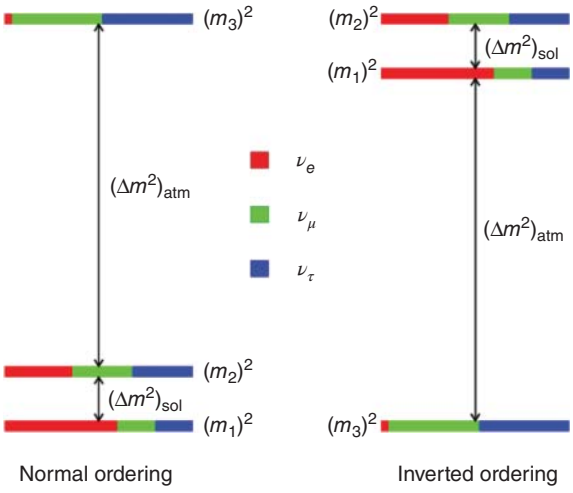

Figure 3.43 Normal and inverted mass ordering or hierarchies (abbr. NMO) of neutrino mass eigenstates in a vertical scale. The color represents the admixtures of the weak eigenstates.

There are several ways to get hands on the mass ordering: one can exploit matter effects like it was already done for solar neutrinos in the m_2, m_1 subsystem successfully; one can resolve the oscillation pattern with high accuracy; one can exploit a combination of both, namely, matter effects and neutrino oscillation pattern. In order to take advantage of matter effects, higher energies with respect to solar neutrinos are necessary, because of the larger mass splitting. Considering the history of ν-oscillation discovery, it is natural to think about using atmospheric neutrinos as a source for such a measurement. Indeed, it turns out that neutrino energies in the range of a few GeV and a baseline of a few thousands of kilometers are ideal for measuring the NMO. The currently most sensitive detector for atmospheric neutrinos at these energies is SK. Unfortunately, it cannot scrutinize NMO, because of its limited statistics even considering the long period of data taking, which started in 1996. SK, in an early phase (2014), was reporting atmospheric neutrino data, which slightly favor normal mass ordering at a bit less than 1σ. At the present time, as we have discussed above, a global analysis of neutrino data favors the normal mass ordering at 3σ level. Yet, a more robust and conclusive measurement is needed.

In the Precision IceCube Next Generation Upgrade (PINGU) [224] project, the inner part of the huge IceCube detector at the south pole should be equipped with additional strings of PMTs in order to push the energy threshold below the ~10 GeV border and to establish an improved resolution for particle tracking, still keeping a large detection volume in the multi-megaton scale. The initial design foresees an array of 40 strings with an average spacing of 20 m deployed in the deep core region of IceCube, and each string shall be equipped with 60 optical modules at a spacing of 5 m. With this design the collaboration will study atmospheric neutrino interactions in the relevant energy region between 5 and 15 GeV at a very high statistics, where the effect is most distinct. PINGU will be a ν_μ disappearance experiment. As PINGU cannot distinguish between muon and muon antineutrinos and as the survival probabilities of antineutrinos in normal ordering are basically identical to the those of neutrino in the inverted case, it

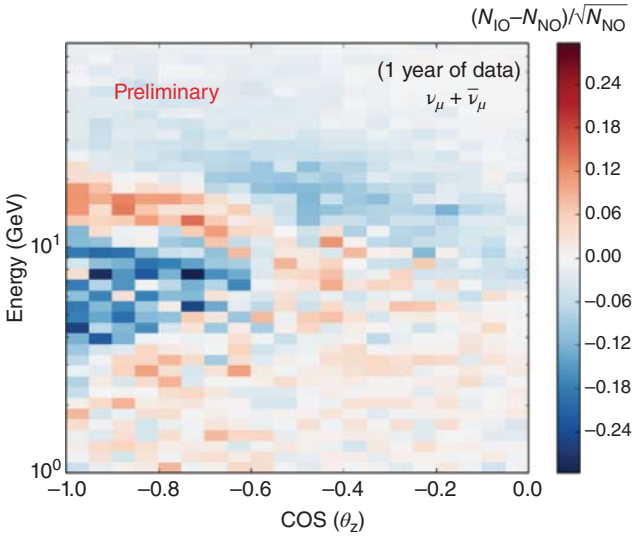

Figure 3.44 Scatter plot (energy versus azimuth angle) of the normal versus inverted ordering asymmetry $(N_{IO} - N_{NO})/\sqrt{N_{NO}}$ in the combined ν_μ and $\overline{\nu}_\mu$ signal of atmospheric neutrinos in PUNGU. Source: From Aartsen et al. 2014 [224].

seems impossible to disentangle NMO. However, asymmetries in the production rates as well as in kinematics and cross sections of interactions with nuclei lead to significant differences in the counting rates (depending on the energy and on the zenith angle) after several years of measurement. In Figure 3.44 the asymmetry of events expected for inverted ordering versus normal ordering $(N_{IO} - N_{NO})/\sqrt{N_{NO}}$ of the combined ν_μ and $\overline{\nu}_\mu$ signal in energy and the azimuth angle of the reconstructed tracks is shown.

PINGU can also extend our knowledge about other neutrino mixing parameters, like the octant for θ_{23}. In addition, it will improve IceCube's sensitivity to a galactic supernova neutrino burst. Today the funding for PINGU is not yet ensured, but in an optimistic view its installation might be completed in 2021 or 2022. In this context we would like to mention the ORCA and INO projects, which aim for NMO measurement using atmospheric neutrinos as well. Instead of using deep ice in the Antarctic, ORCA plans to deploy a large array of photosensors in the Mediterranean Sea and INO in India is a planned underground experiment using a magnetized iron calorimeter with 52 kt mass. More details about these projects and an overview about future NMO experiments can be found in [225].

Reactor-based experiments with baseline around 60 km are in principle well suited for NMO determination by resolving the location of maxima and minima of the oscillation pattern in the energy spectrum. Matter effects are negligible in this case and the energy dependent survival probability P for reactor neutrinos is

$$P(E) = 1 - P_{21} - P_{31} - P_{32} \tag{3.82}$$

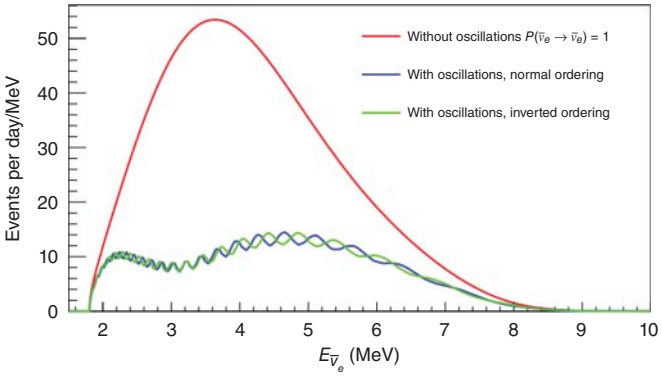

Figure 3.45 Calculated reactor neutrino spectrum at a distance of 53 km with a total thermal power of 36 GW as it will be the case for the future JUNO experiment. The red curve shows the no-oscillation case, whereas the blue and green lines show the total disappearance effect with the actual best fit mixing parameter. In blue the normal and in green the inverted NMO scenarios are assumed, respectively. They can be resolved by measuring precisely the spectral locations of the local maxima and minima.

with the "solar" term

$$P_{21} = \cos^4(\theta_{13})\sin^2(2\theta_{12})\sin^2(\Delta_{21}) \tag{3.83}$$

and two "atmospheric terms"

$$P_{31} = \cos^2(\theta_{12})\sin^2(2\theta_{13})\sin^2(\Delta_{31}) \tag{3.84}$$

$$P_{22} = \sin^2(\theta_{12})\sin^2(2\theta_{13})\sin^2(\Delta_{32}) \tag{3.85}$$

with the phases $\Delta_{ij} \propto |m_i^2 - m_j^2|L/E$, where L is the distance and E the neutrino energy. The oscillation consists of a disappearance effect large in amplitude but smoothly depending on the energy due to θ_{12} and Δ_{21}, which is superimposed by a fast oscillation pattern governed by the atmospheric mass splitting Δ_{31} and Δ_{32}. Now, for normal ordering, $|m_3^2 - m_1^2| > |m_3^2 - m_2^2|$ and therefore $\Delta_{31} > \Delta_{32}$, a relation that is upside down in case of an inverted ordering. This implies that the frequent oscillation maxima and minima coming from P_{31} and P_{32} have different positions in the energy spectrum, depending on which NMO scenario is realized in nature. The effect is most pronounced at around 60 km, as at this distance the relative shift in the spectrum is at its maximum at around 4–5 MeV as it is shown in Figure 3.45. The amplitude is influenced by the size of θ_{13} as one can see from the formulas above and fortunately it is large enough to make this observation possible.

A large detector is needed for gaining the required statistics and in addition it has to have a superb energy resolution. Calculations show that at least a resolution of about 3% at 1 MeV (1σ) is needed. This is the aim of the future Jiangmen Underground Neutrino Observatory (JUNO) project close to Jiangmen in China, which will setup a liquid scintillator detector with a mass of 20 kton [226]. Works on the new underground facility started in January 2015 and it is planned to complete the detector assembly in 2019 in order to be ready for data taking in 2021.

The scintillator shall be contained in a spherical vessel made out of acrylic. It will be immersed in a large water pool, which will act as an active muon veto. A high yield and very long scatter and absorption lengths are required for the liquid scintillator in order to achieve the required resolution. A large optical coverage close to 75% and the use of photosensors with high quantum efficiency are foreseen to match the design goals needed to fulfill the proposed physics case. In order to interpret the data correctly the total energy response of the detector has to be known quite precisely and it has to be calibrated online with high accuracy. A similar project also based on the technology of liquid scintillators is planned in South Korea under the name RENO-50. There, an 18 kt liquid scintillator underground detector at a baseline of 50 km to the reactor station is taken into consideration [227].

Accelerator-based neutrino experiments are also sensitive to the neutrino mass ordering, exploiting matter effects in the Earth, if the distance between the source and the detector is not too small. Of particular interest is here the observation of ν_e appearance in an originally pure ν_μ beam. The first oscillation maximum occurs at a distance $d = L_{\text{osc}}/2 \approx (1/2)\ 2.5\ \text{km}\ (E/\text{GeV})/(\Delta m^2/\text{eV}^2)$. With $\Delta m^2 \approx 2.4 \times 10^{-3}\ \text{eV}^2$ the numerical value accounts for $d/E \approx 520\ \text{km/GeV}$ and this sets roughly the lower limit on the baseline as matter effects in the Earth requires energies above ~ 1 GeV. ν_e appearance long baseline experiments are sensitive to δ_{CP}. At the first oscillation maximum, the Earth matter effect influences the oscillation probability depending on the NMO scenario. A NO would enhance ν_e oscillations but suppress it for antineutrinos. The effect would be exactly the opposite in the case of an inverted mass ordering scenario. Therefore, NMO scenarios can be disentangled by an accurate measurement of $\nu_\mu \to \nu_e$ and $\overline{\nu}_\mu \to \overline{\nu}_e$ oscillation probabilities. The NOνA experiment with its 2 GeV narrow band neutrino beam and a baseline of 810 km has a chance to get hands on NMO due to this matter effects. However, both NMO as well as the CP value δ can induce differences between neutrino and antineutrino oscillations, and therefore there are degeneracies and interferences in searching for these quantities. NOνA can reach a sensitivity to about 3σ of NMO determination for some favorable CP values after six years of measurement. As of summer 2018, the normal mass ordering is favored at about 2σ level.

In future long baseline experiments, the sensitivity on NMO and on the CP value δ should be significantly improved. Initially, there were two proposals: the European Large Apparatus for Grand Unification and Neutrino Astrophysics and Long Baseline Neutrino Oscillations (LAGUNA-LBNO) [228] and the US Long-Baseline Neutrino Experiment (LBNE). The LAGUNA consortium first followed the idea to identify a new deep underground laboratory in Europe, capable to host a very large new detector based either on water Cherenkov, liquid scintillator, or liquid argon technology. As the name LAGUNA indicates, first non-accelerator physics like solar and supernova neutrinos were in the scientific focus of this project. With the underground mine at Pyhäsalmi in Finland ($\sim$ 4050 m.w.e. shielding), an almost perfect location for hosting a detector with a size even in the megaton scale was found. In the succeeding LAGUNA-LBNO, the performance of large detectors based on liquid scintillators and on liquid argon were studied in the context of a long baseline experiment from CERN

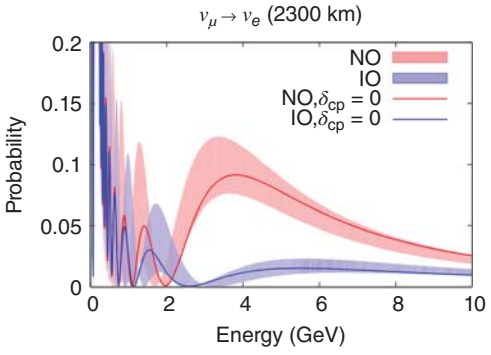

Figure 3.46 Calculated oscillation probability for ν_μ to appear as ν_e at a distance of 2300 km for a hypothetical neutrino beam from CERN to the underground laboratory in Pyhšalmi, Finland. The bands for normal and inverted hierarchies (NO and IO, respectively) show all possible values for CP-δ. Above ∼3 GeV the degeneracy due to the unknown CP-δ parameter is resolved.

to Pyhäsalmi with a distance of about 2300 km. The oscillation probability for $\nu_\mu \rightarrow \nu_e$ oscillations at this distance as a function of the neutrino energy is shown in Figure 3.46.

For energies above ∼ 3 GeV, the degeneracy due to the unknown value for CP-δ is resolved and the NMO scenario can be determined without any large systematic uncertainties besides a quite precise understanding of the density profile along the beamline through the Earth. Therefore, a CERN to Pyhšalmi beam would indeed offer the opportunity to measure the NMO with high precision. This is of course true for a large liquid argon detector with the capability to resolve individual tracks with high precision, but even a 50 kt liquid scintillator detector, named LENA, with its limited resolution for high energy events would be able to discriminate between the two scenarios. In this framework we note that in the future long baseline neutrino experiments might be used to determine the Earth's density profile with a high accuracy.

In the United States, the possibilities for a future neutrino beam have been also explored, basically in parallel to the European studies. Taking into account the high costs for such enterprises, it is clear that there can only be one experiment financed. Finally, it was agreed on to follow the high energy neutrino project within the United States, where a beam from Fermilab, close to Chicago, should be directed to the SURF underground laboratory in South Dakota (previously known as Homestake) at a distance of 1300 km. This project is given the name DUNE. It consists of a high power, wideband neutrino beam (GeV energy range) made at Fermilab, a far detector of 40 kt liquid argon (divided in four modules), and a near detector, located at about 500 m from the neutrino source. The detector technology exploited in DUNE will be based on liquid argon TPC. DUNE was developing out of the US-design LBNE [229] integrating most of the European members from LAGUNA-LBNO. The plan foresees the construction of four times 10 kt large detectors and a successive upgrading of the beam intensity of neutrinos as well as antineutrinos, until a power of 2 MW is reached, aiming for a luminosity of about 200 kton MW yr in total. For separating NMO scenarios via the matter effect and simultaneously avoiding the CP-δ degeneracy, a minimum distance of ∼1200 km between source and detector is required and DUNE just fulfills this requirement, although the separation power is not as great as it would be for the much longer LBNO project in Europe. In Figure 3.47 the $\nu_\mu \rightarrow \nu_e$ oscillation probabilities at 1300 km is shown for both scenarios. From these plots it

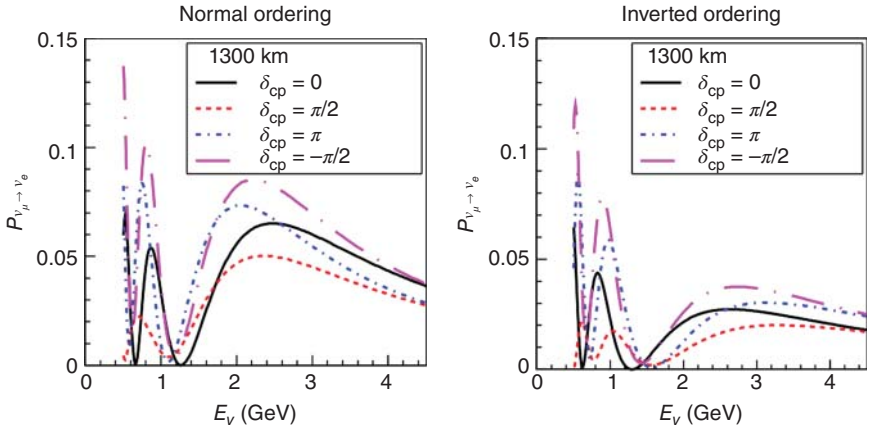

Figure 3.47 Calculated oscillation probability for ν_μ to appear as ν_e at a distance of 1300 km for the DUNE project. Different curves represent different values of CP-δ. Source: Qian and Vogel 2015 [225]. Reproduced with permission of Elsevier.

becomes clear that the maximal sensitivity is at an energy interval between 2 and 4 GeV.

For NO the ν_e appearance is enhanced at $\sim$ 2.5 GeV but suppressed for antineutrinos, and the opposite holds for the inverted scenario. Liquid argon TPCs of a size in the 10 kt range require a large R&D program. Both single phase and double phase TPC detector technology to be used in DUNE is being developed in the ProtoDUNE modules in operation at the CERN Neutrino Platform. In order to hold the aimed spatial resolution of about 1–2 mm an electric field of $\sim$ 500 V/cm is necessary, which leads to a potential in the multi-MV regime. Due to the long drift length the purity of the liquid has to be maintained continuously at a very high level, because electronegative atoms and molecules will diminish the electronically signal significantly otherwise. In addition a very large number of electronic channels has to be provided for reconstructing the particle tracks with high accuracy. On the accelerator side, the research is focused on the development of a high intensity neutrino beam, fed by a broad band photon beam with energies between 60 and 120 GeV at Fermilab. The DUNE detector will consist of four 10 kt liquid argon TPCs. The new excavation for DUNE at SURF is planned to begin in 2019 with the first detector installation starting in 2022 and the neutrino beam ready by ~2026. The remaining three detectors modules will follow over several years. Initially, the beam will operate with 1.2 MW power, followed by an upgrade to 2.4 MW. In Figure 3.48 the expected sensitivity of the NMO separation as a function of the total exposure is shown for a 3σ and a 5σ measurement. After ~200 kton MW yr, the probability for obtaining a 5σ measurement is above 80% in all cases.

As mentioned earlier, the T2K experiment has also some sensitivity on the mass ordering and on the δ_{CP}. At present, the experiment reports a 2σ evidence for CP violation. The present program aims to reach 20×10^{21} protons-on-target (POT) (now at 7.8×10^{21}) and reach a 3σ sensitivity for CP violation if near the current best-fit values. The T2K sensitivity should be enhanced significantly in

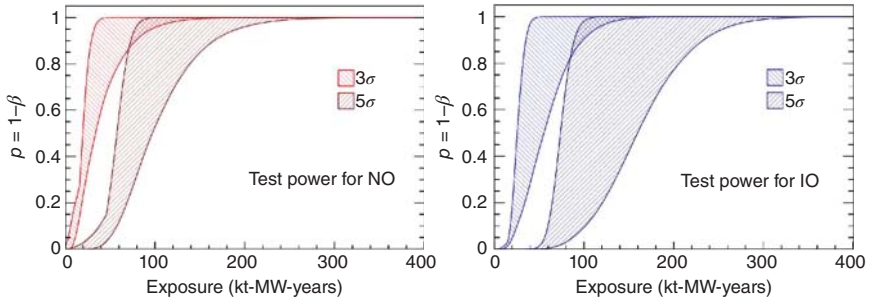

Figure 3.48 Probabilities for accepting the correct NMO scenario while excluding the incorrect hypothesis at 3σ and 5σ in the DUNE experiment as a function of the total exposure in kt-MW years. Source: Qian and Vogel 2015 [225]. Reproduced with permission of Elsevier.

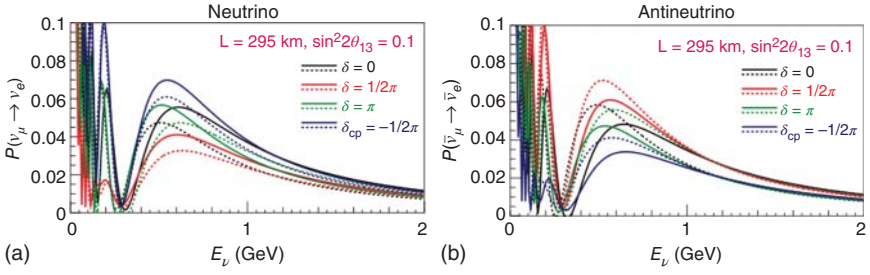

Figure 3.49 Energy-dependent oscillation probabilities for (a) neutrinos and (b) antineutrinos at a baseline of 295 km for several values of CP-δ and a fixed parameter $\sin^2\theta_{13}$. Solid (dashed) lines represent the case for normal (inverted) mass ordering. Source: Abe et al. 2015 [230]. Reproduced with permission of Oxford University Press.

Hyper-Kamiokande [230], a planned Mton water Cherenkov detector in Japan. In September 2018 funding for the construction of the detector was ensured. The excavation for the experimental site is planned to start in 2020. The detector will be divided in two parts each with 520 kt mass in total at a distance of 295 km from the neutrino source. The baseline implies moderate neutrino energies and matter effects would be smaller with respect to DUNE.

In this case the $\nu_\mu \to \nu_e$ oscillation probability depends mainly on the vacuum mixing angles and on δ only as it is shown in Figure 3.49 for $\sin^2\theta_{13} = 0.1$. The remaining dependence on the NMO scenario is also shown in Figure 3.49. Near detectors are planned for Hyper-Kamiokande in order to minimize instrumental uncertainties and the off-axis method should be used to constrain the neutrino energies to a small band in the region of interest. A beam power of 0.75 MW is planned and after three years of data taking the experiment would allow to reach a 3σ significance on δ for a large parameter space of 76% and above 5σ for 58% including the parameter range favored today. According to the present schedule, the data taking in Hyper-Kamiokande is expected to start in 2026. By the time the experiment will take data one may expect that the NMO scenario will be clear from other experiments. This would of course minimize systematic effects connected with this question and enhance the sensitivity on δ_{CP}. This is

even more true for the DUNE experiment for it has also a high sensitivity on the CP-δ parameter. A 5σ discovery potential in half of the possible phase space should be possible after a measuring period of about 10 years [229].

All together one can stand that there is reasonable hope to answer the two still open questions about the neutrino mass ordering and the δ_{CP} value within the next decade or so. Presumably, the final answer will be provided by a combination of different experiments as it has been the case in neutrino physics in the past 50 years. Indeed, the use of atmospheric, reactor, and accelerator neutrinos is a very complementary approach as completely different sources are used and the effects searched for differ significantly from each other. Therefore, a global analysis including all neutrino experiments will be as important as it has been in the past.

3.5.4 Are There Sterile Neutrinos?

So far we have discussed all experimental results in the framework of three active neutrinos ν_e, ν_μ, and ν_τ, which are eigenstates of the Hamiltonian describing cc weak interactions. Each of these states is a linear superposition of mass eigenstates ν_1, ν_2, and ν_3 and they all are purely left-handed in terms of chirality. In this context right-handed states are not existing. However, for constructing mass terms within the Higgs mechanism and very small Yukawa couplings, right-handed states are needed. As they do not participate in weak interactions, they are called sterile neutrinos. In this sense these very elusive particles would only underly gravitation as a fundamental force. This however implies that sterile neutrinos may have an important influence on the development and structure forming of our universe – if they do exist. Indeed, sterile neutrinos are discussed to play a role in the context of dark matter today. This is basically motivated by astrophysical observations of a weak X-ray line at an energy 3.55 keV from X-ray-multi-mirror (XMM) Newton data [231], which seems to be hardly explainable by usual X-ray sources in the cosmos. Yet, a sterile neutrino with a mass around 7 keV could decay radiatively into a light neutrino and a γ, which share the energy equally. In order to do so the sterile neutrino has to mix to the active, standard neutrinos and the mixing matrix has to be expanded. Dark matter would then consist at least partially of these sterile neutrinos, which are not thermally produced in the early universe but are generated by mixing. The mixing parameter has to be very small, because otherwise the 7 keV mass would overclose the total mass energy density of our universe $\Omega_{\mathrm{tot}} = 1$, which is confirmed so nicely by CMB data. A small mixing implies also a small decay rate and it turns out that oscillation amplitudes around $\sin^2 2\theta \sim 10^{-10}$ would be consistent with cosmology as well as astrophysical observations [232]. The allowed parameter space for a sterile neutrino is shown in Figure 3.50, where limits from dark matter abundance, from X-ray observations, and from phase-space density are considered. The latter comes from violation of the Pauli principle for spin 1/2 particles. The lower the neutrino mass, the higher the number density in order to explain dark matter in galaxies and galaxy clusters. However, the neutrinos have to obey the Pauli principle and at a certain value the

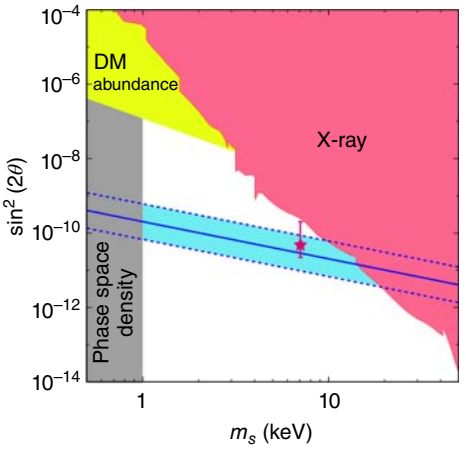

Figure 3.50 Exclusion plot for the mixing of a massive sterile neutrino with mass m_s to the active neutrinos via a mixing angle θ. The shaded regions are excluded by X-ray observations, dark matter overproduction, and limits due to phase-space density. The red spot at 7 keV indicates the mass and mixing that can explain the observed X-ray line at 3.55 keV. The blue band shows the predicted parameter space for sterile neutrinos within a special model. Source: Ishida et al. 2014 [232]. Reproduced with permission of Elsevier.

Fermi energy exceeds the energy necessary to escape the gravitational potential in which they are trapped.

Can this sterile neutrino be detected by laboratory measurements – if it exists? The tiny mixing amplitude makes this extremely difficult. There are proposals to search for small kinks in the energy spectra of β decays, but the sensitivity range will be limited. The best prospects in this context may come from the KATRIN experiment, where a sensitivity of $\sin^2 2\theta \sim 4 \times 10^{-8}$ may be reached [233].

A completely different motivation for sterile neutrino searches is coming from the so-called reactor anomaly. Reviewing the neutrino production mechanism in nuclear reactors with enhanced precision a group of physicists came to the conclusion that the predicted neutrino flux should be higher by about 3% with respect to previous estimations [165]. In addition, the average value for the neutron lifetime was shifting to somehow lower values, which leads to a slightly higher cross section for the detection of $\overline{\nu}_e$ coming from nuclear reactors. A reanalysis of older reactor experiments performed at distances below ~100 m, taking into account the new calculated fluxes and cross section, may suggest the disappearance of reactor neutrinos [234], which cannot be explained in the framework of the three active neutrinos. With the new flux calculations, the ratio R between the measured and expected no-oscillation flux shifts to a value of $R = 0.943 \pm 0.023$ (1σ), suggesting an almost 2.5σ disappearance effect [234]. The distribution of the individual R-values of the different short-baseline experiments is illustrated in Figure 3.51. The discrepancy, quantified by R, is known as the *reactor anomaly*.

This scenario is even enforced by considering the results of calibration runs with terrestrial neutrino sources performed for the radiochemical neutrino experiments GALLEX and SAGE, described in the Chapter 4. For both experiments strong radioactive ^{51}Cr sources have been placed in the vicinity of the tanks filled with gallium. Later the SAGE collaboration repeated this experiment with a ^{37}Ar source. In both cases mono-energetic ν_e are emitted at low energies of about 1 MeV. In this sense this calibration runs are oscillation experiments at very short distances of ~1 m and at low energies. GALLEX and SAGE observed an average deficit of $R_G = 0.86 \pm 0.06$ (1σ) as reviewed by Giunti and

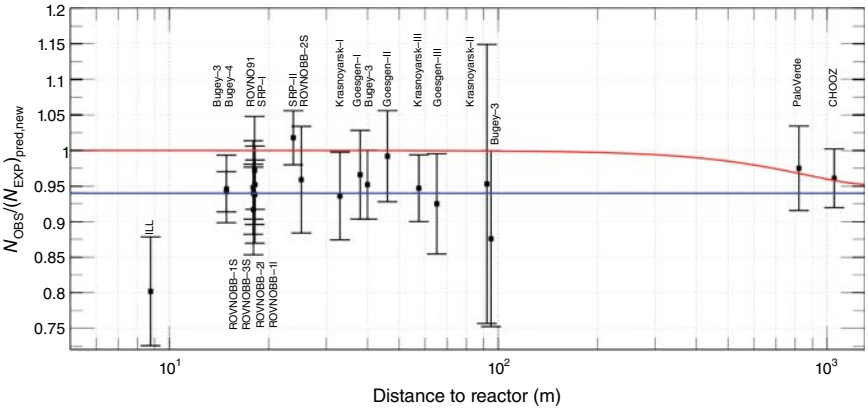

Figure 3.51 Distribution of the ratio between observed and expected neutrino luxes of short baseline reactor experiments, recalculated by Mention et al. [234]. In the scenario without a fourth sterile neutrino, the values should scatter around the red curve. The blue line shows the best-fit value for a sterile neutrino scenario with $\Delta m^2 > 1$ eV^2 and $\sin^2 2\theta = 0.12$. Source: Mention et al. 2011 [234]. Reproduced with permission of American Physical Society.

Laveder [235]. A fourth sterile neutrino, which mixes with the well-known three flavors with parameters $\Delta m^2 > 1$ eV^2 and $\sin^2 2\theta \sim 0.1$, could indeed explain all these results. Of course, it is not excluded that systematic effects may mimic the reactor and solar calibration anomalies. As an example, a fundamental question is this: How reliable are the flux predictions and their uncertainty estimate? It is well known that, among the many β decays to be taken into account, several are forbidden processes with a not-well-known decay shape factor. Further studies are underway, including the measurement with high accuracy of the near detector spectrum in Daya Bay. In addition, future short baseline experiments are underway to probe the existence of a sterile neutrino in this parameter range. For further reading, see [236]. As of 2019, short-baseline reactor experiments have not found evidence for oscillations to sterile neutrinos. A better experimental understanding of the flux predictions is required in the coming years to explain the anomalies.

4

Solar Neutrino Experiments

4.1 Introduction

As described in detail in Chapter 1, the Sun emits a huge flux of electron neutrinos, ν_e, named *solar neutrinos*. Electron neutrinos are created in the core of the Sun by means of the following process:

$$4p \rightarrow {}^4\mathrm{He} + 2e^+ + 2\nu_e + Q \tag{4.1}$$

where $Q = 26.73$ MeV also accounts for positron annihilation. The average energy of solar neutrinos is about 0.53 MeV, which is about 2% of the total energy released in Eq. (4.1). Some 6.5×10^{10} $\mathrm{cm}^{-2}\mathrm{s}^{-1}$ solar neutrinos reach the Earth. In addition, neutrinos, being weakly interacting particles, stream out from the interior of the star almost at the speed of light. They carry information on the energy source inside the core and on the inner structure of the star. The first experimental effort to search for solar neutrinos started in 1968. In about 50 years seven detectors have searched for solar neutrinos with different techniques and in different energy windows. The field has collected fundamental information on neutrino physics and astrophysics. Neutrino observations started with the so-called *solar neutrino problem* (SNP). Detected solar neutrinos were fewer than predicted. At the beginning, it was not clear whether the missing solar neutrinos could have been caused by an unknown effect of astrophysics or new neutrino physics. It took about 30 years to understand the nature of the problem. Collected data provided a solution in the framework of neutrino mixing and neutrino interactions in matter.

Solar neutrino research has gone through a number of fundamental findings. Early observations from the chlorine and Kamiokande-II experiments established the SNP. Later, between 1991 and 1997, data from the gallium experiments has shown that a new physics is the primary cause of the SNP. In 2001 a 3.7σ evidence from SNO and Super-Kamiokande for solar neutrino flavor change during propagation to Earth was provided. In 2002 the evidence became more robust with the neutral current measurement in SNO. In 2007 Borexino measured sub-MeV ^{7}Be solar neutrinos in real time and in 2014 probed the energy source in the Sun with pp neutrinos at 10% level. Recently, Super-Kamiokande has measured a 3σ evidence for the regeneration of ν_e going through the Earth during nighttime. In 2018 Borexino reports a measurement of the complete pp chain.

Solar Neutrino Physics: The Interplay between Particle Physics and Astronomy,
First Edition. Lothar Oberauer, Aldo Ianni, and Aldo Serenelli.

Table 4.1 Summary of the main characteristics of solar neutrino experiments.

Detector	Active mass	Threshold (MeV)	Data taking
Homestake	615 tons	0.814	1967–1994
	C_2Cl_4		
Kamiokande-II/III	3 kt	9/7.5/7.0	1986–1996
	H_2O		
SAGE	50 tons	0.233	1990–2010[a)]
	molten metal Ga		
GALLEX	30.3 tons	0.233	1991–1997
GNO	$GaCl_3$–HCl		1998–2003
Super-Kamiokande	50 kt	5	1996–2001
	H_2O	7	2003–2005
		4.5	2006–2008
		3.5	2008–2018
		3.5	2019–present
SNO	1 kt	6.75/5/6	1999–2006
	D_2O		
Borexino	300 tons	0.2	2007–present
	C_9H_{12}		
Borexino	300 tons	0.2	2007–present
KamLAND	1 kton	0.4b	2009–2011[b)]

a) The experiment is still in operation, yet last published data refer to 2010 [237a].
b) To allow detailed study of low energy backgrounds, the threshold is reduced to 0.2 MeV for 1 ms once per second [237b].
Source: Ianni 2017 [237]. Reproduced with permission of Elsevier.

Eventually, the SNP brought us to the discovery of neutrino mixing and neutrino flavor conversion in matter. However, recently a new controversy came into play, the *solar abundance problem*. A significant disagreement has been identified between helioseismology data and the solar model, namely, the theoretical framework we believe could provide the most robust description of the Sun (see Chapter 1).

In this chapter we review the solar neutrino experiments. In Table 4.1 we summarize details about the experiments that have been measuring solar neutrinos. Solar neutrinos have been searched for using different techniques (radiochemical experiments, imaging water Cherenkov, and organic liquid scintillator experiments) and over different energy windows. At present, we have collected about 50 years of observations on solar neutrinos. The experimental challenges faced in searching for solar neutrinos have improved enormously the ability to detect rare events. As a matter of fact, the experimental knowledge developed in this field has been used in the last several years in the direct search for dark matter, where eventually solar neutrinos will become an irreducible background source [238].

4.2 The ^{37}Cl Experiment

The Homestake experiment [239–241], also known as the ^{37}Cl experiment, was for two decades the first and only operating solar neutrino detector. This is a so-called radiochemical experiment, which exploits the reaction:

$$\nu_e + {}^{37}_{17}\mathrm{Cl} \rightarrow e^- + {}^{37}_{18}\mathrm{Ar} \tag{4.2}$$

The energy threshold of this reaction is equal to the difference in the nuclear masses of ^{37}Ar and ^{37}Cl and is equal to 813.9 keV. The ^{37}Ar is unstable and decays 100% back to ^{37}Cl by electron capture with a half-life equal to 35.04 days. In a radiochemical experiment, incoming neutrinos might capture on specific nuclei and form radioactive isotopes over a specific exposure. These radioactive isotopes are chemically separated and counted. This detection method was first proposed by B. Pontecorvo in 1946 [242] and later independently proposed by L. Alvarez in 1949 [243]. In the Homestake experiment, the target is a tank filled with 615 tons of C_2Cl_4 (tetrachloroethylene) deep in the Homestake Gold Mine in Lead, South Dakota, United States. The experiment has taken data from 1967 to 1994. At present, the Homestake Mine houses the Sanford Underground Research Facility (SURF) [244] for dark matter and neutrino research. In the ^{37}Cl experiment the basic idea is to expose the tank to the solar neutrino flux for a time of the order of 40 days. After the exposure the ^{37}Ar in the tank, made by the solar neutrino captures, is taken out and its radioactivity counted for a few months in order to determine the initial number of atoms, $\mathrm{N}(^{37}\mathrm{Ar}; t_{\mathrm{run}})$, where t_{run} is the exposure time. $\mathrm{N}(^{37}\mathrm{Ar}; t_{\mathrm{run}})$ will allow to determine the solar neutrino capture rate. During an exposure some ^{37}Ar atoms are made by neutrino interactions, and some decay to ^{37}Cl with a decay rate $\lambda = 0.0198\ \mathrm{day}^{-1}$. Therefore, the fundamental equation of the experiment is written:

$$\mathrm{N}(^{37}\mathrm{Cl}) \sum_i \int_{0.814\ \mathrm{MeV}}^{15\ \mathrm{MeV}} \phi_i(E_\nu)\sigma(E_\nu) = \frac{\lambda \mathrm{N}(^{37}\mathrm{Ar}; t_{\mathrm{run}})}{\epsilon_e \epsilon_c (1 - e^{-\lambda t_{\mathrm{run}}})} - b \tag{4.3}$$

where the left-hand side gives the solar neutrino capture rate from the different components, namely, $i = (\mathrm{pep}, {}^7\mathrm{Be}, {}^8\mathrm{B}, \mathrm{CNO})$, and $\mathrm{N}(^{37}\mathrm{Cl}) = 2.16 \times 10^{30}$ is the number of ^{37}Cl atoms. The relative contribution to the total rate from the different solar neutrino components is determined to be 3%, 13%, 81%, and 3%. The right-hand side of Eq. (1.2) gives the ^{37}Ar production rate taking into account that these atoms can decay back to ^{37}Cl while they are produced. Moreover, $\mathrm{N}(^{37}\mathrm{Ar}; t_{\mathrm{run}})$ gives the number of ^{37}Ar atoms produced in the exposure time, considering the extraction efficiency, ϵ_e, and the counting efficiency, ϵ_c. The ^{37}Ar background rate, b, from cosmic rays, muon-induced fast neutrons, and natural radioactivity is subtracted.

The capture cross section in Eq. (4.2) and in similar neutrino capture reactions requires knowledge of nuclear matrix elements, which in most cases are not known. The matrix element includes the contribution of Fermi and Gamow–Teller matrix elements. For transitions to excited states, the Gamow–Teller matrix element is generally uncertain. Yet, there are a few exceptions. Equation (4.2) is one example for which the cross section can be estimated with accuracy

for a transition both to the ground state and to excited states. As a matter of fact, this is an exceptional case (see discussion in [245]) where the Gamow–Teller matrix element can be estimated from the mirror process: ${}^{37}_{20}\mathrm{Ca} \rightarrow {}^{37}_{19}\mathrm{K} + e^+ + \nu_e$.

The extreme challenge of this experiment is the extraction of a very small number of ^{37}Ar atoms produced during an exposure. For 40 days of exposure, we determine 41 atoms produced by solar neutrinos without considering oscillations. This corresponds to an interaction rate of 1.5 ± 0.2 captures/day or 8 ± 1 SNU, where 1 SNU $= 10^{-36}$ captures/target nucleus/second.

The Homestake experiment was installed at 1478 m below the surface level (about 4200 m of water equivalent or m.w.e.). Background sources for ^{37}Ar production underground must be considered. Cosmic rays can produce ^{37}Ar atoms by means of ^{37}Cl(p, n)^{37}Ar from protons produced in muon interactions. This background was studied by direct measurement of the ^{37}Ar production in a 11 ton C_2Cl_4 movable tank located in shallow sites and at a depth of 1800 m.w.e. in the Homestake mine [239]. The extrapolation at the depth of the detector gives 0.047 ± 0.013 atoms/day. The scaling procedure was validated by direct counting of the production process $\mu \rightarrow {}^{39}\mathrm{K} \rightarrow {}^{37}\mathrm{K} \rightarrow {}^{37}\mathrm{Ar}$ [241]. Fast neutrons induced by cosmic rays deep underground, by natural radioactivity through (α, n) reactions, and ^{238}U spontaneous fission can produce ^{37}Ar by the reaction sequence ^{35}Cl(n, p)^{35}S with an energy threshold of about 1 MeV, followed by ^{37}Cl(p, n)^{37}Ar. The fast neutron flux in the detector's cave was measured by the reaction ^{40}Ca(n, α)^{37}Ar. From this measurement the background induced by fast neutrons is determined to be 0.05 ± 0.025 ^{37}Ar atoms/day. This background is reduced by a passive shielding external to the tank. Initially a water shielding was used. In 1984 this latter was replaced by a 30 cm liquid scintillator shielding. When the shielding is taken into account, the fast neutrons background is reduced to 0.03 ± 0.025 ^{37}Ar atoms/day. Another background source is due to the radioactivity of U and Th in the tank and in the C_2Cl_4. This contamination can produce ^{37}Ar atoms by (α, p) and (p, n) reactions. The U and Th contamination in the liquid was determined to be at the level of 10^{-9} g/g. This sets the intrinsic ^{37}Ar production background from the liquid. To reduce the contribution from the tank, the strict requirements in the design were (i) vacuum tightness to avoid argon contamination from air (0.934% of argon in air) and (ii) radio-purity of the steel and weldings. The tank was vacuum-leak tested with helium gas at the level of 10^{-6} cm^3/s. The steel to make the tank was measured to determine the U and Th radioactivity to be not critical. The tank components were welded in place underground with thorium-free welding rods. The tank as built was flushed with radon-free air before filling with C_2Cl_4. Taking into account this information, the background due to natural radioactivity in the tank and in the liquid is determined to be < 0.017 ^{37}Ar atoms/day. In Table 4.2 we summarize the information about expected solar neutrino interaction rate and backgrounds. From the data reported in this table, it turns out that the solar neutrino capture rate measurement is feasible, in spite of the very small number of atoms produced, provided a high efficiency of ^{37}Ar extraction and counting.

In Figure 4.1 a sketch of the detector and ancillary facilities are shown [241]. The 95% of the tank is filled with C_2Cl_4 and the remaining 5% with helium gas at 1.5 bar pressure. The cavity can be flooded with water to provide neutron shielding. The extraction of argon is based on the consideration that argon being a noble gas will not chemically or physically attach to C_2Cl_4. Therefore, an ancillary helium gas purging system with 40 eductors was used to remove air argon from C_2Cl_4.

Table 4.2 Homestake experiment: expected signal, background, and measurement.

Background	^{37}Ar atoms/day
Cosmic rays	0.047 ± 0.013
Fast neutrons	0.03 ± 0.025
Radioactive contaminants in tank and in C_2Cl_4	< 0.017
Signal	**^{37}Ar atoms/day**
Expected solar neutrino rate	1.5 ± 0.2
Measurement	**^{37}Ar atoms/day**
	0.48 ± 0.04

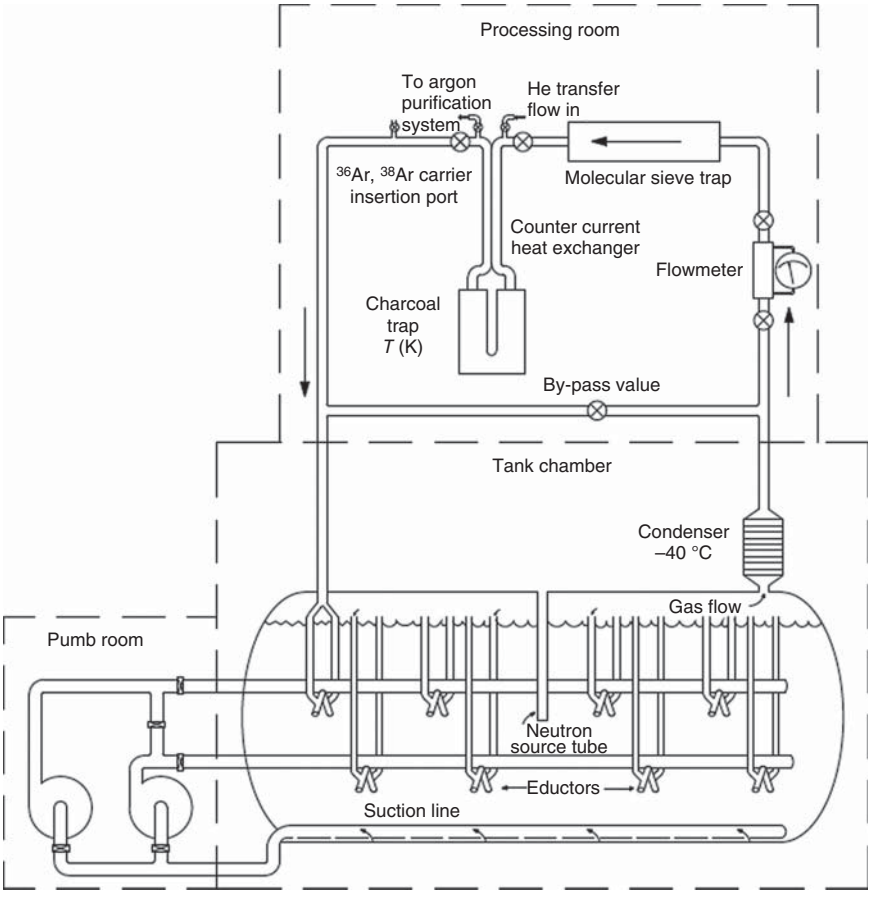

Figure 4.1 Homestake detector and ancillary facilities [241]. This drawing is only a schematic. Source: Cleveland et al. 1998 [241]. Reproduced with permission of IOP Publishing.

The procedure for a run follows the sequence: (i) before starting the run, 0.2 cm^3 of either ^{36}Ar or ^{38}Ar (some 10^{19} atoms) is added to measure later the extraction efficiency; (ii) the tank is exposed to the solar neutrino flux for some 40 days; (iii) the tank is purged with helium gas for 20 hours (one tank volume of helium); (iv) the gas goes through a condenser at −40 °C to freeze C_2Cl_4 vapors and later to a flow meter and to a molecular sieve trap to remove residual C_2Cl_4 vapors; (v) the gas is sent to a charcoal trap at liquid nitrogen temperature, 77 K, to adsorb argon (melting point at 83.8 K) and let the helium go back to the tank. After 20 hours of purging, 95% of argon is collected. The final step before counting the ^{37}Ar radioactivity is the extraction and purification of the argon sample from the charcoal. The charcoal is heated to 200 °C and purged with helium gas. Active gas such as oxygen and nitrogen are removed by exposing the gas to a titanium metal powder at 900 °C. The gas sample goes to a smaller charcoal trap at liquid nitrogen temperature. Later heavy elements such as radon, xenon, and krypton are removed by gas chromatography. Finally, the gas is sent to a very small charcoal trap at 77 K and remaining helium is pumped off. The charcoal is heated at −50 °C to reduce radon contamination at this stage. The argon sample is loaded into a 0.5 cm^3 proportional counter with 7% in volume of tritium-free methane, which serves as counting gas.

A critical measurement is that of the argon extraction efficiency. This measurement is based on the ratio of number of atoms of either ^{36}Ar or ^{38}Ar recovered to the number of atoms inserted before starting the run. As an example for an ^{36}Ar-based run, the initial number of atoms is given by

$$n_{36}^{\text{start}} = \frac{p_{36} V_{36} f_{36}}{k T_{\text{start}}} \tag{4.4}$$

where p_{36} is the pressure of carrier gas measured at the time of the insertion, V_{36} is the corresponding volume, T_{start} is the temperature and f_{36} is the isotopic purity of the sample. A similar measurement is performed after the counting of ^{37}Ar where the isotopic purity is determined by mass spectrometry. The extraction efficiency is given by $\epsilon = n_{36}^{\text{end}}/n_{36}^{\text{start}}$. Averaging over some 120 runs, the extraction efficiency is determined to be 0.958 ± 0.007. To test the process of the argon extraction, a small neutron source was located in the center of the tank through a tube installed for calibration purposes. Neutrons produce ^{37}Ar in the C_2Cl_4. Recovering of ^{37}Ar produced by the neutron source with the carrier gas was measured. This test showed a high recovering efficiency. The use of an artificial neutrino source from ^{65}Zn was proposed ($e^- + {}^{65}Zn \rightarrow \nu_e + {}^{65}Cu$) [246]. The detector irradiation with an electron neutrino source of known intensity would have been the ultimate test of the extraction efficiency. The intensity of the source must have been of the order 1 MCi (3.7×10^{16} Bq). Preliminary studies were done at a reactor in Oak Ridge, but later the project was abandoned.

The ^{37}Ar counting was performed by a custom proportional counter. The counter has about 0.48 cm^3 active volume, 30 mm long, and 4.5 mm in diameter. The housing of the active volume is the cathode. A wire going through the center is the anode. In the ^{37}Ar decay the main observed channel corresponds to a K orbital electron capture with the emission of Auger electrons whose total energy is 2.823 keV (81.5%). In addition, 8.7% of the decays involve a K electron capture with the emission of an X-ray. Considering the dimensions of the counter, some 10% of these X-rays produce 2.8 keV of deposited energy. Therefore, the 2.8 keV

energy channel contains in total 82.4% of the ^{37}Ar decays. The expected counting rate is less than 1 per day. Therefore, the counter must have a background that should be less than a few counts per week to have a signal-to-background ratio of order greater than 2. A careful choice of construction materials was critical together with an effective shielding and veto of external background. The counter turned to have a background less than 1 count per month. In the counter Auger electrons produce a high localized energy deposition, resulting in a short rise time of the recorded charge pulse. On the contrary, background events have a much longer rise time because the energy is distributed over a wider region. This difference is used to discriminate signal against background charge pulses. Counters are calibrated with a low energy X-ray source from ^{55}Fe for the energy scale and with ^{60}Co for pulse shape discrimination. Typical values of counting efficiency are 42% inside 1 full width half maximum (FWHM) of the 2.8 keV peak. This counting efficiency requires a long counting time: for an exposure of 40 days in 100 days of counting, we expect two decays, taking into account an overall efficiency of 0.40.

The measured ^{37}Ar production rate in the Homestake experiment is determined to be $0.478 \pm 0.030_{\text{stat}} \pm 0.029_{\text{syst}}$ day^{-1} [241], where the systematic error is due to the uncertainty on the extraction and counting efficiency, on the background production rate predictions, and on the event selection procedure. This production rate corresponds to a neutrino interaction rate of 2.56 ± 0.23 SNU. From Table 4.2 we can conclude that the prediction and the measurement are in disagreement. To quantify this result, we can determine the p-value, which turns to be 4.2×10^{-6} (4.6σ). This disagreement was the first evidence of the SNP. At the time of the Homestake experiment, two inferences could have been made to explain this result: (i) the standard solar model calculations are wrong and (ii) the physics of the solar neutrino interactions is not well known. At the present time this discrepancy is understood in the framework of neutrino oscillations.

The Homestake experiment has paved the way for future experimental efforts in searching for solar neutrinos. Raymond Davis Jr. for the Homestake Collaboration was awarded the 2002 Nobel Prize in Physics for the detection of cosmic neutrinos.

4.3 Kamiokande-II/III

The Kamiokande water Cherenkov detector was built in 1983 to search for proton decay. In 1985 the detector was upgraded to search for solar neutrinos. The upgrade ended in 1986, just in time to observe electron antineutrinos from the supernova SN1987A on 23 February 1987 [247]. The upgrade reduced the water's intrinsic radioactivity and the detection threshold initially to 9 MeV. Further improvements reduced the threshold to 7 MeV. In a water Cherenkov detector, solar neutrinos are measured by means of the electron neutrino elastic scattering:

$$\nu + e^- \rightarrow \nu + e^- \tag{4.5}$$

The maximum kinetic energy of the recoil electron is given by $T_{\max} = \frac{2E_\nu^2}{2E_\nu + m_e c^2}$, with E_ν as the neutrino energy and m_e the electron rest mass. Moreover, for a fixed

recoil electron kinetic energy, T, the minimum possible neutrino energy is given by $E_\nu^{\min} = \frac{T}{2}\left(1+\sqrt{1+\frac{2m_ec^2}{T}}\right)$. The differential cross section for this interaction process is reported in [248]. In the energy range of 5–10 MeV, the total cross section can be approximated as $\sigma(\nu_e e^- \to \nu_e e^-) = 9.52\times10^{-44}(E_\nu/10\text{ MeV})\text{ cm}^2$; $\sigma(\nu_\mu e^- \to \nu_\mu e^-) = 1.55\times10^{-44}(E_\nu/10\text{ MeV})\text{ cm}^2$, $\sigma_{\nu_e e}/\sigma_{\nu_\mu e} \sim 6$. The expected solar neutrino rate is written:

$$R = A\int_{T_{\text{Th}}}^{T_{\max}(E_\nu)} \mathrm{d}T\eta(T)\int_{E_\nu^{\min}(T)}^{E_\nu^{\max}} \mathrm{d}E_\nu \frac{\mathrm{d}\phi_\nu}{\mathrm{d}E_\nu}(E_\nu)\frac{\mathrm{d}\sigma}{\mathrm{d}T}(E_\nu, T) \tag{4.6}$$

where A is a normalization constant, T_{Th} is the detection threshold, $\mathrm{d}\phi_\nu/\mathrm{d}E_\nu$ is the differential solar neutrino flux, η is the detection efficiency, and $\mathrm{d}\sigma/\mathrm{d}T$ is the differential interaction cross section.

Scattering experiments such as Kamiokande can directly measure the precise arrival time of neutrinos and probe correlations with time-dependent effects. Neutrino-electron elastic scattering is sensitive to all neutrino flavors, although the cross section for $\nu_{\mu,\tau}$ is much smaller than that for ν_e. On the contrary, radiochemical detectors based on a charged current interaction are only sensitive to ν_e. In addition, scattering experiments have not a specific tagging signature on an event-by-event measurement. This is the case of Kamiokande, which is sensitive to ^{8}B solar neutrinos. Natural radioactivity, producing β or γ ionizing particles, gives the same response as from a neutrino interaction. Therefore, the reduction of the background is of great importance for these experiments. The maximum energy produced by natural radioactivity from β and γ ionization is due to ^{208}Tl from the ^{232}Th radioactive decay chain. For ^{208}Tl $Q_\beta = 5$ MeV and the decay proceeds always through the emission of a 2.614 MeV γ-ray. Therefore, for intrinsic ^{232}Th contamination in the target mass, a full contained ^{208}Tl decay can produce tail background events at energies up to ∼8 MeV, taking into account an energy resolution of 20% at 5 MeV. A very high radio-pure water has some 10^{-14} g/g of ^{232}Th, which means 3.5 counts/day/ton background events from ^{208}Tl.[1] This number must be compared with the solar neutrino expected rate. As an example, the most numerous pp solar neutrinos in water give 2 counts/day/ton by neutrino elastic scattering. Therefore, an extreme background reduction is the great challenge for scattering experiments. Only solar neutrinos above 3–5 MeV can be measured with an ideal water detector by means of elastic scattering. We will see later in this chapter that to search for solar neutrinos below 3 MeV in real time, a different technique must be exploited: a detector based on liquid organic scintillator.

Cherenkov radiation was discovered in 1934 [249]. A charged particle emits electromagnetic radiation while moving in a medium with a velocity greater than the phase velocity of light in that medium. This is a threshold effect. The minimum kinetic energy for an electron to produce Cherenkov radiation is given by $T_{\text{Th}} = m_ec^2\left(\frac{1}{\sqrt{1-1/n^2}}-1\right)$ with n as the index of refraction and c the speed of light. For water, $n = 1.33$ and $T_{\text{Th}} = 0.264$ MeV. The radiation is emitted in a

1 The conversion factor 10^{-9} g/g = 4.06 mBq/kg for ^{232}Th in the assumption of secular equilibrium is used.

cone of half angle, θ_C, and centered on the direction of the moving particle. The angle θ_C is given by the equation: $\cos\theta_C = 1/n\beta$ with $\beta = v/c$. The number of photons emitted per unit of length in the optical range (400 nm $\leq \lambda \leq$ 700 nm) is written: $\mathrm{d}N/\mathrm{d}x \approx 490 \sin^2\theta_C$ photons/cm. For a relativistic particle moving in water, $\theta_C = 41.2°$, hence $\mathrm{d}N/\mathrm{d}x \approx 213$ photons/cm. Photons are detected by photomultiplier tubes (PMTs), which are extremely sensitive light detectors. Incident photons on the PMT photocathode make photoelectrons (ph.e.), which move under an electric field toward the dynodes chain. The latter works as an electron multiplier, which from one primary electron can make as much as 10^7 electrons, depending on the operating high voltage. These electrons make an electric current, which can be measured. The number of ph.e. in a detector such as Kamiokande can be estimated as follows:

$$N_{\text{ph.e.}} \approx (213\gamma/\text{cm})L(\text{cm})e^{-l/\lambda}\eta Q_{\text{PMT}}C \tag{4.7}$$

where $\lambda \sim 50$ m is the attenuation length of light; $Q_{\text{PMT}} = 0.25$ is the quantum efficiency of PMTs, which is the probability to convert one hitting photon onto the photocathode to 1 ph.e.; $\eta = 0.9$ is the collection efficiency on the first dynode of the PMTs; $C = 0.2$ is the PMTs coverage, which gives the probability that one photon is detected; L is the range of electrons; and l is the detector liner dimension. Considering $l = 10$ m and $L = 5$ cm for 10 MeV electrons, $N_{\text{ph.e.}} \approx 39$ ph.e., which corresponds to some 16% energy resolution at 10 MeV. The recoil electron is scattered in the forward direction. By measuring the recoil energy and direction, we can reject the background and identify the neutrino source and spectrum.

The upgraded Kamiokande detector is known as Kamiokande-II and was in operation from 1986 to 1990 [250]. The Kamiokande-II detector was installed in the Kamioka mine in the Japanese Alps. The detector site has a horizontal access of 2800 m long. The underground cave has a depth of 2400 m.w.e. A schematic view of the detector is shown in Figure 4.2. The entire volume of water, about 3000 tons, is contained inside a steel cylindrical tank 15.6 m in diameter and 16 m in height. The inner surface was painted in black with an epoxy resin. An inner mass of 2140 tons of water, separated by black sheets, is viewed by 948 20-in. PMTs. This makes the inner detector. The total photocathode coverage is 20%. PMTs are shielded against the Earth's magnetic field by a system of coils. Considering the large photocathode area, this shielding is important to keep a high collection efficiency on the first dynode of each PMT. An outer detector with 123 20-in. PMTs facing outward works as muon veto. The outer detector surrounds the inner one with 1.5 m thickness of water and provides shielding against γ rays from the steel of the outer tank and neutrons from the environment underground. A water purification system with an ion exchange column provides high purity water with an attenuation length of the order of 50 m and uranium content at about 37 μBq/kg, which corresponds to 3 ppt.

The energy calibration is performed by means of a γ rays source of energy up to 9 MeV from $Ni(\mathrm{n},\gamma)\mathrm{Ni}$, with electrons from cosmic muons decaying within the inner detector, and with β decay emitter produced by muons interactions. From calibrations the energy scale is determined at 3% level with an rms resolution for an electron of $0.22/\sqrt{T/10\ \text{MeV}}$.

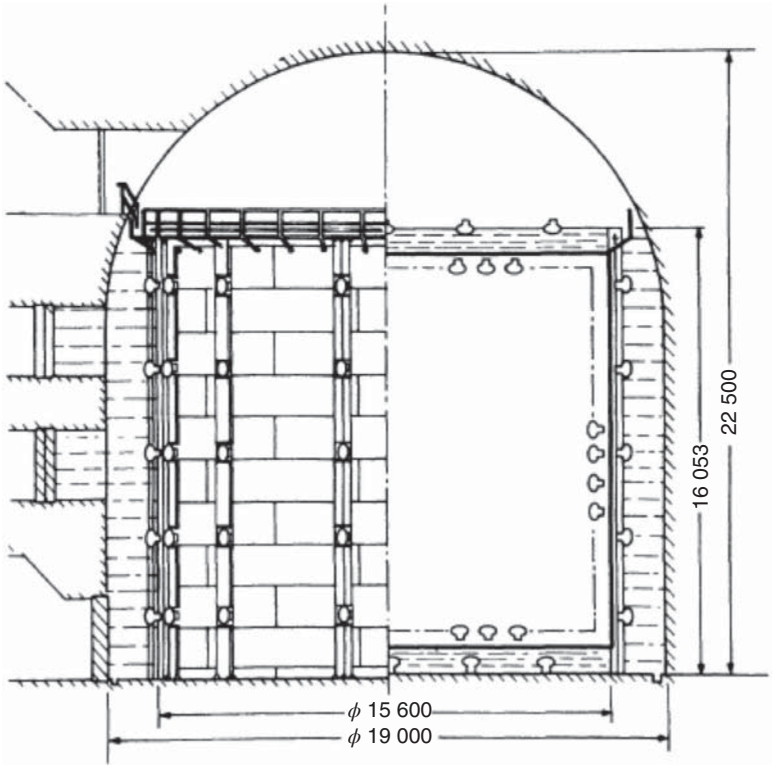

Figure 4.2 Schematic view of the Kamiokande-II detector. Source: Hirata et al. 1988 [247]. Reproduced with permission of American Physical Society.

Event selection requires [250] that (i) total number of ph.e. in the inner detector must be less than 100 (30 MeV); (ii) total number of ph.e. in the outer detector must be less than 30 for event containment; and (iii) time gap from preceding event must be longer than 100 μs to reject electrons from muon decays ($\tau_\mu = 2.2$ μs). The vertex of the event is reconstructed by using the time and position of hit PMTs. The rms for the position of the vertex is 1.7 m for 10 MeV electrons. Events induced by γ rays from the wall of the detector are excluded by a fiducial volume cut. The fiducial volume has a mass of 680 tons, which is 2 m away from the bottom and side walls of the PMT array and 3 m from the top PMT layer. The fiducial volume cut reduces the event rate by 1 order of magnitude. More background is due to muons going through the detector, which by spallation on ^{16}O make β-emitter radioactive isotopes. These events are divided in two categories on the basis of the lifetime of the radioactive isotope produced. ^{8}B ($Q_\beta = 18$ MeV; $\tau = 1.1$ s), ^{8}Li ($Q_\beta = 16$ MeV; $\tau = 1.2$ s), and ^{16}N ($Q_\beta = 10.4$ MeV; $\tau = 10$ s) have lifetimes of the order of 1–10 s; ^{12}B ($Q_\beta = 13.4$ MeV; $\tau = 29$ ms) and ^{12}N ($Q_\beta = 17.3$ MeV; $\tau = 16$ ms) have lifetimes of the order of 20 ms. The β decay nuclei produced by spallation are removed by a time and space correlation cut with respect to the preceding muon. This cut is energy dependent and reduces this background by as much as 70% for electron energy greater than

10 MeV and introduces a dead time of about 10%. The low energy spectrum is dominated by $^{214}_{83}$Bi ($Q_\beta = 3.272$ MeV), which is a decay product of ^{222}Rn. ^{222}Rn is an α-emitter and a noble gas from the ^{238}U radioactive chain with a half-life of 3.82 days.

In Kamiokande-II, the poor energy resolution sets the energy threshold for the analysis of solar neutrino data at 9.3 MeV (90% efficiency) to reduce the background component from radon daughters. The background due to external γ rays was removed by rejecting events with reconstructed vertex close to the edge of the fiducial volume and inward direction. Recirculation of water through the purification plant can remove uranium and reduce radon. After a few months of recirculation, the trigger rate (20 hit PMTs in 100 ns) decreased (from 10^3) to 0.7 Bq, of which 0.37 Bq was due to cosmic ray muons. For a detection threshold of 9.3 MeV, the minimum neutrino energy is 9.5 MeV. So, only ^{8}B solar neutrinos give a significant contribution in Kamiokande-II. The fiducial volume of 680 tons contains 2.27×10^{32} target electrons. The expected high metallicity SSM rate is determined to be 0.22 ± 0.03 events/day/680 tons above 9.3 MeV. The trigger rate is about 10^5 larger than the expected signal. Further background reduction is needed.

The direction of solar neutrino candidate events must be correlated with the position of the Sun relative to the detector at a given time. Such a correlation is possible in a Cherenkov detector. This test provides an additional reduction of the background by 1 order of magnitude. As an example, data collected from January 1987 through May 1988, corresponding to 450 live detector days, are shown in Figure 4.3. In Figure 4.3 $\cos\theta_{\text{Sun}} = 1$ corresponds to the expected direction for solar neutrino-induced events. The result, rescaled to 2016 SSM from 1988 calculations [99], can be cast in the form:

$$\frac{\text{data}}{\text{theory}} = 0.43 \pm 0.13_{\text{stat}} \pm 0.08_{\text{syst}} \tag{4.8}$$

where the systematic uncertainty is due to the energy scale calibration and to the angular resolution.

Kamiokande-II performed the first direct measurement of ^{8}B solar neutrino flux. The disagreement with the theory is at 3σ level. This result is consistent with the one from the Homestake experiment for ^{8}B solar neutrinos, where data/theory ~ 0.32. This finding was of great importance since in 1988 for almost two decades the only observation of solar neutrino had come from the Homestake experiment. Kamiokande-II confirmed the SNP. For completeness we give the expected rate with neutrino oscillations in the same assumptions used for the Homestake experiment: 0.094 ± 0.017 events/day/680 tons above 9.3 MeV. In the framework of neutrino oscillations, the ratio between data and theory is consistent with the Kamiokande-II measurement, being $0.094/0.22 = 0.43$.

The electronics and the water purification were further improved in Kamiokande-III [251]. More than 100 dead PMTs were changed and new light reflectors were mounted. The coverage increased to 25%. The number of hit PMTs increased from 30 to 40 for 10 MeV electrons. Kamiokande-III has been in operation since December 1990. The energy threshold was set at 7.5 MeV for the first 200 days and later to 7 MeV. The predicted ^{8}B solar neutrinos is 0.84 ± 0.12

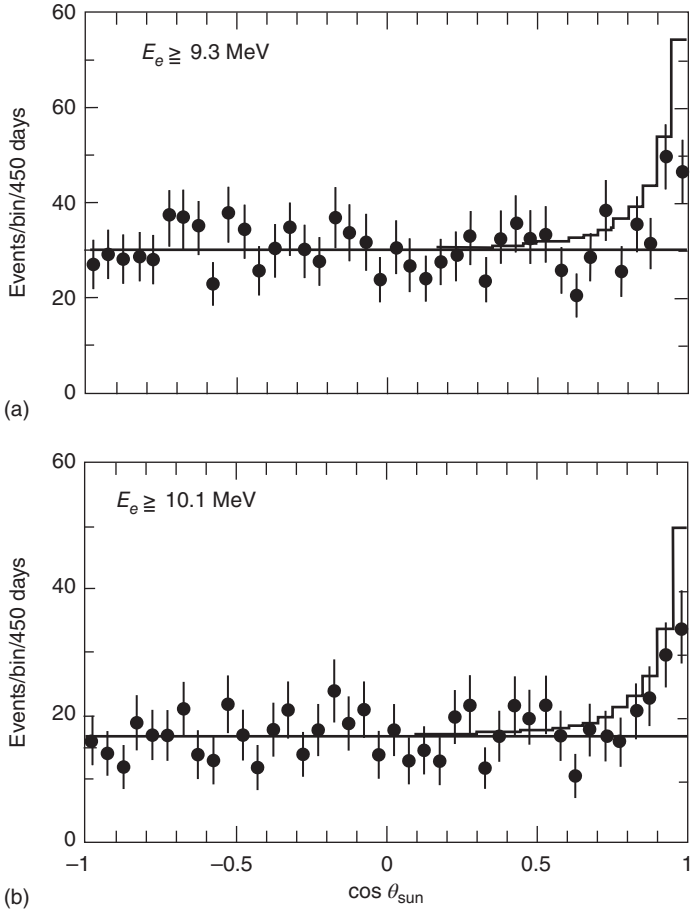

Figure 4.3 Distribution in $\cos\theta_{\text{Sun}}$, the cosine of the angle between the trajectory of a detected electron and the direction of the Sun from the Earth at a given time. The data shown are from the 680 tons fiducial volume after rejection of background from spallation products and γ rays. The solid line corresponds to a Monte Carlo calculation based on the standard solar model. Source: Hirata et al. 1989 [250]. Reproduced with permission of American Physical Society.

events/day/680 tons above 7 MeV using 2016 SSM [66]. Kamiokande-II/III ran until February 1995, collecting 2079 days of data. The data recorded from 1988 to 1995 covered almost the entire solar cycle 22 (March 1986 to June 1996). For 2079 live days, taking into account the change in threshold, the expected number of solar neutrinos is determined to be 1166±163, including an average detection efficiency of 86%. For Kamiokande-III [251], the number of observed solar neutrino events is 390^{+35}_{-33}; in contrast the expected number is 785, based on 1988 SSM [99]. From these numbers it turns out that

$$\frac{\text{data}}{\text{theory}} = 0.496^{+0.044}_{-0.042}(\text{stat}) \pm 0.048_{\text{syst}} \tag{4.9}$$

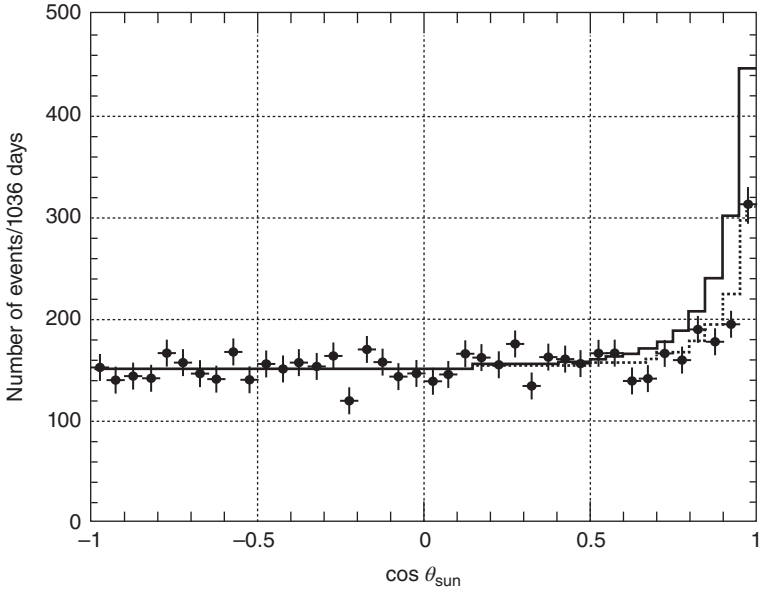

Figure 4.4 Distribution in $\cos\theta_{\text{Sun}}$ corresponding to 1036 life days in Kamiokande-III data [251]. The solid line corresponds to a Monte Carlo calculation based on the standard solar model calculations [99]. The dashed line is the best fit for a flat background distribution. Source: Adapted from J.N. Bahcall and R.K. Ulrich 1988 [99] and Y. Fukuda et al. 1996 [251].

where the systematic uncertainty of about 10% comes mainly from the measurement of the angular resolution (7%), the definition of the energy scale (5.3%), and the fiducial volume cut (4%). The $\cos\theta_{\text{Sun}}$ distribution of Kamiokande-III data is shown in Figure 4.4.

Combining results from Kamiokande-II and Kamiokande-III [251], the total number of solar neutrino events observed is 597^{+41}_{-40} and the prediction 1213 with 1988 SSM. The ratio of the observed flux to the prediction is $0.492^{+0.034}_{-0.033}(\text{stat}) \pm 0.058_{\text{syst}}$. The ratio to the SSM updated with the 2016 ^{8}B solar neutrino flux is calculated to be $0.523^{+0.036}_{-0.035}(\text{stat}) \pm 0.062_{\text{syst}}$. The disagreement with the theory is at the level of 3.4σ, including the uncertainty of 12% in the 2016 SSM prediction. In conclusion, Kamiokande-II/III confirmed in 1995 the SNP with high significance.

With about 10 years of real-time observation of solar neutrinos, Kamiokande-II/III made a study of time variations correlated with solar activity [251]. As it is shown in Figure 4.5, the sunspot numbers changed from a minimum to a maximum and to a minimum again during the Kamiokande-II/III data-taking period. The correlation of the neutrino flux measurement to the sunspot numbers was studied assuming that data/theory $= \alpha N_{\text{sunspot}} + \beta$, with N_{sunspot} is the average number of sunspots in each bin. It turns out that $\alpha = 9.4^{+7.2}_{-7.0} \times 10^{-4}$ and $\beta = 0.398^{+0.088}_{-0.078}$. This analysis shows that there is no correlation between the sunspot numbers and the neutrino flux.

The Kamiokande collaboration studied the daytime and nighttime flux difference [252]. A difference in the flux is expected due to neutrino oscillations.

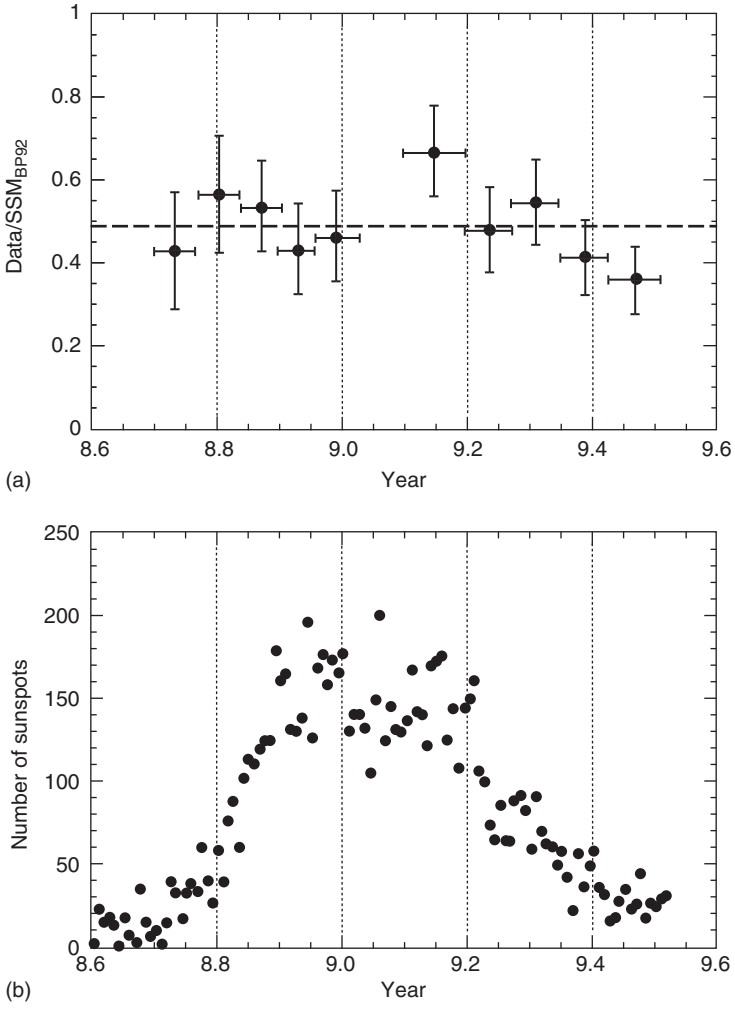

Figure 4.5 (a) Ratio of data to standard solar model in 200 days bins from Kamiokande-II (first five points) and Kamiokande-III. The dashed horizontal line corresponds to the average ratio for all data set. (b) Sunspots numbers. No correlation between solar neutrinos and sunspots numbers is determined from Kamiokande data. Source: Fukuda et al. 1996 [251]. Reproduced with permission of American Physical Society.

When neutrinos travel through the Earth, matter interactions are expected to produce a regeneration of electron neutrinos. Therefore, the electron neutrino flux is expected to change during the daytime and nighttime. This difference depends on the neutrino energy and oscillation parameters. The day–night asymmetry, A_{DN}, is defined as

$$A_{\mathrm{DN}} = \frac{\phi_D - \phi_N}{\frac{1}{2}(\phi_D + \phi_N)} \tag{4.10}$$

where $\phi_{D,N}$ is the measured flux during the daytime or nighttime. For the day–night asymmetry the Kamiokande data gives

$$A_{\mathrm{DN}} = 0.06 \pm 0.10 \tag{4.11}$$

Kamiokande data could not establish a day–night asymmetry.

The Kamiokande experiment has paved the way for the very successful Super-Kamiokande in searching for solar neutrinos with a water Cherenkov detector. The Super-Kamiokande experiment is discussed later in this chapter. In addition to solar and atmospheric neutrinos, on 23 February 1987 Kamiokande detected some 10 events from a core collapse supernova in the Large Magellanic Cloud. Masatoshi Koshiba for the Kamiokande Collaboration was awarded the 2002 Nobel Prize in Physics.

4.4 The ^{71}Ga Experiments

Detection of solar neutrinos by means of ^{71}Ga target is based on the reaction:

$$\nu_e + {}^{71}_{31}\mathrm{Ga} \rightarrow e^- + {}^{71}_{32}\mathrm{Ge} \tag{4.12}$$

This reaction has a threshold of $\Delta_{\mathrm{gs}} = 0.233$ MeV. Ga-based experiments are radiochemical as much as the ^{37}Cl experiment. By means of ^{71}Ga, it is possible to detect pp solar neutrinos, which have a maximum energy of 0.423 MeV. Two experiments using ^{71}Ga have been performed: GALLEX [253, 254] at the Gran Sasso underground laboratory, Italy, and SAGE [255] in Baksan, Caucasus, Russia.

At the time the ^{71}Ga experiments were considered, this seemed the only feasible method to detect pp solar neutrinos. The observation of these neutrinos was thought to be decisive because the flux of pp neutrinos depends mainly on the solar luminosity and not on details of the SSM as much as ^{8}B solar neutrinos. Therefore, an observation of these neutrinos would have been a critical test to understand the origin of the SNP.

The radioactive ^{71}Ge, produced by the solar neutrino capture, decays with a mean life of 16.5 days. The overall procedure of the Ga-based experiments is similar to the one discussed for the ^{37}Cl experiment. The idea to make use of Ga was first proposed by Kuzmin [256]. The expected capture rate on ^{71}Ga is 128 ± 5 SNU, which corresponds to 0.038 ± 0.001 events per day per ton of Ga. The contribution of the different solar neutrino components is calculated as follows: (pp, pep, ^{7}Be, ^{8}B, CNO) = (56%, 2%, 28%, 11%, 3%). The largest uncertainty in the capture prediction rate comes from the interaction cross section. The transition $^{71}\mathrm{Ga}(3/2^-, \mathrm{gs}) \rightarrow {}^{71}\mathrm{Ge}(1/2^-, \mathrm{gs})$ has low threshold (0.233 MeV) and can be used to detect pp solar neutrinos. This transition is well known and gives about 88% of the neutrino capture rate. The transition to the first excited state, $^{71}\mathrm{Ga}(3/2^-, \mathrm{gs}) \rightarrow {}^{71}\mathrm{Ge}(5/2^-, \delta = \Delta_{\mathrm{gs}} + 0.175\ \mathrm{MeV})$, is known with a larger uncertainty. Uncertainties in Gamow–Teller matrix elements change the capture cross section by as much as a factor of 2 [245]. In addition, the first excited state lies at an energy at which only 2% of the pp neutrinos could contribute.

As anticipated above, the ^{71}Ga detection of solar neutrinos is of great importance to disentangle the astrophysics solution against the physics solution to the

SNP. In fact, the minimum predicted solar neutrino rate in ^{71}Ga experiments is due only to pp and pep neutrinos and it is about 80 SNU [257]. This rate is slightly larger than that calculated just using the expected rate from pp and pep neutrinos, namely, 74 SNU, because in the minimum model all pp fusion reactions are terminating with the ^{3}He + ^{3}He reaction, which produces two pp or pep neutrinos. Any measurement that is less than this minimum rate can only be explained with a physics solution perturbing the neutrino propagation from the Sun to the Earth. Moreover, a direct observation of pp neutrinos implies an experimental proof of the energy production inside the Sun.

In GALLEX the target consists of 100 tons of gallium chloride with 30.3 tons of gallium. The target contains 12 tons of ^{71}Ga, which correspond to 1.02×10^{29} nuclei. The target is in the form of an 8.13 M aqueous solution acidified at 2 M in HCl. The predicted solar neutrino interaction rate on this target corresponds to 1.13 atoms/day of ^{71}Ge or about 16 atoms of ^{71}Ge in the whole target after 20 days of exposure. Therefore, the extraction procedure aims to identify some 20 atoms against 10^{29}. The main background source, which can produce ^{71}Ge atoms, is from ^{71}Ga(p,n)^{71}Ge with a threshold of 1.02 MeV. The protons are induced by cosmic ray muons, fast neutrons, and radioactivity in the target by means of (α,p), (n,p) processes. This implies the need of a low radioactivity target and a shielding against high energy neutrons, which can produce secondary protons: an underground location offers the best opportunity. As far as crossing muons background is concerned, a dedicated study at CERN muon beam was carried out to determine the ^{71}Ge production rate in $GaCl_3$ [258]. This test showed that the ^{71}Ge production rate by crossing muons corresponds to (4.3±1.2) SNU [252]. The intrinsic radioactivity of the target was checked with neutron activation and by radon determination with proportional counters. U and Th were found at the level of <0.04 ppb and ^{226}Ra< 1.48 mBq/kg [253]. The background due to intrinsic radioactivity was estimated to be at the level of 0.2 SNU. Fast neutrons from the underground environment and from the target containment tank were detected by means of a 470 l $Ca(NO_3)_2$ solution deployed inside the target. Neutrons are detected by the reaction ^{40}Ca(n,α)^{37}Ar. The ^{71}Ge production rate estimated from this measurement is 0.15 ± 0.10 SNU. Unidentified radon events can produce as much as (2.2±1.7) SNU [254]. In the early operating phase of GALLEX, a cosmogenic background from ^{68}Ge with half-life of 288 days was identified. This radioactive isotope was produced while the target solution was exposed to cosmic rays on surface. Therefore, a total of less than 7 SNU of background rate is predicted from the main sources described above. This corresponds to one atom of ^{71}Ge in three weeks of exposure. A signal-to-background ratio much larger than one is predicted. Therefore, the challenge in GALLEX is the extraction and counting of ^{71}Ge atoms.

The Ge produced by neutrino interactions is in the form of tetrachloride, $GeCl_4$, and is volatile. The Ga is in the form of $GaCl_3$ and is not volatile. This difference allows the Ge separation by bubbling inside the target vessel an inert gas such as nitrogen. A known amount of non-radioactive Ge of about 1 mg is added to the target solution at each run to determine the extraction efficiency. The $GeCl_4$ extracted is reabsorbed in water and converted to germane gas, GeH_4. The germane together with xenon is introduced in a miniaturized low

background proportional counter (1 cm linear dimension). The ^{71}Ge in the counter decays back to ^{71}Ga by K (87.6%) and L (10.3%) electron capture. The holes in the corresponding shells are filled with electrons from higher shells. The energy released is emitted as Auger electrons. In the case of K to L transition, a 9.3 keV X-ray can be emitted. In the counter three different kinds of events can be observed: (i) a single energy deposit of 10.37 keV, (ii) a single energy deposit of 1.17 keV, and (iii) two energy deposits of 1.17 and 9.3 keV. The counter stays in operation for a few months. The extraction efficiency for Ge was tested with ^{69}Ge, produced by ^{69}Ga(p, n)^{69}Ge, by detecting 1106 keV γ's of ^{69}Ge with a high purity germanium counter. This test showed an extraction efficiency > 99%. The recovery efficiency was measured to be (99.8±3.7)% by ^{71}Ge produced by EC decay of ^{71}As. In spite of these results, a full-scale test of the experiment was carried out by means of a high intensity artificial neutrino source in 1993 [259].

The GALLEX experimental setup consists of two 7 m high, 70 m^3 target tanks, the Ge extraction facility, a duplicate GeH_4 synthesis, and a counting station inside a Faraday cage. Only one target tank is used at a time. The second tank is for safety use. The tanks are made with a low U and Th vinyl ester resin reinforced by glass fibers. The inner surface of the tanks and sparking pipes are lined with a Teflon-like material. The main tank is equipped with a tube closed at one end to insert the calibration neutrino source and with a 470 l vessel to accommodate a calcium nitrate solution to monitor fast neutrons.

A new run in GALLEX starts by introducing about 1 mg of stable germanium carrier (^{72}Ge, ^{74}Ge, and ^{76}Ge) and steering the target solution with nitrogen for 9 hours in a closed loop. The Ge concentration is monitored with mass spectroscopy. At the end of an exposure time of about three weeks, the Ge is recovered by flushing with 1900 m^3 of nitrogen in 20 hours at 20 °C. The volatile tetrachloride is recovered by scrubbing the gas with 50 l of counterflowing water in three absorber columns (3 m in height, 0.3 m in diameter) packed with glass helices. Further volume reduction is performed by acidifying the solution and extracting the germanium in 500 ml of carbon tetrachloride. In turn the tetrachloride is extracted in 50 ml tritium-free water. This final solution is used to generate germanium hydride, GeH_4 [253]. At this point the counter is filled with the germanium hydride and counting lasts more than six months.

The first set of runs in GALLEX went from 14 May 1991 to 29 April 1992 [253]. During this 50 week window, 16 solar neutrino runs were performed. During counting a number of selection cuts are applied to remove background from radon daughters outside and inside the counter. Moreover, ^{71}Ge candidates signals from L-peak (1.17 keV) and K-peak (10.37 keV) are selected by means of cut on energy and pulse shape rise time. An unbinned likelihood analysis is performed on the candidate events with the method described in [260]. The likelihood fit determines the initial number of ^{71}Ge atoms, the counter background, and a contribution from the decay of ^{68}Ge. In Figure 4.6 we show from [253] the count rate of selected L-peak and K-peak events averaged over the all first 14 runs against the counting time.

The GALLEX detector monitored solar neutrinos from 1991 to 1997. In 1998 GALLEX detector turned into the so-called Gallium Neutrino Observatory (GNO) [261, 262], which took data till 2003. In 2010 a reanalysis of all GALLEX

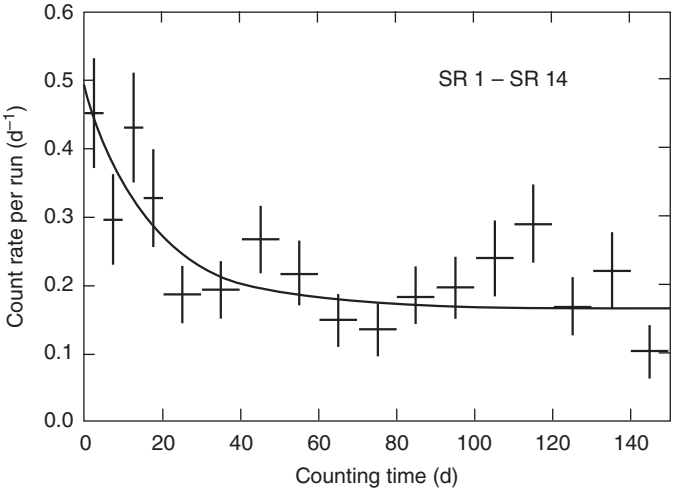

Figure 4.6 Count rate of selected L-peak and K-peak events averaged over the all first 14 GALLEX solar neutrino runs against the counting time. The solid line shows the likelihood best fit. Source: Anselmann et al. 1992 [253]. Reproduced with permission of Elsevier.

solar neutrino runs, based on pulse shape discrimination, were performed [263] giving an average capture rate equal to $73.4^{+6.1}_{-6.0}(\text{stat})^{+3.7}_{-4.1}$ SNU. In Figure 4.7 from [263], the summary results of GALLEX solar neutrino runs are shown.

The goal of GNO was to carry out a long-term program for the observation of low energy neutrinos and to measure the pp rate with an accuracy of 5 SNU. At the same time GNO aimed for studying pp solar neutrinos over a whole solar cycle with a sensitivity of about 15%. In GNO the electronics was upgraded with respect to GALLEX. In particular, the preamplifiers, pulse shape recording, and data acquisition were replaced. This upgrade made it possible to carry out a pulse shape analysis, which performs better than the previous rise time analysis. GNO was shut down for non-scientific reasons in 2003. Between May 1998 and April 2003, GNO completed 58 solar neutrino runs. The average capture rate for the whole GNO data set is determined to be $62.9^{+6.0}_{-5.9}$ SNU.

In Figure 4.8 we show the energy spectrum of selected ^{71}Ge events. In this plot the signal is clearly shown with the empty histogram corresponding to the first 50 days of data taking, which is $3\tau_{\text{Ge}}$. The peak at about 1.2 and 10.4 keV are clearly seen. The filled histogram shows the background acquired for a time greater than $3\tau_{\text{Ge}}$.

The combined GALLEX and GNO result, corresponding to 123 solar neutrino runs over 12 years, is equal to $67.13^{+4.64}_{-4.63}$ SNU, which is a 6.8% measurement of the solar neutrino capture rate on ^{71}Ga. This result is about 3σ smaller than the minimum predicted capture rate. As it has been pointed out above, this result implies a physics solution for the SNP. With GALLEX+GNO a solar neutrino deficit of about 50% is observed. This deficit is well in agreement with neutrino oscillations in vacuum. As a matter of fact, subtracting the ^{8}B solar neutrino contribution of about 6 SNU, using Eq. (4.8), we obtain a suppression factor equal to 0.57. The expected vacuum oscillation suppression factor is $1 - \frac{1}{2}\sin^2(2\theta_{12})$=0.577 with $\theta_{12} = 33.5°$.

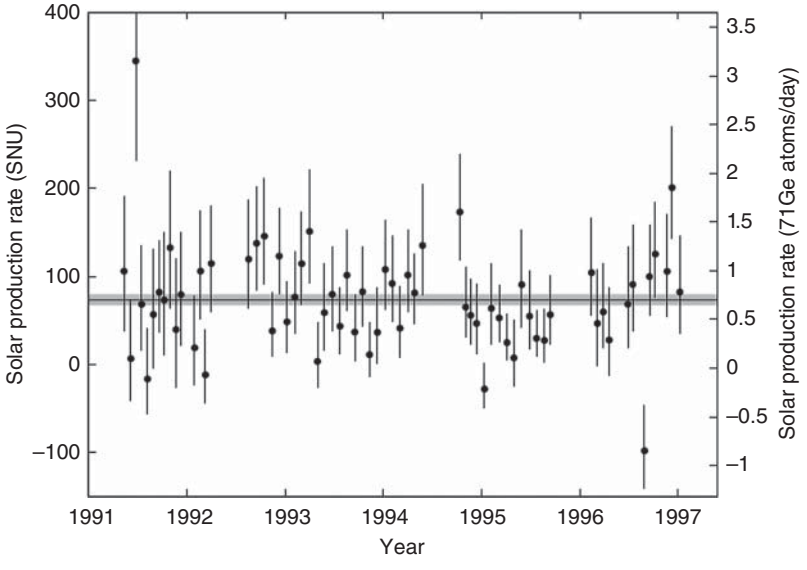

Figure 4.7 Summary of 65 solar neutrino runs in GALLEX. The right-hand scale corresponds to the ^{71}Ge production rate. The left-hand scale corresponds to the net solar neutrino rate in units of SNU after subtracting the predicted background. Error bars are $\pm 1\sigma$. Source: Kaether et al. 2010 [263]. Reproduced with permission of Elsevier.

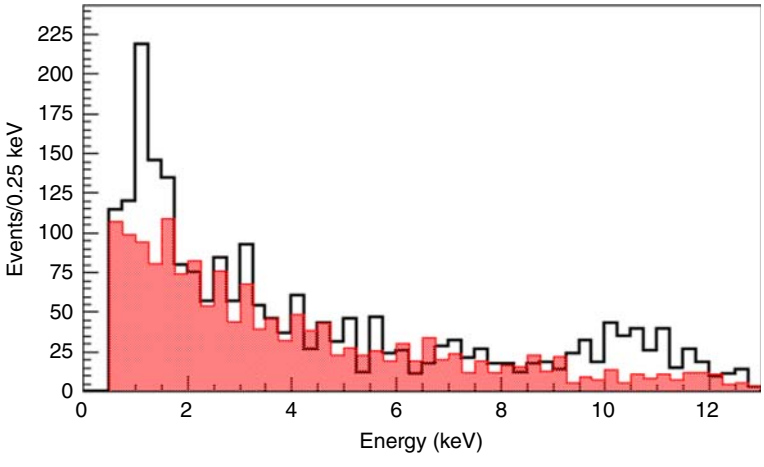

Figure 4.8 GNO energy spectrum of selected ^{71}Ge events for the whole data set. The empty histogram shows the counts occurring in the first 50 days ($3\tau_{Ge}$). The filled histogram superimposed and normalized shows the data occurring after the first 50 days. Source: Altmann et al. 2005 [262]. Reproduced with permission of Elsevier.

Considering the complexity of the extraction procedure and the very few atoms to deal with in counting to determine the capture rate, a critical test was carried out in GALLEX with an artificial neutrino source [259]. The basic idea was to make a portable neutrino source with known intensity, which could produce neutrinos in the sub-MeV range. The GALLEX target will be exposed to neutrinos from the source. The same procedure used in solar neutrino runs will be checked after the exposure. In GALLEX a ^{51}Cr source was used twice in 1994 and 1995 [259, 264]. ^{51}Cr is produced by neutron capture on ^{50}Cr. ^{51}Cr has a half-life of 27.703 days. ^{51}Cr decays by electron capture with a Q-value of 751 keV. The neutrino spectrum from ^{51}Cr consists of four monoenergetic lines: 746 keV (81%), 751 keV (9%), 426 keV (9%), and 431 keV (1%). The required activity of the source in GALLEX is of the order of 50 PBq. Taking into account the natural isotopic abundance of ^{50}Cr, 4.345%, and the required activity, it was needed to use chromium enriched in ^{50}Cr. The sample of enriched chromium, in the form of CrO_3, had 38.6% of ^{50}Cr. The CrO_3 was turned into metallic chromium by electrolysis. The Cr metal was broken in small irregular chips, outgassed in vacuum, and irradiated in the nuclear reactor. About 35.5 kg of metal enriched chromium was used to make the source. At the time of the source experiment, the 35 MW thermal power Siloé reactor in Grenoble, France, was used. During irradiation the neutron flux had a mean value of 5.2×10^{13} cm^{-2} s^{-1}. The irradiation lasted 23.8 days. The irradiated chromium was loaded inside a stainless steel container and inside an 8.5 cm thick tungsten shielding housing for radio protection purposes. The external dose at the surface of the tungsten was measured to be less than 7 μSv/h, well below the maximum allowed of 200 μSv/h. In order to determine the activity of the source, 31 samples of metal chips were taken. The activity of each sample was measured by means of the 320 keV γ-ray from ^{51}Cr EC decay to ^{51}V. The average activity for the first source was determined to be 1.71 ± 0.04 TBq/g. In turn the source activity was calculated to be 60.8 ± 1.4 PBq at the end of irradiation. A second method for measuring the source activity made use of a calorimeter. Immediately after irradiation the source into the shielding was located inside a calibrated thermally shielded vacuum vessel. The ^{51}Cr releases energy by 320 keV γ-rays. Because the concentration of impurities in the irradiated sample was very small, only the energy coming from the 320 keV γ-rays accounts for the heat measured in the calorimeter. The deduced source activity was 65.9 ± 3.0 PBq. A third method carefully determined the neutron flux inside the reactor and used the knowledge of the cross section to make ^{51}Cr. This method gave 64.4 ± 5.2 PBq. The weighted average of the measurements gives, for the source used in 1994, 61.9 ± 1.2 PBq at the end of the irradiation. The transportation time of 3.69 days from Grenoble to Gran Sasso must be taken into account to determine the activity at the start of the exposure to calibrate the GALLEX detector.

The ratio of measured to predicted ^{71}Ge events from the source experiments in 1994 and 1995 gives $r = A_{\text{meas}}/A_{\text{pred}} = 0.882 \pm 0.078$ with the pulse shape analysis [263]. This result is based on the capture cross section of gallium $\sigma = 58.1^{+2.1}_{-1.6} \times 10^{-46}$ cm^2 [265]. As reported above, the capture process mainly goes from the ground state of ^{71}Ga to the ground state of ^{71}Ge, which is well known. However, the possibility to have a transition from the ground state of ^{71}Ga to the first two excited states of ^{71}Ge should be taken into account. This transition is not well

known. In the cross section calculation by Bahcall [265], a 5% contribution of the transition to the excited states is considered. The source calibration experiments in GALLEX, including the contribution from the excited states, give a result only 1.5σ away from the expected value 1.0. We notice that from some authors [266] the contribution to the excited state could be rather smaller than 5%. This fact would change the reported ratio from the source experiments: r would be closer to one.

The Soviet-American Gallium Neutrino Experiment (SAGE) [255] aimed to detect solar neutrinos with gallium similarly to GALLEX. The SAGE detector was installed in the Baksan Neutrino Observatory of the Institute for Nuclear Research of the Russian Academy of Sciences in Northern Caucasus, Russia [266a]. In the underground site the measured muon flux is $(3.03 \pm 0.10) \times 10^{-9}$ cm^{-2} s^{-1} [267]. Initially, SAGE used 30 tons of liquid metallic gallium contained in four Teflon-lined chemical reactors, each holding 7 tons of the target mass. The metallic gallium is kept at 30 °C to remain molten. The extraction of germanium from metallic gallium was tested on small-scale experiments before running the experiment underground [268]. A solar neutrino run started by adding 160 μg of natural Ge carrier into each chemical reactor. The Ge content added is mixed in order to distribute it throughout the reactor gallium mass. After an exposure of three to four weeks, the Ge carrier and any ^{71}Ge atom produced by neutrino captures are extracted by mixing a hydrochloric acid solution with metallic gallium and hydrogen peroxide. Ge is extracted into aqueous phase. The solutions extracted from the four chemical reactors are combined and reduced in volume by vacuum evaporation. By argon purging $GeCl_4$ is moved into 1.2 l of water. Finally, Ge is extracted into 0.1 l of low tritium water. GeH_4 is synthesized and purified by gas chromatography for counting. The total extraction efficiency equal to 95±3% is measured by the ratio of mass of Ge in GeH_4 to the initial mass of the carrier. The GeH_4 is mixed with xenon and measured for six months by means of a 0.75 cm^3 proportional counter, which is located in the well of a NaI detector inside a passive shielding. The volume inside the shielding is purged with boil-off gas from a dewar of liquid nitrogen to reduce the effect of ^{222}Rn background. Pulse shape discrimination based on rise time is used to disentangle the signal from the background. The counter is calibrated with ^{55}Fe, regularly ($\sim$ 6 keV X-rays with $\sim$ 17% B.R.). The calibration source is located close to the counter through a thin side window. The data analysis selects ^{71}Ge K-peak events with no NaI signal in coincidence. A likelihood analysis similar to the one performed by GALLEX is carried out. The goodness-of-fit is determined by the Smirnov–Cramer–Von Mises method, which is independent of the binning of the data. In SAGE operations started in May 1988. From 1988 to 1990 the main activity was focused on removing ^{68}Ge, produced by cosmic ray muons while the gallium was on the surface. Solar neutrino search started in January 1990. In 2005 the carrier used to measure the extraction efficiency was enriched in ^{72}Ge or ^{76}Ge. At the end of the extraction process, a sample was taken and analyzed with an inductively coupled plasma mass spectrometer (ICP-MS) to determine the content of Ge isotopes. This procedure reduces the systematic due to unknown Ge sources, which could contaminate the extracted mass at the end of the run. In Figure 4.9 we show from [267] the count rate against the energy and rise time for events detected during

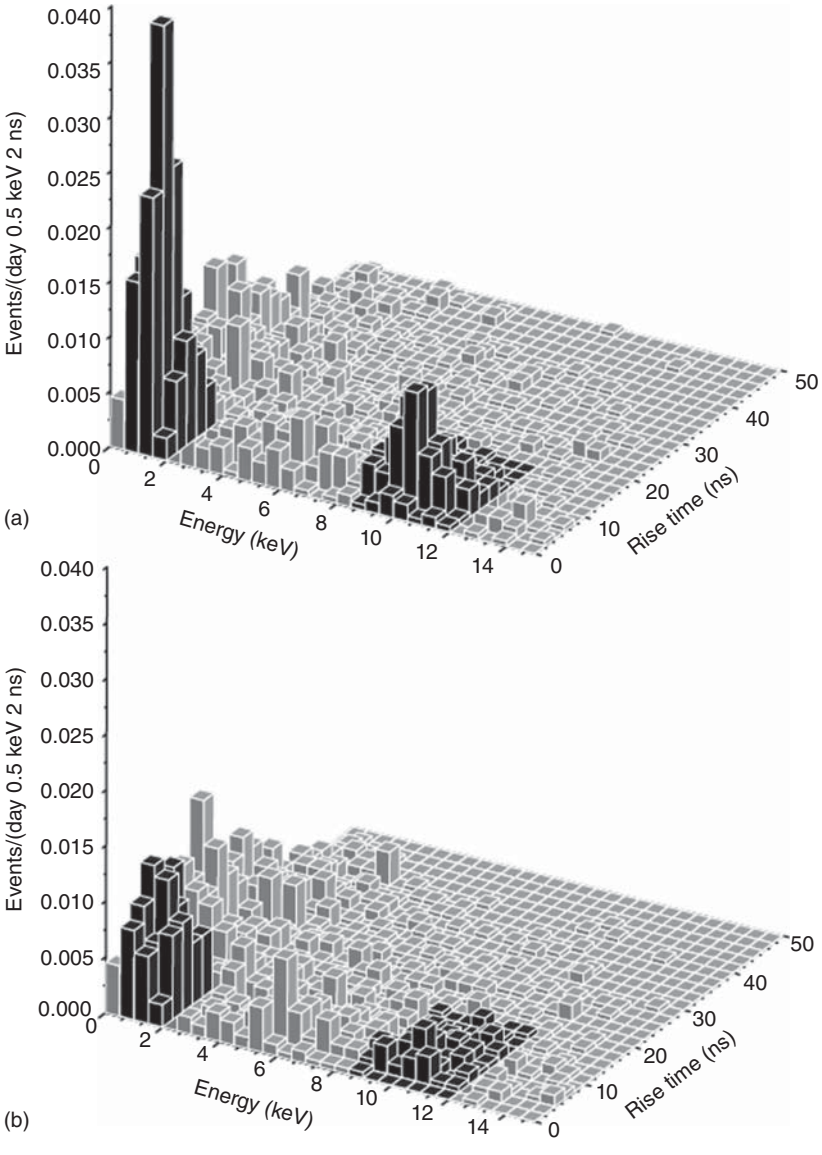

Figure 4.9 (a) Count rate in SAGE [267] against energy and rise time for events during the first 30 days of counting. The darkened regions correspond to the L and K peaks. (b) Same data taken beginning at day 100 after extraction. Source: Abdurashitov et al. 2009 [267]. Reproduced with permission of American Physical Society.

the first 30 days of counting and beginning at day 100 after extraction: the L and K peaks are clearly visible and shown by the darkened regions. The lower plot shows that some background contaminates the L and K peaks regions, mainly in the low energy. This background component is taken into account as a free parameter in the likelihood analysis.

SAGE similarly to GALLEX has performed a calibration experiment with a ^{51}Cr source [269]. The source activity was equal to 19 PBq, produced by irradiating 512.7 g of 92.4% enriched ^{50}Cr. The ratio of measured-to-predicted number of events is determined to be $0.95 \pm 0.12(\text{expt})^{+0.035}_{-0.027}(\text{theor})$, using the capture cross section from Bahcall. Therefore, the source experiment shows that the experimental procedure in SAGE does not contain unknown systematic effects at the level of 13%. In addition, SAGE has performed a calibration with an ^{37}Ar source [270]. This isotope decays exclusively to the ground state of ^{37}Cl, producing a mono-energetic neutrino with 811 keV with 90.2% probability. Due to the decay ∼100% BR and higher energy, the cross section in this case exceeds that for ^{51}Cr by some 20% [271]. Moreover, the half-life of 35 days is greater than that of the ^{51}Cr. The net result is a need for a smaller activity. From a safety standpoint the advantage of using ^{37}Ar against ^{51}Cr is the absence of γ-ray accompanying the decay. ^{37}Ar could be produced by irradiation of enriched ^{36}Ar (the natural abundance of ^{36}Ar is only 0.337%). Yet, due to the large (n, α) and (n, p) cross sections for ^{37}Ar, a burn-up problem can arise during irradiation, limiting the maximum source activity achievable. [271]. ^{37}Ar can also be produced by $^{40}\text{Ca}(\text{n}, \alpha)^{37}Ar$ with an energetic neutron source [271]. A practical method to make ^{37}Ar from ^{40}Ca at a reactor with fast neutrons was proposed by Gavrin et al. [272]. SAGE collaboration made the ^{37}Ar source in the fast neutron breeder reactor BN-600 at Zarechny in Russia. The fast neutron flux was 1.7×10^{14} cm^{-2} s^{-1} above the 1.75 MeV threshold of the production reaction. Some 17 kg of CaO were irradiated from 31 October 2003 until 12 April 2004. After cooling CaO was dissolved in a nitric acid solution. The argon was extracted by purging with helium and stored in a charcoal at liquid nitrogen temperature. The source experiment is run by first removing any Ge, which might be present, from two gallium reactors and pump the gallium into reactor 6. The source is placed at the center of reactor 6 and exposure starts. The source activity was measured with three different methods in the source production location. In the first method the volume of the gas and the isotopic composition were measured before putting the purified argon inside the holder. The volume of the gas was measured by warming the charcoal where the gas was frozen and pump it into a calibrated volume and reading the pressure. In the second method, the source holder was evacuated and weighed before and after filling. The difference in mass of 4.400 ± 0.042 g allows to calculate the source activity. In the third method, the heat output of the source was measured with a calorimeter, previously calibrated with electrical heaters of known power. At Baksan the calorimeter used for the ^{51}Cr was also used for ^{37}Ar. In 2004 after the source experiment, the argon was returned to the fabrication facility. The source holder was opened and a sample of gas was measured in a proportional counter. At this time argon had decayed by about a factor of 300 [271]. The weighted average of source activity was determined to be 15.13 ± 0.07 PBq from all source activity measurements. The ratio of measured to predicted production rates has been determined to be $0.79^{+0.09}_{-0.10}$, including systematic errors. This result is some 2.3σ different than one, which is the expected value.

In Figure 4.10 we show the full data collected by SAGE from 1990 to 2007 for a total of 168 runs. The global best-fit result from SAGE is $65.4^{+3.1}_{-3.0}(\text{stat})^{+2.6}_{-2.8}(\text{syst})$ SNU. This is consistent with the GALLEX+GNO measurement. Combining all

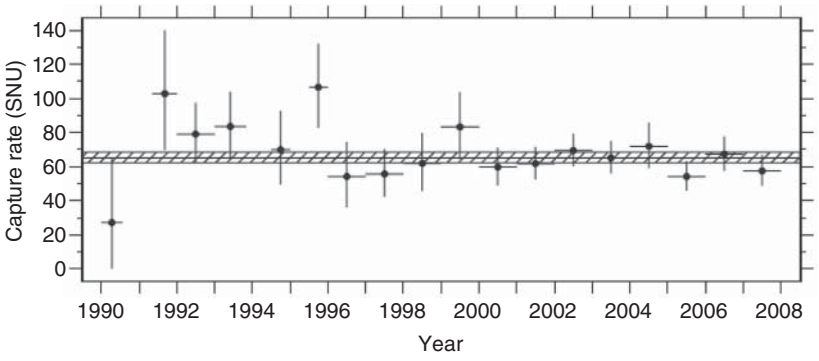

Figure 4.10 Combined result for each year in SAGE from 1990 to 2007. The shaded area shows the 1σ error band for the best fit for all years. Source: Abdurashitov et al. 2009 [267]. Reproduced with permission of American Physical Society.

Ga results, we obtain 66.2 ± 3.1 SNU, a 4.7% measurement. At present, considering that the CNO neutrino flux is unknown, the gallium measurements allow to determine the pp solar neutrino flux at the level of about 7–9% by subtracting the signal of ^{7}Be and ^{8}B from Borexino and SNO, respectively (Section 4.8).

4.5 Super-Kamiokande

Super-Kamiokande is the first second-generation solar neutrino experiment. The detector is located at a depth of 2700 m.w.e. in the Kamioka mine, next to Kamiokande. The detector is a 50 000 ton imaging water Cherenkov with a cylindrical geometry, 39.3 m in diameter and 41.4 m in height. The inner detector (ID) is 36.2 m in height and 33.8 m in diameter and contains 32 000 tons of water. The ID was viewed by 11 146 50-cm PMTs at the time Super-Kamiokande was built. In this configuration the PMTs coverage is equal to 40%. Outside the ID, 2.6–2.75 m thick layer of water makes the outer detector (OD), which is viewed by 1885 20-cm PMTs. To prevent light transmission between the ID and OD, a region of 60 cm is equipped with black sheets. This region is inactive. A fiducial volume of 22 500 tons of water within the ID is used to search for solar neutrinos. This provides about 4.75 m of water shielding against radiation coming from the rock [273]. The fiducial volume contains 7.5×10^{33} electrons. Super-Kamiokande started operation on 1 April 1996. In this early operating phase, the trigger threshold was defined by 29 hits within 200 ns coincidence window. This was equivalent to about 5.7 MeV total recoil electron energy. The analysis threshold was set at 6.5 MeV total electron recoil energy, with a 0.2% inefficiency of the hardware trigger. The expected rate due to electron neutrinos from ^{8}B is 40 counts/day in the fiducial volume, assuming a 90% detection efficiency. This was a major improvement with respect to Kamiokande. The trigger rate was about 11 Hz. From the charge and timing of the hit PMTs, the solar neutrino interaction was reconstructed. The recoil energy for each event is determined in a 50 ns time window. The dark noise of PMTs, which is about

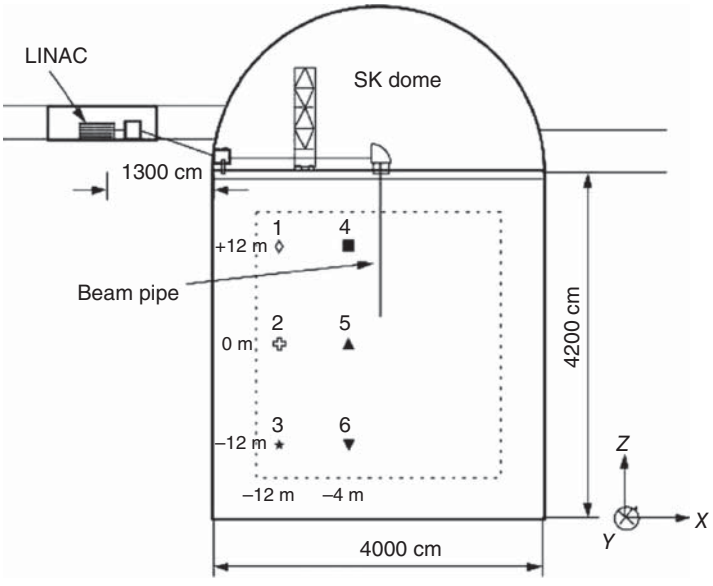

Figure 4.11 The LINAC calibration system in Super-Kamiokande is shown. The dotted line shows the fiducial volume. The numbers 1–6 indicate where LINAC calibration data were taken in SK-II. Source: Cravens et al. 2008 [274]. Reproduced with permission of American Physical Society.

3.3 kHz, contributes with 1.8 hits in 50 ns. The energy scale, angular distribution, and vertex position resolution are calibrated with an electron linear accelerator (LINAC).

In Figure 4.11 the LINAC system for calibration of the energy scale in Super-Kamiokande is shown. The LINAC injects monoenergetic electrons with energy ranging from 5 to 16 MeV. This range matches the energy of solar neutrinos, which can be detected in Super-Kamiokande. The uncertainty of the beam energy is of 20 keV in the whole range covered by the LINAC. LINAC data were taken at six different positions in the detector. The energy calibration by LINAC and the position dependence of the energy scale is supported by using gamma rays from Ni(n,γ)Ni (similarly to the Kamiokande experiment) and beta decays of ^{16}N (Q_β =10.4 MeV) produced by neutrons induced by cosmic ray stopping muons (^{16}O(n, p)^{16}N) or by a deuterium tritium ($D + T \rightarrow n$+^{4}He, E_n = 14.1 MeV) neutron generator. Agreements at the level of 1% with Monte Carlo calculations were obtained.

A major background in Super-Kamiokande is the radioactivity from radon from U and Th in the water. The water in the detector comes from natural underground water and it is purified on site. The U and Th contamination in the water sets the detection threshold. The water transparency is an important parameter together with its radio-purity. The water transparency changes slightly with time. This parameter is monitored by means of the Michel spectrum of electrons produced by stopping muons. Some 1200 of such electrons are observed every day. The peak of the Michel spectrum was kept stable within ±0.5%.

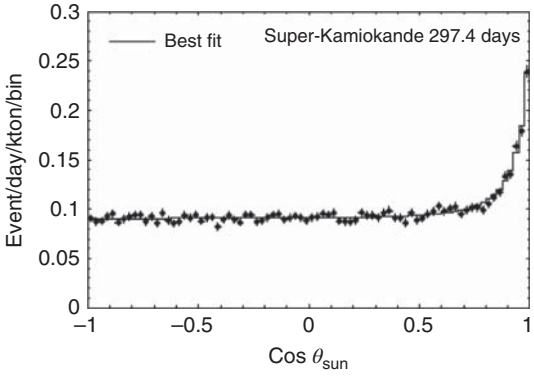

Figure 4.12 Cosine of the angle between the electron direction and the direction of the Sun with respect to the Earth for the first Super-Kamiokande data on solar neutrinos published in 1998. The solid line shows the best fit to the data. Source: Fukuda et al. 1998 [273]. Reproduced with permission of American Physical Society.

Data reduction method was similar to the one used in Kamiokande-II/III. The reduction process required that the selected event was contained (less than 20 hits in the OD for the data published in 1998 [273]), more than 20 μs from any previous event in the trigger and less than 1000 ph.e.

Above threshold, the main sources of background are noise events in the energy bin and events due to muon-induced spallation products. Offline cuts, tuned by Monte Carlo, reduce the number of events by about a factor of 10. The first results reported by Super-Kamiokande on solar neutrinos correspond to about 297 live days between 31 May 1996 and 23 June 1997. The live time of the detector was greater than 90% and limited only by calibration operations. In Figure 4.12 we show the cosine of the angle between the direction of the recoil electron and the Sun–Earth direction in the final data sample after cuts. A clean signal from solar neutrinos in the forward direction is provided by the Super-Kamiokande data. In addition, the improvement with respect to Kamiokande is evident. The solar neutrino events were calculated to be $4017 \pm 104(\text{stat})^{+161}_{-116}(\text{syst})$ in [6.5,20] MeV energy range. This measurement corresponds to data/SSM$= 0.385 \pm 0.010(\text{stat})^{+0.015}_{-0.011}(\text{syst})$, using the SSM 2016 with high metallicity. The largest systematic errors are coming from the uncertainty on the energy scale and angular distribution. Considering a detection efficiency of 94.2% [273] and a cross section, folded on the neutrino energy spectrum, equal to $\langle\sigma_e\rangle = 9.14 \times 10^{-45}$ cm^2, the ^{8}B solar neutrino flux is determined to be $(2.42 \pm 0.06^{+0.10}_{-0.07}) \times 10^6$ cm^{-2} s^{-1}, which is only 43% of the expected flux. Therefore, Super-Kamiokande in 1998 observes a reduction of the solar neutrino flux in agreement with Kamiokande. In addition, Super-Kamiokande in the same year discovers the neutrino oscillations by measuring atmospheric neutrinos [275].

In 2001 an accident in the Super-Kamiokande detector took place. A shock wave initiated by an imploding PMT located at the bottom of the ID was propagating inside the water. Many PMTs were destroyed. After the accident, blast shields were installed to protect PMTs against such an event. The shields are 1 cm thick transparent acrylic dome installed on the photocathode area. Interaction of light with the acrylic material is accounted for in the Monte Carlo simulation. The second phase of Super-Kamiokande (SK-II) took place between December 2002 and October 2005 [274]. The PMTs coverage was only 20% with 5182 PMTs

in the ID. SK-II had two level of triggering for solar neutrinos: low energy (LE) and super low energy (SLE) threshold, corresponding to 14 and 10 PMT hits, respectively. In 2002 only the LE trigger was applied and the efficiency was 100% above 8 MeV. In the second phase the SLE was used with a threshold at 6.5 MeV. Ultimately, in SK-II the analysis threshold was set at 7 MeV. In spite of the low coverage, data were collected for 791 live days. The extracted number of solar neutrinos above 7 MeV was $7212.8^{+152.9}_{-150.9}(\text{stat})^{+483.3}_{-461.6}(\text{syst})$. A 6.7% systematic error measurement was achieved in SK-II. The energy resolution in SK-II was much worse than in SK-I.

In October 2006 the third phase of Super-Kamiokande began [276] (SK-III). The PMTs coverage was 40% as in the first phase. A number of improvements on the water purification system, Monte Carlo simulation, and data analysis allowed a more accurate measurement of the solar neutrino flux above 5 MeV. The water purification system was improved by adding a heat exchanger and two reverse osmosis units. However, an important improvement came after a test with radon-enriched water injected inside the detector. It was discovered an effect due to stagnation of water at the top and bottom of the detector volume. To prevent the stagnation of water, the flow was changed and the background from radon decreased. The flow rate was equal to 60 tons/h. In SK-III the trigger efficiency above 4.5 MeV was greater than 99%. The analysis threshold was set at 5 MeV. The energy scale error was determined to be 0.53% due to water transparency, LINAC calibration, position, and angular energy dependence. A better understanding of the light propagation in water, including the effect of the black sheets, which separate the OD and ID, improved the agreement with the calibration data. In SK-III the event selection went through the following cuts: (i) charge in ID < 2000 ph.e. to reject muons, (ii) events due to electronic noise are rejected, (iii) events that have the reconstructed vertex within 2 m from the ID wall are rejected, (iv) spallation cut to reject events due to cosmic ray muons, (v) quality cut (vertex, hit patter, PMTs response, etc.), (vi) external event cut, (vii) cosmogenic ^{16}N cut, and (viii) reject events with clustered hits. In SK-III the better vertex reconstruction improved the energy resolution at low energy by 5%. The energy resolution is well described by a Gaussian function with $\sigma(E) = -0.123 + 0.376\sqrt{E} + 0.0349E$, being E the total recoil electron energy in units of MeV. In September 2008 a new phase, named SK-IV, started [277]. This phase is characterized mainly by a new front-end electronics and a new water temperature control system at the level of $\pm 0.01^{\circ}$. Convection within the tank is reduced and kept at minimum. This allows to reduce the detection threshold to 3.5 MeV recoil electron kinetic energy in a specific tightened fiducial volume cut [277], which is applied below 5 MeV with a selection on $r^2 = x^2 + y^2$ and z, where x, y, and z are the reconstructed coordinates of the event. The trigger efficiency in SK-IV is 84% in [3.5,4] MeV recoil electron kinetic energy and 100% above 4.5 MeV. This is a major breakthrough in searching for solar neutrinos with a water Cherenkov detector.

In May 2018 SK-IV came to an end. SK-I, SK-II, SK-III, and SK-IV collected 5695 days of data on solar neutrinos. In 2018 Super-Kamiokande went through a refurbishment work, which consisted in (i) reinforcing the sealing of the water

Table 4.3 Super-Kamiokande: Different detector configurations and running modes.

Phase	Period	Live days (days)	Fiducial volume (kton)	Number of PMTs [coverage %]	Threshold (MeV)
SK-I	4/1996 to 7/2001	1496	22.5	11146 [40]	4.5
SK-II	10/2002 to 10/2005	791	22.5	5182 [20]	6.5
SK-III	7/2006 to 10/2005	548	22.5 (>5.5 MeV) 13.3 (<5.5 MeV)	11129 [40]	4.5
SK-IV	9/2009 to 5/2018	2860	22.5 (>5.5 MeV) 16.5 (4.5< E< 5.5 MeV) 8.9 (<4.5 MeV)	11129 [40]	3.5
SK-V	1/2019 to Present		TBD		

The threshold energy corresponds to electron kinetic energy.

tank, (ii) improving the water circulation rate to 120 ton/h, and (iii) replacing broken or malfunctioning PMTs. SK-V restarted data taking in January 2019. During SK-V gadolinium (Gd) salt ($Gd_2(SO_4)_3$)) at 0.2% level will be added to the water. With Gd in the water SK-V aims to detect supernova relic neutrinos [278].

In Table 4.3 the different phases of Super-Kamiokande are reported with some details. Super-Kamiokande has searched for solar neutrinos for 20 years, collecting about 5695 days of data. The present data of Super-Kamiokande covers two solar cycles, namely, solar cycle 23, from June 1996 to January 2008, and solar cycle 24, from December 2008 to late 2019 (projected). In Figure 4.13 the energy resolution for the different phases of Super-Kamiokande is shown. In SK-I, SK-III, and SK-IV, the resolution is similar; it is much worse in SK-II due to the poor light coverage. In Figure 14.14 the vertex resolution in SK-I, SK-II, SK-III and SK-IV is shown. In SK-III and SK-IV the improved data handling and reduction has fundamental impact on the vertex resolution.

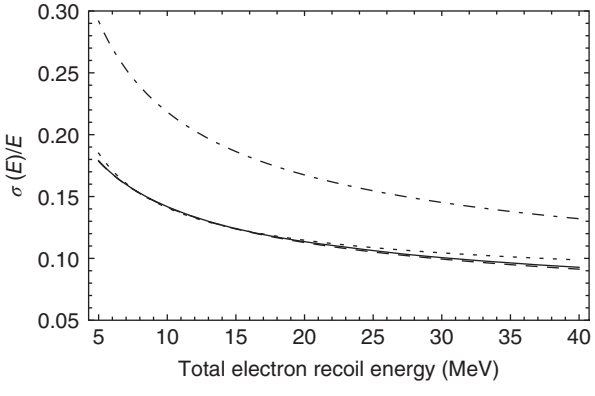

Figure 4.13 Energy resolution is Super-Kamiokande. Solid line: SK-IV. Dashed line: SK-III. Dotted-dashed line: SK-II. Dotted line: SK-I.

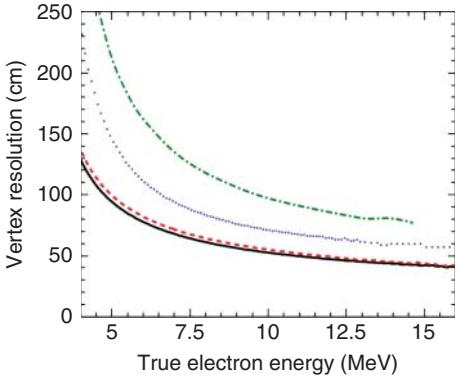

Figure 4.14 Vertex resolution for SK-I (dotted line), SK-II (dashed-dotted line), SK-III (dashed line), and SK-IV (solid line).

An extended maximum likelihood fit is used for data analysis in Super-Kamiokande. The likelihood function is defined as follows:

$$L = e^{-(\sum_i B_i + S)} \prod_{i=1}^{N_{\text{bin}}} \prod_{j=1}^{n_i} (B_i \cdot b_{ij} + S \cdot Y_i \cdot s_{ij}) \tag{4.13}$$

where $N_{\text{bin}} = 23$ is the number of bins in the energy spectrum, n_i is the number of observed events in the i-th bin, S is the total number of expected solar neutrino events, B_i is the background in the i-th bin, Y_i is the fraction of the signal in the i-th bin, and s_{ij} and b_{ij} are the signal and background weights calculated from the pdf of the predicted solar neutrino and background spectra. S and B_i are free parameters.

In Table 4.4 the measured solar neutrino flux extracted from the data during the different phases of Super-Kamiokande is reported. The combined solar neutrino flux is $\phi_{^8B} = (2.345 \pm 0.014(\text{stat}) \pm 0.036(\text{syst})) \times 10^6$ cm^{-2} s^{-1}, which is about 1.6% measurement. In Figure 4.15 the energy spectrum of solar neutrinos is shown as the data to the predicted un-oscillated rate ratio. The average, energy-independent ratio, is equal to 0.451 and shown by the horizontal dashed line. The p-value for this energy independent ratio is determined to be 32%.

A fundamental measurement carried out in Super-Kamiokande is the day–night asymmetry, A_{DN}. It turns out that $A_{\text{DN}} \propto E/\delta m^2_{21}$, with E the neutrino energy and $\delta m^2_{21} = m^2_2 - m^2_1$, being m^2_i the neutrino mass eigenstate. As specified

Table 4.4 Super-Kamiokande measured solar neutrino flux for the different detector phases.

Detector phase	Flux ($\times 10^6$ cm^{-2} s^{-1})
SK-I	$2.380 \pm 0.024^{+0.084}_{-0.076}$
SK-II	$2.41 \pm 0.05^{+0.16}_{-0.15}$
SK-III	$2.404 \pm 0.039 \pm 0.053$
SK-IV	$2.308 \pm 0.020^{+0.039}_{-0.040}$
Combined	$2.345 \pm 0.014 \pm 0.036$

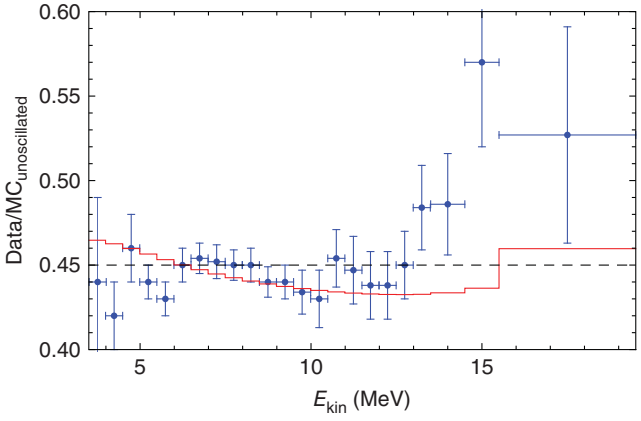

Figure 4.15 Super-Kamiokande IV energy spectrum measured as the ration of the observed rate to the predicted unoscillated rate. Source: Abe et al. [277]. Dashed line: energy independent ratio. Solid line: MSW scenario.

above, the propagation of solar neutrinos through the Earth during nighttime produces an enhancement of the ν_e flavor content. For this measurement the PREM model for the Earth's interior has been used [279]. The combined (SK-I, II, III, IV) A_{DN} measurement is

$$A_{\mathrm{DN}}^{\mathrm{SK}} = (-3.3 \pm 1.0_{\mathrm{stat}} \pm 0.5_{\mathrm{syst}})\% \tag{4.14}$$

In Figure 4.16 a summary of the DN asymmetry from SK-IV is shown [277]. The solar zenith angle is defined to separate day ($\cos\theta_z \leq 0$) and night ($\cos\theta_z > 0$). The zenith angle determines the size of matter seen by solar neutrinos going through the Earth and, as a result, the survival probability for electron neutrinos. In Figure 4.16 the first point on the left side corresponds to the average from Figure 4.15. The average daytime and nighttime ratios are shown as well. The ratio data/MC(unoscillated) is given as a function of the solar zenith angle for daytime and nighttime for five and six bins, respectively.

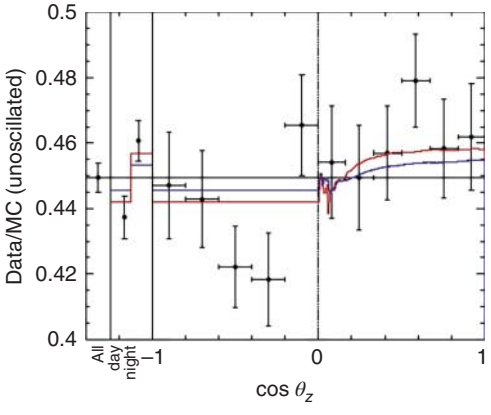

Figure 4.16 SK-IV day–night asymmetry as a function of the solar zenith angle. The day data are divided into five bins. The night data are divided into six bins. The red (blue) line corresponds to predictions from the best-fit solar neutrino data (solar neutrino + KamLAND). Error bars are statistical uncertainties only. Source: Abe et al. 2016 [277]. Reproduced with permission of American Physical Society.

The $A_{\rm DN}^{\rm SK}$ is a clean and direct method to look for matter effects in neutrino oscillations. Super-Kamiokande reports a fundamental result of $A_{\rm DN} \neq 0$ at 3σ level. A 2σ tension exists between the δm^2_{21} best fit from Super-Kamiokande and that from KamLAND (see Chapter 3). The expected $A_{\rm DN}^{\rm SK}$ from the KamLAND best fit is -1.7%. This tension could be a hint of new physics.

As reported above Super-Kamiokande has detected solar neutrinos over two solar cycles. It turns out that Super-Kamiokande does not observe any correlation of the solar neutrino rate with the 11 years of solar cycle activity: the solar neutrino flux is constant in time.

Ultimately, we mention that Super-Kamiokande is a multipurpose detector, which, besides solar neutrinos, is sensitive to atmospheric neutrinos, neutrinos from a core collapse supernova, neutrinos from the J-PARC accelerator, and subsequently supernova relic neutrinos. Takaaki Kajita for the Super-Kamiokande collaboration was awarded the 2015 Nobel Prize in Physics for the discovery of neutrino oscillations.

4.6 SNO

The Sudbury Neutrino Observatory (SNO) [280] has been built to detect solar neutrinos by means of absolute charged current (cc) and absolute neutral current (nc) interactions at the same time. SNO is a Cherenkov detector based on heavy water (D_2O). The heavy water permits to observe solar neutrinos through the following processes:

$$\begin{aligned} \nu_x + e^- &\rightarrow \nu_x + e^- \\ \nu_e + d &\rightarrow e^- + p + p \\ \nu_x + d &\rightarrow \nu_x + n + p \end{aligned} \tag{4.15}$$

The first process is an elastic scattering (ES) interaction and works as in Kamiokande or Super-Kamiokande. ES is sensitive to both ν_e and $\nu_{\mu,\tau}$, mainly to ν_e. The second process is sensitive only to ν_e by means of a cc interaction and it measures any deviation affecting the neutrino flux and spectrum produced in the core of the Sun once detected at 1 AU distance and after propagation through the interior of the star. The visible energy is generated from the electron interactions in the target mass. The third process is sensitive to all active neutrino flavors through an nc interaction. The visible energy comes indirectly from the neutron interactions in the target mass. The cc(nc) process has a threshold of 1.442(2.224) MeV. The ES interaction is a mixture of cc and nc interactions and for this reason it turns out that $\phi^{\rm cc}(\nu_e) \leq \phi^{\rm ES}(\nu_e)$ in the presence of neutrino oscillations or any process that suppresses ν_e. This comparison is a method to probe if neutrinos from the Sun change into other active flavors while moving to the Earth. The nc measurement of the neutrino flux is a direct observation of the total flux emitted in the Sun without reference to any solar model calculation. Therefore, SNO has at the same time the capacity to make a model-independent measurement of the solar neutrino flux and to observe any flavor change affecting the neutrino propagation. In case $\phi^{\rm nc} < \phi^{\rm SSM}$, the difference can be due to a transformation

of solar neutrinos to sterile neutrinos or to a wrong SSM prediction. The idea to make use of heavy water was proposed by Herb Chen [281].

SNO was built at a depth of about 6000 m.w.e. in the INCO, Ltd., Creighton mine near Sudbury in Ontario, Canada. At this depth only 70 muons per day cross the inner volume of the detector. The detector contains 1 kton of 99.92% isotopically high purity D_2O inside a 12 m diameter transparent spherical acrylic vessel (AV). This vessel is surrounded by a shielding of 7 kt of light high purity water in a cavity of maximum diameter equal to 22 m and 34 m in height. A stainless steel structure 17.8 m in diameter supports 9456 inward-looking 20-cm PMTs with light concentrators to increase the photocathode coverage, which is about 55%. The SNO PMTs were made with low radioactivity glass and had a time resolution of 1.5 ns and a quantum efficiency of 21.5% at 440 nm [282]. Ninety-one additional outward-looking PMTs were installed on the stainless steel structure to veto cosmic ray muons. In Figure 4.17 a sketch of the SNO detector taken from [280] is shown.

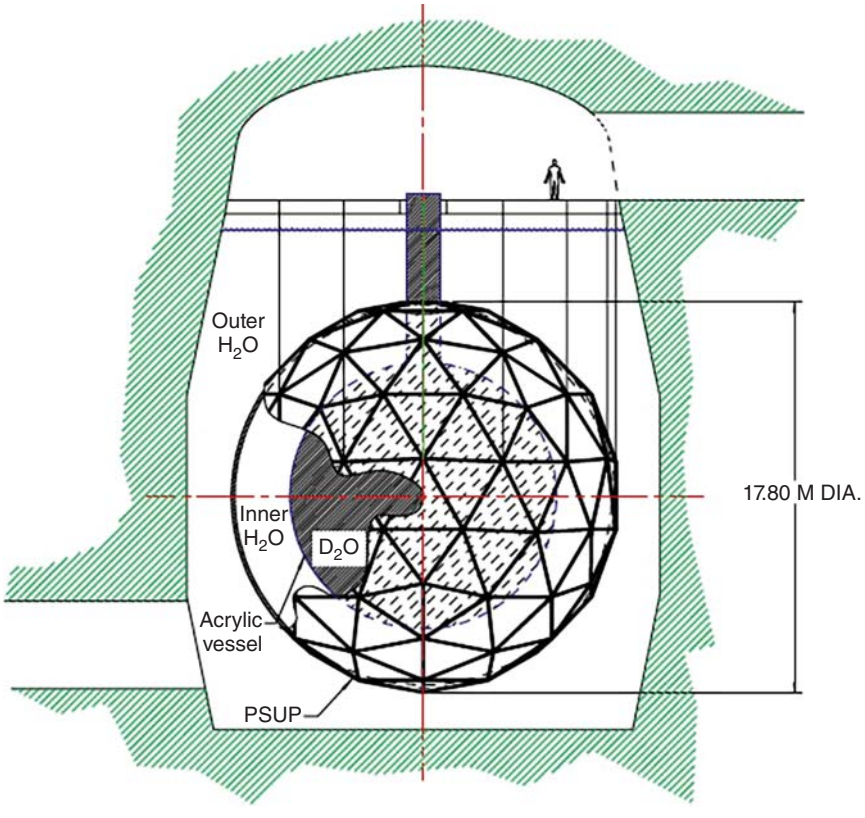

Figure 4.17 Sketch of the SNO detector [280]. The AV that contains the D_2O is visible at the center. The structure to support the PMTs is also shown. Source: SNO 2000 [280]. Reproduced with permission of Elsevier.

Table 4.5 The three phases of the SNO experiment.

Detector phase	Start date	End date	Live time [days] Day	Night
D_2O	11/1999	05/2001	119.9	157.4
Salt	07/2001	08/2003	176.5	214.9
NCD	11/2004	11/2006	176.6	208.6

SNO started data taking in November 1999. The SNO experimental activity is divided in three different phases. In Table 4.5 we report some details about the three phases. In each phase the method to detect neutrons was changed. In the first phase the detection medium consisted only of pure D_2O. In this phase neutrons are tagged by capture on deuterons. This reaction releases a single 6.25 MeV gamma ray, which creates Compton electrons as well as electron–positron pairs. These particles make Cherenkov radiation, which is detected by the PMTs. For the second phase, 2 tons of NaCl were added to the D_2O. In this phase neutrons are detected by the capture on Cl. The Cl nuclei have a capture cross section 10^5 larger than D_2O nuclei. This allows to increase the neutron detection efficiency significantly. Moreover, the capture on Cl produces an energy release of 8.6 MeV, which is larger than the one from the capture on the deuteron. This also improves the detection efficiency of neutrons, being the total visible energy much larger than the maximum energy produced by natural radioactivity (5 MeV from internal ^{208}Tl, 2.614 MeV from external ^{208}Tl from ^{232}Th, and 3.27 MeV from internal ^{214}Bi from ^{238}U). The combination of these effects increases the neutron tagging efficiency by a factor of 2.6 with respect to phase one. In the third phase, the salt was removed and an array of 40 vertical neutral current detectors (NCDs) was deployed in the AV. The NCDs were made of three or four high purity 2 m long nickel tubes welded together to make a string. Thirty-six out of 40 were filled with ^{3}He gas, which has a neutron capture cross section about 120 larger than chlorine. In Figure 4.18 a top view of the positions of the strings deployed inside the AV is shown [283]. The outer circle is the equator plane of the AV (x-y plane). The inner circle is the neck of the AV, through which the NCDs were deployed. Strings I2, I3, I6, and I7 are the ones filled with ^{4}He. In the third phase, the neutrons detection efficiency was five times larger than in the first phase. Neutrons are detected by the reaction: $n + {}^3\mathrm{He} \rightarrow {}^3\mathrm{H} + p + 764$ keV, where ^{3}H and p have energies equal to 191 and 573 keV, respectively. This energy is measured in a proportional counter. In order to combine the data from NCDs and PMTs, the trigger of the NCDs is added to the global trigger, which, normally, in SNO is generated by the coincidence of 17 PMT hits in 100 ns. In order to study the background of the NCDs, four units were filled with ^{4}He, which is not sensitive to neutrons. This allowed to understand the background due to alpha events. In addition, NCDs were calibrated using ^{252}Cf and AmBe neutron sources.

In SNO the background is coming from the radioactivity of ^{238}U and ^{232}Th in the target mass and in the surrounding materials. Electrons and gamma rays from β decays produce electron-like events. In addition, neutrons can be created by

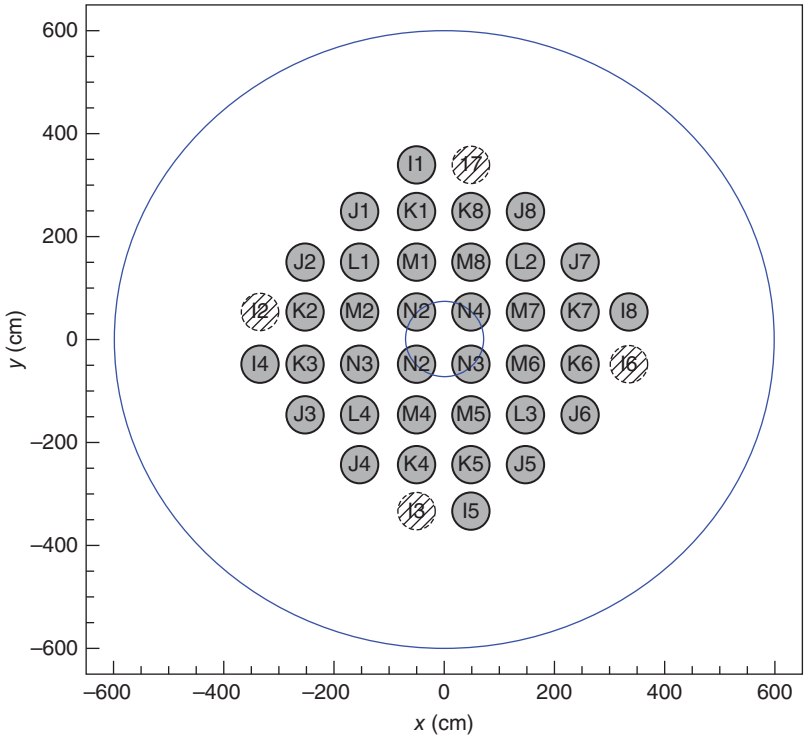

Figure 4.18 Distribution of the NCDs strings deployed inside the AV in SNO. Source: Ahrmim et al. 2013 [283]. Reproduced with permission of American Physical Society.

photo disintegration of deuterons by gamma rays with energy greater than 2.2 MeV and by (α,n) reactions mainly in the AV. These background sources produce neutron-like events. During the salt phase, neutron activation of ^{23}Na took place after the deployment of a calibration neutron source. The resulting ^{24}Na emitted gamma rays with energy equal to 2.75 MeV (BR=99.94%), which could photo disintegrate deuterons. This was an additional source of background.

Due to the different background sources in SNO, the detection threshold is set at >5 MeV. For cc interactions this corresponds to $E_\nu^{\min} = T_{\text{th}} + 1.442$ MeV. Therefore, SNO cc interaction is mainly sensitive to ^{8}B solar neutrinos (at first order we neglect the low contribution of hep neutrinos). In addition, with a threshold at >5 MeV the nc interaction is also only sensitive to ^{8}B neutrinos. For ES the corresponding minimum neutrino energy is calculated to be > 5 MeV. Again, the ES is only sensitive to ^{8}B neutrinos.

In SNO in order to determine the visible energy, it is necessary to calculate the energy distribution of the different interaction processes for a given initial neutrino energy. The visible energy distribution for cc and ES depends, although in a different way, on the neutrino energy. On the contrary, in the nc interaction the visible energy depends on the neutron interaction process and is uncorrelated with the neutrino energy. The distribution of each interaction process

against the visible energy must be determined by Monte Carlo calculations and calibrations. In addition, the background distribution as a function of the distance from the center of the detector must be also determined similarly. The external background mainly from gamma rays emitted in the AV or shielding water is expected to decrease exponentially. The internal background from β and gamma decays is homogeneously distributed inside the AV. The radial distribution of each component is determined by Monte Carlo calculations and calibrations. The radial distribution of internal neutron-like events decreases at large radii because some neutrons can escape the AV due to the large neutron random walk. This feature provides a method to disentangle neutron-like against electron-like events. The reconstructed direction of the incoming neutrino is exclusively used to discriminate ES events, which are very sensitive to the solar zenith angle. The cc interaction is slightly sensitive to the solar zenith angle, the pdf has a correlation proportional to $1 - 0.34 \cos\theta_{\odot}$. On the contrary, the nc interaction gives isotropic Cherenkov light, which allows good statistical separation of neutron-like events.

The different distributions for cc, ES, and nc interactions are defined as a function of the visible energy, T_{eff}, the effective volume, $(R/R_{\text{AV}})^3$, and the solar zenith angle, $\cos\theta_{\odot}$ [284]. These probability density functions are used to fit experimental data and are determined by Monte Carlo calculations and calibration data. The SNO detector has been calibrated with a number of sources: ^{16}N (6.13 MeV γ), ^{8}Li (Q_{β}=16 MeV), ^{3}H(p,γ)^{4}He (19.8 MeV γ), ^{24}Na, ^{222}Rn injection, ^{252}Cf, and AmBe for both electron-like and neutron-like events.

In the first SNO publication [285], data reduction reduces the number of events by a factor of about 2.9×10^6, while only the fiducial volume cut ($R < 5.5$ m) reduces the number of selected events by a factor of 15.

In Figure 4.19, as an example, the distribution of selected events above the detection threshold (6.75 MeV) and inside the fiducial volume as a function of the solar zenith angle for the first SNO data taken between 1999 and 2001 is reported [285]. The increase toward $\cos\theta_{\odot} = -1$ is due to cc interactions. From the first

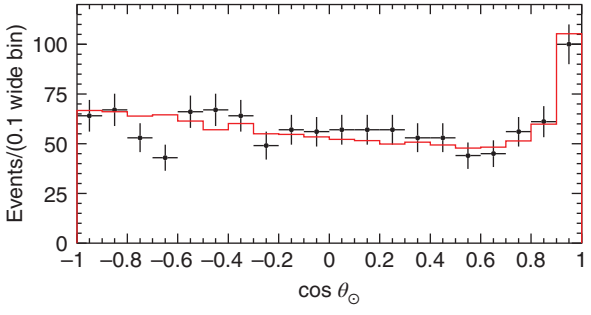

Figure 4.19 Solar zenith angle distribution of selected events with visible energy greater than 6.75 MeV and with $R < 5.5$ m from first SNO data in 2001. The peak at $\cos\theta_{\odot} = 1$ is due to ES neutrino interactions. The slight increase toward $\cos\theta_{\odot} = -1$ is due to cc interactions. Source: Ahmad et al. 2001 [285]. Reproduced with permission of American Physical Society.

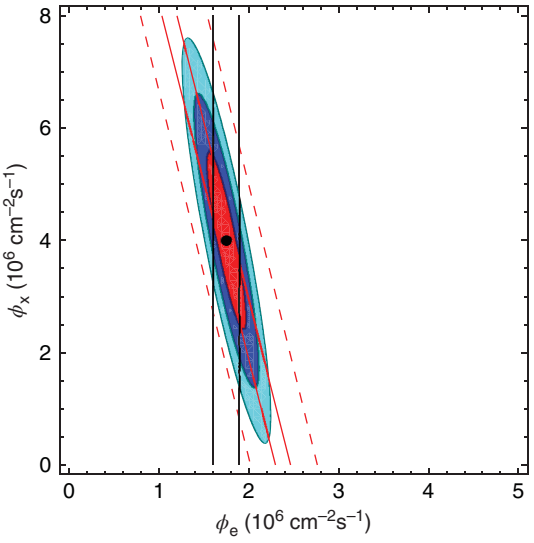

Figure 4.20 Flux of ^{8}B solar neutrinos from SNO-I and SK-I that have been detected as $\nu_{x=\mu,\tau}$ vs. the fraction detected as ν_e. The solid red line is from SK-I. The dashed red line is from SNO-I ES. The vertical solid line is from SNO-I cc. Ellipses are the 1,2,3σ contours after combining SNO with SK.

phase SNO obtained [285], searching for ^{8}B solar neutrinos:

$$\begin{aligned}\phi^{\rm cc}_{\rm SNO} &= (1.75 \pm 0.07(stat)^{+0.12}_{-0.11}(syst) \pm 0.05(theor)) \times 10^6 \text{ cm}^{-2}\text{s}^{-1} \\ \phi^{\rm ES}_{\rm SNO} &= (2.39 \pm 0.34(stat)^{+0.16}_{-0.14}(syst)) \times 10^6 \text{ cm}^{-2}\text{s}^{-1}\end{aligned} \tag{4.16}$$

where the theoretical uncertainty is related to the uncertainty on the cc cross section. As it is expected in the case of flavor change it turns out that $\phi^{\rm cc}_{\rm SNO} < \phi^{\rm ES}_{\rm SNO}$. In particular, the difference of the ES and cc fluxes is calculated to be $(0.64 \pm 0.4) \times 10^6$ cm^{-2}s^{-1}, that is, 1.6σ, assuming the systematic errors are normally distributed. If $\phi^{\rm cc}_{\rm SNO}$ is compared with the first SK-I result in Table 4.4 from 2001, the difference is 0.63 ± 0.17, that is, 3.7σ. This was a significant result supporting the hypothesis of flavor change solar neutrino propagation. In Figure 4.20 we show the result obtained by combining the data from SK-I and SNO first phase (SNO-I). The best fit from the combined analysis is determined to be $\phi_{x=\mu,\tau} = 4.0^{+1.1}_{-1.0} \times 10^6$ cm^{-2}s^{-1}. This is the first measurement of solar ν_e transition to $\nu_{\mu,\tau}$. We underline that a 3σ significance was only possible by combining SNO-I with SK-I data for the SNO-I uncertainty on ES events was too large in 2001.

In 2002 the SNO collaboration reported about the first nc measurement [286]. The detection threshold was set at 5 MeV and the fiducial volume radius was 5.5 m. The neutron detection efficiency from capture on deuterons was determined to be about 30% with a ^{252}Cf calibration source. This efficiency becomes about 14% for events above threshold and inside the fiducial volume. The primary background source for neutron-like events in this phase is the photodisintegration of deuteron from the radioactivity of ^{214}Bi and ^{208}Tl from ^{238}U and ^{232}Th, respectively, in the D_2O. The contamination of ^{238}U and ^{232}Th in the D_2O was determined to be smaller than the goal levels, which were $< 4.5 \cdot 10^{-14}$ g(U)/g(D_2O) and $< 3.7 \cdot 10^{-14}$ g(Th)/g(D_2O). A second source of background is due to photodisintegration events in the shielding water and in the AV. This source produces a factor of about two smaller background than the

main component. Cosmic ray and atmospheric neutrino events can generate neutron-like events. This component is removed by a so-called neutron cut, which veto 250 ms after any event with more than 60 PMTs fired. After the first observation of nc interactions in SNO, the neutrino fluxes were determined to be [286]

$$\begin{aligned}\phi_{\rm SNO}^{\rm cc} &= (1.76^{+0.06}_{-0.05}(stat)^{+0.09}_{-0.09}(syst)) \times 10^6 \ {\rm cm}^{-2}{\rm s}^{-1} \\ \phi_{\rm SNO}^{\rm ES} &= (2.39^{+0.24}_{-0.23}(stat)^{+0.12}_{-0.12}(syst)) \times 10^6 \ {\rm cm}^{-2}{\rm s}^{-1} \\ \phi_{\rm SNO}^{\rm nc} &= (5.09^{+0.44}_{-0.43}(stat)^{+0.46}_{-0.43}(syst)) \times 10^6 \ {\rm cm}^{-2}{\rm s}^{-1}\end{aligned} \tag{4.17}$$

These fluxes are determined by using pdfs in $T_{\rm eff}$, $(R/R_{\rm AV})^3$, $\cos\theta_\odot$ and background distributions, assuming standard ^{8}B spectral shape and no flavor transformation. Removing the constraint on the ^{8}B spectrum, it turns out $\phi_{\rm SNO}^{\rm nc} = 6.42^{+1.57}_{-1.57}(stat)^{+0.55}_{-0.58}(syst)$ cm^{-2}s^{-1} [286]. In Figure 4.21 from [286] we show the distributions of the fundamental variables in SNO for data analysis, namely, $\cos\theta_\odot$, $(R/R_{\rm AV})^3$ and $T_{\rm eff}$. The distributions of these variables are shown and scaled to fit the data. The main features of these distributions, which we have described above, are clearly seen from the plots. In Figure 4.22 we report the SNO data from [286]. Using these results we can determine $\phi_{x=\mu,\tau} = (3.4 \pm 0.6) \times 10^6$ cm^{-2}s^{-1}, that is, a 5.6σ measurement of the flavor transition of ν_e to active $\nu_{\mu,\tau}$ from only SNO. This is a breakthrough achievement from SNO in understanding solar neutrino phenomenology.

The SNO-I/II/III results are in good agreement. In Table 4.6 energy-unconstrained cc, ES, and nc fluxes are reported from SNO-I/II/III [283]. In the three phases the threshold was selected to optimize the signal-to-background ratio near the threshold. In SNO-III the threshold was increased due to loss of energy resolution in PMTs data because of the shadowing introduced by the NCDs.

About 1080 days of neutrino data have been collected and a combined analysis for the whole data set has been performed [287]. The events observed in the PMTs and NCDs phases are uncorrelated. Therefore, a global log-likelihood is defined by summing the two contributions: $logL_{\rm data} = logL_{\rm PMT} + logL_{\rm NCD}$. The combined fit to all data from SNO gives a total flux of active neutrino flavors from ^{8}B decays in the Sun equal to $\phi_B = 5.25 \pm 0.16(stat)^{+0.11}_{-0.13}(syst) \times 10^6$ cm^{-2}s^{-1} [287]. As reported in Chapter 1, the predicted ^{8}B flux is equal to $\phi_B = (5.46 \pm 0.66) \times 10^6$ cm^{-2}s^{-1} and $\phi_B = (4.50 \pm 0.54) \times 10^6$ cm^{-2}s^{-1} for the HZ and LZ, respectively.

In SNO the day–night asymmetry should characterize the ES and cc interactions. For neutrino oscillations between active flavors, the nc interactions should not manifest any day–night asymmetry. A day–night asymmetry in this channel could be evidence of sterile neutrino admixture or nonstandard matter interactions during the propagation inside the Earth. Therefore, in SNO the day–night is measured either constraining $A_{\rm nc} = 0$ or by allowing for a nc day–night asymmetry. The SNO data were divided into day and night periods, depending on the Sun being above or below the horizon. The most general day–night analysis has been performed placing no constraint on $A_{\rm nc}$ and on energy dependence. In Table 4.7

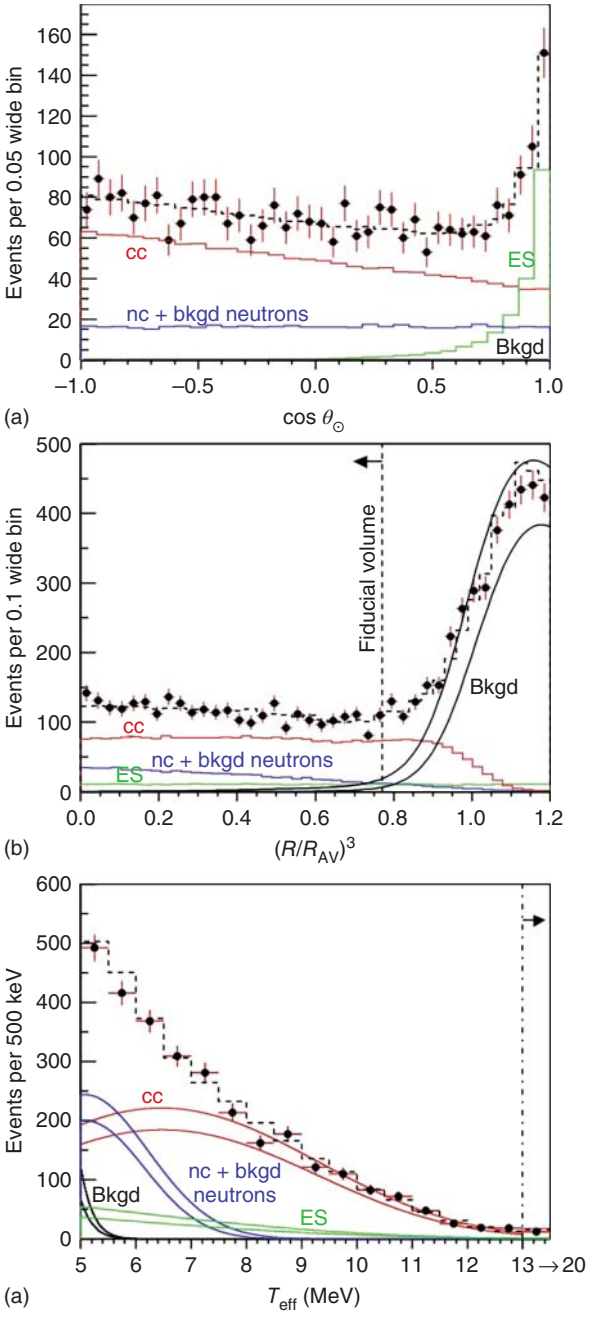

Figure 4.21 Data and Monte Carlo distributions for the main variables used in SNO, namely, $\cos\theta_\odot$, $(R/R_{AV})^3$, and T_{eff}. The dashed lines are the summed components and the bands show $\pm 1\sigma$ uncertainty. Source: Ahmad et al. 2002 [286]. Reproduced with permission of American Physical Society.

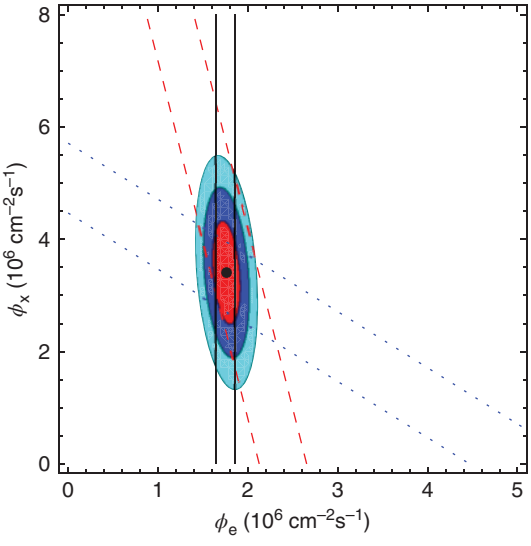

Figure 4.22 Flux of ^{8}B solar neutrinos from SNO-I, which have been detected as $\nu_{x=\mu,\tau}$ against the fraction detected as ν_e. The dashed red line is for ES interactions. The dotted blue line is for nc interactions. The vertical solid line is for cc interactions. Ellipses are the 1,2,3σ contours after combining SNO results on cc, ES, and nc.

Table 4.6 Energy-unconstrained fluxes in units of 10^6 cm^{-2}s^{-1} from SNO-I/II/III.

Detector phase	Live days	ϕ_{cc}	ϕ_{ES}	ϕ_{nc}	Threshold (MeV)
SNO-I	306	–	–	$6.42^{+1.57}_{-1.57}(stat)^{+0.55}_{-0.58}(syst)$	5.0
SNO-II	391	$1.68^{+0.06}_{-0.06}(stat)^{+0.08}_{-0.09}(syst)$	$2.35^{+0.22}_{-0.22}(stat)^{+0.15}_{-0.15}(syst)$	$4.94^{+0.21}_{-0.21}(stat)^{+0.38}_{-0.34}(syst)$	5.5
SNO-III	385	$1.67^{+0.05}_{-0.04}(stat)^{+0.07}_{-0.08}(syst)$	$1.77^{+0.24}_{-0.21}(stat)^{+0.09}_{-0.10}(syst)$	$5.54^{+0.33}_{-0.31}(stat)^{+0.36}_{-0.34}(syst)$	6.0

Source: Ahrmim et al. 2013 [283]. Reproduced with permission of American Physical Society.

Table 4.7 Day–night asymmetry measurement in SNO.

Signal	A_{DN}^{SNO} $A_{nc} \neq 0$	A_{DN}^{SNO} $A_{nc} = 0$
cc	$-0.056 \pm 0.074 \pm 0.053$	$-0.015 \pm 0.058 \pm 0.027$
ES	$0.146 \pm 0.198 \pm 0.033$	$0.070 \pm 0.197 \pm 0.054$
nc	$0.042 \pm 0.086 \pm 0.072$	0

Source: Ahrmim et al. 2005 [288]. Reproduced with permission of American Physical Society.

results on the day–night asymmetry is reported with and without the constraint on A_{nc} [288]. No significant day–night asymmetry is observed in SNO.

In SNO the solar neutrino survival probability is studied by means of the parameterization [287]:

$$P_{ee}^{d}(E_\nu) = c_0 + c_1(E_\nu - 10) + c_2(E_\nu - 10)^2. \tag{4.18}$$

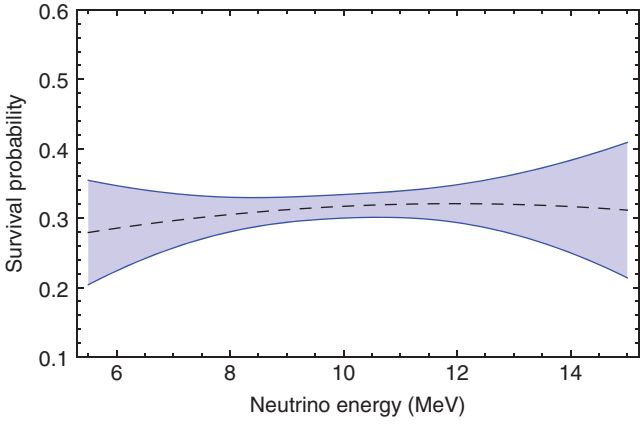

Figure 4.23 Solar neutrino survival probability determined using the polynomial parameterization in Eq. (4.18).

Equation (4.18) is an expansion of the survival probability around 10 MeV, which corresponds to the peak of the detected ^8B spectrum. In Eq. (4.18) the neutrino energy, E_ν, is in units of MeV and $c_{0,1,2}$ are free parameters in the fit. In particular, $c_0 = 0.317 \pm 0.016 \pm 0.009$, $c_1 = 0.0039 \pm 0.0066 \pm 0.0045$ MeV^{-1} and $c_2 = -0.0010 \pm 0.0029 \pm 0.0015$ MeV^{-2} [287]. The day–night asymmetry is parameterized as follows:

$$A_{\rm ee}(E_\nu) = a_0 + a_1(E_\nu - 10) \tag{4.19}$$

where $a_{0,1}$ are free parameters in the fit. It turns out that $a_0 = 0.046 \pm 0.031^{+0.014}_{-0.013}$ and $a_1 = -0.016 \pm 0.025^{+0.010}_{-0.011}$ MeV^{-1}. In Figure 4.23 we show the solar neutrino survival probability from Eq. (4.18) with $\pm 1\sigma$ uncertainty band determined using the correlation matrix from [287].

Arthur B. McDonald for the SNO collaboration was awarded the 2015 Nobel Prize in Physics for the discovery of neutrino oscillations and matter effects.

4.7 Borexino

Borexino has been the first successful experimental attempt to observe in real time solar neutrinos below 5 MeV [289]. In late 1980s it was understood that Cherenkov experiments hardly could have pushed the detection threshold below a 3–5 MeV due to ^{238}U and ^{232}Th intrinsic contamination in the target water, where limits at the level of 10^{-14} g(U,Th)/g were established. It was proposed that an organic liquid scintillator could have been purified to reach levels of about 10^{-16} g(U,Th)/g [290], low enough to detect solar neutrinos by ES in the MeV range. In a liquid scintillator, a neutrino interaction through ES will produce isotropic emission of scintillation light with a yield of order 10^4 photons/MeV, much larger than in a Cherenkov detector. The high light yield will allow to decrease the detection threshold. However, the lack of directionality asks for a

higher radio-purity because an electron recoil from a neutrino ES interaction will produce the same response due to an electron emitted by a beta decay. Therefore, in such an experiment the signal-to-background ratio must be as much as possible greater than one, that is, a high level of radio-purity is required.

In an early phase it was proposed a massive liquid scintillator detector [290, 291] with a mixture of trimethylborate (TMB, 85%) and pseudocumene (PC, 15%). This project was named Borex due to the boron in the liquid scintillator. Solar neutrinos on ^{11}B, which has an isotopic abundance of 80.1%, could produce the following interaction processes:

$$\begin{aligned} \nu_e + {}^{11}\mathrm{B} &\rightarrow {}^{11}C + e^- \\ \nu_x + {}^{11}\mathrm{B} &\rightarrow \nu_x + {}^{11}\mathrm{B} \end{aligned} \tag{4.20}$$

In Eq. (4.20) the first process is a cc interaction between the mirror nuclei $^{11}_{5}\mathrm{B}_6$ and $^{11}_{6}\mathrm{C}_5$ with $E_{\mathrm{vis}} = E_\nu - 1.982$ MeV. The interaction can go through a ground-to-ground state or to one excited state transition [291]. This cc process is sensitive to ^{8}B solar neutrinos. The second process is a nc interaction, which can produce a gamma ray of 2.11, 4.4, or 5.0 MeV. The nc interaction rate is about eight times smaller than the cc rate and it is also sensitive to ^{8}B solar neutrinos. Besides these interaction channels, the ES can also be exploited. The Borex program should have had two phases: the first phase being a detector with 0.1 kton fiducial mass, named Borexino, and the second phase a detector with 2 kton fiducial mass. However, due to the available space at the Gran Sasso Laboratory and to the interest on sub-MeV solar neutrinos, the project turned to a 0.1 kton fiducial mass detector without TMB with the main goal of searching for ^{7}Be solar neutrinos.

In order to prove the feasibility to make an organic liquid scintillator with radio-purity in the range of 10^{-16} g(U,Th)/g, the Counting Test Facility (CTF) was built at the Gran Sasso Laboratory at about 3400 m.w.e. depth [292]. The CTF started taking data in 1995. It was built to address the technology, which will be used later in a size detector for solar neutrinos, namely, Borexino. The CTF made use of 4 tons of liquid scintillator in a 500 μm thick and 2.1 m in diameter nylon vessel. The scintillator was viewed by 100 8-in. PMTs with light concentrators, installed on a stainless steel open structure. The PMTs had a quantum efficiency of 26% at 420 nm and a transit time jitter of the order of 1 ns. An external water tank (WT) 11 m in diameter and 10 m in height filled with 1000 m^3 of high purity water worked as muon veto. The WT was made of carbon steel coated with Permatex on the inside surface. In the WT PMTs were installed at the bottom floor of the tank. A hut was built on the upper floor of the WT. This hut contained a purification unit directly connected to the nylon vessel through a vertical pipe. The purification system was designed to implement nitrogen sparging, water extraction, and distillation of the liquid scintillator. During detector assembling, the inside of the WT was conditioned to be a class ISO8 clean room. Detector components were selected to contain low level of U and Th. A fluid handling system provided the possibility to fill the nylon vessel with water or liquid scintillator. The water was produced underground by a water purification plant, which was able to delivery water with low radon (< 5μBq/l)

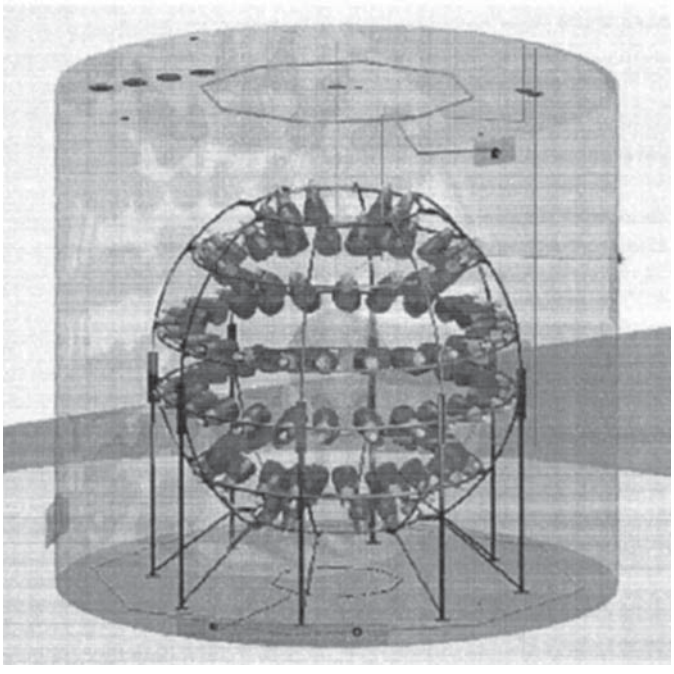

Figure 4.24 Sketch of the CTF detector. The external water tank, the open structure with 100 PMTs, and the nylon vessel at the center are shown. Source: Adapted from G. Alimonti et al. 1998 [292] and G. Alimonti et al. 1998 [293].

and U and Th at the level of 10^{-14} g(U,Th)/g. In Figure 4.24 a sketch of the CTF detector is shown [293].

In the CTF the total charge collected by the PMTs was measured to determine the energy of the event. The timing of PMT hits was measured to reconstruct the vertex of the interaction using the PMT positions and the scintillation light time of flight. The pulse shape of each event was recorded to implement offline a pulse shape analysis to disentangle electron-like event against alpha-like events. A fundamental method exploited in the CTF to measure low level of radioactivity was the possibility to tag the $\beta - \alpha$ fast decays sequence of ^{214}Bi-^{214}Po from ^{238}U and ^{212}Bi-^{212}Po from ^{232}Th. These decays produce events correlated in space and time, which allow to measure the intrinsic radioactivity of ^{222}Rn and ^{220}Rn, respectively. In addition, in the assumption of secular equilibrium, the Bi-Po events rate can be related to the intrinsic contamination of U and Th in the liquid scintillator. Another radioactive contaminant, ^{85}Kr, was also detected in the CTF. ^{85}Kr is anthropogenic with an activity of about 1 Bq/m^3 in air. ^{85}Kr can be an important source of background in the sub-MeV energy range. ^{85}Kr can be tagged by means of the fast decay sequence ^{85}Kr(β)-^{85}Rb(γ, 514 keV, $\tau = 1.46$ μs). Yet, the branching ratio of this decay is only 0.43%. To avoid ^{85}Kr contamination the fluid handling system must be leak tight and any purging should be done with Kr-free nitrogen.

The liquid scintillator for the CTF was pseudocumene (PC, C_9H_{12}) with 1.5 g/l of PPO (2,5-diphenyloxazol). The fluorescence peak emission for this scintillator is at 365 nm. The light yield in the CTF was about 300 p.e./MeV, which corresponds to an energy resolution of about 5.8% at 1 MeV. The liquid scintillator contains ^{14}C, which decays beta with endpoint energy of 156 keV. ^{14}C is cosmogenic and long-lived (half-life = 5730 years), produced by cosmic rays spallation products through the process $^{14}N(n, p)^{14}C$. Therefore, the ^{14}C production underground is minimized. In the CTF the liquid scintillator was chosen to come from petroleum in order to have a low content of ^{14}C. In fact, the ^{14}C present in the precursor organic material to the petroleum has had millions of years to decay away. The decay rate of ^{14}C is the dominant intrinsic and irreducible background at low energy. The ^{14}C measured in the CTF was [293]:

$$\frac{^{14}C}{^{12}C} = 1.94 \pm 0.09 \times 10^{-18} \tag{4.21}$$

At this concentration level, the activity above 200 keV is about 0.5 counts/day/ton. A remark is in order; in organic mixtures from modern carbon of biological origin, we expect a fraction level of the order of 10^{-12}. Therefore, for a real-time sub-MeV solar neutrino detector based on an organic liquid scintillator, the ^{14}C content relative to ^{12}C is a fundamental parameter. A concentration level as from Eq. (4.21) is needed to make a solar neutrino measurement in the sub-MeV range. As far as U and Th contaminations in the liquid scintillator are concerned, the CTF could determine the intrinsic contamination after purification at the level of $3.5 \pm 1.3 \times 10^{-16}$ and $4.4^{+1.5}_{-1.2} \times 10^{-16}$ g/g for ^{238}U and ^{232}Th, respectively [292]. This ultralow radio-purity level in the range of 10^{-4}μBq/kg has been a breakthrough in the field of solar neutrino and rare events search.

Aiming to define the best strategy for Borexino in the CTF, a second scintillator mixture was investigated [294]. This alternative scintillator consists of PXE (phenylxylylethane, C_9H_{18}) as a solvent and PTP (para-terphenyl) as primary (2–3 g/l) and bis-MSB as secondary (20 mg/l) solute. The density of this mixture (0.988 g/cm^3 at 15 °C) is closer to that of water with respect to the PC-based scintillator (∼ 0.88 g/cm^3). This better match could permit using water as buffer liquid. In addition, the high flash point of PXE (145 °C) and low vapor pressure makes PXE a nonhazardous liquid. On the contrary, the lower flash point of PC (44 °C) and high vapor pressure makes the PC-based scintillator more difficult to handle from a safety standpoint. As far as the scintillator purification is concerned, the high boiling point of PXE (295 °C) in comparison with PC (169 °C) makes it more difficult using distillation as purification method. A high purity solid silica gel column was shown to be successful to purify the PXE-based scintillator [294]. The PXE-based scintillator was loaded in the CTF in October 1996 and data were acquired until January 1997. After this run and because of the reduced number of PMTs in operation, the CTF was upgraded and a second run with PXE started in 1999. Eventually the Borexino collaboration selected PC as the scintillator for the solar neutrino experiment, and after the PXE phase the CTF was again loaded with the PC-based scintillator for radio-purity studies. In 2004–2007 the CTF was used for commissioning the Borexino fluid handling system and the purification plant.

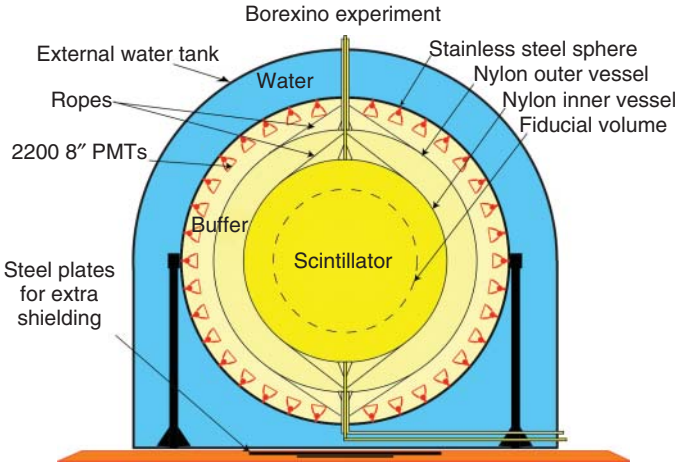

Figure 4.25 Sketch of the Borexino detector. Source: Alimonti et al. 2009 [295]. Reproduced with permission of Elsevier.

Based on the fundamental work in the CTF, the Borexino detector was designed and built [295]. The detector construction started in 1998. Borexino started data taking in 2007. In Figure 4.25 a sketch of the Borexino detector is shown [295]. The inner part of the detector consists of a stainless steel sphere (SSS) 13.7 m in diameter, which contains about 1 kton of pseudocumene (PC). The SSS is the support structure for 2212 8-in. inward-looking PMTs. All PMTs but 384 are equipped with a light concentrator and a μ metal. The light concentrators are designed to collect light from the inner 300 m^3 volume of the SSS. Inside the SSS two thin nylon vessels of 4.25 and 5.50 m in radius are installed. The inner one, named inner vessel (IV), contains about 300 tons of scintillator. The outer vessel (OV) is a barrier against radon diffusion from the SSS and the PMTs toward the core of the detector. The nylon vessels were built inside a class 100 radon reduced ($\sim$ 1 Bq/m^3) clean room using selected nylon with U and Th contamination at the level of 1 ppt. Outside the IV the volume is filled with PC and 3.5 g/l of dimethylphthalate (DMP), which is added to quench the light emission of the PC. Therefore, the volume outside the IV is a passive shielding. The decision to use PC instead of water for the outer volume was mainly driven by the higher radio-purity of PC. The scintillator mixture in Borexino is the same as in the CTF. The SSS is enclosed in a water tank (WT), which serves as shielding against environmental γ-rays and neutrons. Two-meter water shielding is enough to stop the background from the surrounding rock. The WT is instrumented with 208 PMTs to work as a Cherenkov muon veto. About 4000 muons per day are expected to cross the detector. A reduction factor of order 10^4 is provided by the muon veto. The inner surface of the WT and the outer surface of the SSS are covered with Tyvek to improve light collection. As ancillary plant Borexino is equipped with a purification system for the scintillator, which could perform distillation, water extraction, and nitrogen sparging. In addition, the water plant of CTF is used to produce high purity water. A specific system to delivery low ^{85}Kr and ^{39}Ar nitrogen has been designed and built for Borexino. A fluid handling

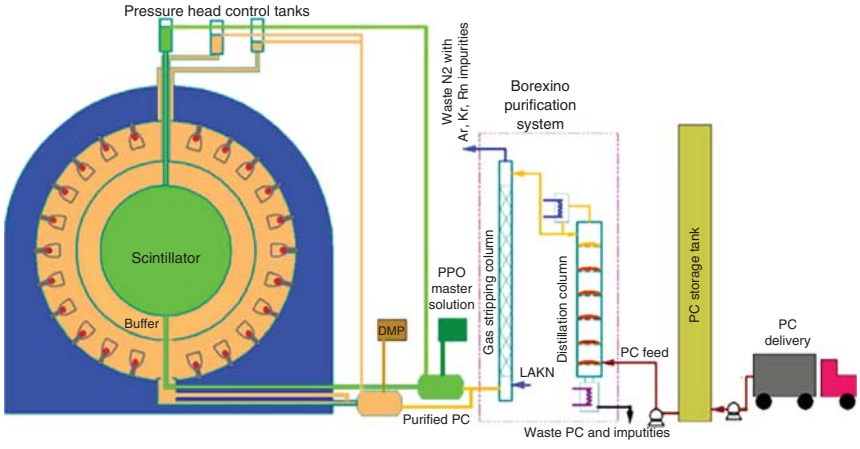

Figure 4.26 Schematic view of pseudocumene unloading, purification, and filling in Borexino. A truck with a special 20 m^3 container brings PC from the production plant. The PC is unloaded into a storage vessel with active nitrogen sparging. From the storage vessel the PC is moved to the purification plant and later mixed with PPO and filled into the IV or mixed with DMP and filled into the OB or IB. Source: Benziger et al. 2008 [296]. Reproduced with permission of Elsevier.

system connected to a storage area is able to contain 300 m^3 of PC. The whole fluid handling system and vessels in Borexino were conditioned with a precision cleaning of the system as-built before commissioning of the detector. A cleanliness class equal or better than 50 according to the standard MILSTD-1246C has been obtained. Class 50 implies for particulate with 2 g/cm^3 density a contamination of 3.6 μg/l in the liquid scintillator. Considering a conservative ppm level of uranium and thorium and submicron filtration, this is equivalent to a residual contamination of less than 10^{-16} g/g.

In Borexino in order to minimize the storage of PC and avoid radon contamination due to emanation, it was decided to unload the PC and make purification and detector filling into a continuous process [296]. In Figure 4.26 a schematic view of the unloading, purification, and filling process is shown. The purification consists in distillation and gas stripping. Online mixing is done to add PPO to distilled PC at 1.5 g/l. Borexino was first filled with high purity water. Later, three volumes were filled at the same time replacing water with scintillator (inner volume) and PC with DMP (buffer volume). The three volumes are the IV, the inner buffer (IB; the volume between the IV and the OV), and the outer buffer (OB; the volume between the OV and the SSS). A great effort was done to purify by water extraction and distillation a PC solution with a high concentration of PPO, which was used for the mixing online.

As of 2019, the Borexino data set is divided into Phase-I and Phase-II. In Phase-I from May 2007 to May 2010, 740.7 live days of solar neutrino data have been collected [297]. In 2011 a purification campaign of the liquid scintillator by water extraction took place. After the purification, the Phase-II data taking started and is still underway. In 2015 a passive thermal insulation system was installed outside the WT in order to reduce convection inside the inner vessel due to temperature changes in the underground experimental Hall. In addition, an active

Table 4.8 Calibration sources used in Borexino in the inner vessel and in the outer buffer.

Source	Type/location	Energy [keV]
^{57}Co	γ/IV	136(11%)
^{139}Ce	γ/IV	165
^{203}Hg	γ/IV	279
^{85}Sr	γ/IV	514
^{54}Mn	γ/IV	834
^{65}Zn	γ/IV	1115
^{60}Co	γ/IV	1173, 1332
^{40}K	γ/IV	1460
^{222}Rn	$\alpha\beta$/IV	0 - 3200
^{14}C	β/IV	<156
Am-Be	neutron/IV	0 - 11000
n+H capture	γ/IV	2233
n+C capture	γ/IV	4946
^{228}Th(^{208})	γ/OB	2615

Source: Bellini et al. 2014 [297]. Reproduced with permission of American Physical Society.

temperature control system, made with water pipes, was installed in contact with the WT outside surface. The goal of the system is to establish a fixed temperature gradient inside the liquid scintillator, taking into account that the WT sits on the cold floor (about 6 °C) of the experimental hall. This control system has been upgraded in 2019 to reduce to a negligible level seasonal effects. The temperature stability in Borexino is a crucial factor to measure CNO neutrinos, as we will detail later.

Calibration campaigns in Borexino were carried out in 2008 and 2009. A number of radioactive sources were deployed inside the IV in about 100 different positions. In 2010 and 2011 an external γ source was used in the outer buffer and close to the SSS to determine the external background inside the IV. In Table 4.8 from [297] we report all calibration sources used in Borexino. These calibration campaigns allowed to tune the Monte Carlo code, determine the quenching of the liquid scintillator, and adjust the reconstruction algorithm in an energy range 0–10 MeV. The energy resolution in Borexino scales roughly as $4.5\%/\sqrt{E_{\rm vis}}$ and the vertex reconstruction resolution is about 10 cm in the energy region of interest for ^{7}Be solar neutrinos. The quenching parameter, kB, quantifies the nonlinear relationship between the deposited energy and the emitted light [298]. The value of kB depends on the specific scintillator mixture and has to be determined experimentally. The value determined for the Borexino scintillator is kB = 0.0115±0.0007 cm/MeV. The number of emitted photons, $N_{p.e.}$, is related to the deposited energy, E, as follows:

$$N_{p.e.} = LY \cdot Q(E; kB) \cdot E \tag{4.22}$$

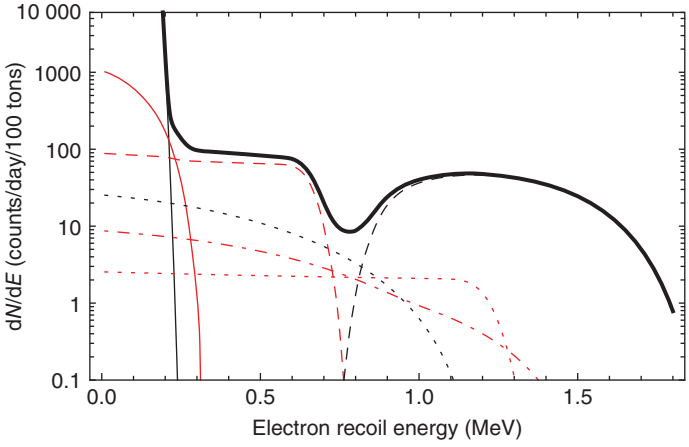

Figure 4.27 Electron recoil spectrum from solar neutrinos in Borexino. pp: solid red line. ^{7}Be: dashed red line. pep: dotted red line. CNO: dot-dashed red line. The ^{14}C (solid black line), ^{210}Bi (dotted black line) and ^{11}C (dashed black line) backgrounds are also shown.

where $LY \sim 500$ p.e./MeV is the light yield and $Q(E; kB) < 1$ is called the quenching factor. $Q(E; kB)$ depends on the ionizing particle (α, β, or γ). For β particles, $Q(E; kB)$ is written:

$$Q_{\beta}(E; kB) = \frac{1}{E} \int_0^E \frac{dE}{1 + kB \cdot dE/dx} \tag{4.23}$$

In addition, a radial dependence in Eq. (4.22) has to be considered for events with vertex close to the IV. The radial dependence is a function of the light collection efficiency, which is optimized for the central core of Borexino. As a matter of fact, in the central fiducial mass of about 100 tons, this dependence is negligible.

In summer 2007 Borexino released the first real-time spectroscopic observation of the mono-energetic ^{7}Be solar neutrino line at 862 keV [299]. At that time only 0.01% of the total solar neutrino flux had been measured in real time above 5 MeV. Due to the ES kinematic, the mono-energetic neutrinos will produce a recoil electron with a sharp cut-off edge at 665 keV. In Figure 4.27 the expected electron recoil spectrum for solar neutrinos in Borexino is shown. At low energy below 200 keV, the spectrum is dominated by ^{14}C (in Figure 4.27: $^{14}C/^{12}C = 2.7 \times 10^{-18}$). The pp solar neutrinos (solid red line) are dominant around 200–300 keV. The shoulder due to ^{7}Be at about 660 keV is clearly visible. CNO and pep solar neutrinos above 800 keV are overwhelmed by ^{11}C (28 counts/day/100 tons in this plot). The ^{210}Bi (20 counts/day/100 tons in this plot) is also shown (dotted black line). In Table 4.9 the expected unoscillated rates in the fiducial volume and from SSM (GS98-2016) are reported.

In Borexino the analysis threshold was set at about 200 keV due to the activity of ^{14}C (see Figure 4.27). The geometrical coverage of the detector is 30%. The PMTs are similar to those used in the CTF and the light yield is about 500 p.e./MeV, which gives an energy resolution of 4.5% at 1 MeV, as highlighted above. The main trigger fires when at least 30 PMTs detect one hit in a time

Table 4.9 Unoscillated rates in Borexino based on SSM (GS98-2016).

Source	Energy range (MeV)	Rate (counts/ day/100 tons)
pp	0.16–0.5	21.90 ± 0.13
pep	0.2–1.5	3.66 ± 0.02
^{7}Be	0.2–0.8	48.7 ± 3.5
CNO	0.2–1.5	5.3 ± 0.7

Uncertainties are only from SSM errors on neutrino fluxes.

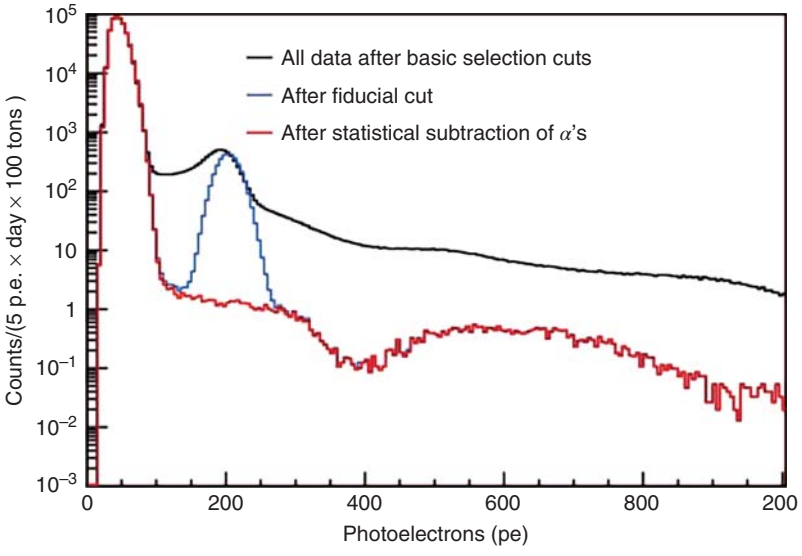

Figure 4.28 Spectrum of recorded data in Borexino. The spectrum after the fiducial volume cut is shown. The peak corresponds to the α decay of ^{210}Po. The spectrum after the $\alpha - \beta$ discrimination cut is also shown. Source: Arpesella et al. 2008 [300]. Reproduced with permission of American Physical Society.

window of 60 ns. After a trigger the time and charge of each PMT with at least one hit is recorded in a time gate of 7.2 μs. In Figure 4.28, as an example, the spectrum of data recorded after the first 192 days of data taking in Borexino is shown [300]. A comparison of Figure 4.27 and Figure 4.28 shows that the spectrum in Borexino consists mainly of solar neutrinos, ^{14}C, ^{11}C, and ^{210}Po (the peak at about 200 photoelectrons). ^{210}Po together with ^{210}Bi in the liquid scintillator are produced by ^{210}Pb: $^{210}Pb(Q_\beta = 63.5\ keV, \tau = 32.2\ y) \rightarrow\ ^{210}Bi(Q_\beta = 1.162\ MeV, \tau = 7.2\ d) \rightarrow\ ^{210}Po(E_\alpha = 5.4\ MeV, \tau = 199.6\ d)$. However, from Figure 4.27 and Figure 4.28 it is clear that a component of ^{210}Po not in equilibrium with ^{210}Pb is present and dominant. From present understanding the ^{210}Po can be introduced in the liquid scintillator during fluid handling operations and during the water replacement with scintillator. It is understood that water can

be an important source of ^{210}Po. In addition, there is experimental evidence that the nylon vessel and nylon end-caps at the vessel's poles are sources of ^{210}Po. This ^{210}Po detaches from the nylon vessel and end-caps and migrates within the fiducial volume due to convective movements. A good thermal insulation will reduce these movements and consequently the ^{210}Po background. The α decay of ^{210}Po can be removed offline by pulse shape discrimination as shown in Figure 4.28.

At the beginning of data taking and mainly in Phase-I, a ^{85}Kr contamination was also present at the level of 30 counts/day/100 tons [301]. This contamination was due to a small air leak during filling operations. The ^{85}Kr has been be removed by Kr-free nitrogen sparging in 2011.

The study of fast coincidence Bi-Po decays yields, with the assumption of secular equilibrium, a contamination of ^{238}U and ^{232}Th equal to $(1.6 \pm 0.1) \times 10^{-17}$ g/g and $(6.8 \pm 1.5) \times 10^{-18}$ g/g, respectively [301]. These results on radio-purity are better than initially expected from the experience of CTF. The interaction rate of 862 keV ^{7}Be solar neutrinos is measured to be $46.0 \pm 1.5(stat)^{+1.5}_{-1.6}(syst)$ counts/day/100 tons in 740.7 live days from 16 May 2007 to 8 May 2010 [301]. The equivalent unoscillated ν_e flux is $(2.79 \pm 0.13) \times 10^9$ cm^{-2} s^{-1}. The day–night asymmetry measured for selected ^{7}Be events is determined to be $A(^7Be)_{\mathrm{DN}} = -0.001 \pm 0.012(stat) \pm 0.007(syst)$ [302]. Therefore, Borexino does not detect any day–night effect. This is expected in the framework of the MSW-LMA solution (see Chapter 3).

Borexino could also perform a real-time measurement of the pp solar neutrinos. This is a fundamental measurement, for the pp neutrinos are directly related to the energy released by the Sun. It is a real-time test of the energy production, which eventually changes hydrogen into helium. As a matter of fact, the primary reaction in the pp chain is the fusion of two protons with the emission of low energy pp neutrinos. The pp neutrino energy spectrum has an endpoint energy equal to 423 keV, which corresponds to a maximum recoil electron kinetic energy of 264 keV. The data set used for pp solar neutrinos corresponds to 408 days of Phase-II from January 2012 to May 2013. After the water extraction purification in 2011, the ^{85}Kr contamination was reduced by a factor of 10. This improves the spectral fit at low energy. The minimum visible energy detectable in Borexino is about 50 keV, which corresponds to 25 PMT hits with a trigger efficiency of about 100% [297]. In this energy range the signal is dominated by ^{14}C. As a matter of fact, most of the trigger rate in Borexino ($\sim$ 30 counts/s) above the trigger threshold is dominated by ^{14}C in spite of the small isotopic abundance (^{14}C/^{12}C $\approx 2.7 \times 10^{-18}$). Because of this the ^{14}C rate was determined independently from the main analysis for pp neutrinos. In particular, looking at events following the main trigger and within a time window of 16 μs (predominantly from ^{14}C), it is possible to determine the spectrum and rate of ^{14}C without the constraint of the hardware trigger threshold. The ^{14}C activity in 100 tons is measured to be 40 ± 1 Bq. Another important background source for the pp measurement is due to the ^{14}C pile-up events, which produces a total energy deposit up to about 300 keV. A dedicated study by Monte Carlo calculations was carried out to determine the contribution of the pile-up events. A rate of 154 ± 10 pile-up events/day/100 tons is determined, which is similar to the expected pp solar neutrino rate equal to 131 ± 2 counts/day/100 tons in the

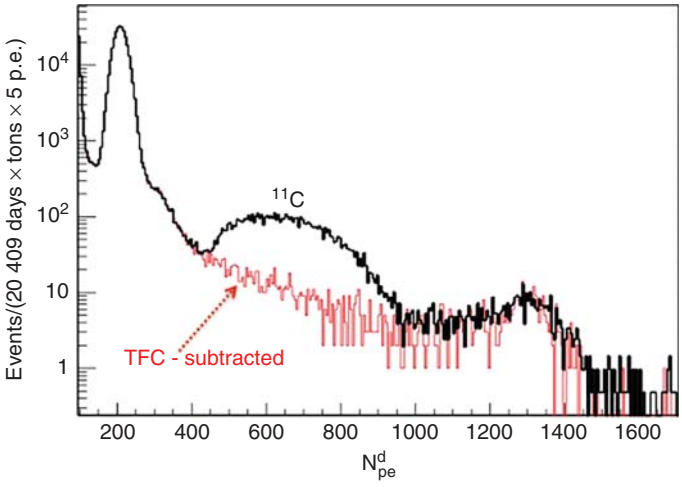

Figure 4.29 Energy spectrum in Borexino for neutrino-like events in the fiducial volume before and after the TFC tag to remove ^{11}C. Source: Bellini et al. [297]. Reproduced with permission of American Physical Society.

whole energy range. Using these constraints the pp solar neutrino rate measured by Borexino through a spectral fit is calculated to be $144 \pm 13(stat) \pm 10(syst)$ counts/day/100 tons [303].

The dominant muon-induced cosmogenic background in Borexino is ^{11}C: $\mu + {}^{12}C \rightarrow \mu + n + {}^{11}C$, followed by $^{11}C \rightarrow {}^{11}B + e^+ + \nu_e$ with τ=29.4 minutes. The total energy released in the scintillator by the ^{11}C decay is between about 1 and 2 MeV ($\sim$ 500–1000 p.e.). It is possible to tag ^{11}C events by a threefold coincidence [304]. This coincidence exploits the time and space correlation between a muon crossing the IV, a γ event at 2.22 MeV from neutron capture on H and a positron decay in the energy bin 1–2 MeV. The threefold coincidence can be used to tag and remove ^{11}C events. This cut reduces the data sample by about 30%. This idea was implemented to measure pep and CNO neutrinos [305]. In Figure 4.29 the spectrum of selected neutrino-like events in the fiducial volume is shown with and without the threefold coincidence (TFC) tagging [297]. The rates of pep and CNO neutrinos measured with a spectral fit and using the TFC tagging are $R(pep) = 3.1 \pm 0.6(stat) \pm 0.3(syst)$ counts/day/100 tons and $R(CNO) < 7.9$ counts/day/100 tons at 95% C.L. [305]. The dominant background, which limits the sensitivity to CNO neutrinos in Borexino, is the beta decay of ^{210}Bi from ^{210}Pb. There is a strong correlation between CNO and ^{210}Bi due to a degeneracy of the two energy spectra around 800 keV (see Figure 4.27). Therefore, an accurate CNO neutrinos measurement in Borexino asks for a further purification of the liquid scintillator to remove this background component. In addition, a deeper experimental site could improve the sensitivity to CNO due to a reduction of the ^{11}C background, which in Borexino limits the statistics of collected neutrino-like data.

Neutrinos from ^{8}B decays in the Sun were also measured in Borexino [306]. The detection threshold was set at 3 MeV. The SSM (GS98-2016) expected

Table 4.10 Summary of solar neutrino measurements in Borexino.

Source	Rate (counts/day/100 tons)
pp	$144 \pm 13(stat) \pm 10(syst)$
pep	$3.1 \pm 0.6(stat) \pm 0.3(syst)$
^{7}Be	$46.0 \pm 1.5(stat)^{+1.5}_{-1.6}(syst)$
^{8}B	$0.217 \pm 0.038(stat) \pm 0.008(syst)$
CNO	< 7.9 95% C.L.
Day–night asymmetry	$-0.001 \pm 0.012(stat) \pm 0.007(syst)$

rate is calculated to be 0.50 ± 0.07 counts/day/100 tons above threshold. In Borexino muons crossing the liquid scintillator produce cosmogenic radioactive isotopes. Some of these isotopes are short-lived and have a mean-life of the order of one second. or less: ^{12}B, ^{8}He, ^{9}C, ^{9}Li, ^{6}He, and ^{8}Li. Others such as $^{10}C(Q_{\beta^+} = 3.6\ MeV)$ and $^{11}Be(Q_{\beta^+} = 11.5\ MeV)$ are long-lived with mean-life of order 20–30 seconds. In addition, ^{7}Be and ^{11}C are also produced by cosmic rays. However, these latter isotopes contribute to the background rate below threshold and are not taken into account for the ^{8}B analysis. A cut of 6.5 seconds after each muon allows to reject all short-lived cosmogenic background isotopes with a 29.2% fractional dead time [306]. A threefold coincidence, similar to the one discussed for ^{11}C, is applied for ^{10}C and ^{11}Be. The residual rate from ^{10}C and ^{11}Be after this cut is of the order of 6×10^{-3} and 3×10^{-2} counts/day/100 tons, respectively. The background mainly from ^{214}Bi and ^{208}Tl internal and external (from the IV and PMTs) is studied with a fit to the radial distribution of events with energy above threshold. The corresponding background rate from ^{214}Bi and ^{208}Tl are determined to be of the order 10^{-4} and 6×10^{-3} counts/day/100 tons. Background subtraction allows to determine the ^{8}B solar neutrino rate above 3(5) MeV to be $0.217 \pm 0.038(stat)^{+0.008}_{-0.008}(syst)(0.134 \pm 0.022(stat)^{+0.008}_{-0.007}(syst))$ counts/day/100 tons for 345.3 day data set after selection cuts. The unoscillated flux above 5 MeV is calculated to be $(2.7 \pm 0.4(stat) \pm 0.2(syst)) \times 10^{6}$ cm^{-2} s^{-1} in agreement with Super-Kamiokande and SNO.

In Table 4.10 a summary of the solar neutrino measurements in Borexino is reported. This table shows the potentiality of Borexino in performing a real-time spectroscopy of solar neutrinos.

In 2018 [70] the Borexino collaboration has performed a complete study of solar neutrinos from the pp chain. A simultaneously fit of the energy spectrum, the spatial and pulse shape estimator distributions allows to determine the different solar neutrino and background components. In Table 4.11 a summary of the 2018 solar neutrino measurement in Borexino is reported.

The simultaneous measurement of pp and ^{7}Be solar neutrinos allows to determine the ratio, $R_{I/II}$, between ^{3}He-^{4}He and ^{3}He-^{3}He fusion rates. Neglecting the ^{8}B small contribution, $R_{I/II} = 2\phi(^{7}Be)/[\phi(pp) - \phi(^{7}Be)]$. It turns out that $R_{I/II} = 0.178^{+0.027}_{-0.023}$, in agreement with the HZ and LZ predictions, namely, 0.180 ± 0.011 and 0.161 ± 0.010, respectively.

Table 4.11 Summary of 2018 solar neutrino measurements in Borexino.

Source	Rate (counts/day/100 tons)	Fux (cm^{-2} s^{-1})
pp	$134 \pm 10^{+6}_{-10}$	$(6.1 \pm 0.5^{+0.3}_{-0.5}) \times 10^{10}$
pep(HZ)	$2.43 \pm 0.36^{+0.15}_{-0.22}$	$(1.27 \pm 0.19^{+0.08}_{-0.12}) \times 10^{8}$
pep(HZ)	$2.65 \pm 0.36^{+0.15}_{-0.24}$	$(1.39 \pm 0.19^{+0.08}_{-0.13}) \times 10^{8}$
^{7}Be	$48.3 \pm 1.1^{+0.4}_{-0.7}$	$(4.99 \pm 0.11^{+0.06}_{-0.08}) \times 10^{9}$
^{8}B	$0.223^{+0.15}_{-0.16} \pm 0.006$	$(5.68^{+0.39}_{-0.41} \pm 0.03) \times 10^{6}$
CNO	< 8.1 95% C.L.	$< 7.9 \times 10^{8}$
hep	< 0.002 90% C.L.	$< 2.2 \times 10^{5}$

The result for pep neutrinos depends on whether it is assumed the HZ or LZ SSM prediction to constrain the CNO neutrino flux.

Another important measurement carried out in Borexino is the seasonal modulation of ^{7}Be solar neutrino rate [307]. The absence of the annual modulation is rejected at 99.99% C.L.: the orbit of the Earth is measured underground by means of solar neutrinos. Data worth 1456 astronomical days from Phase-II are used for this study with reduced background with respect to Phase-I. Electron-like events are selected in the energy region from 215 to 715 keV in a 3 m radius fiducial volume. The stability of the energy scale over the data set period was proven to be better than 1%. The fiducial mass change was measured to be 0.1% by monitoring the temperature (and density) change over time. The modulation analysis returns an eccentricity equal to 0.0174 ± 0.0045 and a period of 367 ± 10 days.

At present, Borexino aims to detect CNO solar neutrinos. The strategy adopted is based on a spectral fit with the ^{210}Bi rate in the fiducial volume constrained by ^{210}Po measurement [308]. The ^{210}Po rate in the scintillator consists of two components: a contribution from ^{210}Pb inside the liquid scintillator and a contribution from ^{210}Po coming from the inner vessel. A good thermal insulation is crucial to disentangle the two components. Without convection the ^{210}Po coming from the vessel should decay and the dominant contribution in the fiducial volume will become the one in equilibrium with ^{210}Pb. The pulse shape discrimination might allow to measure this component at 10% level. Because this component is in equilibrium with ^{210}Bi, the degeneracy between CNO and ^{210}Bi in the spectral fit is broken and the CNO solar neutrino rate can be measured. As of 2019 Borexino is attempting to measure CNO neutrinos.

A final remark is in order as far as ^{7}Be solar neutrinos are concerned. In 2015, the KamLAND collaboration has reported a measurement of ^{7}Be solar neutrinos [237b] equal to $(3.26 \pm 0.50) \times 10^{9}$ cm^{-2} s^{-1}, assuming a pure electron flavor, and a solar flux of $(5.82 \pm 0.98) \times 10^{9}$ cm^{-2} s^{-1}. KamLAND ^{7}Be solar neutrino measurement is in agreement with Borexino. The KamLAND detector has been introduced in Chapter 3.

Table 4.12 Summary of solar neutrino measurements.

Source	Fux (cm^{-2} s^{-1}) SSM-HZ	Fux (cm^{-2} s^{-1}) SSM-LZ	Fux (cm^{-2} s^{-1}) data
pp	$5.98(1 \pm 0.006) \times 10^{10}$	$6.03(1 \pm 0.005) \times 10^{10}$	$6.1(1 \pm 0.10) \times 10^{10}$
pep(HZ CNO)	$1.44(1 \pm 0.009) \times 10^{8}$	$1.46(1 \pm 0.009) \times 10^{8}$	$1.27(1 \pm 0.17) \times 10^{8}$
pep(LZ CNO)			$1.39(1 \pm 0.15) \times 10^{8}$
^{7}Be	$4.93(1 \pm 0.06) \times 10^{9}$	$4.50(1 \pm 0.06) \times 10^{9}$	$4.99(1 \pm 0.03) \times 10^{9}$
^{8}B	$5.46(1 \pm 0.12) \times 10^{6}$	$4.50(1 \pm 0.12) \times 10^{6}$	$5.35(1 \pm 0.03) \times 10^{6}$
CNO	$4.88(1 \pm 0.11) \times 10^{8}$	$3.51(1 \pm 0.10) \times 10^{6}$	$< 7.9 \times 10^{8}(2\sigma)$
p-value	0.96	0.43	

4.8 Summary and Open Questions

In 50 years of observations on solar neutrinos, we have learned a lot about radioactive backgrounds in experiments for rare events, on neutrino physics, and the physics of the Sun. In Table 4.12 a summary of the main results on solar neutrino measurements is given. Experimental results are reported together with predictions from the SSM. The measurement on pp neutrinos is calculated without using the luminosity constraint. The p-value in Table 4.12 determines the compatibility between the predictions and the data when results from Borexino, SNO, and Super-Kamiokande on pp, ^{7}Be, and ^{8}B solar neutrinos are considered. To determine the p-value, using the data shown, we calculate $\chi^2 = \sum_{i,j=1}^{3} (\phi_i^{\rm th} - \phi_i^{\rm exp}) \sigma_{ij}^{-2} (\phi_j^{\rm th} - \phi_j^{\rm exp})$ with $\sigma_{ij}^2 = \rho_{ij} \sigma_i^{\rm th} \sigma_j^{\rm th} + \delta_{ij} \sigma_i^{\rm exp} \sigma_j^{\rm exp}$, being ρ_{ij} the predicted correlations between fluxes from the SSM. At present, data cannot distinguish the SSM-HZ against the SSM-LZ. This important information can come from an accurate measurement of the CNO neutrino flux. When results from radiochemical experiments are considered, the pp be determined at the level of about 8%, namely $(6.5 \pm 0.5) \times 10^{10}$ cm^{-2} s^{-1}.

As far as neutrino oscillations are concerned, in Figure 4.30 solar and KamLAND data against the neutrino oscillation hypothesis is shown. This figure shows a longstanding tension at 2σ level on the best-fit δm^2 between solar and KamLAND oscillation analysis. This tension can be a hint for new physics: CPT invariance, nonstandard interactions, some subtle effect not accounted for yet. Current and future experiments will attempt to settle this problem.

In Figure 4.31 the electron neutrino survival probability is shown as a function of the neutrino energy. Different assumptions are used to draw the survival probability, including the possibility of nonstandard interactions with $\epsilon = -0.16, -0.25$ [310]. From the figure it is evident that the energy region between 2 and 4 MeV is crucial to disentangle the various scenarios. As we have discussed in the context of SNO and Super-Kamiokande a measurement in this energy range is very demanding in terms of background rejection.

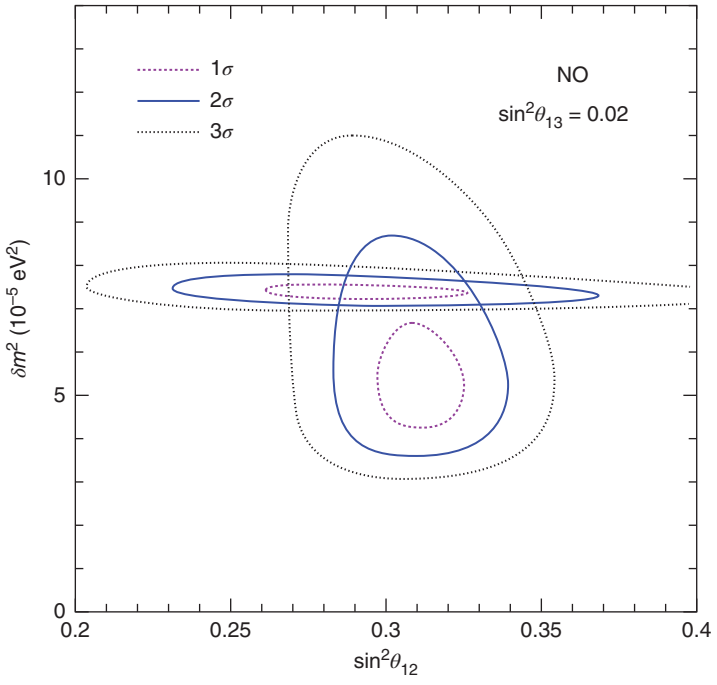

Figure 4.30 Gobal solar and KamLAND neutrino oscillations fit. Source: Capozzi et al. 2018 [309]. Reproduced with permission of Elsevier.

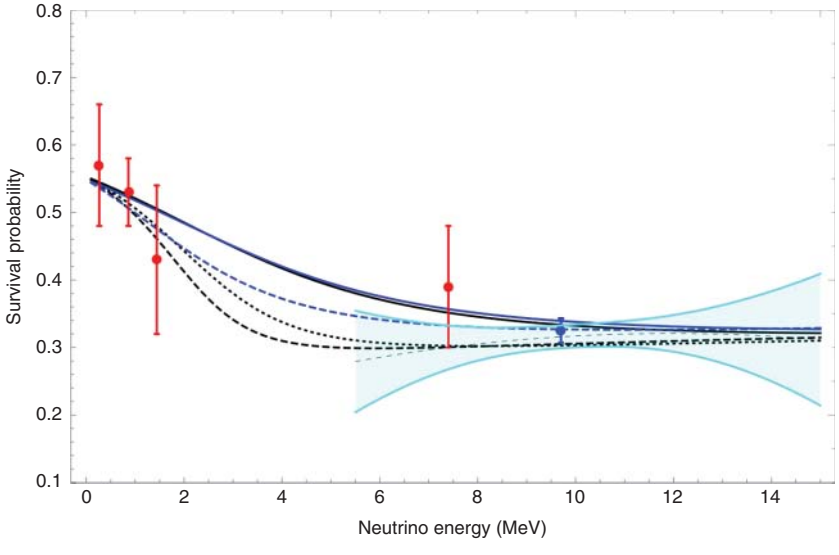

Figure 4.31 Electron neutrino survival probability. Red points: Borexino data. Blue point: SNO and Super-Kamiokande combined data. Colored area: SNO LETA analysis. Solid black line: global LMA analysis. Solid blue line: KamLAND best fit. Dashed blue line: global solar neutrino fit. Dashed and dotted black line: nonstandard interactions included.

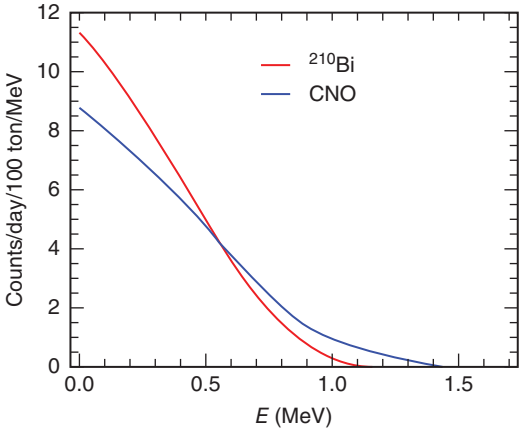

Figure 4.32 Energy spectrum of CNO solar neutrinos and ^{210}Bi.

As we have already discussed, the CNO neutrino flux measurement is crucial to solve the solar abundance problem. Furthermore, a measurement of CNO neutrinos is crucial to understand the initial chemical composition of the gas cloud from which our solar system formed. At present, the Borexino collaboration is attempting this difficult measurement. The main challenge consists in breaking the degeneracy between the CNO neutrino energy spectrum and the ^{210}Bi energy spectrum. As it is shown in Figure 4.32, the two spectra are similar around 500 keV. Therefore, a reduction of the ^{210}Bi contamination below 5 cpd/100 tons (in order to have a signal-to-background ratio greater than 1) or a constraint of the ^{210}Bi rate are the possible methods, which might allow such an important measurement.

In the next years the Super-Kamiokande collaboration detector is attempting, by means of the refurbished detector, to measure the day–night asymmetry at 3.9σ level, assuming the present systematic uncertainty can be reduced to 0.4%. In addition, Super-Kamiokande aims to measure the upturn of the survival probability about 3 MeV at 3σ level. These measurements, if successful, will improve significantly the present understanding of solar neutrino physics.

In conclusion, despite the great achievements obtained by past and present solar neutrino experiments and two related Nobel Prizes in Physics, there are important open questions to be answered.

5

Future Solar Neutrino Experiments

Although solar neutrino experiments have resolved the long-standing puzzle of the missing neutrinos (the Solar Neutrino Problem) by the discovery of neutrino oscillations, there are still several open issues in this field. One of them is connected to the astrophysical topic about the solar metallicity, as discussed in detail in this book (the Solar Abundance Problem); others concentrate more on the intrinsic neutrino properties, either on a better understanding of oscillation parameters or on the search for new physics.

The accurate measurements of the ^{7}Be- as well as the ^{8}B-neutrino flux (see Table 4.2) have a small impact on our knowledge of the solar metallicity. Future experimental results on these two values might be useful to obtain only hints on the solution for the so-called Solar Abundance Problem. Currently, the experimental data are just in between the low-Z and high-Z scenarios, as shown in Figure 5.1.

The smoking gun for solving the metallicity problem is a CNO neutrino measurement with an accuracy of about 10% or better. So far the best limit on the solar CNO flux of $\phi_{\mathrm{CNO}} < 7.9 \times 10^{8}$ cm^{-2} s^{-1} (95% C.L.) comes from the Borexino experiment [311]. This limit is not far (a factor of 2) from the expected flux value and hence there is a real possibility that either this limit may be significantly improved with time or even a first measurement would be possible by Borexino. Yet, two problems for a successful CNO measurement have to be overcome. In the first place, as it has been discussed previously in this book, ^{11}C nuclei generated in spallation reactions of high energy muons with ^{12}C in the liquid scintillator give a large background contribution within the relevant energy regime for a measurement of CNO neutrinos. The Borexino collaboration developed ways to identify these muon events with a high efficiency, but still a fraction of about 5% remains as background with 30% exposure reduction. In addition, intrinsic beta decays due to residual ^{210}Bi atoms produce background events within the fiducial volume of the detector at a rate that exceeds the event rate expected for the CNO neutrinos ($\sim$ 5 cpd/100 ton). There is no way to tag the ^{210}Bi-signals (half-lifetime $T_{1/2} = 5$ days) on an event to event basis and eventually further purification of the scintillator may be necessary. As it has been discussed in the previous chapter, perhaps there is an indirect way to determine the absolute ^{210}Bi-activity within the fiducial volume by measuring accurately the subsequent ^{210}Po α decay, which can be identified by means of an energy and pulse shape selection cut. Then the

Solar Neutrino Physics: The Interplay between Particle Physics and Astronomy,
First Edition. Lothar Oberauer, Aldo Ianni, and Aldo Serenelli.

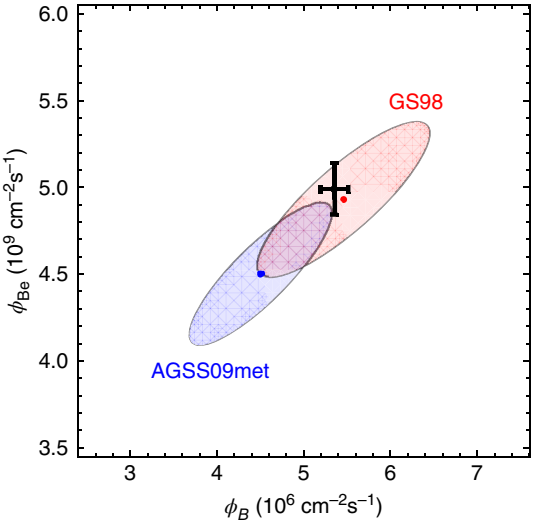

Figure 5.1 Current measurement of solar ^{8}B (x-axis) and ^{7}Be (y-axis) neutrino fluxes against 1σ contour for high-Z(red) and low-Z(blue) Standard Solar Models (SSM) predictions. Data are taken from Table 4.12.

^{210}Bi background could be subtracted at least statistically from the raw data and the residual spectrum could be fitted to determine the CNO spectrum contribution to the total neutrino rate. The fit then may provide a signal or an improved limit on the CNO neutrino flux. This method only works in the case of secular equilibrium (with ^{210}Pb, $T_{1/2} = 22.3$ years) which was clearly broken at the beginning of the data taking period of Borexino and therefore the ^{210}Po α-activity has to flatten out and shall come at least close to a constant value asymptotically before this procedure can be applied. In the previous chapter we have underlined how critical the absence of convective motions is to exploit this method successfully.

In the following of this chapter, we present a brief review of future experiments on solar neutrinos, indicating in particular their potential and the scale of time.

5.1 SNO+

SNO+ is the new project developed after the closure of sudbury neutrino observatory (SNO) [312]. SNO+ has been installed in the Sudbury (ON, Canada) underground mine in the same cavity that was occupied previously by the SNO detector. The heavy water will be replaced by ~ 0.8 kton of LAB-based liquid scintillator, which may open the door for low energy solar neutrino physics, similarly to the case of Borexino. Yet, we underline that the main focus of SNO+ is the search for the neutrinoless double beta decay with ^{130}Te. For this purpose the scintillator will be loaded with Te-atoms[1], which will introduce a level of radioactivity in the energy region below ~ 2 MeV. Therefore, the tellurium loading will make the CNO neutrino detection and sub-MeV solar neutrino detection impossible. However, the SNO+ collaboration intends to use

1 The isotope ^{130}Te is a nucleus undergoing double beta decay. It has a quite high natural abundance of ~34%.

an unloaded liquid scintillator for a certain period of time in order to perform solar neutrino spectroscopy, if the radio-purity measured after the scintillator filling will be of the order of the Borexino scintillator radio-purity. Since the underground laboratory at the Sudbury mine (SNOlab) has an overburden of 2070 m, which is equivalent to 6010 m of water shielding, the cosmic muon flux is much lower with respect to the case of Borexino. Therefore, the cosmogenic background situation is much more favorable for SNO+ and this experiment has good chances to detect CNO neutrinos, provided the demanding goals on the intrinsic levels of radio-purity will be reached. For the same reason, with SNO+ there are also very good perspectives to perform pep neutrino detection with high accuracy. Such a measurement could improve the precision of the value of the ν_e survival probability at 1.4 MeV, which is currently only coming from the Borexino experiment. As it has been discussed in the previous chapter, for particle physics a precise measurement of the energy dependence of the ν_e survival probability, P_{ee}, would be of great interest. Especially the transition region between vacuum and matter dominated oscillations (upturn) is sensitive to new physics. For instance, the existence of sterile neutrinos with a certain parameter range of masses and mixing angles could influence not only the transition curve $P_{ee}(E_\nu)$ but also deviations from the standard model like flavor-changing neutral current weak interactions would modify it. In Figure 5.2 the survival probability $P_{ee}(E_\nu)$ is shown for solar ^{8}B-neutrinos in the standard

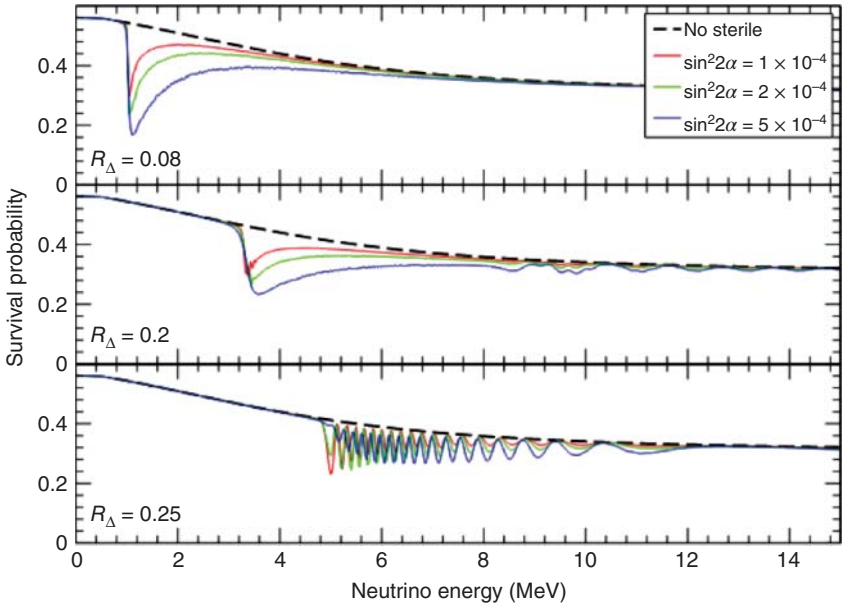

Figure 5.2 Survival probability $P_{ee}(E_\nu)$ for solar ^{8}B-neutrinos in the standard MSW case and assuming the existence of sterile neutrino admixture to active flavors. Significant deviations from the standard case are expected for specific values of the sterile-active mixing parameter $\sin^2 2\alpha$ and mass scaling factor $R_\Delta = \Delta m^2_{01}/\Delta m^2_{21}$. Source: de Hollanda and Smirnov 2011 [313]. Reproduced with permission of American Physical Society.

Mikheyev–Smirnov–Wolfenstein (MSW) case as well as for scenarios with different mixing angles of sterile neutrinos [313].

The transition region is sensitive to hypothetical sterile neutrino states which are light and mix to active flavors very weakly. Typical values for the mass splitting would be $\Delta m^2_{01} \sim 10^{-5}$ eV^2 and $\sin^2 2\alpha \sim 10^{-3}$. The insert parameter of Figure 5.2 are denoted as $R_\Delta := \Delta m^2_{01}/\Delta m^2_{21}$, where $\Delta m^2_{01} = m^2_0 - m^2_1$ and m_0 is the value of the new mass eigenstate.

In Figure 5.3 the survival probability $P_{ee}(E_\nu)$ is shown for solar ^{8}B-neutrinos in the standard MSW case (curve with number 3) as well as for different scenarios with flavor-changing neutral current weak interactions [314]. The differences arise due to varying amplitudes of the nonstandard interaction strengths between neutrinos of a specific flavor and left- and right-handed components of fermions.

Therefore, a more accurate determination of P_{ee} at the fixed energies of ^{7}Be- and pep lines would be very welcome. The theoretical uncertainty of the ^{7}Be intensity (6%) is quite high and already at present the experimental precision from Borexino is better (3%). Therefore, a better understanding of the theoretical uncertainties would improve the situation for ^{7}Be solar neutrinos. On the other hand, the pep neutrino flux prediction has a very small uncertainty due to its direct link to the constraint of the solar luminosity, similarly to the case of pp neutrinos. For pep neutrinos, at present, the main uncertainty is due to the statistical limitation of the Borexino detector and to the cosmogenic background at the depth of the Gran Sasso Laboratory. Future experiments, such as SNO+, with larger fiducial volumes and a deeper location may obtain a better determination of the P_{ee} at 1.4 MeV. At this point a remark is in order, the survival probability depends not only on the neutrino energy and oscillation parameters but also on the distribution of the fusion reaction considered within the Sun. Therefore, $P_{ee}(E_\nu)$ should in principle be plotted for every specific thermal fusion branch separately, as these distributions may differ significantly. An average P_{ee} as a function of the energy, which depends on the oscillation parameters as well as the specific neutrino source, should be considered.

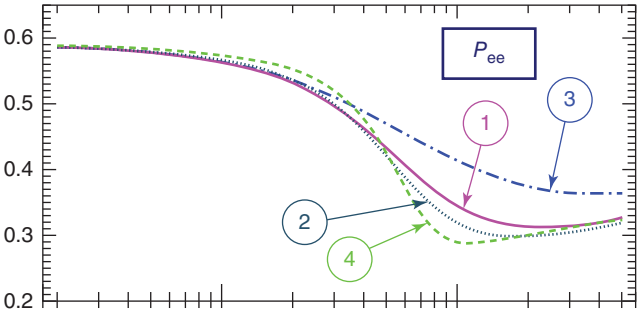

Figure 5.3 Survival probability $P_{ee}(E_\nu)$ for solar ^{8}B-neutrinos in the standard MSW case (curve number 3) and different values for amplitudes describing nonstandard interactions between neutrino flavors and charged fermions. Source: Friedland et al. 2004 [314]. Reproduced with permission of Elsevier.

As of December 2019 SNO+ filling with scintillator without tellurium loading is in an advanced phase. With the water run prior to the scintillator filling the collaboration has measured the ^{8}B solar neutrino flux above 5.5 MeV visible energy, showing that the refurbished detector works well. We can assume that SNO+ will start taking data with the scintillator by 2020.

The main goals of SNO+ before tellurium loading will be precision measurement of pep solar neutrinos in the upturn region, ^{8}B solar neutrinos above 2 MeV and day–night asymmetry, and CNO solar neutrinos. A high radio-purity in SNO+ will allow the experiment to contribute to answer the open questions discussed at the end of the previous chapter.

5.2 JUNO and LENA

Another upcoming project is JUNO (Jiangmen Underground Neutrino Observatory) in the south of China, which aims to start data taking in 2021. Currently (May 2019), JUNO is under construction in a new underground laboratory at a depth of ~ 700 m. JUNO consists of an acrylic sphere filled with 20 kton of liquid scintillator with 78% photomultiplier tubes (PMTs) coverage. The acrylic sphere is built inside a water tank equipped with 18k 20-in. and 25k 3-in. PMTs. At the top of the water tank a muon tagging and track reconstruction system is installed. The expected energy resolution in JUNO is of the order of 3% at 1 MeV. This is a crucial parameter for the proposed physics case. Although the main objectives of JUNO are the precise measurement of neutrino oscillation parameters via spectroscopy of nuclear reactor neutrinos, the experiment has also a rich program in astroparticle physics. One of them is solar neutrino spectroscopy via electron neutrino elastic scattering, whereas reactor neutrinos will be detected via the inverse beta decay on protons. As far as CNO neutrino detection is concerned, the limited shielding against cosmic muons might affect this measurement. However, JUNO may have a potential to perform solar ^{8}B-neutrino spectroscopy at a low energy threshold of ~ 2 MeV in order to probe the transition region between the vacuum and matter dominated regions. A total signal rate of ~ 4.5 counts per day and per kt fiducial volume is expected in JUNO. In Figure 5.4 the result of a Monte Carlo simulation is shown, where the solar ^{8}B-signal and several background contributions are depicted [226]. In JUNO the cosmogenic background plays an important role, but it can be assumed that a significant part of the ^{11}C and ^{10}C contributions can be rejected on an event-by-event basis by applying a threefold coincidence cut, as it has been done successfully by the Borexino collaboration in the pep neutrino analysis. This cut follows that in almost any case of a ^{10}C nucleus generation, one or more neutrons will be released. Therefore, for any muon going through the scintillator, a 2.2 MeV gamma signal due to neutron capture in a proton (with a time constant of about 200 µs) and the ^{10}C (lifetime $T_{1/2} = 19.3$ seconds) positron emission builds a unique signal pattern. A simpler twofold coincidence would presumably not work, as the muon rate in JUNO with about 3 Hz is too high. In Figure 5.4 the raw data distribution is shown without any

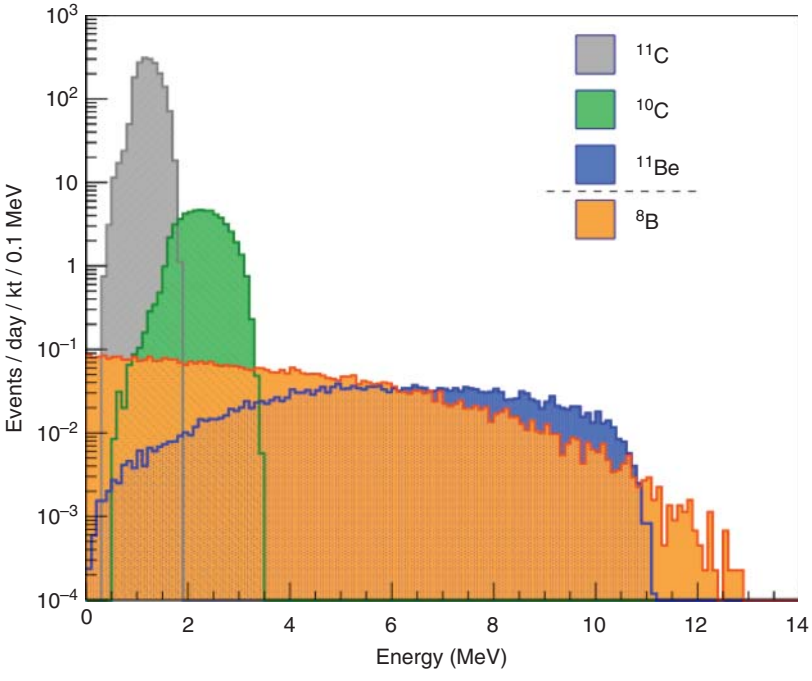

Figure 5.4 Expected solar ^{8}B-spectrum coming from elastic neutrino electron scattering plus several background contributions due to cosmogenic generated isotopes in JUNO. A significant reduction of ^{11}C and ^{10}C should be possible by applying a Borexino like cut on the threefold coincidence of a muon, a neutron and the following beta-plus event. This reduction is not applied in the figure. Source: An et al. 2015 [226]. Reproduced with permission of IOP Publishing.

cut applications and it is clear that a reduction factor of ~ 60 will be necessary in order to achieve an energy threshold of about 2 MeV. The ^{11}Be contribution ($Q_\beta = 11.5$ MeV; $T_{1/2} = 13.8$ seconds) cannot be rejected via this method. In this case a precise spectral analysis plus a proper understanding of the detector light output should allow an accurate control of the^{11}Be background. As in the case of Borexino candidate, ^{11}Be events can be selected with $E > 6$ MeV from a time window [10, 150]s following a preceding muon. The lower time cut excludes events from other cosmogenic candidates. To reduce accidental background, the energy must be greater than 5 MeV and the ^{11}Be candidate must be spatially confined within 2 m from the muon track. An intrinsic background contribution due to ^{208}Tl from the ^{232}Th radioactive decay chain may appear in the form of a beta-gamma cascade, which adds up to a Q-value of ~ 5 MeV. This contribution cannot be rejected by a fiducial volume cut, as one can apply for reducing external gamma and neutron background. However, the background level can be measured by identifying the delayed $\beta - \alpha$ coincidence of the preceding ^{212}Bi-^{212}Po decays and statistically subtracted. Nevertheless, the internal ^{232}Th concentration of the scintillator should not exceed the 10^{-17} g/g level. Even reactor neutrinos via elastic scattering of electrons with a counting rate of about

0.5 per day and per kt reaching a maximal visible energy of about 8 MeV will form a nonnegligible background for solar ^{8}B-neutrino spectroscopy in JUNO.[2] This reactor correlated background contribution is not shown in Figure 5.4. One can assume that its ∼5% level can be correlated accurately to the measured inverse beta decay rate and statistically subtracted with high precision.

There exists also the possibility to detect solar ^{8}B-neutrinos via a charged current reaction on ^{13}C in the case of liquid scintillator detectors like JUNO. This option was pointed out first by Arafune et al. [315] and then discussed in [316] for the cases of Borexino, KamLAND, and SNO+. Organic liquid scintillators consist mainly of hydrogen and carbon. Among all stable carbon atoms, there is ^{13}C with a natural isotopic abundance of 1.07% and hence present also in liquid scintillators. Electron neutrinos, ν_e, can be detected via the charged current weak interaction.

$$\nu_e + {}^{13}\mathrm{C} \rightarrow e^- + {}^{13}\mathrm{N} \tag{5.1}$$

with a Q-value of 2.22 MeV. Therefore, only solar ^{8}B-neutrinos are detectable, when we neglect the tiny contribution from hep neutrinos. The generated nitrogen isotope ^{13}N is unstable and undergoes β^+-decay back to ^{13}C with a lifetime of $T_{1/2} = 9.96$ minutes. This offers the possibility to apply a delayed coincidence cut in time and space in order to suppress accidental background efficiently, as the delayed signals form a continuous spectrum between ∼ 1 and ∼ 2.2 MeV. Unfortunately, the counting rate in detectors of the size of Borexino, KamLAND, and SNO+ is small, as the interaction rate should be around 24 counts per kt and per year. However, in JUNO this charged current (cc) reaction could offer an interesting additional channel for probing the vacuum–matter transition region by comparing counting rates and spectral shapes with the cc + nc reaction in the case of elastic electron scattering. A remark is in order; the cross section of reaction (5.1) to the ground state is known with great accuracy [316] from the decay of ^{13}N. The cross section to the lowest excited state at 3.51 MeV can be calculated theoretically with an uncertainty of the order of 30%. Likewise the cross section for the neutral current (nc) interaction channel on ^{13}C to an excited state at 3.68 MeV can be calculated with a 30% uncertainty. This latter process, however, can be used to measure the total ^{8}B neutrino flux.

In addition, high statistic solar ^{7}Be-neutrino spectroscopy seems feasible, because the cosmogenic background is not playing such a severe role in the energy range below 1 MeV. This is a fact, as the dominant cosmogenic long-lived isotopes are positron emitter with a minimal energy release of 1 MeV due to the positron annihilation. Only ^{11}Be is a β^- isotope, but its contribution in the energy range of ^{7}Be solar neutrinos is indeed negligible. All short-lived isotopes with $T_{1/2} < 1$ second can be efficiently suppressed by vetoing a cylindrical volume with 1 m radius around each muon track. Therefore, a high efficient muon tracking algorithm is required for efficient background rejection. The counting rate of solar ^{7}Be neutrinos due to elastic scattering of electrons is expected to be around 520 per day and kt. At this high statistics, one may

2 The JUNO detector is located at a distance of 53 km to two nuclear power complexes with a total thermal power of 36 GW.

search for time variations in the ^{7}Be-signal and for an anomalous day–night asymmetry due to the Earth's matter effect. Moreover, improving the precision of a ^{7}Be neutrino measurement in combination with other solar neutrino data like a CNO measurement by Borexino and/or SNO+, or a new ^{8}B neutrino measurement, would give helpful hints in order to solve the metallicity problem. Last but not least, one could use it for the search of an anomalous magnetic moment of the neutrino, as this would give an additional energy depending contribution to the cross section for scattering of electrons. The perspectives for a successful solar ^{7}Be neutrino measurement in JUNO are not bad if the scintillator intrinsic background levels of ^{238}U and ^{232}Th are below 10^{-16} g/g, and if the limit for ^{40}K is below 10^{-17}. However, the most dangerous contribution is expected to come from the beta decay of ^{210}Bi as one has to assume that the secular equilibrium is broken below ^{210}Pb ($T_{1/2} = 22.3$ years) as it is observed in the Borexino experiment. In Figure 5.5 the recoil spectra for low energy solar neutrinos plus relevant background contributions are shown for the conditions that are close to those reached in Borexino.

The edge of the ^{7}Be distribution at 660 keV is very well observable due to the expected excellent energy resolution of 3% (at an energy deposition of 1 MeV) which is aimed for in JUNO. Not shown in Figure 5.5 is the mono-energetic α-peak from ^{210}Po, which however should be well separated from the ^{7}Be-edge. In addition, the JUNO scintillator should be capable of pulse shape analysis where α-events will be separated efficiently from electron events. It is interesting to note

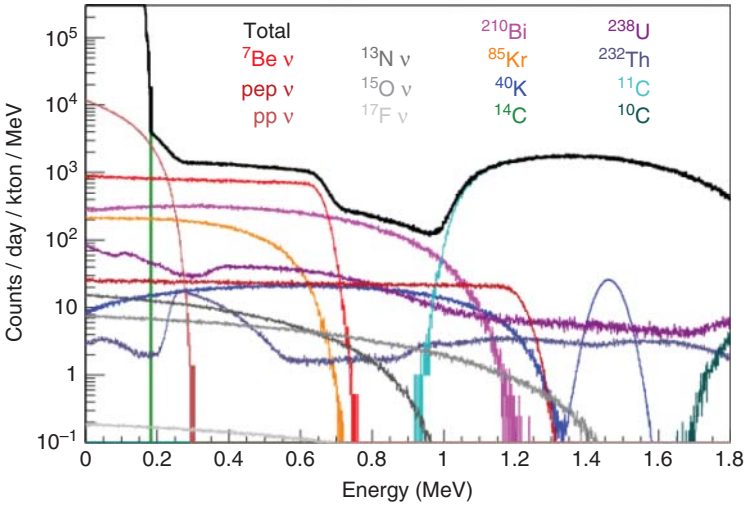

Figure 5.5 Expected recoil spectrum due to elastic neutrino scattering of electrons at low energies in the JUNO detector plus relevant background contributions. The assumed background levels are close to the situation observed in the first phase of Borexino. Not shown is the mono-energetic α-peak from ^{210}Po, which should be well separated from the ^{7}Be edge at around 660 keV. Source: An et al. 2015 [226]. Reproduced with permission of IOP Publishing.

that the high energy resolution would also allow a solar pp neutrino measurement, clearly visible in the spectrum around 0.3 MeV.

The possibility for the search of a matter induced upturn in the solar ^{8}B spectrum in massive liquid scintillator detectors before JUNO was studied in the frame of the LENA (Low Energy Neutrino Astrophysics) collaboration, which proposed the construction of a deep underground (i.e. 4000 m.w.e. shielding) liquid scintillator detector with a total mass of about 50 kt [317]. The Pyhšalmi mine in Finland was identified to be an almost ideal facility for such an enterprise. Among other topics solar neutrino spectroscopy is one of the most important features of the LENA scientific case and the detector design as well as the shielding was optimized for a high efficient low energy neutrino detection. Background studies for the solar program of LENA showed that a fiducial volume corresponding to $\sim$ 30 ton mass could be achieved for the ^{13}C reaction, yielding a detection rate of about 2 counts per day [318]. Together with the electron scattering channel, a clear separation between the expected matter-induced ^{8}B upturn and new exotic physics could be achieved after a measurement time of five years at a 5σ level [318]. Also the solar ^{7}Be detection via elastic electron scattering was studied in LENA. Monte Carlo simulations on the background predict a counting rate of 1.7×10^4 per day for a fiducial mass of 35 kton [319]. Based on such a high statistical signal a search for periodic modulations of the counting rate on a sub-percent level in the amplitude could be conducted. The range of accessible time variations from several minutes, corresponding to modulations caused by helioseismic g-modes, to tens of years, allows to study long-term changes in solar fusion rates. Gravity driven waves (g-modes) are based on the restoring force of g-waves, which is caused by adiabatic expansion or compression of convective packets in the inner regions where the temperature gradient is small. Movement of the packets, for instance, from the inner to outer radii will lead to an adiabatic expansion with a temperature decrease and therefore a density increase, which exceeds the value of the surrounding matter. This mechanism does not work in the outer solar convective zone by definition, and therefore g-mode waves propagating from the core toward the outer region of the Sun are damped. This is why g-mode detection by standard helioseismology, based on Doppler observations of surface radial velocities, is very challenging, and it is an interesting option to look into the possibility to search for this and related effects with solar neutrinos. In principle g-modes should have a direct impact on neutrino generation as they occur in the same region where thermonuclear fusion takes place. In addition, density variations in the inner solar zone may also have an impact on the matter effect of neutrino flavor conversion. In reference [320] such a process is discussed, where a resonance between helioseismic and magnetic driven So-called Alfven waves may provide a mechanism for generating fluctuations in the solar environment, which have a measurable influence on neutrino oscillations.

In the framework of the next-generation detectors based on liquid scintillators, an interesting alternative is the so-called hybrid solution of a water-based scintillator [321], which can have still a high light output and on the other hand the

capability of analyzing the signal pattern, which is typical for Cherenkov detectors [322]. Another advantage could be a significant lower price with respect to organic scintillators, which would allow the construction of very large detectors in the range of 100 ton or even more. This development is especially interesting for high energy neutrino physics in the context of accelerator long baseline oscillation experiments, because of the improved reconstruction possibilities of high energy events. However, if once such a detector should be realized, it may also offer interesting features for solar neutrino physics. If one would be able to distinguish between Cherenkov and scintillation light via a fast timing with newly developed large area picosecond photo-detectors (LAPPDs), the directionality of events could be measured and this would allow to separate background from solar neutrino signals. The chemistry of water-based liquid scintillators allows loading of metallic ions as additional target for solar neutrinos. The loading of ^{7}Li is discussed [322], which would allow neutrino detection via the cc reaction $\nu_e + {}^{7}\mathrm{Li} \rightarrow e^{-} + {}^{7}\mathrm{Be}$ with a Q-value of 0.862 MeV, opening the possibility to perform low energy neutrino spectroscopy. Besides, elastic scattering of electrons could be used for solar neutrino detection and with the information of the directionality the background should be rejected efficiently. Of course many problems have to be solved beforehand, not only the quest of light output when a quite large fraction of ionic isotopes is loaded to the liquid but also, for instance, the question how one can purify the liquid to such low values, which are required for solar neutrino spectroscopy.

5.3 Hyper-Kamiokande

The water Cherenkov Hyper-Kamiokande detector consists of 258 kt of water with 187 kt of fiducial mass. Likewise in Super-Kamiokande, the water tank is divided into an inner and outer detector. The outer detector has a thickness of 1 and 2 m on the side and at the top and bottom, respectively. Between the inner and outer detector, there will be a dead area of 60 cm. The design goal is to reach a factor of 2 better light collection with respect to Super-Kamiokande. The inner detector photocoverage is equal to 40%. Moreover, a possible twin detector is under investigation to double the fiducial mass. The inner detector will be equipped with 40k 20-in. PMTs, while the outer detector with 6.7k 8-in. PMTs. In size the Hyper-Kamiokande detector will be a cylinder with 74 m in diameter and 60 m in height. As far as solar neutrinos are concerned, the physics case will be (i) $\sim 5\sigma$ measurement of the day–night asymmetry with ^{8}B neutrinos in a timescale of 10 years and with an expected systematic uncertainty of the order of 0.3–0.1%, (ii) a 3σ measurement of the upturn in 10 years with a conservative detection threshold at 4.5 MeV (a 5σ is expected with a threshold at 3.5 MeV), and (iii) a first direct observation of hep neutrinos at 3σ level. In Figure 5.6 a schematic view for the single cylindrical tank is shown [323].

The construction of the Hyper-Kamiokande detector is expected in April 2020 as of May 2019. The physics case of such a detector is not limited to solar neutrinos, but covers long baseline neutrino physics and astrophysics. As a matter

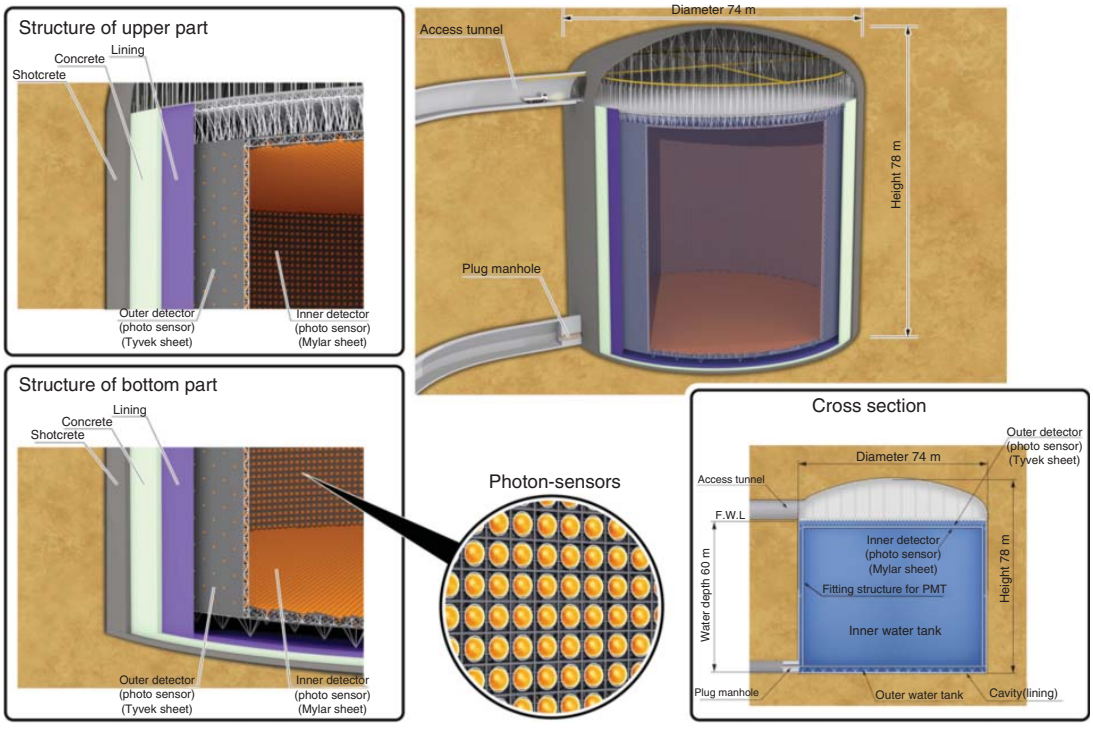

Figure 5.6 Schematic view of the Hyper-Kamiokande single cylindrical tank.

of fact, the main physics goal of Hyper-Kamiokande is long baseline neutrino physics.

5.4 DUNE

The deep underground neutrino experiment (DUNE) is a next-generation project for neutrino physics and proton decay. DUNE consists of two detectors: a near detector close to a neutrino source at Fermi National Accelerator Laboratory in Batavia, Illinois (United States) and a second detector, much larger, deep underground at Sanford Laboratory (SURF) in South Dakota (United States). The two detectors will be 1300 km apart. DUNE is mainly a long baseline neutrino project. DUNE official start was announced in 2017. As far as beam neutrino physics is concerned, DUNE is complementary to Hyper-Kamiokande. The far detector consists of 40 kt of liquid argon divided into four 10 kt time projection chamber (TPC) modules. The TPC modules are developed at CERN and will be in single phase or double phase (liquid and gas). A schematic view of the DUNE far detector with the four TPCs and the cryogenic systems in the middle is shown in Figure 5.7 [324].

At SURF the excavation for DUNE started in 2019. The first single-phase module is expected to be deployed in 2022 and the beam ready in 2026. The whole detector should be in operation by 2027.

As far as solar neutrinos are concerned, DUNE can exploit two detection channels [309]: a cc interaction, $\nu_e + {}^{40}Ar \rightarrow e^- + {}^{40}K^*$ and the neutrino electron elastic scattering. The detection threshold is at 5 MeV, so ^{8}B and hep neutrinos can be measured, similarly and complementary to Hyper-Kamiokande. The simultaneous measurement of these two interaction channels will break the degeneracy between $\sin^2\theta_{12}$ and $\phi({}^8B)$. This potentiality together with the high statistics is expected to improve the measurement of ϕ_x against ϕ_e made in SNO and shown in Figure 4.20. Moreover, DUNE can probe Δm^2_{21} by measuring the day–night asymmetry. $A_{\mathrm{DN}} \propto E/\Delta m^2_{21}$. Considering only statistical uncertainties, $A_{\mathrm{DN}} \approx$ -$(7.9 \pm 0.8)\%$ ($\sim 10\sigma$).

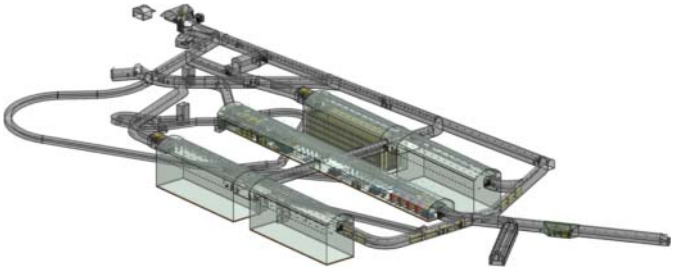

Figure 5.7 Schematic view of the DUNE far detector with the four 10 kt TPCs and the cryogenic system.

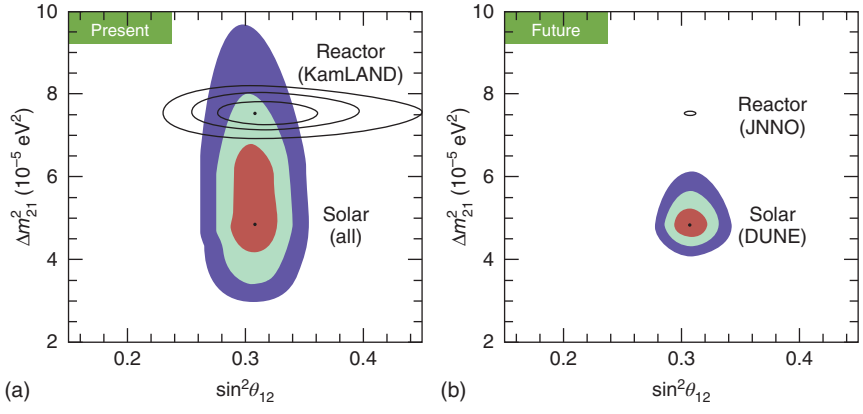

Figure 5.8 Present (a) and future (b) precision measurements of solar neutrino oscillation parameters including DUNE and JUNO [309]. Filled areas are at 1, 2, 3σ C.L. JUNO along contour are at 3σ. DUNE exposure is assumed equal to 100 kt $\times$ year. Source: Capozzi et al. 2018 [309]. Reproduced with permission of Elsevier.

As far as neutrino physics is concerned in this context, in Figure 5.8 from [309], we show the potentiality of DUNE with 100 kt $\times$ year exposure to probe the tension on Δm^2_{21} between solar neutrino global fit and KamLAND in the framework of neutrino oscillations and matter effects.

References

1 Böhm-Vitense, E. (1958). *Z. Astrophys.* 46: 108.
2 Kippenhahn, R., Weigert, A., and Weiss, A. (2012). *Stellar Structure and Evolution*, Astronomy and Astrophysics Library. Berlin Heidelberg: Springer-Verlag. ISBN: 978-3-642-30255-8.
3 Cox, J.P. and Giuli, R.T. (1968). *Principles of Stellar Structure*. New York: Gordon and Breach.
4 Althaus, L.G., Serenelli, A.M., Córsico, A.H., and Montgomery, M.H. (2003). *Astron. Astrophys.* 404: 593–609.
5 Maeder, A. (2009). *Physics, Formation and Evolution of Rotating Stars*, Astronomy and Astrophysics Library. Berlin Heidelberg: Springer. ISBN: 978-3-540-76948-4.
6 Perez Hernandez, F. and Christensen-Dalsgaard, J. (1994). *Mon. Not. R. Astron. Soc.* 269: 475–492.
7 Bahcall, J.N., Pinsonneault, M.H., and Wasserburg, G.J. (1995). *Rev. Mod. Phys.* 67: 781–808.
8 Christensen-Dalsgaard, J., Dappen, W., Ajukov, S.V. et al. (1996). *Science* 272: 1286–1292.
9 Michaud, G. (1977). *Highlights in Astronomy* vol. 4, 177–191.
10 Burgers, J.M. (1969). *Flow Equations for Composite Gases*. New York: Academic Press.
11 Thoul, A.A., Bahcall, J.N., and Loeb, A. (1994). *Astrophys. J.* 421: 828–842.
12 Paquette, C., Pelletier, C., Fontaine, G., and Michaud, G. (1986). *Astrophys. J. Suppl.* 61: 177–195.
13 Michaud, G., Alecian, G., and Richer, J. (2015). *Atomic Diffusion in Stars*, Astronomy and Astrophysics Library. Switzerland: Springer International Publishing. ISBN: 978-3-319-19853-8.
14 Mihalas, D. (1978). *Stellar Atmospheres*, 2e. San Francisco: W.H. Freeman.
15 Holweger, H. and Mueller, E.A. (1974). *Sol. Phys.* 39: 19–30.
16 Vernazza, J.E., Avrett, E.H., and Loeser, R. (1981). *Astrophys. J. Suppl.* 45: 635–725.
17 Magic, Z., Collet, R., Asplund, M. et al. (2013). *Astron. Astrophys.* 557: A26.
18 Trampedach, R., Stein, R.F., Christensen-Dalsgaard, J. et al. (2014). *Mon. Not. R. Astron. Soc.* 442: 805–820.
19 Ludwig, H.G., Caffau, E., Steffen, M. et al. (2009). *Mem. Soc. Astron. Ital.* 80: 711.

Solar Neutrino Physics: The Interplay between Particle Physics and Astronomy,
First Edition. Lothar Oberauer, Aldo Ianni, and Aldo Serenelli.

20 Jörgensen, A.C.S., Mosumgaard, J.R., Weiss, A. et al. (2018). *MNRAS* 481: L35–L39.
21 Rogers, F.J. and Nayfonov, A. (2002). *Astrophys. J.* 576: 1064–1074.
22 Däppen, W., Mihalas, D., Hummer, D.G., and Mihalas, B.W. (1988). *Astrophys. J.* 332: 261–270.
23 Trampedach, R., Däppen, W., and Baturin, V.A. (2006). *Astrophys. J.* 646: 560–578.
24 Cassisi, S., Salaris, M., and Irwin, A.W. (2003). *Astrophys. J.* 588: 862–870.
25 Weiss, A., Hillebrandt, W., Thomas, H.C., and Ritter, H. (2004). *Cox and Giuli's Principles of Stellar Structure*. Cambridge, UK: Cambridge Scientific Publishers Ltd.
26 Huebner, W.F. and Barfield, W.D. (2014). *Astrophysics and Space Science Library* 402. New York: Springer Science+Business Media. ISBN: 978-1-4614-8796-8.
27 Krief, M., Feigel, A., and Gazit, D. (2016). *Astrophys. J.* 821: 45.
28 Iglesias, C.A. and Rogers, F.J. (1996). *Astrophys. J.* 464: 943.
29 Badnell, N.R., Bautista, M.A., Butler, K. et al. (2005). *Mon. Not. R. Astron. Soc.* 360: 458–464.
30 Colgan, J., Kilcrease, D.P., Magee, N.H. et al. (2016). *Astrophys. J.* 817: 116.
31 Blancard, C., Cossé, P., and Faussurier, G. (2012). *Astrophys. J.* 745: 10.
32 Mondet, G., Blancard, C., Cossé, P., and Faussurier, G. (2015). *Astrophys. J. Suppl.* 220: 2.
33 Krief, M., Feigel, A., and Gazit, D. (2016). *Astrophys. J.* 824: 98.
34 Bailey, J.E., Nagayama, T., Loisel, G.P. et al. (2015). *Nature* 517: 56–59.
35 Nahar, S.N. (2018). *Astron. Soc. Pac. Conf. Ser.* 515: 93.
36 Gamow, G. (1928). *Z. Phys.* 51: 204–212.
37 Atkinson, R.D.E. and Houtermans, F.G. (1929). *Z. Phys.* 54: 656–665.
38 Bonetti, R., Broggini, C., Campajola, L. et al. (1999). *Phys. Rev. Lett.* 82: 5205–5208.
39 Iliadis, C. (2007). *Nuclear Physics of Stars*. Wiley-VCH.
40 Adelberger, E.G., García, A., Robertson, R.G.H. et al. (2011). *Rev. Mod. Phys.* 83: 195–246.
41 Marcucci, L.E., Schiavilla, R., and Viviani, M. (2013). *Phys. Rev. Lett.* 110 (19): 192503.
42 Zhang, X., Nollett, K.M., and Phillips, D.R. (2015). *Phys. Lett. B* 751: 535–540.
43 Marta, M., Formicola, A., Bemmerer, D. et al. (2011). *Phys. Rev. C* 83 (4): 045804.
44 Salpeter, E.E. (1954). *Aust. J. Phys.* 7: 373.
45 Gruzinov, A.V. and Bahcall, J.N. (1998). *Astrophys. J.* 504: 996–1001.
46 Amelin, Y. and Ireland, T.R. (2013). *Elements* 9: 39–44.
47 Nyquist, L.E., Kleine, T., Shih, C.Y., and Reese, Y.D. (2009). *Geochim. Cosmochim. Acta* 73: 5115–5136.
48 Wood, B.E. (2004). *Living Rev. Sol. Phys.* 1: 2.
49 Schou, J., Kosovichev, A.G., Goode, P.R., and Dziembowski, W.A. (1997). *Astrophys. J. Lett.* 489: L197.
50 Fröhlich, C. (2013). *Space Sci. Rev.* 176: 237–252.

51 Kopp, G. and Lean, J.L. (2011). *Geophys. Res. Lett.* 38: L01706.
52 Gustafsson, B., Edvardsson, B., Eriksson, K. et al. (2008). *Astron. Astrophys.* 486: 951–970.
53 Castelli, F., Gratton, R.G., and Kurucz, R.L. (1997). *Astron. Astrophys.* 318: 841–869.
54 Nordlund, A.A., Stein, R.F., and Asplund, M. (2009). *Living Rev. Sol. Phys.* 6: 2.
55 Asplund, M. (2005). *Annu. Rev. Astron. Astrophys.* 43: 481–530.
56 Bergemann, M., Kudritzki, R.-P., and Davies, B. (2014). *Determination of Atmospheric Parameters of B-, A-, F- and G-Type Stars*, GeoPlanet: Earth and Planetary Sciences (ed. E. Niemczura, B. Smalley, and W. Pych), 217–232. Springer International Publishing (Cham). ISBN: 978-3-319-06955-5.
57 Asplund, M., Grevesse, N., Sauval, A.J., and Scott, P. (2009). *Annu. Rev. Astron. Astrophys.* 47: 481–522.
58 Caffau, E., Ludwig, H.G., Steffen, M. et al. (2011). *Sol. Phys.* 268: 255–269.
59 Lodders, K., Palme, H., and Gail, H.P. (2009). *Landolt-Börnstein - Group VI Astronomy and Astrophysics* 4B. Berlin Heidelberg: Springer-Verlag. ISBN: 978-3-540-88054-7.
60 Basu, S. and Antia, H.M. (2004). *Astrophys. J. Lett.* 606: L85–L88.
61 Grevesse, N. and Sauval, A.J. (1998). *Space Sci. Rev.* 85: 161–174.
62 Boothroyd, A.I. and Sackmann, I.J. (1988). *Astrophys. J.* 328: 641.
63 Salaris, M. and Cassisi, S. (2005). *Evolution of Stars and Stellar Populations*. Wiley.
64 Magic, Z., Weiss, A., and Asplund, M. (2015). *Astron. Astrophys.* 573: A89.
65 Arnett, W.D., Meakin, C., Viallet, M. et al. (2015). *Astrophys. J.* 809: 30.
66 Vinyoles, N., Serenelli, A.M., Villante, F.L. et al. (2017). *Astrophys. J.* 835: 202.
67 Bergström, J., Gonzalez-Garcia, M.C., Maltoni, M. et al. (2016). *J. High Energy Phys.* 3: 132.
68 Bahcall, J.N. (2002). *Phys. Rev. C* 65 (2): 025801.
69 The Borexino Collaboration (2014). *Phys. Rev. D* 89 (11): 112007.
70 The Borexino Collaboration (2018). *Nature* 562 (7728): 505–510.
71 Bahcall, J.N. and Ulmer, A. (1996). *Phys. Rev. D* 53: 4202–4210.
72 Haxton, W.C. and Serenelli, A.M. (2008). *Astrophys. J.* 687: 678–691.
73 Serenelli, A., Pe na-Garay, C., and Haxton, W.C. (2013). *Phys. Rev. D* 87 (4): 043001.
74 Serenelli, A.M., Haxton, W.C., and Pe na-Garay, C. (2011). *Astrophys. J.* 743: 24.
75 Villante, F.L. (2015). *Phys. Lett. B* 742: 279–284.
76 Leighton, R.B., Noyes, R.W., and Simon, G.W. (1962). *Astrophys. J.* 135: 474.
77 Ulrich, R.K. (1970). *Astrophys. J.* 162: 993.
78 Leibacher, J.W. and Stein, R.F. (1971). *Astrophys. Lett.* 7: 191–192.
79 Deubner, F.L. (1975). *Astron. Astrophys.* 44: 371–375.
80 Rhodes, E.J. Jr., Ulrich, R.K., and Simon, G.W. (1977). *Astrophys. J.* 218: 901–919.

81 Aerts, C., Christensen-Dalsgaard, J., and Kurtz, D.W. (2010). *Asteroseismology*, Astronomy and Astrophysics Library. Springer Science+Business Media B.V. ISBN: 978-1-4020-5178-4.

82 Scherrer, P.H., Bogart, R.S., Bush, R.I. et al., MDI Engineering Team (1995). *Sol. Phys.* 162: 129–188.

83 Basu, S., Chaplin, W.J., Elsworth, Y. et al. (2009). *Astrophys. J.* 699: 1403–1417.

84 Broomhall, A.M., Chaplin, W.J., Davies, G.R. et al. (2009). *Mon. Not. R. Astron. Soc.* 396: L100–L104.

85 Christensen-Dalsgaard, J. (2002). *Rev. Mod. Phys.* 74: 1073–1129.

86 Haxton, W.C., Hamish Robertson, R.G., and Serenelli, A.M. (2013). *Annu. Rev. Astron. Astrophys.* 51: 21–61.

87 Basu, S. and Antia, H.M. (1997). *Mon. Not. R. Astron. Soc.* 287: 189–198.

88 Basu, S. and Antia, H.M. (2008). *Phys. Rep.* 457: 217–283.

89 Basu, S. (2016). *Living Rev. Sol. Phys.* 13: 2.

90 Vorontsov, S.V., Baturin, V.A., Ayukov, S.V., and Gryaznov, V.K. (2013). *Mon. Not. R. Astron. Soc.* 430: 1636–1652.

91 Bahcall, J.N., Serenelli, A.M., and Basu, S. (2005). *Astrophys. J. Lett.* 621: L85–L88.

92 Guzik, J.A., Watson, L.S., and Cox, A.N. (2005). *Astrophys. J.* 627: 1049–1056.

93 Delahaye, F. and Pinsonneault, M.H. (2006). *Astrophys. J.* 649: 529–540.

94 Castro, M., Vauclair, S., and Richard, O. (2007). *Astron. Astrophys.* 463: 755–758.

95 Christensen-Dalsgaard, J. (2009). The sun as a fundamental calibrator of stellar evolution. In: *The Ages of Stars*, IAU Symposium, vol. 258 (ed. E.E. Mamajek, D.R. Soderblom, and R.F.G. Wyse). Cambridge University Press, 431–442.

96 Villante, F.L. (2010). *Astrophys. J.* 724: 98–110.

97 Villante, F.L., Serenelli, A.M., Delahaye, F., and Pinsonneault, M.H. (2014). *Astrophys. J.* 787: 13.

98 Bahcall, J.N. (1989). *Neutrino Astrophysics*. Cambridge University Press.

99 Bahcall, J.N. and Ulrich, R.K. (1988). *Rev. Mod. Phys.* 60: 297–372.

100 Thompson, M.J., Christensen-Dalsgaard, J., Miesch, M.S., and Toomre, J. (2003). *Annu. Rev. Astron. Astrophys.* 41: 599–643.

101 Fossat, E., Boumier, P., Corbard, T. et al. (2017). *Astron. Astrophys.* 604: A40.

102 Pinsonneault, M.H., Kawaler, S.D., Sofia, S., and Demarque, P. (1989). *Astrophys. J.* 338: 424–452.

103 Palacios, A., Talon, S., Turck-Chièze, S., and Charbonnel, C. (2006). Dynamical processes in the solar radiative interior. In: *Proceedings of SOHO 18/GONG 2006/HELAS I, Beyond the spherical Sun* (ESA SP-624) (7-11 August 2006), Sheffield, UK: Editor: Karen Fletcher. Scientific Editor: Michael Thompson, Published on CDROM, id.38. ESA Special Publication, 624, 38.1.

104 Turck-Chièze, S., Palacios, A., Marques, J.P., and Nghiem, P.A.P. (2010). *Astrophys. J.* 715: 1539–1555.

105 Tassoul, J.L. (1978). *Theory of Rotating Stars*, Princeton Series in Astrophysics. Princeton: University Press.
106 Schlattl, H. and Weiss, A. (1999). *Astron. Astrophys.* 347: 272–276.
107 Andrássy, R. and Spruit, H.C. (2013). *Astron. Astrophys.* 559: A122.
108 Proffitt, C.R. and Michaud, G. (1991). *Astrophys. J.* 380: 238–250.
109 Rogers, T.M., MacGregor, K.B., and Glatzmaier, G.A. (2008). *Mon. Not. R. Astron. Soc.* 387: 616–630.
110 Brun, A.S., Miesch, M.S., and Toomre, J. (2011). *Astrophys. J.* 742: 79.
111 Alvan, L., Brun, A.S., and Mathis, S. (2014). *Astron. Astrophys.* 565: A42.
112 Press, W.H. and Spergel, D.N. (1985). *Astrophys. J.* 296: 679–684.
113 Faulkner, J. and Gilliland, R.L. (1985). *Astrophys. J.* 299: 994–1000.
114 Gilliland, R.L., Faulkner, J., Press, W.H., and Spergel, D.N. (1986). *Astrophys. J.* 306: 703–709.
115 Griest, K. and Seckel, D. (1987). *Nucl. Phys. B* 283: 681–705.
116 Taoso, M., Iocco, F., Meynet, G. et al. (2010). *Phys. Rev. D* 82 (8): 083509.
117 Cumberbatch, D.T., Guzik, J.A., Silk, J. et al. (2010). *Phys. Rev. D* 82 (10): 103503.
118 Vincent, A.C., Serenelli, A., and Scott, P. (2015). *J. Cosmol. Astropart. Phys.* 8: 040.
119 Peccei, R.D. and Quinn, H.R. (1977). *Phys. Rev. Lett.* 38: 1440–1443.
120 Schlattl, H., Weiss, A., and Raffelt, G. (1999). *Astropart. Phys.* 10: 353–359.
121 Vinyoles, N., Serenelli, A., Villante, F.L. et al. (2015). *J. Cosmol. Astropart. Phys.* 10: 015.
122 Vinyoles, N. and Vogel, H. (2016). *J. Cosmol. Astropart. Phys.* 3: 002.
123 Schael, S. et al., ALEPH, DELPHI, L3, OPAL, SLD Collaboration (2006). *Phys. Rep.* 427: 257.
124 Cowan, C., Reines, F. et al. (1956). *Science* 124: 103.
125 Pauli, W. (1994). *Writing on Physics and Philosophy*. Berlin: Springer-Verlag.
126 Reines, F. (1997). *Nobel Lectures, Physics 1991–1995* (ed. G. Ekspong). Singapore: World Scientific Publishing Co.
127 Fermi, E. (1934). *Z. Phys.* 88: 161.
128 Fukuda, Y. et al., SuperKamiokande Collaboration. (1998). *Phys. Rev. Lett.* 8: 1562.
129 Pontecorvo, B. (1958). *Sov. Phys. JETP* 7: 172.
130 Cleveland, B.T. et al. (1998). *Astrophys. J.* 496: 505.
131 Zralek, M. (1998). *Acta Phys. Polon.* B29: 3925. arXiv:9810543.
132 Kayser, B. and Kopp, J. (2010). FERMILAB-PUB-10-168-T, arXiv:1005.4081 (Hep-ph).
133 Suekane, F. (2015). *Neutrino Oscillations*, Lecture Notes in Physics, vol. 898. Springer,
134 Wolfenstein, L. (1981). *Phys. Rev. D* 17: 2369.
135 Mikheyev, S.P. and Smirnov, A.Y. (1985). *Sov. J. Nucl. Phys.* 42: 1441.
136 Mikheyev, S.P. and Smirnov, A.Y. (1986). *Nuovo Cim. C* 9: 17.
137 Rosen, S.P. and Gelb, J.M. (1986). *Phys. Rev. D* 34: 969.
138 Bouchez, J. et al. (1986). *Z. Phys. C* 32: 499.
139 Parke, S.J. and Walker, T.P. (1986). *Phys. Rev. Lett.* 57: 2322.
140 Haxton, X.H. (1987). *Phys. Rev. D* 35: 2353.

141 Barger, V. et al. (1991). *Phys. Rev. D* 44: 1629.
142 de Hollanda, P.C. and Smirnov, A.Y. (2011). *Phys. Rev. D* 83: 113011.
143 Kajita, T. (2010). *Proc. Jpn. Acad. B Phys. Biol. Sci* 86: 303.
144 Honda, M. et al. (2004). *Phys. Rev. D* 70: 043008.
145 Barr, G.D. et al. (2004). *Phys. Rev. D* 70: 023006.
146 Battistoni, G. et al. (2003). *Astropart. Phys.* 19: 269.
147 Ashie, Y. et al., SuperKamiokande Collaboration (2005). *Phys. Rev. D* 71: 112005.
148 Haines, T.J. et al., IMB Collaboration (1986). *Phys. Rev. Lett.* 57: 1986.
149 Hirata, K.S. et al., Kamiokande Collaboration (1988). *Phys. Lett. B* 205: 416.
150 Daum, K. et al., Frejus Collaboration (1995). *Z. Phys. C* 66: 417.
151 Aglietta, M. et al., NUSEX Collaboration (1991). *Europhys. Lett.* 8: 15.
152 Fukuda, Y. et al., SuperKamiokande Collaboration (1998). *Phys. Rev. Lett.* 81: 1562.
153 Ashie, Y. et al., SuperKamiokande Collaboration (2004). *Phys. Rev. Lett.* 93: 101801.
154 Abe, S. et al., SuperKamiokande Collaboration (2018). *Phys. Rev. D* 97: 072001.
155 Abe, K. et al., SuperKamiokande Collaboration (2013). *Phys. Rev. Lett.* 110: 181802.
156 Aartsen, M.G. et al., IceCube Collaboration (2013). *Phys Rev. Lett.* 111: 081801.
157 Ahn, M.H. et al., K2K Collaboration (2006). *Phys. Rev. D* 74: 072003.
158 Michael, D.G. et al., MINOS Collaboration (2006). *Phys. Rev. Lett.* 97: 191801.
159 Adamson, P. et al., MINOS Collaboration (2013). *Phys. Rev. Lett.* 97: 191801.
160 Agafonova, N. et al., OPERA Collaboration (2018). *Phys. Rev. Lett.* 120 (21): 211801 and (2018). *Phys. Rev. Lett.* 121 (13): 139901.
161 Abe, K. et al., T2K Collabortaion (2014). *Phys. Rev. D* 89: 092003.
162 Abe, K. et al., T2K Collabortaion (2013). *Phys. Rev. Lett.* 111: 211803.
163 Abe, K. et al., T2K Collaboration (2014). *Phys. Rev. Lett.* 112: 061802.
164 Sanchez, M. and NOVA Collaboration (2015). Talk at the XVII International Workshop on Neutrino Factories and Future Neutrino Facilities, Rio de Janeiro, Brazil (10–15 August 2015).
165 Mueller, T. et al. (2011). *Phys. Rev. C* 83: 054615.
166 Schreckenbach, K. et al. (1981). *Phys. Lett. B* 99: 251.
167 von Feilitzsch, F. et al. (1982). *Phys. Lett. B* 118: 162.
168 Schreckenbach, K. et al. (1985). *Phys. Lett. B* 160: 325.
169 Hahn, A.A. et al. (1989). *Phys. Lett. B* 218: 365.
170 Haag, N. et al. (2014). *Phys. Rev. Lett.* 112: 122501.
171 Mueller, Th. et al. (2011). *Phys. Rev. C* 83: 054615.
172 Abe, S. et al., KamLAND Collabortion (2008). *Phys. Rev. Lett.* 100: 221803.
173 Gando, A. et al., KamLAND Collaboration (2013). *Phys. Rev.* D88 (3): 033001.
174 Capozzi, F., Lisi, E., Marrone, A., and Palazzo, A. (2018). *Prog. Part. Nucl. Phys.* 102: 48–72.

175 Sekeia, H. (2018). Updates on Super-Kamiokande, NDM2018, Daejeon, South Korea, July 3rd.
176 Apollonio, M. et al., Chooz collaboration (1999). *Phys. Lett. B* 466: 415.
177 Abe, Y. et al., Double Chooz Collaboration (2012). *Phys. Rev. Lett.* 108: 131801.
178 An, F.P. et al., Daya-Bay Collaboration (2012). *Phys. Rev. Lett.* 108: 171803.
179 Ahn, J.K. et al., RENO Collaboration (2012). *Phys. Rev. Lett.* 108: 191802.
180 An, F.P. et al., Daya-Bay Collaboration (2016). *Phys. Rev. Lett.* 116: 061801. arxiv:1508.04233.
181 Abe, Y. et al., Double Chooz Collaboration (2014). *JHEP* 10: 086.
182 Seo, S.H. et al., RENO Collaboration (2014). Neutrino 2014, XXVI International Conference on Neutrino Physics and Astrophysics, Boston, MA, USA (2–7 June 2014).
183 Capozzi, F. et al. (2014). *Phys. Rev. D* 89 (9): 093018. arXiv:1312.2878.
184 Forero, D.V., Tortola, M., and Valle, J.W.F. (2014). *Phys. Rev. D* 90 (9): 093006. arXiv:1405.7540.
185 Gonzalez-Garcia, M.C., Maltoni, M., and Schwetz, T. (2014). *JHEP* 1411: 052. arXiv:1409.5439.
186 Lobashev, V.M. (2003). *Nucl. Phys. A* 719: 153.
187 Kraus, Ch. et al. (2005). *Eur. Phys. J. C* 40: 447.
188 Picard, A. et al. (1992). *Nucl. Instrum. Methods* 63: 345.
189 Weinheimer, C. (2002). Proceedings of CLII, Course of International School of Physics "Enrico Fermi", Varenna (Italy). arxiv:hep-ex/0210050v2.
190 Osipowicz, A. et al., KATRIN Collaboration. arxiv:hep-ex/0109033.
191 Monreal, B. and Formaggio, J.A. (2009). *Phys. Rev. D* 80: 051301. arXiv:0904.2860.
192 Blaum, K. et al. (2013). Proceedings for the NuMass 2013 Workshop, Milano, Italy (4–7 February 2013). arXiv:1306.2655.
193 Giachero, A. et al., HOLMES Collaboration (2017). *JINST* 12 (02): C02046.
194 Monfardini, A. et al. (2006). *Nucl. Instrum. Methods A* 559: 346. arXiv:hep-ex/0509038.
195 Hirata, K. et al., Kamiokande Collaboration (1987). *Phys. Rev. Lett.* 58: 1490.
196 Bionta, R.M. et al., IMB Collaboration (1987). *Phys. Rev. Lett.* 58: 1494.
197 Alekseev, E.N. et al. (1988). *Phys. Lett. B* 205: 209.
198 Stodolsky, L. (1988). *Phys. Lett. B* 201: 353.
199 von Feilitzsch, F. and Oberauer, L. (1988). *Phys. Lett. B* 200: 580.
200 Raffelt, G. (1999). *Phys. Rep.* 320: 319.
201 Lesgourgues, J. and Pastor, S. (2014). *New J. Phys.* 16: 065002. arXiv:1404.1740.
202 Mangano, G. and Serpico, P.D. (2011). *Phys. Lett. B* 701: 296.
203 Said, N., Di Valentino, E., and Gerbino, M. (2013). *Phys. Rev. D* 88: 023513.
204 Ade, P.A.R. et al., Planck Collaboration (2014). *Astron. Astrophys.* 571: A16. arXiv:1303.5076.
205 Lee, B. and Weinberg, S. (1977). *Phys. Rev. Lett.* 39: 165.
206 Mertens, S. and KATRIN Collaboration (2015). *Phys. Proc.* 61: 267.
207 Schechter, J. and Valle, J. (1982). *Phys. Rev. D* 25: 2951.
208 Bilenky, S. and Giunti, C. (2015). *J. Mod. Phys. A* 30: 1530001.

209 Weinberg, S. (1979). *Phys. Rev. Lett.* 43: 1566.
210 Bari, P.D. (2012). *Contemp. Phys.* 53: 4.
211 Fong, C.S., Nardi, E., and Riotto, A. (2012). *Adv. High Energy Phys.* 2012: 158303.
212 Päs, H. and Rodejohann, W. (2015). Proceedings for the 'NJP focus issue on Neutrino Physics'. arxiv:1507.00170.
213 Agostini, M. et al., GERDA Collaboration (2013). *Phys. Rev. Lett.* 111: 122503. arXiv:1307.4720.
214 Klapdor-Kleingrothaus, H.V. et al. (2004). *Phys. Lett. B* 586: 198.
215 Agostini, M. et al., GERDA Collaboration (2018). *Phys. Rev. Lett.* 120: 132503.
215a Agostini, M. et al., GERDA collaboration (2017). *Nature*, 544, 7648: 5–132.
216 Klapdor-Kleingrothaus, H.V. et al., Heidelberg-Moscow Collaboration (2001). *Eur. Phys. J. A* 12: 147.
217 Aalseth, C.E. et al., IGEX Collaboration (2002). *Phys. Rev. D* 65: 092007. arXiv:0202.026.
217a Aalseth, C. et al., Majorana collaboration (2017). *Phys. Rev. Lett.* arXiv: 1710.11608.
217b Agostini, M. et al., Gerda collaboration (2017). *Nature* 544: 47.
218 Albert, J. et al., EXO Collaboration (2014). *Nature* 510: 229. arXiv:1402.6956.
219 Gando, A. et al., KamLAND-Zen Collaboration (2013). *Phys. Rev. Lett.* 110: 062502. arXiv:1211.3863.
220 Gando, A. et al., KamLAND-Zen Collaboration (2016). *Phys. Rev. Lett.* 117: 082503.
221 Andreotti, E. et al., CUORICINO Collaboration (2011). *Astropart. Phys.* 34: 822. arXiv:1012.3266.
222 Alduino, C. et al., CUORE Collaboration (2018). *Phys. Rev. Lett.* 120: 132501. arXiv:1710.07988.
223 Arnold, R. et al., NEMO Collaboration (2014). *Phys. Rev. D* 89: 111101. arXiv:1311.5695.
224 Aartsen, M. et al., PINGU Collaboration (2014). Instrumentation and Detectors (physics.ins-det). arXiv:1401.2046.
225 Qian, X. and Vogel, P. (2015). *PPNP* 83: 1. arXiv:1505.01891.
226 An, F. et al., JUNO Collaboration (2016). *J. Phys. G* 43: 030401. arXiv:1507.05613.
227 Kim, S.B. (2014). High Energy Physics - Experiment (hep-ex). arXiv:1412.2199.
228 Agarwalla, S.K. et al. (2014). *JHEP* 1405: 094. arXiv:1312.6520.
229 Adams, C. et al., LBNE Collaboration (2013). arXiv:1307.7335.
230 Abe, K. et al., HyperKamiokande Collaboration (2015). *Prog. Theor. Exp. Phys.* arXiv:1502.05199.
231 Bulbul, E. et al. (2014). *Astrophys. J.* 789: 13. arXiv:1402.2301.
232 Ishida, H., Sik Jeong, K., and Takahashi, F. (2014). *Phys. Lett. B* 732: 196. arXiv:1402.5837.
233 Mertens, S. et al. (2015). *J. Cosmol. Astropart. Phys.* 2015: 20. arXiv:1409.0920.

234 Mention, G. et al. (2011). *Phys. Rev. D* 83: 073006. arXiv:1101.2755.
235 Giunti, C. and Laveder, M. (2011). *Phys. Rev. D* 82: 053005.
236 Gando, A. et al. (2013). Proceedings for the 'Snowmass 2013' Conference, Colorado (USA). arXiv:1309.6805.
237 Ianni, A. (2017). *Prog. Part. Nucl. Phys.* 94: 257–281.
237a Gavrin, V.N. (2011). Proceedings of the International Conference "New Trends on High Energy Physics". Alushta, Crimea, Ukraine, September 3–10, pp. 58–66.
237b Gando, A. et al., KamLAND collaboration (2015). *Phys. Rev.* C92, 5, 055808.
238 Baudis, L. (2014). Proceedings of the 13th International Conference on Topics in Astroparticle and Underground Physics, TAUP 2013 Journal-ref: Physics of the Dark Universe, vol. 4, 50–59.
239 Davis, R.J. (1964). *Phys. Rev. Lett.* 12: 303–305.
240 Davis, R.J., Harmer, D.S., and Hoffman, K.C. (1968). *Phys. Rev. Lett.* 20: 1205–1209.
241 Bruce, T.C. et al. (Homestake) (1998). *Astrophys. J.* 496: 505–526.
242 Pontecorvo, B. (1946). Chalk River Report, PD-205.
243 Alvarez, L.W. (1949). University of California Radiation Laboratory Report, UCRL-328.
244 Sanford Underground Research Facility. https://sanfordlab.org.
245 Fukugita, M. and Yanagita, T. (2003). *Physics of Neutrinos and Applications to Astrophysics*. Springer-Verlag.
246 Alvarez, L.W. (1973). Physics Notes, Memo No. 767, Lawrence Radiation Laboratory (23 March 1973).
247 Hirata, K.S. et al. (1988). *Phys. Rev. D* 38: 448–458.
248 Bahcall, J.N., Kamionkowski, M., and Sirlin, A. (1995). *Phys. Rev. D* 51: 6146–6158.
249 Cherenkov, P.A. (1967). *Usp. Fiz. Nauk* 93: 385.
250 Hirata, K.S. et al. (1989). *Phys. Rev. Lett.* 63: 16–19.
251 Fukuda, Y. et al., Kamiokande Collaboration (1996). *Phys. Rev. Lett.* 77: 1683–1686.
252 Hirata, K.S. et al., Kamiokande Collaboration (1991). *Phys. Rev. Lett.* 66: 9–12.
253 Anselmann, P. et al. (1992). *Phys. Lett. B* 285: 376.
254 (a) Hampel, W. et al. (1999). *Phys. Lett. B* 447: 127; (a) Altmann, M. et al. (2005). *Phys. Lett. B* 616: 174.
255 Abazov, A.I. et al., SAGE Collaboration (1991). *Phys. Rev. Lett.* 67: 3332–3335.
256 Kuzmin, V.A. (1966). *Sov. Phys. - JEPT* 22: 1050.
257 Bahcall, J.N., Cleveland, B.T., Davis, R., and Rowley, J.K. (1985). *Astrophys. J. Lett.* 292: L79.
258 Stolarczyk, T. (1990). PhD thesis. Université de Paris-Sud.
259 Anselman, P. et al., GALLEX collaboration (1995). *Phys. Lett. B* 342: 440–450.
260 Cleveland, B. (1983). *Nucl. Instrum. Methods* 214: 451.
261 Altmann, M. et al., GNO Collaboration (2000). *Phys. Lett. B* 490: 16–26.

262 Altmann, M. et al., GNO Collaboration (2005). *Phys. Lett. B* 616: 174–190.
263 Kaether, F., Hampel, W., Heusser, G. et al. (2010). *Phys. Lett. B* 685: 47–54.
264 Hampel, W. et al., GALLEX Collaboration (1998). *Phys. Lett. B* 420: 114.
265 Bahcall, J.N. (1997). *Phys. Rev. C* 56: 3391.
266 Bahcall, J.N. (1997). *Phys. Rev. C* 56: 3391.
266a Kuzminov, V.V. (2012). *Eur. Phys. J. Plus* 127: 113.
267 Abdurashitov, J.N. et al., SAGE Collaboration (2009). *Phys. Rev. C* 80: 015807.
268 (a) Bahcall, J.N. et al. (1978). *Phys. Rev. Lett.* 40: 1351; (b) Barabanov, I.R. et al. (1984). *Proceedings of the Conference on Solar Neutrinos and Neutrino Astronomy, Homestake*, AIP Conference Proceedings No. 126 (ed. M.L. Cherry, K. Lande, and W.A. Fowler), 175. New York: AIP, 1985).
269 Abdurashitov, J.N. et al., SAGE collaboration (1999). *Phys. Rev. C* 59: 2246–2263.
270 Abdurashitov, J.N. et al., SAGE Collaboration (2006). *Phys. Rev. C* 73: 045805.
271 Haxton, W.C. (1988). *Phys. Rev. C* 38: 2474–2477.
272 Gavrin, V.N. et al. (1992). Institute for Nuclear Research of the Russian Academy of Sciences Report No. P-777.
273 Fukuda, Y. et al., Super-Kamiokande Collaboration (1998). *Phys. Rev. Lett.* 81: 1158–1162.
274 Cravens, J.P. et al., Super-Kamiokande Collaboration (2008). *Phys. Rev. D* 78: 032002.
275 Fukuda, Y. et al., Super-Kamiokande Collaboration (1998). *Phys. Lett. B* 433: 9–18.
276 Abe, K. et al., Super-Kamiokande Collaboration (2011). *Phys. Rev. D* 83: 052010.
277 Abe, K. et al., Super-Kamiokande Collaboration (2016). *Phys. Rev. D* 94 (5): 052010. arXiv:1606.07538.
278 Beacom, J. and Vagins, M. (2004). *Phys. Rev. Lett.* 93: 171101.
279 Dziewonski, A.M. and Anderson, D.L. (1981). *Phys. Earth Planet. Inter.* 25: 297.
280 The SNO Collaboration (2000). *Nucl. Instrum. Methods A* 449: 172.
281 Chen, H.H. (1985). *Phys. Rev. Lett.* 55: 1534–1536.
282 Moffat, B.A. (2001). The optical calibration of the sudbury neutrino observatory. PhD thesis. Queen's University.
283 Ahrmim, B. et al., The SNO Collaboration (2013). *Phys. Rev. C* 87: 015502.
284 Ahrmim, B. et al., The SNO Collaboration (2007). *Phys. Rev. C* 75: 045502.
285 Ahmad, Q.R. et al., The SNO Collaboration (2001). *Phys. Rev. Lett.* 87: 071301.
286 Ahmad, Q.R. et al., The SNO Collaboration (2002). *Phys. Rev. Lett.* 89 (1): 011301.
287 Ahrmim, B. et al., The SNO Collaboration (2013). *Phys. Rev. C* 88: 025501.
288 Ahrmim, B. et al., The SNO Collaboration (2005). *Phys. Rev. C* 72: 055502.
289 Alimonti, G. et al., The Borexino Collaboration (2002). *Astropart. Phys.* 16: 205–234.
290 Bellini, G., Raghavan, R. (eds.), and Borexino Collaboration (1991). *Borexino at Gran Sasso - Proposal for a Real Time Detector for Low Energy Solar Neutrinos*. http://borex.lngs.infn.it/papers/.

291 Raghavan, R.S., Pakvasa, S., and Brown, B.A. (1986). *Phys. Rev. Lett.* 57: 1801–1804.

292 Alimonti, G. et al., The Borexino Collaboration (1998). *Astropart. Phys.* 8: 141–157.

293 Alimonti, G. et al., The Borexino Collaboration (1998). *Phys. Lett. B* 422: 349–358.

294 Back, H.O. et al., Borexino Collaboration (2008). *Nucl. Instrum. Methods A* 585: 48–60.

295 Alimonti, G. et al., The Borexino Collaboration (2009). *Nucl. Instrum. Methods A* 600: 568–593.

296 Benziger, J. et al. (2008). *Nucl. Instrum. Methods A* 587: 277–291.

297 Bellini, G. et al., The Borexino Collaboration (2014). *Phys. Rev. D* 89 (11): 112007.

298 Birks, J.B. (1964). *The Theory and Practice of Scintillation Counting*. New York: Macmillan.

299 Arpesella, C. et al., The Borexino Collaboration (2008). *Phys. Lett. B* 658: 101–108.

300 Arpesella, C. et al., The Borexino Collaboration (2008). *Phys. Rev. Lett.* 101: 091302.

301 Bellini, G. et al., The Borexino Collaboration (2011). *Phys. Rev. Lett.* 107: 141302.

302 Bellini, G. et al., The Borexino Collaboration (2012). *Phys. Lett. B* 707: 22.

303 Bellini, G. et al., The Borexino Collaboration (2014). *Nature* 512 (7515): 383–386.

304 Galbiati, C. et al. (2005). *Phys. Rev. C* 71: 055805.

305 Bellini, G. et al., The Borexino Collaboration (2012). *Phys. Rev. Lett.* 108: 051302.

306 Bellini, G. et al., The Borexino Collaboration (2010). *Phys. Rev. D* 82: 033006.

307 The Borexino Collaboration (2017). *Astropart. Phys.* 92: 21–29.

308 Villante, F.L. et al. (2011). *Phys. Lett. B* 701: 336–341.

309 Capozzi, F. et al. (2018). *Prog. Part. Nucl. Phys.* 102: 48–72.

310 Palazzo, A. (2011). *Phys. Rev. D* 83: 101701.

311 (a) Bellini, G. et al. (2012). *Phys. Rev. Lett.* 108: 051302. arXiv:1110.3230; (b) Agostini, M. et al. (2018). *Nature* 562 (7728): 505–510.

312 Kraus, C. et al., SNO+ Collaboration (2010). *Prog. Part. Nucl. Phys.* 64: 273.

313 de Hollanda, P. and Smirnov, A.Y. (2011). *Phys. Rev. D* 83: 113011. arXiv:1012.5627.

314 Friedland, A. et al. (2004). *Phys. Lett. B* 594: 347. arXiv:hep-ph/0402266.

315 Arafune, J. et al. (1989). *Phys. Lett. B* 217: 186.

316 Ianni, A., Montanino, D., and Villante, F.L. (2005). *Phys. Lett. B* 627: 38. arXiv:0506171.

317 Wurm, M. et al., LENA Collaboration (2012). *Astropart. Phys.* 35: 685. arXiv:1104.5620.

318 Möllenberg, R. et al. (2014). *Phys. Lett. B* 737: 251. arXiv:1408.0623.

319 Wurm, M. et al. (2011). *Phys. Rev. D* 83: 032010. arXiv:1012.3021.

320 Burgess, C. et al. (2003). *Astrophys. J.* 588: L65. arXiv:hep-ph/0209094.

321 Yeh, M. et al. (2011). *Nucl. Instrum. Methods A* 660: 51.

322 Alonso, J.R. et al. (2014). BNL-106082-2014-JA. e-Print: arXiv:1409.5864.

323 Abe, K. et al., Hyper-Kamiokande Collaboration. arXiv:1805.04163.
324 Abi, B. et al., DUNE Collaboration. FERMILAB-DESIGN-2018-04. e-Print: arXiv:1807.10334.

Index

a

absolute charged-current (cc) 122, 169, 172–177, 179, 201, 204, 206
absolute neutral-current (nc) 169, 172–177, 179, 201
absolute neutrino mass scale 111–120
accelerator based neutrino experiments 131
accelerator experiments 79, 94, 96, 109–110
acrylic vessel (AV) 170–174
AGSS09 composition 34, 45, 57
Alven-waves 203
ancillary helium gas purging system 142
^{37}Ar counting 144
arbitrary hadronic final state 86
argon extraction efficiency 144
astrophysical factors 27, 30, 58–59
asymmetric dark matter massive particles (ADM) 66
atmospheric neutrinos 1, 74, 84–94, 105, 109–110, 128–129, 153, 164, 169, 175
atomic diffusion 12–15
attenuation length of light 147
Auger electrons 115, 144–145, 155
Avogadro number 82
axion-like particles (ALPs) 66–67
axions 66–67

b

^{8}B solar neutrino flux 45, 46, 149, 151, 164, 199
^{8}B solar neutrinos 146, 149–151, 156, 164, 172, 174, 177, 179, 189, 191, 199
B16-AGSS09 model 52, 55–56
B16-GS98 52, 55–56
B16 SSMs 45, 54–55, 59
baryon number 15–16
baryonic acoustic oscillations (BAO) 119
baryons 15–16, 65–66, 69, 117–119, 121
^{7}Be solar neutrinos 43, 45, 46, 139, 179, 184–185, 187, 189–190, 198, 201
BEGe detectors 124
Bing Bang nucleosynthesis (BBN) 118
Birmingham Solar Oscillations Network (BiSON) 48–49
Boltzmann–Saha equations 19
Borex program 179
Borexino 2, 45, 109–110, 139, 162, 178–192, 195–202
Borexino fluid handling system 181
Borexino rates 189
Borexino scintillator 184, 197
bound-bound (bb) transitions 21, 24
bound-free (bf) transitions 23–24

c

Cabibbo angle 102
calibrating standard solar models
  free parameters 35–36
  solar age 31
  solar luminosity 32
  solar mass 31
  solar radius 32
  surface composition 32–35

Solar Neutrino Physics: The Interplay between Particle Physics and Astronomy,
First Edition. Lothar Oberauer, Aldo Ianni, and Aldo Serenelli.

γ-catcher 106–107
CERN Neutrino Platform 133
charge leptons 86
charged current weak interaction 72, 201
charged muons 79, 85, 102
chemical composition, changes in
  atomic diffusion 12–15
  convective mixing 11–12
  macroscopic and microscopic mixing processes 16
  nuclear reactions 15–16
constitutive physics
  equation of state (EoS) 18–21
  nuclear reaction rates 25–31
  radiative opacity 21–25
Cherenkov muon veto 182
Cherenkov radiation 146, 171
CI-chondrites 34
^{37}Cl experiment 140–145, 153
CNO-bicycle 25–26, 29–31, 37–39, 42–44, 46–47, 62, 67
CNO-neutrino detection 196, 199
cold dark matter 66, 117–118, 120
conduction 5–7, 21
conservation of momentum in spherical symmetry 4
constitutive physics 18–31, 61–62
contributing isotopes 101
convection 5, 7, 9–12, 16, 18, 20, 23, 32–33, 35, 38, 41–42, 62, 65, 165, 183, 190
convective diffusion coefficient 12
convective mixing 11–12, 36
core mass-luminosity 39
cosmic microwave background (CMB) 117–119, 135
cosmic muon flux 197
cosmic muons 86, 99, 104, 107, 114, 124, 147, 197, 199
cosmic-ray muons 149, 154, 159, 165
cosmology 117, 123, 135
Cowling 49
CUORE experiment crystals 124

d

Daya-Bay experiment 105–110, 137
β decay emitter 147
β decay nuclei 148
Deep Underground Neutrino Experiment (DUNE) 2, 97, 132–135, 206–207
DeepCore detector 92
detection threshold 145–146, 149, 163, 165, 172–174, 178, 188, 204, 206
differential solar neutrino flux 146
diffusion approximation 6, 17
diffusion coefficient 12, 14, 64
dimethylphthalate (DMP) 182–183
Dirac and Majorana neutrinos 2, 119
Dirac particles 120–127
dominant cosmogenic long-lived isotopes 201
Double Chooz 105–107, 110
double β decaying nuclei 72, 120–123, 127
dynamical instability, criterion for 7–9

e

Eddington atmosphere 18
effective oscillation length 81
elastic neutrino electron scattering experiments 74, 199, 200
elastic scattering (ES) interaction 145–146, 169, 177, 199–201, 204, 206
electromagnetic coupling constant 74, 119
electron anti-neutrino survival probability 103
electron number density 14
electron recoil spectrum 185
electron scattering 23–24, 74, 200–201, 203
electron-antineutrinos 100, 103–104, 145
electrostatic filter potential 112
element abundances 32, 34, 62
energy conservation and transport
  convection 9–11
  criterion for dynamical instability 7–9

by radiation and conduction 5–7
equation of state (EoS) 8–9, 11–12, 18–21, 37, 53, 60
extended maximum likelihood fit 167

f

fast coincidence Bi-Po decays 187
fast neutron breeder reactor BN-600 161
Fermi constant 73–74, 81, 111, 119
Fermi matrix elements 141
Fermi's golden rule 111
fermions 69, 71, 73, 198
fiducial volume 87–88, 91, 148–151, 162–163, 165–166, 173–174, 185–188, 190, 195, 198–200, 203
flavor changing neutral currents (FCNC) 84
forward scattering amplitude 80
free parameters 10, 35–36, 42, 54, 64, 76, 91, 119, 160, 167, 178
free-free (ff) transitions 23–24
Friedman–Robertson–Walker metric 117

g

Ga-based experiments 153
GALLEX detector monitored solar neutrinos 155, 158
Gallium Neutrino Observatory (GNO) 155–157, 161
Gamow peak 27–29
Gamow–Teller matrix elements 141, 153
Gd-loaded liquid scintillators 106
Gd-loaded scintillator 107
Ge-semiconductor detectors 124
general Lagrange-density-function 73
GERDA experiment Ge-detectors 124–125
Glashow–Salam–Weinberg theory 74
global structure inversions 51–53
global uncertainties in SSMs 60–62
gravothermal energy 5, 37, 40–41
GS98 composition 34, 57
1-GW reactor 100

h

Hamiltonian H^{α} 81
helioseismic techniques 9, 34, 51
helioseismology 1
  global structure inversions 51–53
  other constraints 53–54
  overview 4
Hertzsrpung–Russell diagram (HRD) 36
high efficient muon tracking algorithm 201
high energy electron-neutrinos 83
high-resolution β-spectrometer 112
Homestake experiment 75, 140–143, 145, 149
Homestake solar neutrino experiment 1
Hubble parameter 119
Hubble Space Telescope (HST) 119
Hyper-Kamiokande 2, 134, 204–206

i

IceCube 92, 128–129
imaging water Cherenkov experiment 140, 162
inductively-coupled plasma mass spectrometer (ICP-MS) 159
inverse β decay 70, 101–102, 115
inverse bremsstrahlung 23
inverted ordering (IO) 110–111, 123
isospin groups 70
isotopic purity 144

j

Jiangmen Underground Neutrino Observatory (JUNO) project 2, 130, 199–204, 207

k

Kaija, Takaaki 75
Kajita, Takaaki 1, 85, 88, 89, 92, 169
Kamiokande 2, 88, 90, 110, 115, 145–146, 151–153, 162–164, 169
Kamiokande-II experiments 139, 145–153, 164

Kamiokande-III 145–153, 164
KamLAND detector 104
kaons 85
KATRIN collaboration 114
Kramers' law 23

l

Laboratory of Underground Nuclear Astrophysics (LUNA) experiment 28
Large Apparatus for Grand Unification and Neutrino Astrophysics and Long Baseline Neutrino neutrino Oscillations (LAGUNA-LBNO) 131–132
Large Area Picosecond Photo-Detectors (LAPPDs) 204
large electron positron (LEP) collider 69
large mixing angle 104, 109
large water Cherenkov detector 86
Ledoux criterion 9
Lee–Weinberg limit 119
left-handed leptons 70–73
leptogenesis mechanism 121
lepton number 72, 75, 120–122
leptons 69–73, 75–76, 79, 86–88, 91, 94, 96, 102, 110, 119–122, 127
τ-leptons 102
light collection efficiency 185
linear accelerator (LINAC) 163, 165
liquid argon TPCs 132–133
liquid scintillator 186
liquid scintillator detector 44, 99, 101, 103, 106, 124, 130–132, 140, 142, 178–181, 183–184, 186, 188–190, 195–197, 199, 201, 203–204
local thermodynamic equilibrium (LTE) 6–7, 33, 56
long baseline experiment 94, 97–100, 105, 131
low energy (LE) threshold 165, 199
Low Energy Neutrino Astrophysics (LENA) 2, 132, 199–204

m

magnetic-adiabatic collimation electrostatic (MAC-E) filter 112–113
Majorana neutrinos 2, 121–123, 126
Majorana-particles 76, 120–122, 127
MARE collaboration 115
matter effects 2, 43, 66, 69, 80–95, 98, 109, 127–129, 131–132, 134, 169, 178, 202–203, 207
McDonald, Arthur 1, 75, 178
measured solar neutrino flux 1, 167
mechanical structure of stars 3
mesons 1, 69, 85–87, 92, 94
meteoritic abundances 34
5.7 MeV total recoil electron energy 162
6.5 MeV total electron recoil energy 162
Michelson Doppler Imager (MDI) 48–49
microscopic diffusion 14–16, 38–39, 59, 61
mixing length theory (MLT) 10–12, 32, 42
mono-energetic 7Be solar neutrino line 185
mono-energetic pep-neutrino measurement 83
Mton water Cherenkov detector 134
muon neutrino 77, 83, 93, 97, 100
muon-induced fast neutrons 141
muon-induced spallation products 164
muon-like neutrinos 85
muon-neutrino spectrum 100
muon-veto systems 106
35 MW thermal power Siloé reactor 158

n

natural radioactivity 141–142, 146, 171
near detector 93–94, 96, 98–99, 102, 106, 132, 134, 137, 206
Neutral Current Detectors (NCDs) 171–172, 175
neutral Higgs boson 69
neutrino interaction vertex 87

neutrino mass eigenstates 2, 75, 111–112, 128
neutrino mass hierarchy (NMH) 91, 99–100, 127–135
neutrino oscillation experiments 1, 75
  appearance experiments 84
  atmospheric neutrinos 84–92
  reactor neutrino 100–109
neutrino-electron elastic scattering 145, 146, 206
neutrinoless double β decays 120–121, 123, 196
neutrino physics
  matter effects 80–84
  neutrino oscillation experiments, *see* neutrino oscillation experiments
  neutrino oscillations 75–80
  neutrinos in the standard model 69–75
neutrinos in the standard model 69–75
Newton–Raphson scheme 36
non-oscillated neutrino spectrum 102
non-oscillated reactor neutrino spectrum 102
non-relativistic neutrinos 119
non-scintillating buffer liquid 107
non-standard particle physics 65–67
non-standard solar physics 63–65
non-trivial neutrino mixing parameter 75
non-vanishing neutrino masses 1
non-zero neutrino masses 75, 115
normal ordering (NO) 25, 38, 110–111, 123, 131
normalization constant 146
normalized two-component spinors 71
nuclear rate uncertainties 61
nuclear reaction rates 25–31, 37, 44, 52, 58–59, 61
nuclear reactions 15–16, 42, 58, 67

o

obey Maxwellian distributions 25
organic liquid scintillator experiment 140, 179
oscillation wavelength 78
oscillation-generated τ-neutrinos 91
overadiabaticity 11, 42

p

pep neutrinos 29, 30, 43, 45, 46, 62, 83, 154, 190, 197–199
phenylxylylethane 181
photomultiplier tubes (PMTs) 147–149, 162, 164–166, 170–171, 175, 179–182, 185–187, 189, 199, 204
Planck mission 118
Pontecorvo, Bruno 75, 141
Pontecorvo–Maki–Nakagawa–Sato matrix 76
positron annihilation energy 102
pp chains 25, 26, 29, 30, 37, 40, 41, 43
pp neutrinos 30, 43, 45, 46, 62, 40, 43, 139, 153–154, 187, 190, 198, 203
Precision IceCube Next Generation Upgrade (PINGU) project 128–129
pressure ionization 20
ProtoDUNE modules 133
pseudocumene (PC) 179, 181–183
pseudocumene unloading 183
PXE based scintillator 181

q

quark-antiquark pairs 69
quarks 69, 72, 86
quasi-elastic scatter interactions 86, 88
quenching factor 185
quenching parameter 184

r

radiative neutrino decay 117
radiative opacity 6, 24, 41, 55, 57, 59
^{232}Th radioactive decay chain 146, 200
radiochemical detectors 146
radiochemical experiments 2, 44, 65, 140–141, 191
reactor neutrino 79, 100–109, 129–130, 136, 199–200
real time sub-MeV solar neutrino detector 181

red giant branch (RGB) phase 38–39
relativistic Lorentz boost factor 88
relic neutrinos 117, 119, 166, 169
RENO 105–107, 110
RENO-50 131
right-handed charged leptons 70
Rosseland mean opacity 7, 17, 21, 23–24, 57

S

Sanford Underground Research Facility (SURF) 132–133, 141, 206
satellite based X-ray telescopes 120
Schwarzschild criterion 9, 55, 64
see-saw mechanism 121
short baseline reactor neutrino experiment 103
Smirnov–Cramer–Von Mises method 159
solar abundances 12, 33–35, 56–57
  problem 1, 47, 54–59, 62, 140, 191, 195
  tables of 34
solar age 31, 35, 39
solar CNO-neutrinos 83
solar composition/solar modeling problem 1, 19, 34, 42, 44–46, 52, 56, 59
solar convective envelope 11–12, 14, 41, 48
solar luminosity 32, 40, 43, 45, 59, 66–67, 153, 198
solar mass 31
solar metallicity 195
solar modeling 1, 56, 65
solar models beyond SSM 2, 62–67
solar neutrino problem (SNP) 65, 139–140, 149, 151, 153–154, 156, 195
solar neutrino puzzle 2
solar neutrino survival probability 1777–178
solar neutrinos 1
  fluxes 44
  neutrino production 42
  power-law 45
  solar abundance problem 47
  solar luminosity 43
solar neutrino experiments 140
  Borexino 178–190
  ^{37}Cl experiment 140–145
  Deep Underground Neutrino Experiment (DUNE) 206–207
  Hyper-Kamiokande 204–206
  JUNO and LENA 199–204
  Kamiokande-II experiments 139
  Kamiokande-II/III 145–153
  positron annihilation 139
  super-Kamiokande 162–169
solar radius 32, 35, 41, 59, 83
solar structure and evolution
  changes in chemical composition 11–17
  energy conservation and transport, *see* energy conservation and transport
  full Set of equations and boundary conditions 17–18
  mechanical structure of stars 3
solar zenith angle distribution 173
solar maximum mission 117
Soviet-American Gallium neutrino Experiment (SAGE) 136, 153, 159–162
spectroscopic abundances 32–34, 65
β spectroscopy 112
standard solar models 3, 31–42, 58, 65, 145, 150–152, 196
  previous and future evolution 36–39
Stefan–Boltzmann constant 18
sterile neutrinos 2, 84, 119–120, 127, 135–137, 170, 175, 197–198
sub-MeV solar neutrino detection 179, 181, 196
Sudbury Neutrino Observatory (SNO) 2, 45, 109, 139, 162, 169–178, 189, 191–192, 196, 206
The Sun today 39–42, 67
super low energy (SLE) threshold 165
Super-Kamiokande (SK) experiment 2, 74, 85–88, 90–97, 109–110, 116, 128, 139, 153, 162–169, 174, 189, 191–193, 204

Supernova modeling 115
surface composition 32–35, 44, 54

t
tachocline 64
Teflon-lined chemical reactors 159
terrestrial (geo-) neutrinos 104
thermal nuclear reactions 25
thermo-nuclear fusion reactions 1, 203
Thomson scattering 23
threshold effect 146
time-dependent Friedmann equation 117
total atmospheric neutrino flux 85
total solar irradiance (TSI) 32
trimethylborate (TMB) 179
two-component spinors 71, 121
two-dimensional Pauli-matrices 71

u
U- and Pu-isotopes 101–102
uncertainties in SSMs
  equation of state 60
  luminosity and age 59
  microscopic diffusion 59
  nuclear reaction rates 58–59
  radiative opacity 59
  solar composition 59
  solar radius 59
underground water detector SuperKamiokande 74
unoscillated rate ratio 167, 168, 185–186
unstable mesons 85
upgraded Kamiokande detector 147

v
Valle–Schechter theorem 121
vinyl ester resin 155
virial theorem 36
visible energy 101–102, 169, 171–173, 187, 199, 201

w
warm dark matter 120
water Cherenkov detectors 44, 85–86, 91, 134, 145, 153, 165
water Cherenkov Hyper-Kamiokande 204
wave number-frequency diagram 48
weak coupling constant 73–74, 102
weak exchange bosons 72, 74
weak screening/Salpeter approximation 29
weakly interacting massive particles (WIMPs) 65
Weinberg-angle 73–74

y
Yukawa couplings 121, 135